# POSITRON-NEUTRINO CORRELATION MEASUREMENTS IN THE BETA DECAY OF MAGNETO-OPTICALLY TRAPPED $^{38\mathrm{m}}$K ATOMS

by

Alexandre I. Gorelov
Diploma of Physics, Moscow Institute of Physics and Technology, 1977

A thesis submitted in partial fulfillment
of the requirements for the degree of
DOCTOR OF PHILOSOPHY
in the
Department of Physics

Simon Fraser
University

SIMON FRASER UNIVERSITY
Summer 2008

TRIUMF

# APPROVAL

| | |
|---|---|
| **Name:** | Alexandre I. Gorelov |
| **Degree:** | Doctor of Philosophy |
| **Title of thesis:** | **Positron-Neutrino Correlation Measurements in the Beta Decay of Magneto-Optically Trapped $^{38m}$K Atoms** |
| **Examining Committee:** | Dr. Karen Kavanagh – Chair<br>Professor |
| | Dr. Peter Jackson – Senior Supervisor<br>Senior Research Scientist Emeritus, TRIUMF |
| | Dr. John D'Auria<br>Professor Emeritus |
| | Dr. Howard Trottier<br>Professor |
| | Dr. Alejandro Garcia – External Examiner<br>Professor, UNIVERSITY OF WASHINGTON (SEATTLE) |
| | Dr. Paul Haljan – Internal Examiner<br>Assistant Professor |
| **Date Approved:** | July 21, 2008 |

# Abstract

This thesis describes the measurement of the angular correlation between the positron and the neutrino emitted in the beta decay of the isomer $^{38\mathrm{m}}$K. This is a superallowed transition between nuclear states of the same spin and parity ($0^+$) which is known to result primarily from the vector component of the weak interaction. The angular correlation involves two parameters. In the Standard Model of the weak interaction these have the values $a = 1$ and $b = 0$. Any meaningful deviation from this result can be interpreted as evidence for the existence of a scalar component in the weak interaction.

The fundamentally new method that was used involved selectively confining neutral atoms of the isomer in a magneto-optical trap located between two detectors, one to measure the energy and direction of the positron and the other to detect the $^{38}$Ar nuclei that recoil with a momentum $\boldsymbol{p}_{R} = -(\boldsymbol{p}_e + \boldsymbol{p}_\nu)$. The $^{38\mathrm{m}}$K atoms were produced using the TRIUMF/ISAC facility. The trap provided a pure, cold, compact source essential to avoid distortion of the recoil momenta. For those events in which the positron was detected, the recoil momenta were deduced by measuring the time of flight from the trap to the recoil detector.

About 500,000 positron-recoil coincident events were recorded. When the analysis, based on detailed Monte Carlo simulations, was restricted to positrons with kinetic energy $> 2.5\,\mathrm{MeV}$, it showed that the angular correlation could be characterized by a "reduced" correlation parameter $\tilde{a} = 0.9988 \pm 0.0028(\mathrm{stat}) \pm 0.0034(\mathrm{syst})$ ($68\%$ $CL$) where $\tilde{a} = a/(1 + 0.1503\, b)$. This measurement is consistent with the Standard Model and is 33% more restrictive than the only comparable previous measurement for such a transition.

In the most general form, the strength of a possible scalar interaction can be specified in terms of two complex numbers, $L$ and $R$, which define, respectively, the coupling to left- and right-handed neutrinos. This experiment did not usefully restrict the value of $\mathcal{R}e(L)$ (or $b$). Other experiments do provide rather strict limits on $\mathcal{R}e(L)$. If these are combined with the result of the present experiment one obtains the most restrictive direct limits available on $\mathcal{R}e(R)$, $\mathcal{I}m(R)$ and $\mathcal{I}m(L)$.

# Table of Contents

**Approval** ii

**Abstract** iii

**Table of Contents** iv

**List of Tables** viii

**List of Figures** x

**Chapter 1 Beta-Neutrino Correlations in Nuclear Beta Decay.** 1

1.1 Introduction. . . . . . . . . . 1
1.2 Nuclear beta decay: Superallowed Fermi transitions. . . . . . . . . . 5
1.3 The Present Experiment. . . . . . . . . . 7

**Chapter 2 Beta-Neutrino Correlation Experiment.** 8

2.1 $^{38m}$K - the isotope of choice. . . . . . . . . . 9
2.2 Magneto-optical trap. Damping and confining forces . . . . . . . . . . 11
2.3 Radioactive potassium source. . . . . . . . . . . 14
  2.3.1 Target, ion source, separator. . . . . . . . . . 14
  2.3.2 Ion neutralization - choice of material. . . . . . . . . . 17
2.4 TRINAT double MOT system. . . . . . . . . . 20
  2.4.1 Collection trap. . . . . . . . . . 20
  2.4.2 Atom transfer. . . . . . . . . . 22
  2.4.3 Detection chamber. . . . . . . . . . 23
2.5 Nuclear detection system. . . . . . . . . . 25
  2.5.1 The recoil detector. . . . . . . . . . 27
  2.5.2 The recoil detector spatial calibration. . . . . . . . . . 30

2.5.3 The positron detector. . . . . . . . . . . . . . . . . . . . . . . . . 33
2.5.4 Electrostatic focusing system. . . . . . . . . . . . . . . . . . . . . . 35
2.5.5 Operation of the experimental apparatus. . . . . . . . . . . . . . 38
2.5.6 Data acquisition system of the experiment. . . . . . . . . . . . . 39

**Chapter 3 Data Analysis. 44**

3.1 Monte Carlo simulations. . . . . . . . . . . . . . . . . . . . . . . . . . 45
3.2 The principles of the data analysis. . . . . . . . . . . . . . . . . . . . 48
3.3 Experimental data. . . . . . . . . . . . . . . . . . . . . . . . . . . . . 49
3.4 Energy calibration of the scintillator with double coincident events. . . 51
3.4.1 Direct fit of the double coincident energy spectrum. . . . . . . . 54
3.4.2 Calibration fit over the two separated regions. . . . . . . . . . . 55
3.4.3 Calibration using the value of the pedestal in the scintillator ADC as an offset. . . . . . . . . . . . . . . . . . . . . . . . 57
3.5 Instant of the beta decay – reference point of the TOF measurements. . 61
3.6 Evaluation of the trap position along the detection axis. Neutral recoils: analysis of the TOF and the detection efficiency. . . . . . . . . . . . . 65
3.6.1 Shape of the $\mathrm{Ar}^0$ TOF spectrum. . . . . . . . . . . . . . . . . 66
3.6.2 MCP detection efficiency of $\mathrm{Ar}^0$. . . . . . . . . . . . . . . . . 67
3.6.3 Fit of the neutral Ar TOF spectrum for longitudinal trap position and size. . . . . . . . . . . . . . . . . . . . . . . . . . 69
3.7 Evaluation of the electric field strength. . . . . . . . . . . . . . . . . . 71
3.7.1 Evaluation of the electric field strength and longitudinal trap size by fitting the front edges of the $\mathrm{Ar}^{+1}$, $\mathrm{Ar}^{+2}$ and $\mathrm{Ar}^{+3}$ TOF spectra. . . . . . . . . . . . . . . . . . . . . . . . . . . . 71
3.7.2 Separate fits of $\mathrm{Ar}^{+1}$, $\mathrm{Ar}^{+2}$ and $\mathrm{Ar}^{+3}$ TOF spectra. . . . . . . . 73
3.7.3 Fit of $\mathrm{Ar}^{+1}$ TOF spectrum from MCP triggered events. . . . . . 74
3.7.4 $^{38\mathrm{m}}\mathrm{K}^{+}$ photoions as a probe of the electric field. . . . . . . . . . 78
3.7.5 Constraints on electric field non-uniformity. . . . . . . . . . . . 83
3.8 Transverse trap size and position. . . . . . . . . . . . . . . . . . . . . 85
3.8.1 Application of the mask calibration to photoions. . . . . . . . . 85
3.8.2 Spatial calibration of the RA with MCP hits by fast $\mathrm{Ar}^{+1}$ ions. 87
3.8.3 Application of the "fast $\mathrm{Ar}^{+1}$" calibration to the photoions. Transverse trap size and position. . . . . . . . . . . . . . . . . 90
3.8.4 Recoil impact energy and spatial dependencies of the MCP detection efficiency. . . . . . . . . . . . . . . . . . . . . . . . . . . 91
3.9 Data selection and binning for analysis of the $\beta-\nu$ correlation. . . . . . 93

3.10 Scintillator energy calibration with triple coincident events. . . . . . . . 96
3.11 Recoiling ion charge state distribution and effects of recoil energy dependent electron shakeoff corrections. . . . . . . . . . . . . . . . . . . . . . 99

**Chapter 4 Fits, Results and Systematic Errors. 103**
4.1 Evaluation of the angular correlation parameters. . . . . . . . . . . . . . 103
 4.1.1 $\chi^2(L,R)$ for scintillator ADC channel range 200−1550. . . . . . 111
 4.1.2 $\chi^2(L,R)$ for scintillator ADC channel range 550−1550. . . . . . 113
 4.1.3 $\chi^2(L,R)$ for scintillator ADC channel range 750−1550. . . . . . 113
4.2 Evaluation of the systematic errors. . . . . . . . . . . . . . . . . . . . . 117
 4.2.1 Effects due to electric field strength uncertainties. . . . . . . . . 118
 4.2.2 Effects due to electric field non-uniformity. . . . . . . . . . . . . 118
 4.2.3 Systematic errors due to the scintillator energy calibration. . . . 119
 4.2.4 Positron detector response function shape: low energy tail. . . . 120
 4.2.5 Positron detector response function shape: Compton summing of the 0.511 MeV annihilation gamma quanta. . . . . . . . . . . 124
 4.2.6 Effects of MCP efficiency dependence on incident recoil angle. . 127
 4.2.7 Effects of MCP efficiency dependence on incident energy. . . . . 128
 4.2.8 Systematic error due to the prompt peak position uncertainties. 129
 4.2.9 Systematic errors due to the transverse trap position uncertainties. 130
 4.2.10 Electron shakeoff correction uncertainties. . . . . . . . . . . . . 130
 4.2.11 Summary of the systematic errors of the experiment. . . . . . . 131
4.3 Results of the present experiment (assuming $\mathcal{I}m(L) = 0$). . . . . . . . 133

**Chapter 5 Discussion of Present Results and Future Development. 134**
5.1 Present Results. . . . . . . . . . . . . . . . . . . . . . . . . . . . . . . 134
5.2 Physics Impact of the Present Experiment. . . . . . . . . . . . . . . . . 137
5.3 Systematic Limitations on the Present Experiment. . . . . . . . . . . . 138
 5.3.1 Quality of the fits $\chi^2(L,R)$ for Scin.ADC$<$ 750. . . . . . . . . . 138
 5.3.2 Incomplete collection of the recoil ions and TOF separation of the $\mathrm{Ar}^{+1}$, $\mathrm{Ar}^{+2}$ and $\mathrm{Ar}^{+3}$ ion distributions. . . . . . . . . . . . 139
 5.3.3 Discrepancy between the predicted and measured strength of the electric field. . . . . . . . . . . . . . . . . . . . . . . . . 140
 5.3.4 Failure to account for the positron double coincident energy spectrum. . . . . . . . . . . . . . . . . . . . . . . . . . . . . 141
 5.3.5 Spatial calibration of the recoil detector. . . . . . . . . . . . . 141
5.4 Future Prospects. . . . . . . . . . . . . . . . . . . . . . . . . . . . . . 142
 5.4.1 Increased population of trapped $^{38\mathrm{m}}$K. . . . . . . . . . . . . . 142

5.4.2 Larger MCP-based recoil detector with delay-line anode readout. 142
5.4.3 Stronger, more uniform electric field. . . . . . . . . . . . . . . . . 143
5.4.4 Beta detector: response and calibration. . . . . . . . . . . . . . 144
5.4.5 Measurements of electron shakeoff dependence on recoil momentum. . . . . . . . . . . . . . . . . . . . . . . . . . . . . . . . . . 145

**Chapter 6 Summary. 146**

**Appendix A Parametrization of the Beta Detector Response. 149**

**Appendix B Electric field by Comsol 3.2. 151**

**Appendix C Kinematic Reconstruction: Measurements of the Beta Detector Response. 154**

**Appendix D Coupling constants. Limits from the present experiment. 157**

**Bibliography 161**

# List of Tables

1.1 Lorentz-invariant forms of interactions. . . . . . . . . . . . . . . . . . . . . 3

2.1 Thermionic work functions of some refractory metals. . . . . . . . . . . . 16
2.2 Calcium zirconate target yield. . . . . . . . . . . . . . . . . . . . . . . . . 17
2.3 Electrode potentials resulting from the fitting procedure. . . . . . . . . 38

3.1 Energy calibration using double coincident events. Channels $90-1800$. 54
3.2 Energy calibration with double coincident events simultaneously fitting the two separated channel ranges $90-165$ and $650-1800$. . . . . . . . . 56
3.3 Numerical results of the fit of the pedestal. . . . . . . . . . . . . . . . . . 58
3.4 Quality of the calibration fits when using ADC pedestal as *Offset* over the set of ADC channel ranges. . . . . . . . . . . . . . . . . . . . . . . . 60
3.5 Fits of the prompt peak with different thresholds in the scintillator signal. 64
3.6 Fitting of the trap position with $\mathrm{Ar}^0$ TOF spectra over three scintillator ADC overlapping ranges. . . . . . . . . . . . . . . . . . . . . . . . 70
3.7 Simultaneous fitting of the electric field strength and trap size along the detection axis with $\mathrm{Ar}^{+1}$, $\mathrm{Ar}^{+2}$ and $\mathrm{Ar}^{+3}$ TOF spectra over three scintillator ADC overlapping ranges. . . . . . . . . . . . . . . . . . . . 72
3.8 Separate fitting of the electric field strength and trap size along the detection axis with $\mathrm{Ar}^{+1}$, $\mathrm{Ar}^{+2}$ and $\mathrm{Ar}^{+3}$ TOF spectra over three overlapping scintillator ADC ranges. . . . . . . . . . . . . . . . . . . . . . . 74
3.9 Fits of the electric field strength with $\mathrm{Ar}^{+1}$, $\mathrm{Ar}^{+2}$ and $\mathrm{Ar}^{+3}$ TOF spectra over three scintillator ADC overlapping ranges for 3 values of the angular correlation parameter. . . . . . . . . . . . . . . . . . . . . . . . 75
3.10 Results of the fits of MCP triggered $\mathrm{Ar}^{+1}$ TOF spectrum over the several TDC channel ranges, with simultaneous variations of the trap size, electric field strength and background level. . . . . . . . . . . . . . 77
3.11 Centroids of the prompt peak with statistical errors. . . . . . . . . . . . 81
3.12 Centroids of photoion peak (with statistical errors). . . . . . . . . . . . 81

3.13 Evaluation of the calibration slope from the triple coincident events over different scintillator ADC channel ranges. . . . . . . . . . . . . . . 99

4.1 Standard input parameters for the simulations used to evaluate the angular correlation parameters. . . . . . . . . . . . . . . . . . . . . . . . 105
4.2 Partial values of $\chi^2$. . . . . . . . . . . . . . . . . . . . . . . . . . . . . . . 111
4.3 The best fit values of the angular correlation parameter $a$ evaluated for the extreme values of the electric field strength with $b = 0$. . . . . . . . 118
4.4 The best fit value of $a$ in the presence of an electric field gradient with $b = 0$. . . . . . . . . . . . . . . . . . . . . . . . . . . . . . . . . . . . . 119
4.5 Angular correlations for extreme values of calibration slope. . . . . . . 120
4.6 Evaluation of the correlation parameter $a$ with modified response function tails. . . . . . . . . . . . . . . . . . . . . . . . . . . . . . . . . . 123
4.7 Calibration of the scintillator ADC and evaluation of the correlation parameter $a$ with a modified Compton summing intensity. . . . . . . . 126
4.8 The dependence of $\chi^2$ on the correlation parameter (with $b = 0$) in the absence and presence of MCP detection efficiency $\varepsilon$ dependence on Ar ion impact angle. . . . . . . . . . . . . . . . . . . . . . . . . . . . . . 127
4.9 Influence of the prompt peak uncertainties on correlation parameter. . . 129
4.10 Values of the fitted angular correlation parameter $a_{min}$ as a function of the shakeoff correction value $s_1$ for $\mathrm{Ar}^{+1}$ ($b = 0$). . . . . . . . . . . . . 131
4.11 Summary of the significant uncorrelated systematic errors. . . . . . . . 132

5.1 Combining the results of the present experiment and those of Adelberger *et al.* [34]. . . . . . . . . . . . . . . . . . . . . . . . . . . . . . 135
5.2 Upper limits of $|R|$. . . . . . . . . . . . . . . . . . . . . . . . . . . . . . . 136

C.1 Quality of the fits to the differential energy spectra. . . . . . . . . . . . 156

D.1 Limits on $\mathcal{I}m(L)$ that can be derived from the present experiment. . . 159

# List of Figures

1.1 The electromagnetism and Fermi's contact model of weak interaction in neutron decay. . . . . . . . . . . . . . . . . . . . . . . . . . . 2

2.1 Schematic of the apparatus arrangement. . . . . . . . . . . . . . . . . . . . 9
2.2 $^{38gs}$K and $^{38m}$K simplified decay schemes. . . . . . . . . . . . . . . . . . . . . . 10
2.3 One-dimensional model of the Magneto-Optical Trap. . . . . . . . . . . 13
2.4 The ISAC radioactive beam facility at TRIUMF, 2000 . . . . . . . . . . 15
2.5 Schematic of the BL1A tests. . . . . . . . . . . . . . . . . . . . . . . 18
2.6 $^{37}$K release measurements. . . . . . . . . . . . . . . . . . . . . . . . 19
2.7 Trapping cell . . . . . . . . . . . . . . . . . . . . . . . . . . . . . 21
2.8 Neutralizer assembly. . . . . . . . . . . . . . . . . . . . . . . . . . . 21
2.9 Schematic of transfer system. . . . . . . . . . . . . . . . . . . . . . . 22
2.10 Central cross section of the detection chamber. . . . . . . . . . . . . . . 24
2.11 Cross section of the detection chamber. . . . . . . . . . . . . . . . . . . 25
2.12 Zoom of the central part of the detection chamber. . . . . . . . . . . . 27
2.13 MCPs assembly in Z-stack configuration. . . . . . . . . . . . . . . . . . 29
2.14 Equivalent schematic of RA. . . . . . . . . . . . . . . . . . . . . . . . 29
2.15 MCP+RA assembly. . . . . . . . . . . . . . . . . . . . . . . . . . . 29
2.16 Mask for resistive anode calibration and calibration coordinates. . . . . 30
2.17 Non-calibrated and pulser calibrated electronic images of the mask. . . 31
2.18 Fit-transformed electronic images of the mask. . . . . . . . . . . . . . . 32
2.19 Beta telescope view. . . . . . . . . . . . . . . . . . . . . . . . . . . 33
2.20 Schematic view of the DSSD. . . . . . . . . . . . . . . . . . . . . . . 34
2.21 Three-dimensional view of the grid volume. . . . . . . . . . . . . . . . . 36
2.22 Element of the focusing system. . . . . . . . . . . . . . . . . . . . . . 37
2.23 Longitudinal component of the electric field. . . . . . . . . . . . . . . . 39
2.24 Electronic schematic diagram of the experiment. . . . . . . . . . . . . . 41

3.1 Monte Carlo simulation of $^{38}$Ar$^{+1}$ recoil TOF spectra with $a = 1.0$ and $a = 0.0$. . . . . 44
3.2 Triple coincident events from the runs, selected for the correlation parameter evaluation. . . . . 49
3.3 Preliminarily filtered triple events. . . . . 51
3.4 Experimental spectrum of energies detected in the scintillator from double coincident events. . . . . 52
3.5 Double coincident backgrounds. . . . . 53
3.6 Energy calibrations over single continuous ranges of ADC channels. . . . 55
3.7 Energy calibration over two separated ranges of ADC channels. . . . . 56
3.8 Pedestal in the scintillator ADC from MCP triggered events. . . . . 57
3.9 The pedestal in the scintillator ADC from MCP triggered events. . . . 58
3.10 Calibration with double coincident events with fixed *Offset*. . . . . 59
3.11 Fit of the scintillator observed energy spectrum with double coincident events. Fixed *Offset*=50.663. . . . . 60
3.12 Distribution of the prompt events as function of the detected time and pulse amplitude. . . . . 62
3.13 Scatter plot (left) and TOF spectrum (right) of the events with positrons scattered off the recoil detector. . . . . 62
3.14 Distribution of the prompt events triggered by positron backscattered off MCP as function of the detected time and pulse amplitude. . . . . 64
3.15 Fit of the prompt peak. . . . . 65
3.16 TOF spectrum of the Ar$^0$ recoiling atoms, detected in coincidence with the positron detector (Scin.ADC>800). . . . . 66
3.17 Fit of the MCP detection efficiency with Ar$^0$ TOF data. . . . . 69
3.18 Fit of trap size and position in $Z-$direction with Ar$^0$ TOF data. . . . . 70
3.19 Overlay of data (error-bars) and fitting function (solid) from fits of the longitudinal trap size and electric field strength using ions Ar$^{+1}$, Ar$^{+2}$ and Ar$^{+3}$ simultaneously. . . . . 72
3.20 MHTDC6 spectrum of MCP triggered events. . . . . 76
3.21 TOF spectrum of the Ar$^{+1}$ ions in the MHTDC6 selected for electric field evaluation and triggered by the MCP. . . . . 76
3.22 Fits and residuals of the MHTDC6 spectrum of MCP triggered events in the region of the Ar$^{+1}$. . . . . 78
3.23 TOF distribution of the photoionization events. . . . . 79
3.24 MCP signal pulse height distribution of the prompt events. . . . . 80
3.25 TOF$-$MCP two-dimensional distributions of the prompt peak events. . 80

3.26 Peak events of the photoions. . . . . . . . . . . . . . . . . . . . . . . . . . 81
3.27 Measured $\Delta t = t_{photo} - t_{prompt}$) for the photoions. . . . . . . . . . . . . 82
3.28 Relations between the field strength in center of the chamber and its gradient conserving TOF. . . . . . . . . . . . . . . . . . . . . . . . . . . 84
3.29 RA pulse height distribution, spatial scatter plot of events in the MCP and transverse density distribution in the MCP for events, triggered by the UV laser. . . . . . . . . . . . . . . . . . . . . . . . . . . . . . . . 86
3.30 Radial and angular distribution of the MCP hits by the $\mathrm{Ar}^{+1}$ ions for triple coincident events for mask calibration. . . . . . . . . . . . . . . . 88
3.31 Radial and angular distribution of the MCP hits by the $\mathrm{Ar}^{+1}$ ions for triple coincident events for aperture spatial calibration. . . . . . . . . . 90
3.32 The scatter plot of the photoion events using the "fast $\mathrm{Ar}^{+1}$" spatial RA calibration. . . . . . . . . . . . . . . . . . . . . . . . . . . . . . . 91
3.33 Absolute MCP detection efficiency as a function of the ion impact energy. 92
3.34 MCP detection efficiency as function of the angle between the channel and velocity of the incident ions $\mathrm{H}^{+}$, $\mathrm{He}^{+}$ and $\mathrm{O}^{+}$. . . . . . . . . . . . . 92
3.35 The events considered for the $\beta$–$\nu$ correlation analysis. . . . . . . . . . 94
3.36 Energy calibration with triple coincident events. . . . . . . . . . . . . . 97
3.37 Energy spectrum of accidental background events. . . . . . . . . . . . . 98
3.38 Test of the Ar ions production and acceptance in Monte Carlo. . . . . . 101

4.1 An example of the recoil TOF spectra (4 ns/bin) comparing the data and simulation. . . . . . . . . . . . . . . . . . . . . . . . . . . . . . . . 106
4.2 An example of the recoil TOF spectra. ADC channel range 400–700. . 107
4.3 An example of the recoil TOF spectra. ADC channel range 700–1000. 108
4.4 An example of the recoil TOF spectra. ADC channel range 1000–1300. 109
4.5 An example of the recoil TOF spectra. ADC channel range 1300–1550. 110
4.6 Contour plot of $\chi^2$ as a function of $L$ and $R$ for the ADC channel range 200–1550. . . . . . . . . . . . . . . . . . . . . . . . . . . . . . . . 112
4.7 Contour plot of $\chi^2$ as a function of $L$ and $R$ for the ADC channel range 550–1550. . . . . . . . . . . . . . . . . . . . . . . . . . . . . . . . 113
4.8 Contour plot of $\chi^2$ as a function of $L$ and $R$ for the ADC channel range 750–1550. . . . . . . . . . . . . . . . . . . . . . . . . . . . . . . . 114
4.9 Contour plot of $\chi^2$ as a function of $L$ and $R$ for the ADC channel range 750–1550 over an extended range of $L$ and $R$. . . . . . . . . . . . . . 114
4.10 Contours of $\chi^2$ as function of $b$ and $a$. . . . . . . . . . . . . . . . . . . 115

4.11 Derivative of the correlation parameter as function of the electric field gradient. . . . . . . . . . . . . . . . . . . . . . . . . . . . . . . . . . . . 119
4.12 Comparison of the data and simulation for slow $\mathrm{Ar}^{+1}$ recoil events. . . 121
4.13 GEANT generated response of the scintillator for "non scattered" positrons of incident energies 1000 and 2000 keV for nominal and reduced by 10% tails. . . . . . . . . . . . . . . . . . . . . . . . . . . . . . . . . . . . . . 122
4.14 GEANT generated responses of the scintillator. . . . . . . . . . . . . . 124
4.15 Comparison of the data and simulation for slow $\mathrm{Ar}^{+1}$ recoil events. . . 126
4.16 $\chi^2$ as function of $a\,(b=0)$. . . . . . . . . . . . . . . . . . . . . . . . . . 127
4.17 Fit of the $\mathrm{Ar}^{+1}$ MCP detection efficiency as function of impact energy. 129

5.1 TOF spectra of Ar ions in upgraded geometry. . . . . . . . . . . . . . . 143

B.1 Potential distribution in the $X-Z$ plane. . . . . . . . . . . . . . . . . . 152
B.2 Axial and radial electric field along the detection chamber. . . . . . . . 152

C.1 The differential energy spectra. . . . . . . . . . . . . . . . . . . . . . . . 155

D.1 $\chi^2$ as function of the imaginary part of $L$. . . . . . . . . . . . . . . . . 158

# Chapter 1

# Beta-Neutrino Correlations in Nuclear Beta Decay.

## 1.1 Introduction.

Nuclear beta decay, which has proved to be an invaluable tool in nuclear and particle physics, was discovered in 1899 when Rutherford observed beta "rays" (as well as alpha "rays") from uranium. In the next year by means of the application of a magnetic field, beta "rays" were identified as electrons while identification of alpha "rays" as a stream of particles happened in 1903. In 1914, using a primitive form of what was later to be called a Geiger counter, Chadwick obtained clear evidence for the continuous spectrum of beta particle energies in contrast with the discrete energy spectra of observed alpha particles and gamma rays. Based on this evidence Pauli in 1931 (twenty-five years before its existence was proved [1, 2]) proposed that beta decay is in reality a 3–body process in which the beta particle shares momentum with a very light (or even massless) evasive neutral particle that interacts very weakly with matter and so escapes detection. Fermi called this particle a "neutrino" and incorporated it in his theory of nuclear beta decay in 1933-1934 [3, 4, 5].

Inspired by the vector structure of the electromagnetic interaction (See Fig 1.1) and suggesting that the interaction is weak, he used perturbation theory and derived an expression for the differential decay rate in beta decay

$$P(E)dE = \frac{G_F^2}{(2\pi)^5}|\mathcal{M}_{fi}|^2 F(E,Z,R)(E_0-E)^2(E^2-1)^{1/2}EdE \tag{1.1}$$

as a function of total beta energy $E$. Here are used natural relativistic units where $\hbar = c = m_e = 1$, $m_e$ is an electron rest mass, and $G_F = 1.16637(1)\times10^{-5}\,(\hbar c)^3\mathrm{GeV}^{-2}$ [6] is the Fermi coupling constant defined now from the measurements of the muon lifetime, and $\mathcal{M}_{fi} = \int \psi_f^* V \psi_i d^3x$ is the matrix element of the interaction. $F(E,Z,R)$

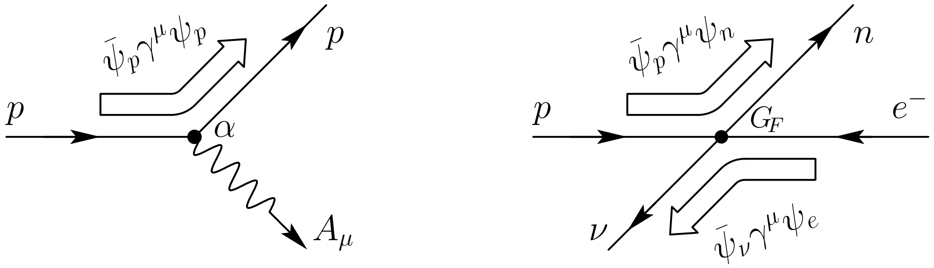

FIGURE 1.1: The electromagnetism (left) and Fermi's contact model of weak interaction in $\beta^+$ decay. The interaction of hadron and lepton currents with coupling $G_F$ is presumed to be an analogue of the interaction of proton and electromagnetic field with coupling $\alpha$. In accordance with the rules of Feynman diagram plotting an outgoing positron is shown as an incoming electron.

is the so called Fermi function accounting for the Coulomb interaction of the beta particle with the daughter nucleus of charge $Z$. Fermi derived it in an analytic form

$$F(E, Z, R) = 4\,(2pR)^{2(s-1)}\,e^{-\pi\eta}\,\frac{|\Gamma(s+i\eta)|^2}{|\Gamma(1+2s)|^2}, \tag{1.2}$$

where $p$ is the momentum of beta particle, $\eta = \pm E/p$ for $\beta^\pm$ decays, $s^2 = 1 - \alpha^2 Z^2$, $R$ is the nuclear radius, and $\alpha = e^2/4\pi$ is the fine structure constant. The rest of expression (1.1) represents the density of the states available in the final state of energy $E$, a so called statistical factor, and mostly defines the shape of the observable beta spectra with $E_0$ being the energy shared between the neutrino and the beta particle.

At the time most known radioisotopes subject to beta-decay were classified by one of two experimental Sargent curves [7], a graph of the logarithms of decay constants against logarithms of the corresponding maximum beta-particle energies. Those graphs were essentially two parallel straight lines.

The Fermi model described the upper curve in terms of "allowed" (vector) transitions involving no change of the spins of the nucleons ($\Delta J = 0$) while those on the lower curve required the leptons to carry one unit of the orbital angular momentum. Gamow and Teller [8] noted that only if the "allowed" nucleus matrix elements could be either vector or axial vector (explicitly involving the spins of the nucleus, $\Delta J = 0, \pm 1$ but $0 \not\to 0$) could one properly account for several known transitions that appeared to lie on the upper Sargent curve.

It is worth noting that when Fermi published his theory, Pauli had already shown [9] that the perturbation could have only five different forms if the Hamiltonian is to be relativistically invariant. These are $S$, the scalar interaction; $V$, vector; $T$, tensor; $A$, axial vector; and $P$, pseudoscalar (See Tab 1.1). The Fermi and Gamow Teller results

TABLE 1.1: Lorentz-invariant forms of interactions.

| Interaction type | Operator form | Parity |
|---|---|---|
| Scalar, $S$ | $\mathbf{1}$ | $+$ |
| Pseudoscalar, $P$ | $\gamma_5$ | $-$ |
| Vector, $V$ | $\gamma_\mu$ | $-$ |
| Axial Vector, $A$ | $\gamma_\mu\gamma_5$ | $+$ |
| Tensor, $T$ | $\gamma^\mu\gamma_\nu - \gamma^\nu\gamma_\mu$ | N/A |

were obtained using just two particular cases: vector and axial vector interactions, but there were no experimental data that would contradict the additional inclusion of scalar or tensor interactions into the Hamiltonian.

There wasn't much experimental activity to clarify the exact form of the Hamiltonian in beta decay until the middle of the 1950's †, when Lee and Yang, analyzing the available experimental data on the decay of kaons, questioned the validity of parity conservation in weak interactions [13]. They wrote the most general expression for the Hamiltonian of beta decay ($S, V, T, A.P$ forms) including both parity conserving and parity violating terms (Eq 1.3):

$$\begin{aligned} H_{int} \quad = \quad & (\overline{\psi}_p\psi_n)(C_S\overline{\psi}_e\psi_\nu + C'_S\overline{\psi}_e\gamma_5\psi_\nu) \\ + \quad & (\overline{\psi}_p\gamma_\mu\psi_n)(C_V\overline{\psi}_e\gamma_\mu\psi_\nu + C'_V\overline{\psi}_e\gamma_\mu\gamma_5\psi_\nu) \\ + & \frac{1}{2}(\overline{\psi}_p\sigma_{\lambda\mu}\psi_n)(C_T\overline{\psi}_e\sigma_{\lambda\mu}\psi_\nu + C'_T\overline{\psi}_e\sigma_{\lambda\mu}\gamma_5\psi_\nu) \\ - \quad & (\overline{\psi}_p\gamma_\mu\gamma_5\psi_n)(C_A\overline{\psi}_e\gamma_\mu\gamma_5\psi_\nu + C'_A\overline{\psi}_e\gamma_\mu\psi_\nu) \\ + \quad & (\overline{\psi}_p\gamma_5\psi_n)(C_P\overline{\psi}_e\gamma_5\psi_\nu + C'_P\overline{\psi}_e\psi_\nu) \quad + \quad \mathrm{HC}\ . \end{aligned} \tag{1.3}$$

They also have pointed out a set of experiments in both particle physics and nuclear beta decay which would provide an answer to the question about parity conservation in weak decays. The initial verification that parity is violated in the weak interaction

---

[†] In fact, earlier the experimenters did not have adequate tools to investigate the problem. With the availability of nuclear reactors, where it became possible to produce short-lived beta radioactive isotopes, such works started to appear. Initial studies of beta-neutrino angular correlations in the Gamow-Teller decay of $^6$He [10] appeared to clearly demonstrate the presence of a tensor interaction in such decays. Later it was shown that the experiment was prone to systematics which reversed the final result. See, e.g., [11]. Radiative corrections in a later analysis changed the answer slightly [12].

came from measurements of the asymmetry in the direction of the emission of betas with respect to the direction of nuclear polarization for the Gamow-Teller decay of $^{60}$Co [14, 15]. This result was followed immediately by the observation of a large asymmetry in the direction of positron emission in the decay of spin-polarized positive muons produced in the decay of stopped positive pions [16] (Both the polarization of the $\mu^+$ and the asymmetry of the subsequent positrons were the result of parity violation). Within the next year there were measurements of the longitudinal polarization of electrons emitted in the decay of (unpolarized) $^{60}$Co [17] and of positrons emitted in the decay of both $^{22}$Na [18] and $^{64}$Cu [19] as well as a remarkable experiment suggesting that the neutrinos emitted in the decay (by electron capture) of $^{152\mathrm{m}}$Eu have a helicity close to $-1$ [20].

The very first suggestions of parity violation in the weak interaction inspired Salam [21], Landau [22] as well as Lee and Yang [23] to independently suggest the possibility that in the weak interaction massless neutrino's are emitted fully polarized (helicity of $\pm 1$) and that parity is maximally violated. The experimental controversy of whether the weak interaction is primarily a Vector/Axial or Scalar/Tensor combination was finally resolved by a series of experiments deducing the beta-neutrino angular correlation from measurements of the energy spectra of the nuclear recoils following the decays of $^{35}$Ar, $^{6}$He and $^{23}$Ne [24, 25, 26].

The contemporary view of the weak interaction is described within a framework of the Standard Model (SM): a theory which describes the strong, weak, and electromagnetic fundamental forces, as well as the fundamental particles that make up all matter. In accordance with the SM the weak interaction is mediated by left-handed vector gauge bosons only: $W^{\pm}$ and $Z^0$, which are responsible for the interaction involving charged and neutral currents, respectively. In the same way, electromagnetism is described by the interaction of electromagnetic currents with photons acting as mediators. However, contrary to electromagnetism, the mediating weak bosons are massive ($M_W \approx 80\,\mathrm{GeV/c^2}$, $Z^0 \approx 91\,\mathrm{GeV/c^2}$), which results in the extremely short range of the weak force (of the order of $1/M_W \approx 0.003\,\mathrm{fm}$). Such a short range explains the high extent of validity of Fermi's contact model of beta decay. The masses of $W^{\pm}$ and $Z^0$ also explain the "weakness" of the weak interaction: despite the fact that the inherent weak coupling $g_w$ is about the same as electromagnetic one ($g_e = \sqrt{4\pi\alpha}$) the effective weak coupling is small due to the masses of mediating bosons. Fermi's coupling can be expressed in terms of the weak coupling and the $W$ boson mass as $G_F = \sqrt{2} g_w^2 / 8 M_W^2$. Despite the great success of the SM † there is a caveat: it con-

---

† The Standard Model predicted the existence of W and Z bosons, the gluon, the top quark and the charm quark before these particles had been observed. Their predicted properties were experimentally confirmed

tains 19 free parameters, such as particle masses, which are defined experimentally and cannot be calculated within the framework of the model. Since the completion of the Standard Model, many efforts have been made to address these problems (Grand Unified Theories, Super Symmetry, etc.) and to search for physics beyond the SM.

The first and the only experimental deviation from the Standard Model came in 1998, when Super-Kamiokande published results indicating neutrino oscillation [27] which implies the existence of non-zero neutrino masses and is forbidden in the SM. The experiments for other deviations from SM such as, for instance, existence of right-handed currents in muon decay [28, 29] still confirmed its validity at the level of experimental accuracy.

Over the last 40 years, although many of the crucial tests of the SM have been made at or near the "high energy frontier", precision measurements involving allowed nuclear beta decay have continued to play an important role [30, 31]. The basis for many of these experiments remains the expression (1.3) defining the most general form of the interaction. Although this could involve 10 complex coefficients, in the SM this is reduced to essentially two real numbers $C_V$ and $C_A$ ($C_S = C'_S = C_T = C'_T = C_P = C'_P = 0$, $C_V = C'_V$, $C_A = C'_A$ and both $C_V$ and $C_A$ are real). Within one year of the original paper by Lee and Yang [13], Jackson, Treiman and Wyld published two papers defining the consequences of (1.3) in terms of the distributions in angle, energy and polarization of the products [32, 33]. The results are expressed in terms of the coefficients $C_i$ with no assumptions regarding time reversal invariance. (The second of these two papers includes the effects of the emitted beta in the Coulomb field of the nucleus.)

## 1.2 Nuclear beta decay: Superallowed Fermi transitions.

Measurements of the positron-neutrino angular correlations for $0^+ \rightarrow 0^+$ transitions (between two nuclear states both with $J^\pi = 0^+$) provide a unique opportunity to test a prediction of the SM, that in (1.3), $C_S = C'_S = 0$. The nuclear spin selection rules forbid contributions from axial vector or tensor interactions. The positron-neutrino

---

with good precision.To get an idea of the success of the Standard Model a comparison between the measured and the predicted values of some quantities are shown in the following table [6]:

| Quantity | Measured [GeV/c$^2$] | SM prediction [GeV/c$^2$] |
|---|---|---|
| Mass of $W^\pm$ | $80.4250 \pm 0.0380$ | $80.3900 \pm 0.0180$ |
| Mass of $Z^0$ | $91.1876 \pm 0.0021$ | $91.1874 \pm 0.0021$ |

correlation can be defined in terms of the momentum vectors $\boldsymbol{p_e}$, $\boldsymbol{p_\nu}$

$$\begin{aligned}\frac{d\Gamma(\boldsymbol{p_e},\boldsymbol{p_\nu})}{dE_e d\Omega_e d\Omega_\nu} &\sim F(E_e,Z)\, p_e E_e E_\nu^2 \times \xi \left(1 + b\frac{m_e}{E_e} + a\frac{\boldsymbol{p_e}\cdot\boldsymbol{p_\nu}}{E_e E_\nu}\right)\\ &= F(E_e,Z)\, p_e E_e E_\nu^2 \times \xi \left(1 + b\frac{m_e}{E_e} + a\frac{p_e p_\nu}{E_e E_\nu}\cos\theta_{e\nu}\right) . \qquad (1.4)\end{aligned}$$

For a $0^+ \rightarrow 0^+$ beta transition the coefficients $\xi$, $a$ and $b$ are given, in the general case, by [33]:

$$\begin{aligned}\xi &= |M_F|^2(|C_V|^2 + |C'_V|^2 + |C_S|^2 + |C'_S|^2)\\ a\xi &= |M_F|^2[|C_V|^2 + |C'_V|^2 - |C_S|^2 - |C'_S|^2 + 2\frac{\alpha Z m}{p_e}\mathcal{I}m(C_S {C_V}^* + C'_S {C'_V}^*)]\\ b\xi &= -|M_F|^2 2\sqrt{1-\alpha^2 Z^2}\,\mathcal{R}e(C_S {C_V}^* + C'_S {C'_V}^*)\ , \qquad (1.5)\end{aligned}$$

where $|M_F|$ is the nuclear matrix element.

In the SM, $C_S = C'_S = 0$, $C_V = C'_V$ and consequently $a = 1$ and $b = 0$. The positron and neutrino are much more likely to be emitted in the same direction ($\theta_{e\nu} = 0$) than in opposite directions ($\theta_{e\nu} = \pi$). If, at the other extreme, the interaction was purely scalar ($C_V = C'_V = 0$,$C_S = C'_S$) the prediction of the angular correlation is exactly reversed ($a = -1$ and $b = 0$). The only pure Fermi transition for which the positron-neutrino correlation has been determined with good precision is the decay of $^{32}$Ar ($J^\pi = 0^+$, $T = 2$, $T_3 = -2$) to the isobaric analogue state ($J^\pi = 0^+$, $T = 2$, $T_3 = -1$) in $^{32}$Cl [34]. This excited state in $^{32}$Cl quickly decays by proton emission ($E = 3350\,\mathrm{keV}$) to the ground state of $^{31}$S. The precise energy of the beta-delayed proton depends on the vector sum of the momenta ($\boldsymbol{p_e} + \boldsymbol{p_\nu}$) and hence the distribution of the proton energies depends in a predictable way on the coefficients $a$ and $b$ in (1.5). Although the full energy width of the proton peak is only 30 KeV, the precisely measured shape was found to be consistent with $a = 1$ and yielded improved constraints on scalar weak interactions.

In contrast to the single example of the precise measurement of a positron-neutrino correlation for a pure Fermi transition [34], there is a long history of many measurements involving the absolute transition strengths and precise energies of decay for a series of superallowed Fermi transitions ranging from $^{10}$C to $^{74}$Rb (see for example [35, 36, 37, 38]). The primary goals of these experiments are precise tests of the Conserved Vector Current hypothesis and of the unitarity of the Cabibo-Kobayashi Maskawa (CKM) matrix. The conclusions drawn from an analysis of these and more recent data in the form of limits on the value of the Fierz interference term $b$ (1.4) are discussed in Chap 4 and Chap 5.

## 1.3 The Present Experiment

This thesis describes in detail the measurements of the positron-neutrino correlation in the superallowed decay of $^{38m}$K. During the completion of this task there have been several publications outlining progress towards this goal [39, 40, 41, 42] and [43].

During this period, in addition to the experiment described in this thesis, the TRINAT (Triumf Neutral Atom Trap) Collaboration was also involved in the completion of two experiments leading to the PhD's of both M. Trinczek [44] and D. Melconian [45].

Both the present experiment and the experiments described in the above references [44, 45] have used for data collection essentially the same apparatus (in the case of [45] two additional positron detectors were added to the original setup). The author of this thesis has made a crucial contribution in its development. In particular, he has designed a vacuum vessel for the collection trap described in Sec 2.4.1 including all elements such as the in-vacuum magnetic coils, the hollow cube-shaped quartz vapor cell, the conical neutralizer and the mechanical mount, which allowed a precise adjustment of this neutralizer near the quartz vapor cell. As described in Sec 2.4.1, the choice of material for these elements and their design was essential for maximization of the trapping efficiency and the following transfer of the trapped atoms into the detection chamber.

The nuclear detectors arranged there were also developed with the author's major contribution. While in the beta side of the detection system telescope he just designed a low $Z$ mount for the silicon double-sided strip $\Delta E$ detector shown in Fig 2.20, the recoil detection was the main part where his efforts were concentrated. A commercial MCP based recoil detector operated as part of the electrostatic focusing system, described in Sec 2.5.4. This system was completely designed by the author and manufactured under his direct supervision. Here the choice of materials was also essential to minimize some potentially harmful effects such as backscattering of positrons off the surfaces or patch effects that could have perturb the electric field.

The author also has substantially modified a TRIUMF-written RELAX3D code creating a package which allowed optimization of the electric field distribution in the detection chamber as also discussed in Sec 2.5.4. And, of course, one cannot omit the author's unique contribution in the development of the "fast" Monte Carlo simulation of the experiment (see Sec 3.1), which allowed him, with available computing power, to perform the data analysis described throughout this thesis.

## CHAPTER 2

# Beta-Neutrino Correlation Experiment.

The considerable progress in atomic physics since the first successful experiment trapping neutral atoms into a **M**agneto-**O**ptical **T**rap (MOT) [46] has provided the possibility of using this technique in nuclear physics experiments involving radioactive decay. The MOT can provide experimenters with a compact (about $1\,\mathrm{mm}^3$) source in the form of a gas with temperature of less than 1 mK. The recoiling nuclei, produced as a result of the decay, escape such a source freely without distortion of their momenta making possible precise measurements of their kinematic parameters.

TRIUMF's positron-neutrino ($\beta - \nu$) correlation experiment in its setup uses the TRINAT (**TRI**UMF **N**eutral **A**tom **T**rap) facility.The TRINAT project was initiated in 1993 with a goal to probe physics beyond the Standard Model (SM) with trapped radioactive neutral atoms. The scientific proposals using this facility suggested measurements of atomic parity non-conservation as a function of the number of neutrons in atomic transitions of trapped isotopes of Francium [47] and studies of the $\beta^+$ decay of short-lived potassium isotopes $^{37}$K ($\mathrm{t}_{1/2} = 1.22\,\mathrm{s}$) and $^{38\mathrm{m}}$K ($\mathrm{t}_{1/2} = 0.92\,\mathrm{s}$) [48]. The first results, which have shown our ability to produce and trap reasonable numbers of these isotopes of potassium resulted in measurements of their isotope shifts [39].

The heart of the experiment is the TRINAT trapping system. It includes a pair of three-dimensional MOTs with two two-dimensional ones in between (see schematic in Fig 2.1). Physically, they reside in two stainless steel vacuum vessels, situated 55 cm apart connected with a narrow pipe 25 mm in diameter. The radioactive $^{38}\mathrm{K}^+$ ion beam is delivered into the collection chamber, where it is thermalized and neutralized, and a portion of the $^{38\mathrm{m}}$K neutral atoms is optically trapped inside the quartz cell. The trapped atoms are resonantly pushed with a pulsed laser beam into the adjacent detection chamber, where they are re-trapped directly from the atomic beam. As shown in Fig 2.1, the positrons emitted in a narrow cone from the trap are observed

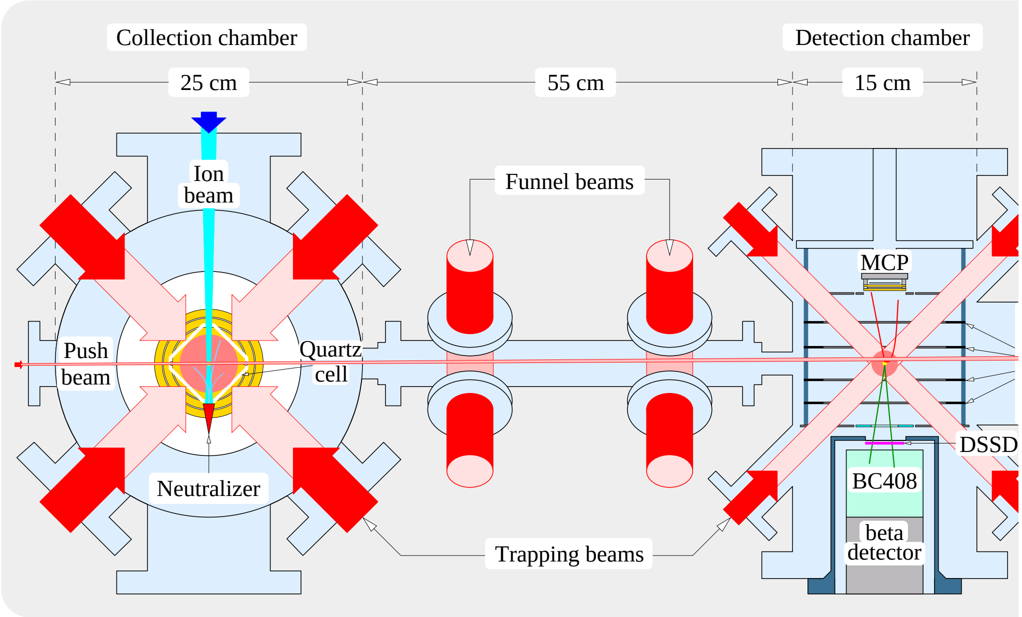

FIGURE 2.1: Schematic of the apparatus arrangement.

in a beta detector and a portion of the coincident recoil $^{38}$Ar atoms is detected in a microchannel plate (centered in the opposite direction). The fraction of $^{38}$Ar atoms detected is enhanced for those emitted as positive Ar ions ($\mathrm{Ar}^{+1}$, $\mathrm{Ar}^{+2}$, ...) ions by a uniform electric field directed toward the MCP. A small portion of the trapped atoms is ionized by a pulsed UV laser creating an image of the trap when these $^{38\mathrm{m}}$K ions are swept to the MCP.

In this chapter we provide the essential idea of the experiment and some details of the apparatus involved in the measurements of the $\beta - \nu$ correlations in $^{38\mathrm{m}}$K decay. In particular, we shall give a brief introduction to trapping techniques, isotope production and both the optical and nuclear experimental setups.

## 2.1 $^{38\mathrm{m}}$K - the isotope of choice.

For the high precision experiment to measure the beta-neutrino correlations in a $0^+ \rightarrow 0^+$ superallowed Fermi decay we have chosen atoms of the isomer, $^{38\mathrm{m}}$K. The decision was made because of the nuclear and atomic properties of this isomer. Besides the fact that $^{38\mathrm{m}}$K decays through a superallowed Fermi transition, it decays essentially exclusively ($> 99.998\%$ [49]) to the ground state of stable $^{38}$Ar (see the decay scheme on the right of Fig 2.2), reducing background activity and basically avoiding the need to observe or account for photons emitted in the decay. Also recoil-order corrections are $< 3\times10^{-4}$ and are calculable [50] while radiative corrections are at the 0.002 level but can be calculated to accuracy an order of magnitude better [51]. Concerning the atomic properties, potassium as an alkali atom has very simple hyperfine structure which facilitates its capture into the magneto-optical Zeeman trap. Last but not least, $^{38\mathrm{m}}$K can be produced at an adequate rate in the TRIUMF ISOL facility and delivered to the experimental apparatus.

However, at the entrance of the TRINAT facility we receive a mixture of $^{38\mathrm{m}}$K and $^{38}$K ground state ions which are produced simultaneously in the ISAC target and cannot be separated by the ISAC isotope separator. The $^{38}$K ground state nuclei have half-life 7.636 min and $\beta^+$ decay (see left side of Fig 2.2) predominantly to the 2.167 MeV state in $^{38}$Ar with the prompt subsequent emission of an energetic photon. Because of the considerably longer half-life of $^{38}$K ground state (7.636 min versus 0.923 s of $^{38\mathrm{m}}$K) and a larger nuclear spin, its abundance in the ion beam was typically 95-97% (see Tab 2.2) resulting in a big source of background in the first MOT. The fact that both MOTs (and the laser push beam) are effective on only the $^{38\mathrm{m}}$K atoms makes the background arising from $^{38}$K ground state essentially negligible in the final $\beta^+$–Ar coincidence data.

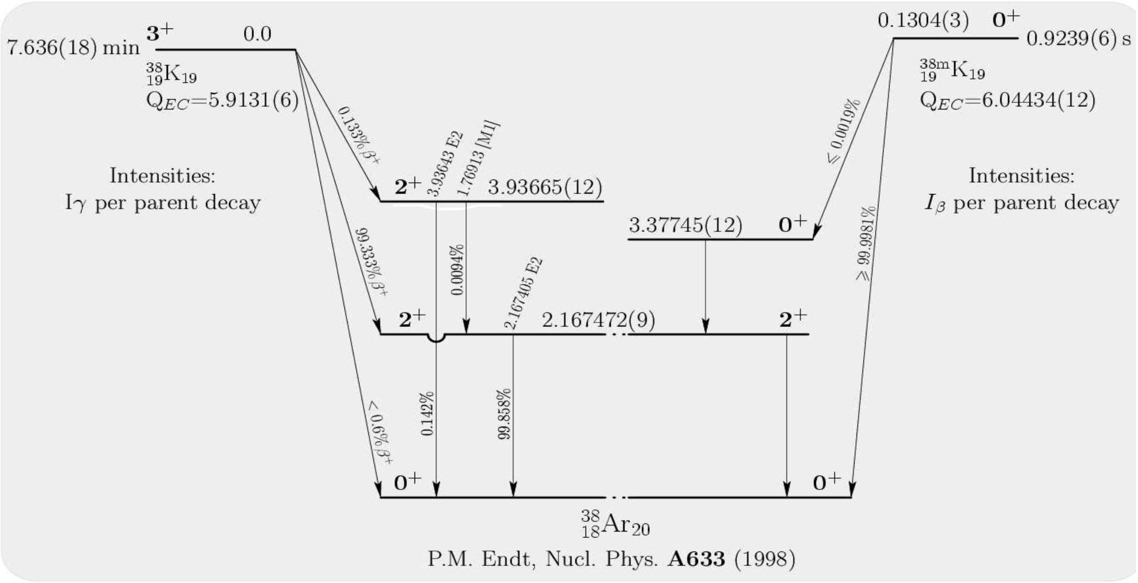

P.M. Endt, Nucl. Phys. **A633** (1998)

FIGURE 2.2: $^{38\mathrm{gs}}$K (left) and $^{38\mathrm{m}}$K (right) simplified decay schemes.

## 2.2 Magneto-optical trap. Damping and confining forces.

Neutral atoms that are placed in an optical field feel a radiation pressure due to the scattering of photons. The scattering rate grows as the light frequency $\omega$ is tuned closer to the atomic resonance frequency $\omega_A$ (when the detuning $\Delta = \omega - \omega_A$ becomes small). Due to the Doppler effect, atoms with different thermal velocities see a different effective frequency of the optical field. Those of them for which

$$|\Delta - \boldsymbol{k}\cdot\boldsymbol{v}| < \Gamma \ , \tag{2.1}$$

interact with the light most strongly. Here the $\boldsymbol{k}, \boldsymbol{v}$ and $\Gamma = 1/\tau$ are the light wave vector, atom velocity and atomic resonance width respectively and $\tau$ is the mean lifetime of the excited atomic state. If the applied light field is red-detuned ($\Delta = \omega - \omega_A < 0$), then atoms that move toward the light with velocities as in (2.1) scatter light most effectively and, hence, slow down. The arrangement of three sets of intersecting orthogonal counter-propagating red-detuned laser beams will create a damping force in all directions, acting as so called "optical molasses". In the approximation of small atomic velocities and light intensities the damping Doppler force can be written as [52]:

$$\boldsymbol{F}_D(\boldsymbol{v}) = 8\hbar k^2 (I/I_s) \frac{2\Delta/\Gamma}{[1 + (2\Delta/\Gamma)^2]^2} \boldsymbol{v} \ , \tag{2.2}$$

where $I$ is the intensity of the laser light and $I_s = \pi h c \Gamma / 3\lambda^3$ is the "saturation" intensity. This expression is valid if the light intensity $I_L$ is low enough that the deexcitation of atoms is dominated by spontaneous rather that stimulated emission. This mechanism, known as Doppler cooling, was suggested by Hänsch and Schawlow [53] and independently by Wineland and Dehmelt [54]. The experimental confirmation of this effect first was done by Philips and Metcalf [55] in the case of two counter-propagating beams and by Chu [56] in three dimensions.

The limits on Doppler cooling of atoms are set by the light intensity and transition width. It can be shown [57, 58] that the lowest temperature reachable with the Doppler cooling is $T_D = \hbar\Gamma/2k_B$, where $k_B$ is the Boltzmann constant, and in the case of $^{38\mathrm{m}}$K is $T_D = 150\,\mu$K. The atomic velocity corresponding to this temperature is about 30cm/s for potassium.

But the presence of damping forces is not enough for successful trapping because even such slow atoms will leave the optical field region, usually $\sim 1{\times}1{\times}1\,\mathrm{cm}^3$, in much less than 100 ms. One needs some spatially dependent force to keep them in place. Such position dependence can be achieved with a combination of optical fields and a non-uniform magnetic field in a Zeeman-induced magneto-optical trap, which was invented by Raab *et al.* [46] and employs a so called spontaneous light force. The operation of such a trap is described below with reference to $^{38\mathrm{m}}$K.

If an atom with magnetic moment $\boldsymbol{\mu}$ is placed in a weak magnetic field $\boldsymbol{B} = \hat{\boldsymbol{z}}B$, the degeneracy of the energy levels will be removed as the atom gains additional energy due to the Zeeman effect [57]

$$\Delta E = g m_F \mu_B B, \tag{2.3}$$

where $g$ is the atomic Landé $g$-factor and $\mu_B = e\hbar/2m_e = 5.788 \times 10^{-8}\,\mathrm{eV/G}$ is the Bohr magneton. If the nucleus has non-zero spin, $I$, the $g$-factor changes its value from usual $g_J$ value

$$g_J = 1 + \frac{J(J+1) + S(S+1) - L(L+1)}{2J(J+1)} \tag{2.4}$$

to

$$g_F = g_J \frac{F(F+1) + J(J+1) - I(I+1)}{2F(F+1)} \tag{2.5}$$

If the magnetic field is not very strong, the atomic angular momentum, $\boldsymbol{J} = \boldsymbol{L} + \boldsymbol{S}$, and nuclear spin, $\boldsymbol{I}$, of an atom are coupled with good total angular momentum $\boldsymbol{F} = \boldsymbol{J} + \boldsymbol{I}$. If the magnetic field is not uniform but rather proportional to the deviation from $z = 0$, the energy levels shift (and also the transition frequencies and scattering rates) will behave as linear functions of the displacement from the origin, where $B = 0$. In the case of $^{38\mathrm{m}}$K, which has no nuclear spin, the Zeeman splitting of ground $S_{1/2}$ and excited $P_{3/2}$ states can be evaluated from (2.3) and (2.4) as $\partial\omega/\partial B$ (in MHz/G)

$$\partial\omega/\partial B|_{S_{1/2}} = 17.6, \quad \partial\omega/\partial B|_{P_{3/2}} = 11.7\ .$$

The one-dimensional schematic of energy levels for the $^{38\mathrm{m}}$K atom in a linearly changing magnetic field is given in Fig 2.3. The application of the two counter-propagating laser beams, with $\sigma^-$ polarization from the right and $\sigma^+$ from the left, will cause the optical transitions between $J = 1/2$ ($4S_{1/2}$) and $J = 3/2$ ($4P_{3/2}$) states. The $\sigma$-polarized light has the property that $\sigma^+$ light drives the transition between the atomic states with increasing angular momentum projection by one, while $\sigma^-$ causes the transitions with that projection reduced. On the right side of the plane atomic transitions $|1/2, 1/2\rangle \rightarrow |3/2, -1/2\rangle$ and $|1/2, -1/2\rangle \rightarrow |3/2, -3/2\rangle$ are closer to the resonance compared to $|1/2, -1/2\rangle \rightarrow |3/2, 1/2\rangle$ and $|1/2, 1/2\rangle \rightarrow |3/2, 3/2\rangle$ transition. But the first pair can be driven only by $\sigma^-$ light. That means that right of the origin $^{38\mathrm{m}}$K atoms will preferentially interact with the $\sigma^-$ laser beam, pushing them toward the origin. On the left side atoms will prefer to interact with the $\sigma^+$ light, again experiencing the restoring force directed toward the origin. It is very important to maintain good quality polarization, as an admixture of wrongly polarized light in any beam might significantly increase the cloud diameter.

This feature can be easily generalized to three dimensions and realized by application of three pairs of counter-propagating, orthogonal, appropriately polarized laser beams and a quadrupole magnetic field. This field is generated by a pair of "anti-Helmholtz" coils, mounted symmetrically above and below the MOT, with the same current flowing in opposite directions. It can be shown [59, 60] that with small light detuning ($\Delta$), atoms in the MOT experience a net force proportional to the $\xi = \boldsymbol{br} + \boldsymbol{kv}$, and exhibit the behavior of a damped harmonic oscillator. Here $\boldsymbol{b}$ and $\boldsymbol{k}$ are vectors proportional to the magnetic field and light wave vector, and $\boldsymbol{r}$ and $\boldsymbol{v}$ are the displacement and velocity of atoms with respect to the origin.

Despite the fact that the MOT depth is small (about 400 mK [46]), it is possible to trap thermal atoms directly, without external cooling. This is known as the vapor cell technique [61]. It assumes that the MOT is located inside a small transparent cell,

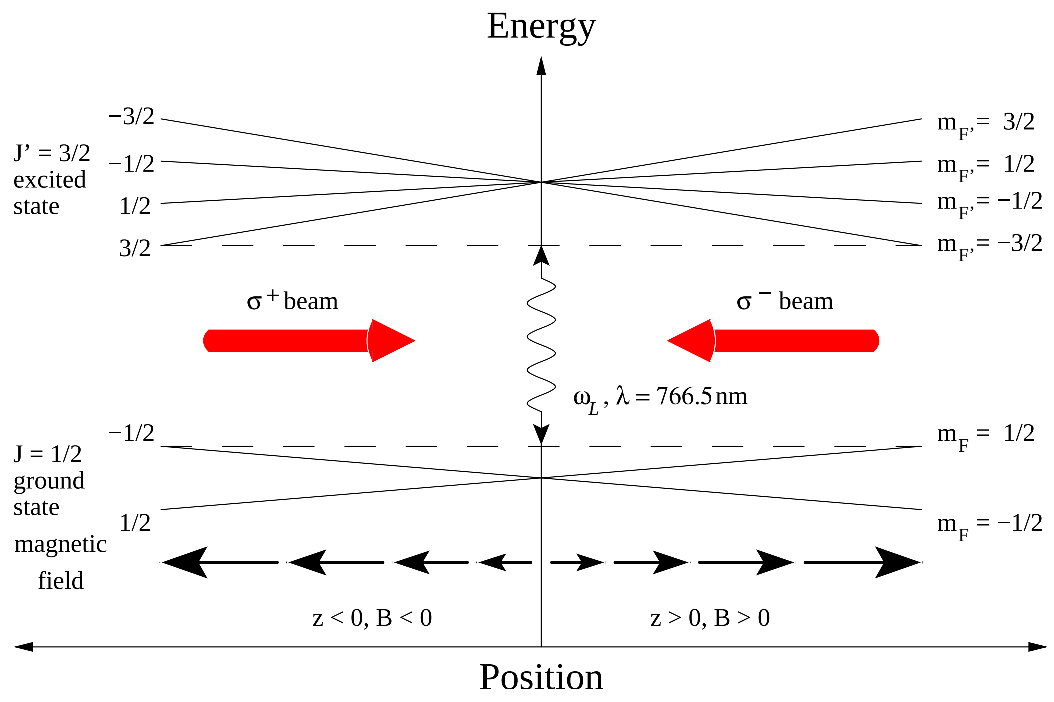

FIGURE 2.3: One-dimensional model of the Magneto-Optical Trap. An inhomogeneous magnetic field of the form $\boldsymbol{B} = B_z\hat{\boldsymbol{z}}$ is applied and the counter-propagating laser beams are tuned to the red of the field-free transition frequency $\omega_A$ with indicated polarizations.

filled by the vapor of atoms, and subjected to trapping. As the vapor atoms are in thermal equilibrium with the cell walls, at room temperature ($\simeq 300\,\mathrm{K}$) about $10^{-4}$ of all atoms will have low enough velocities to be captured into the MOT. Atoms, which at a given moment of time are too fast to be trapped, after collision with the walls will re-populate the Maxwell distribution and some of them can again be trapped. To reduce atom losses from sticking to the walls, the cell is usually coated from the inside by a thin transparent layer of a special silicon-based material, so called Dryfilm [62].

In the trapping of $^{38\mathrm{m}}$K we have used a commercial, $\mathrm{Ar}^+$ ion laser-pumped Ti:sapphire ring laser, locked to $D2$ ($4S_{1/2} \rightarrow 4P_{3/2}$) transition of K (766.5nm) by Zeeman-dithered saturation spectroscopy of natural potassium [63]. The optical power was about 200 mW per beam with detuning from 3 to 7 $\Gamma$, generated by acousto-optic modulators.

## 2.3 Radioactive potassium source.

At TRIUMF experiments with short-lived isotopes (with half-lives in the minute and sub-minute range) involve on-line production, separation and delivery of radioactive isotopes in sufficient amounts. In the first experiments TRINAT received potassium isotopes from the **T**est **I**sotope **S**eparator **O**n **L**ine, TISOL [64, 65]. Later TRINAT was relocated to work with beams from the newer and more powerful isotope facility, ISAC [66] (See Fig 2.4). ISAC (Isotope Separator and Accelerator) was designed to provide radioactive beams to a variety of physics experiments in such fields as weak interaction symmetries [41, 38, 44], nuclear astrophysics [67], nuclear structure [68, 69, 70] and condensed matter physics [71].

Both facilities utilize proton beam from the TRIUMF cyclotron, although ISAC is designated to accept higher proton beam intensities (up to $40\,\mu$A in the initial stages for certain targets [72, 73] compared to TISOL's operational beam current of $1\,\mu$A), and generally deliver more intense radioactive beams. The magnetic separator of ISAC has considerably better mass resolution, which can be as high as $\mathrm{M}/\Delta\mathrm{M}=5000$. Continuing development of ISAC's target station will allow the use of proton beam intensities of up to $100\,\mu$A [74].

### 2.3.1 Target, ion source, separator.

The potassium isotopes are produced along with others through spallation and fragmentation reactions inside a target bombarded by a 500 MeV proton beam from TRIUMF's main cyclotron. To be utilized these isotopes must diffuse through the target

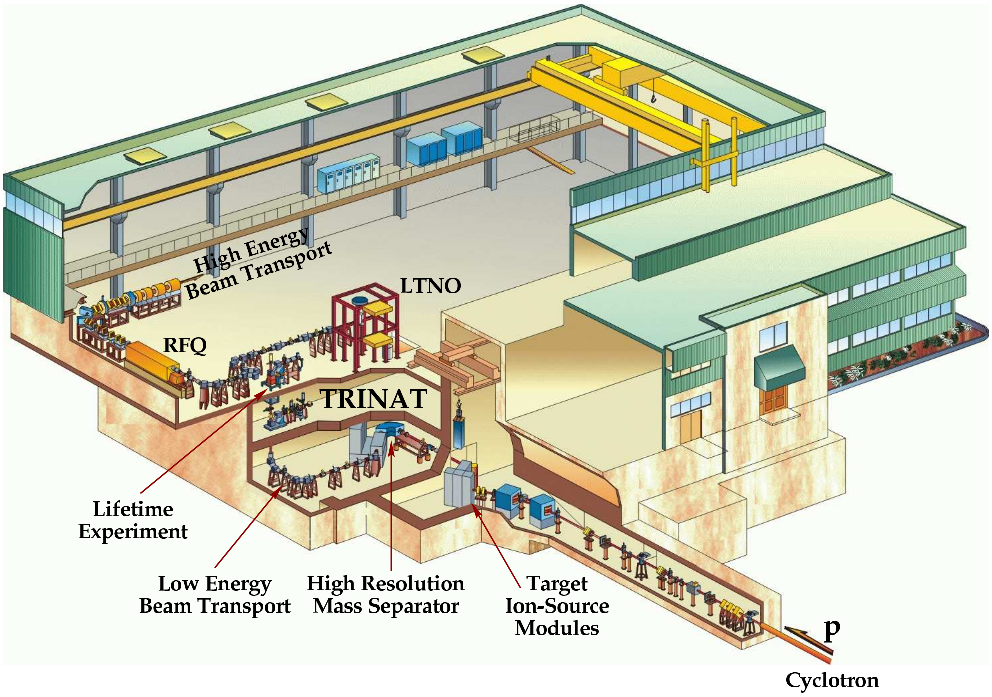

Figure 2.4: The ISAC radioactive beam facility at TRIUMF, 2000.

material. To reduce the diffusion time of the isotopes from the target, it is placed in an oven and kept at high temperature, in some cases as high as 1500 °C. The choice of target material is subject to several considerations. First, under bombardment by the proton beam the target has to provide high yield of the desired isotope and yet remain stable. Second, the target material must be porous, so short lifetime isotopes can diffuse fast and will not decay mostly inside the target.

Once the radionuclides have been produced and have diffused through the target material, they have to be extracted from the target. The simplest way to do the extraction is to use an electric field, if the nuclides are in the form of ions. The ionization of potassium in the ISAC target is done by a surface ionizer, which works using a well known principle, namely: an atom in thermal equilibrium with a metal surface leaves this surface predominantly in the form of a cation when its ionization potential is less than the work function of the metal surface. And vice verse, when the atom's ionization potential is higher than the metal surface work function, most of the nuclides leave the surface as neutral atoms. Again, to minimize the time spent by the atom on the metal surface it has to be very hot, which makes natural a choice of refractory metals as a surface material to withstand high temperatures in the aggressive environment of the target. The work function of such metals and ionization potential of potassium are given in the Tab 2.1.

TABLE 2.1: Thermionic work functions of some refractory metals [75].

| Element | Work function $\phi$(eV) | Potassium ionization potential (eV) |
|---|---|---|
| Rhenium | 4.9 | 4.341 |
| Tantalum | 4.2 | |
| Zirconium | 4.0 | |
| Hafnium | 3.9 | |
| Yttrium | 3.1 | |

The ionizer in ISAC has been manufactured from rhenium foil and kept at 2200 °C during operation. In the earlier stages of our experiment we have used a 22 g/cm$^2$ target, made from cold pressed pellets of Calcium Oxide [76]. This target, irradiated by a 1 $\mu$A, 500 MeV proton beam, provided an excellent yield of potassium isotopes but had one disadvantage. Due to the high vapor pressure of CaO, after 3 weeks of operation a considerable amount of the target material was transferred to the colder outlet hole. This material, being crystallized in the form of elemental calcium, partially clogged the outlet hole, resulting in considerable yield reduction and, eventually, high voltage breakdown. For this reason the CaO target was replaced by one made of calcium zirconate ($CaZrO_3$). The manufacture of this target is more complicated than with CaO [77]. Calcium zirconate powder is pressed into pellets and sintered at 1400 °C. The sintered material, after grinding, is mixed with 25% by volume ammonium nitrate, pressed again into pellets with thickness $\lesssim$1 mm and heated to 1400 °C to volatilize the ammonium nitrate and create a porous substance from which potassium could easily escape. Prepared in this way, calcium zirconate (with density approximately 2 g/cm$^3$) proved to be a very efficient target material when used with modest proton beam intensities.

The ionized nuclei were extracted from a target of 42 g/cm$^2$ of $CaZrO_3$ by an extraction voltage voltage of 30 kV and directed into an analyzing magnet which spatially separated them according to charge to mass ratio. The ions which passed the magnetic analyzer were formed into a beam by a set of electrostatic quadrupoles and steering plates and delivered to the collection station of the experiment, the TRINAT facility, with intensities that were measured during the run and are shown in the Tab 2.2.

TABLE 2.2: Calcium zirconate target yield [78].

| Date | $p^+$ current, $\mu$A | $^{38gs}$K yield, $s^{-1}$ | $^{38m}$K yield, $s^{-1}$ |
|---|---|---|---|
| July 2000 | 1.1 | $7.4\times10^8$ | $8.7\times10^6$ |
| Oct. 2000 | 1.5 | $3.2\times10^8$ | $8.3\times10^6$ |
| Oct. 2000 | 2.0 | $2.0\times10^8$ | $1.0\times10^7$ |
| Oct. 2000 | 2.6 | $2.9\times10^8$ | $1.2\times10^7$ |

### 2.3.2 Ion neutralization - choice of material.

Once delivered to the TRINAT facility, the 30 keV potassium beam has to be thermalized and neutralized to make possible the optical trapping. Both of these processes can be done at once with a foil of hot metal, where K ions are stopped and, after diffusion to the surface, emitted as neutral atoms. However, this time the metal has to be chosen with a work function smaller than the potassium ionization potential. In principle, any metal listed in Tab 2.1, except rhenium, could be used as neutralizer material. It must also have low vapor pressure at working temperatures since it is located in the ultra-high vacuum. The working temperature must also be moderate to avoid damaging the trapping cell coating. The diffusion and release of atoms from the foil has to occur in a time considerably smaller than the lifetime of the potassium isotope to minimize the portion of the atoms, decaying inside the neutralizer.

To choose the most suitable neutralizer material we tested a number of samples on beam line A of the TISOL facility [42]. A collimated 12 keV $^{37}K^+$ beam continuously bombarded the sample as shown in the Fig 2.5, and the fraction of implanted $^{37}$K atoms remaining in the sample was measured as a function of the sample temperature. The fraction released is precisely the quantity of interest for loading the neutral atom trap.

The sample foils, approximately $1.5\times3\,cm^2$ in area, were resistively heated by direct current. The resulting temperature (in the range $500-1700\,°C$) was measured with an optical pyrometer. The beam spot size was approximately 6 mm, so the temperature was uniform across the activity region. The vacuum in this test setup was $2\times10^{-6}$ Torr; so the testing times were kept short to avoid foil contamination such as oxidation. To monitor the release of the potassium as neutral atoms, not as $K^+$ ions, the foil was electrically biased with respect to surrounding media, so $K^+$ ions were turned back to the foil.

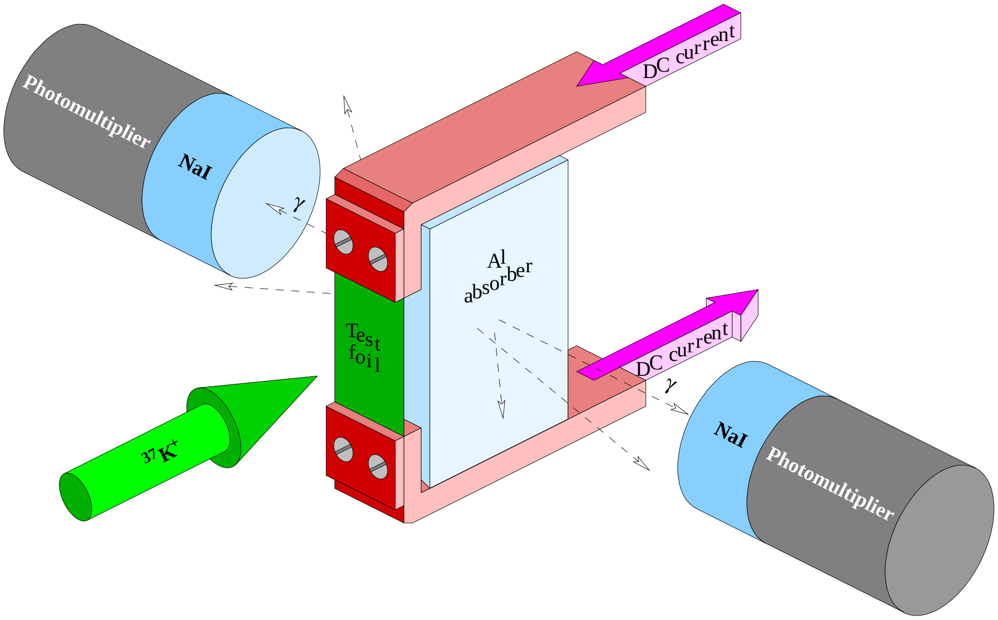

FIGURE 2.5: Schematic of the BL1A tests. Scintillator detectors register in coincidence the 0.511MeV $\gamma-$quanta from positrons, which leave the foil sample, diffuse into aluminum absorber and annihilate there.

To monitor the activity, the sample was mounted in front of a thick aluminum positron stopper. The stopper subtended approximately 40 % of the solid angle for escaping positrons. Two 5 cm diameter and 5 cm long NaI(Tl) scintillator detectors were placed face-to-face each 15 cm away from the stopper. The coincidence rate in the two detectors, which was dominated by decays of positrons from the stopper, was monitored as a function of sample temperature. When $^{37}$K escaped from the sample into the $30\times30\,\mathrm{cm}^2$ chamber, the positrons from its decays were no longer stopped in the aluminum block. So the coincidence rate was directly proportional to the number of $^{37}$K atoms remaining in the sample, and the fraction remaining is equal to one minus the release fraction. A correction of typically 5 % for accidental coincidences was made, measured by the standard technique of delaying one detector signal to eliminate true coincidences. The influence of the possible beam current variations was excluded by normalization of the coincident count rate to singles.

The results of the measurements for the materials listed above are presented in the Fig 2.6 and show that the most suitable neutralizer materials are yttrium and zirconium, which release about 60 % of implanted potassium at a temperature of 950 °C. We have chosen Zr, as at this temperature it has a vapor pressure about four orders of magnitude less than that of yttrium [75]. A working temperature of the neutralizer has been chosen even lower, about 850 °C. That provides release of less than 20 % of implanted $^{38}$K, but extends the lifetime of the Dryfilm coating and allows one to maintain in the collection trap a vacuum of $\simeq 10^{-8}$ Torr.

In order to reduce the portion of atoms which decay in the neutralizer we have tried to use metals with relatively low melting temperature. Semi-empirical expressions exist [79] which relate the enthalpy of adsorption to bulk properties of materials, such as their melting points and work functions. Guided by these, we searched for release from materials with much lower melting points. As one approaches the melting point of a material, diffusion can be expected to almost always increase to the point where fast diffusion can be achieved, and the limitation would be expected to be the rate of desorption.

Aluminum ($\phi = 4.28\,$eV), indium ($\phi = 4.12\,$eV), and lithium ($\phi = 2.9\,$)eV were tested. Aluminum and indium are materials with very low vapor pressures near their melting points. Lithium is an alkali metal and would not be expected to stick permanently to Dryfilm coatings, and might even cure Dryfilm defects, as do other alkalies [80]. The lithium catcher was prepared by scraping the final surface under an argon atmosphere. However, no significant release was seen from these three materials at temperatures up to their melting points. We suspect that this is most likely due to surface contamination.

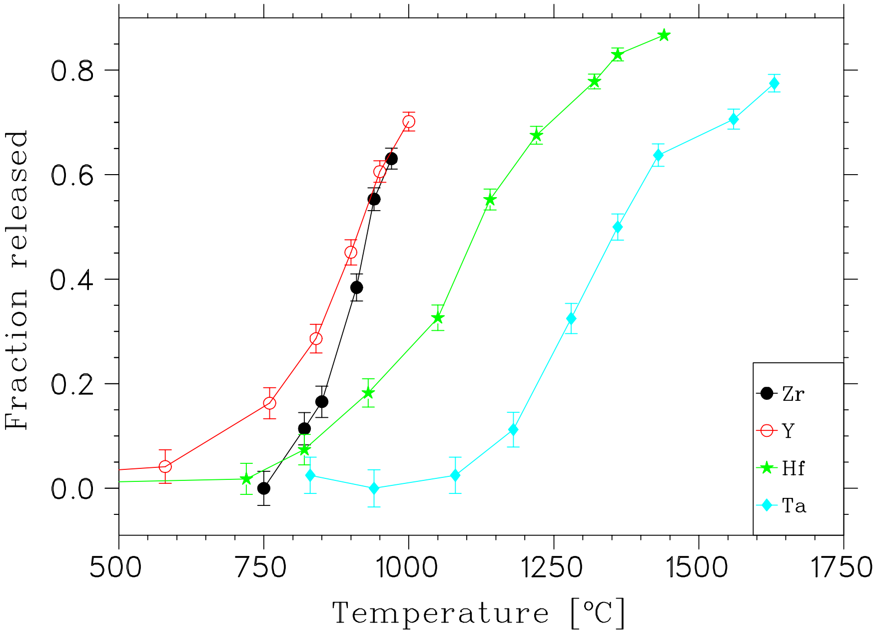

FIGURE 2.6: $^{37}$K release measurements on the TISOL facility. Data presented for Y, Zr, Hf and Ta. At 950°C Y and Zr release about 60% of implanted potassium. See also [42] .

## 2.4 TRINAT double MOT system.

### 2.4.1 Collection trap.

The collection trap (see Fig 2.1) was mounted inside a 25 cm diameter and 20 cm high stainless steel vacuum vessel with ports which allowed access of the laser and ion beams. To provide the magnetic quadrupole field required by the MOT, two 9-turn coils of 90 mm outer diameter, are mounted in the high vacuum volume coaxially, one above the other and separated by 76 mm. The coils, made from oxygen-free copper $6.35\times 6.35\,\mathrm{mm}^2$, were annealed after manufacture. To minimize an azimuthal component of the resulting magnetic field, the coils were designed in a way to ensure that the turns are parallel to each other. Each coil could accept a current up to 100 A, and when operated in the anti-Helmholtz configuration they provided a field gradient in the vertical direction up to 28 G/cm at the mid-point between them. The hollow trapping cell, illustrated in Fig 2.7 was constructed from Quartz with overall dimensions of $50\times 50\times 50\,\mathrm{mm}^3$. The cell was supported by an insulated holder mounted on the lower coil. Three 6 mm diameter holes in the cell walls allowed for the passage of the $^{38}\mathrm{K}^+$($^{38\mathrm{gs}}\mathrm{K}^+$+$^{38\mathrm{m}}\mathrm{K}^+$) beam through the cell into the neutralizer and for the $^{38\mathrm{m}}\mathrm{K}^0$ beam pushed from the collection trap to reach the detection trap.

The neutralizer, heated by direct current, was attached to the outer wall of the trapping cell directly behind the exit hole for the $^{38}\mathrm{K}^+$ beam. It is manufactured from 25 $\mu$m Zr foil, has a conical shape with an attached "sail" and is surrounded by two layers of thermal shield made of 12 $\mu$m Ta foil. The conical shape was chosen to minimize the distance to the surface for a given implantation depth. The cross section of TRINAT's neutralizer, which has a length of about 25 mm and opening hole of 6 mm diameter, is depicted in Fig 2.8. The "sail", which is designed to maintain uniform current density through the material, along with two layers of the tantalum foil heat shield, provided a more or less uniform temperature distribution across the working surface of the cone. Measurements with an optical pyrometer have shown that local temperature differences over the area were about ±150°C at the 1000°C level.

The neutralizer was surrounded by stainless steel plates 5 mm thick where positrons, originating from decays inside the neutralizer, were annihilated with the emission of counter-propagating 0.511MeV photons. Those photons where viewed by two NaI detectors in face-to-face geometry. This setup allowed us to control the potassium ion beam spot position on the neutralizer conical surface in a way similar to the one used for neutralizer material tests. During ion beam tuning the temperature of the cone was lowered down to provide good sticking of the potassium ions (here we have used $^{37}$K) to the metal surface. By maximizing the coincident count of the NaI detectors

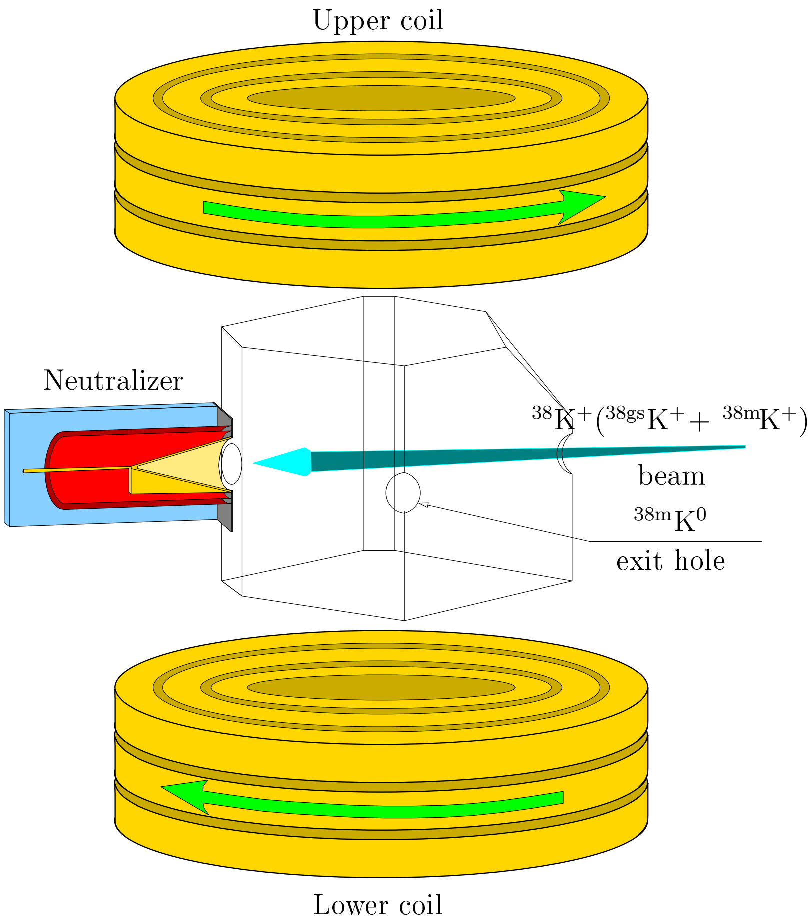

FIGURE 2.7: Trapping cell

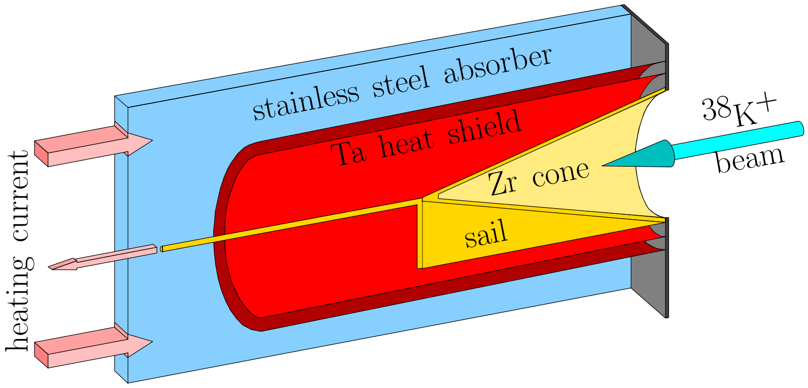

FIGURE 2.8: Neutralizer assembly. The Zirconium foil was heated up to 850°C during operation. The "sail" and Tantalum heat shield help to ensure uniform temperature distribution across the neutralizer working surface.

we have ensured that the ion beam was aimed on the neutralizer and not touching the walls of the trapping cell. This technique of keeping the ion beam spot centered on the neutralizer allowed us to maximize the trapping efficiency and at the same time to avoid excessive damage of the cell's Dryfilm coating by the incoming ion beam.

In the collection chamber, with the neutralizer temperature 850°C, we have achieved a vacuum of $2\times10^{-8}$Torr and that resulted in a trap lifetime of $\simeq 0.5$ s. At this neutralizer temperature, in accordance with TISOL tests (See Fig 2.6), about 20 % of the implanted $^{38\mathrm{m}}$K atoms are neutralized and emitted into the trapping cell.

### 2.4.2 Atom transfer.

In our experimental setup the collection and detection trap volumes are connected with a pipe about 55 cm long and 25 mm inner diameter, which has been chosen to provide some differential pumping between the vacuum vessels. To move trapped $^{38\mathrm{m}}$K atoms into the detection chamber we developed a transfer system, depicted in the Fig 2.9 (not to scale). A detailed description of this transfer system can be found in Ref [40].

We have used a narrow (about 1 mm diameter), slowly diverging few milliwatts pulsed laser beam with small detuning so that it could effectively interact with cold trapped $^{38\mathrm{m}}$K atoms only. When, due to the photon-atom momentum transfer, the

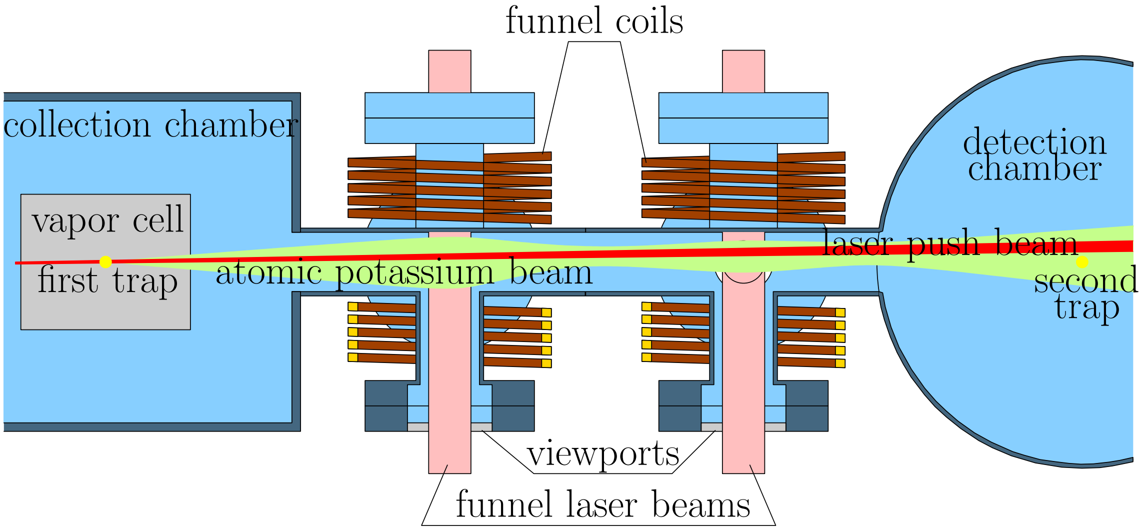

FIGURE 2.9: Schematic of transfer system. The laser beam, aimed about 2 mm above the second MOT, pushes trapped $^{38\mathrm{m}}$K atoms from the collection to the detection chamber through the 25 mm diameter, 55 cm long pipe. Along the pipe there are two two-dimensional MOT systems, that provide transverse focusing of the atomic beam and prevent atoms from hitting the pipe walls.

atoms accelerate to velocities of approximately 20 m/s, the large detuning ≃160 MHz due to the Doppler effect drives the interaction off resonance and the atoms continue moving toward the detection chamber effectively interaction free. The process of the acceleration of the atoms takes place within 2−3 mm of the trap center. Because the push beam can disrupt loading of the second MOT, it is intentionally misaligned a few millimeters so it misses the center of the detection trap. The push beam was typically aimed above that center to miss the second MOT and avoid disrupting it, so that gravity would tend to deflect the atoms back to the center of the trap. The gravitational drop in a 20 ms transit time is 2 mm.

A push beam alone would not provide atomic beam of sufficient quality because atoms leaving the collection trap will retain transverse velocity. Despite the fact that only the coldest atoms interact with the push beam long enough and receive momentum to leave the collection trap (atoms with high transverse velocity cross the push beam too fast and remain in the trap), the resulting atomic beam divergence allows the transfer of only 5 % of trapped atoms (the rest stick to the pipe's wall). To prevent such losses we have arranged along the transfer path a pair of two-dimensional MOTs, each with two pairs of counter-propagating laser beams, normal to the transfer axis and each other. These MOTs operate with 15 mm OD laser beams of 3−10 mW/cm$^2$ power density and with magnetic field gradient of 6 G/cm in vertical direction (3 G/cm in horizontal plane). In this configuration we have been able to successfully transfer 75% of the atoms which had been trapped in the collection chamber.

### 2.4.3 Detection chamber.

The main body of the detection chamber (see Fig 2.10) is a stainless steel (SS) cylinder, 14" long and 6" OD, mounted horizontally with its axis perpendicular to the transfer line delivering the $^{38\mathrm{m}}\mathrm{K}^0$ beam from the collection chamber. The trapping laser beams are delivered through four additional ports (1.5" OD) in the horizontal plane and another two (3.0" OD) along the vertical axis. Not shown in the Fig 2.10 are the two trapping magnetic coils, each about 20 cm diameter and 4 cm high centered on this vertical axis immediately above and below the chamber (separated by ≃15 cm). Each of this air-cooled coils have 32 turns of copper conductor and can accept up to 72 A DC. Operating in anti-Helmholtz configuration they provide magnetic field gradients of ≃28 G/cm in the vertical direction and one-half in any horizontal direction. The $^{38\mathrm{m}}\mathrm{K}$ atoms are collected in the second MOT located as shown on the central axis of the detection chamber.

The nuclear detectors are also centered on this axis, which, in the experiment

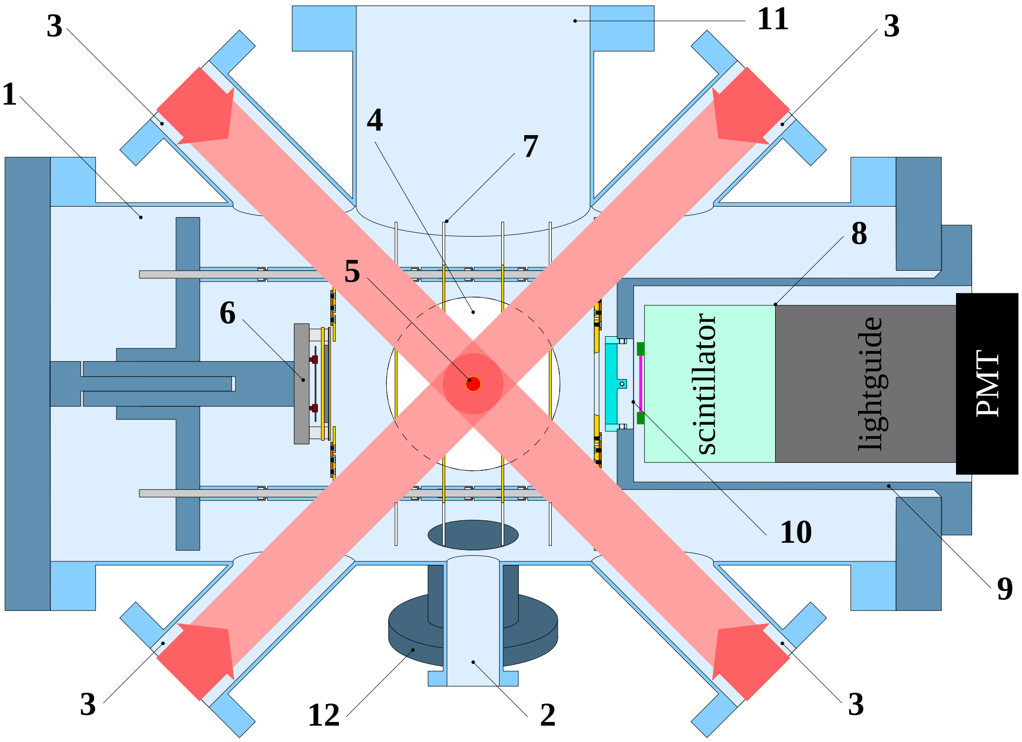

FIGURE 2.10: Central cross section of the detection chamber (top view): **1** main vessel, **2** $^{38\mathrm{m}}$K transfer port, **3** horizontal trapping laser beam ports, **4** vertical trapping laser port, **5** MOT, **6** recoil detector, **7** electrostatic electrode assembly, **8** beta telescope, **9** low vacuum beta telescope housing, **10** Be foil, **11** pumping port, **12** optical diagnostic port.

being described, is designated as the Z-axis with the trap located very close to the origin (which is defined by the axis of the vertical laser ports). The MCP-based recoil detector and the system of electrodes used to define the constant electric field in the Z-direction are mounted, as shown, directly in the main vacuum system. Since there are components incompatible with high vacuum, the beta telescope is mounted in a separate SS vacuum vessel. To allow transmission of positrons from the trap, this vessel has a Be window 127 $\mu$m thick with an OD of 4.6 cm.

In the main chamber the high vacuum is achieved with an ion and getter pumps connected through the 4" OD horizontal port. The typical vacuum was $3\times10^{-10}$ Torr which resulted in mean trapping lifetimes of 45 s (measured with stable isotopes). To improve the uniformity of the electric field and maintain its symmetry in the transverse horizontal direction ($\pm X$), the 4" port is partially screened with a grounded, fine metal mesh with a central hole, 1" in diameter. This hole was used to deliver the laser beam used to photo-ionize the $^{38\mathrm{m}}$K atoms from the trap.

In the Fig 2.10 is also shown one of four additional ports with 1.5" OD used for viewing the trap with CCD cameras and other diagnostic devices. They are located in the vertical plane, Z= 0 at ±30° to the horizontal plane.

## 2.5 Nuclear detection system.

The nuclear detection system is built to detect the $\beta^+$ decay of $^{38\mathrm{m}}\mathrm{K}$

$$^{38\mathrm{m}}\mathrm{K} \rightarrow ^{38}\mathrm{Ar} + \mathrm{e}^+ + \nu$$

and provide the experimenter with the parameters which allow one to deduce the initial momenta of both the positron and the recoil $^{38}$Ar nucleus and, hence, the $\beta - \nu$ angular correlation parameter. This goal has been achieved using two different detectors, one for the recoil and the other for the positron. Both detectors are mounted inside the detection chamber, aligned along the chamber axis and observe the trapped atoms from opposite sides (see Fig 2.11). As the cloud of $^{38m}$K atoms is localized in the near point-like trap (all recoiling particles are assumed to originate from there †),

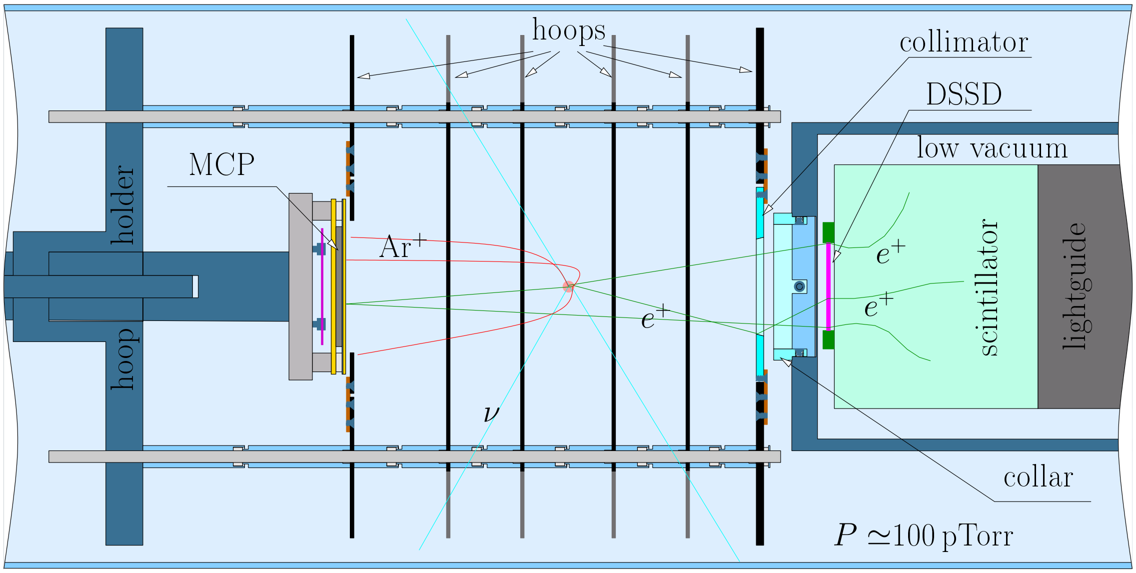

FIGURE 2.11: Cross section of the detection chamber.

---

† Some of the betas and argon ions originate from decays of untrapped potassium on the hoops and walls of the chamber. The collimator, the collar and thick walls of the beta telescope housing significantly suppress the detection of such betas. In addition, the electrostatic focusing system (described in the Sec 2.5.4) provides an electric field guiding ions from such decays away from the MCP. The experimental measurements of the

the geometry of the experiment is well defined. For the purpose of the experiment it is enough to measure the positron energy, the entrance coordinates of the positron into the beta detector, the coincident recoil time of flight (TOF), and the coordinates where the recoil strikes the front surface of the recoil detector. Our detectors have been built to provide these measurements for a well defined fraction of all decays.

The position sensitive recoil detector based on a microchannel plate (MCP) assembly with resistive anode (RA) readout is placed inside the high vacuum volume. The mount is made using BeCu rod of adjustable length attached directly to one of the 8 " OD flanges. The MCP-RA assembly provides us with the recoil TOF and position of the recoil in the front plane of the recoil detector. The opposite 8 " OD flange is used to hold a low vacuum vessel, containing the beta telescope, which consists of a scintillating plastic detector preceded by a thin, position sensitive double-sided silicon strip detector (DSSD) used to measure the energy loss of positrons incident on the plastic scintillator. The DSSD provides the positron position in the front plane of the beta detector while the positron energy is measured by both the DSSD and the plastic scintillator.

The center of the recoil detector is mounted 61 mm from the chamber center and observes the trap with solid angle $\approx 0.01$ of $4\pi$. The front of the beta detector, the DSSD, is 69 mm from the chamber center, observing the trap with about the same solid angle .The scintillator itself subtends a solid angle of $\approx 0.05$ of $4\pi$. The bias voltage required to operate the DSSD was 130 V. To prevent voltage break down without compromising the UHV condition at the trap, both the DSSD and scintillator, as is mentioned above, have been placed into a low-vacuum chamber, separated from the trapping volume by a 127 $\mu$m Be foil.

The stainless steel walls of the low-vacuum chamber are thick enough (12 mm in front and 4 mm on side) to absorb positrons, which would otherwise enter the scintillator after scattering off the walls or other elements of the chamber. For the same purpose, as shown in the Fig 2.12 (not drawn to scale), in front of the beta detector we have mounted a collimator, made of 2 mm thick Ta-W alloy plate and surrounded the Be window by a copper-tungsten "collar". Taking these precautions we have prevented detection of the scattered positrons, except for those which scattered off the inner edges of the collimator or experienced back scattering off the surface of the recoil detector. Detailed Monte Carlo simulations agreed with simple estimates that if a collimator must be thick enough to stop positrons, it is best to make it from high-$Z$ material to keep it as thin as possible to present the smallest area for

---

coincidences during the intentional release of trapped $^{38m}$K atoms revealed a negligible contribution of such events to the experimental data.

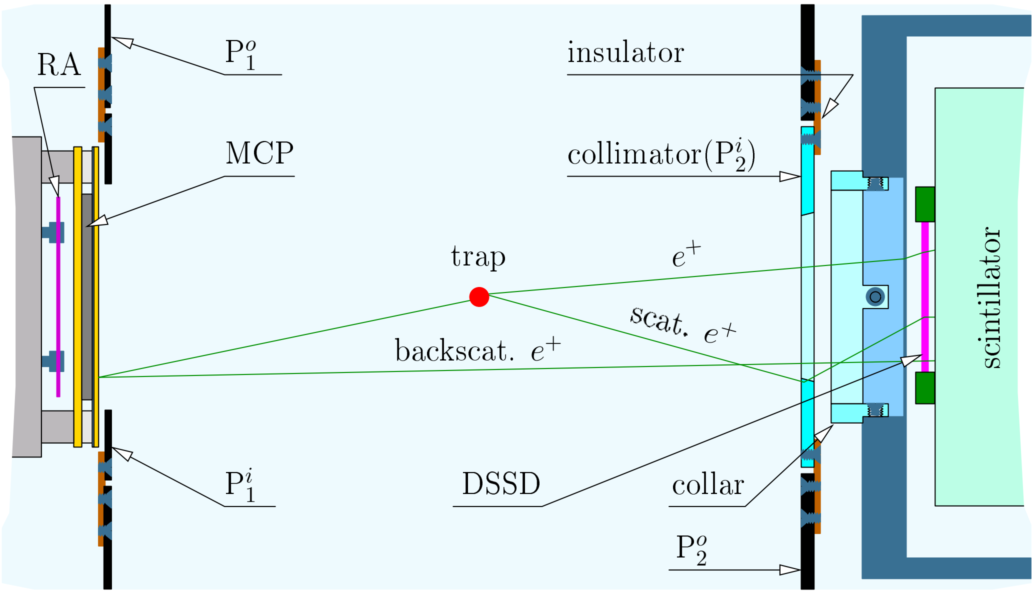

FIGURE 2.12: Zoom of the central part of the detection chamber. The labels $P_1^i$, $P_1^o$, $P_2^i$ and $P_2^o$ refer to the inner and outer segments of the two split plates $P_1$ and $P_2$ which are elements of the electrostatic focusing system discussed in Sec 2.5.4.

scattering. Active collimation by means of double sided silicon with a central hole was also considered as an option. However, as it is very difficult to guarantee charge collection from the inner radius we have decided to proceed with a passive collimator.

On the same rod which holds the recoil detector we have mounted the elements of the electrostatic accelerating system. It consists of a set of low-Z glassy carbon annular hoops and creates a nearly uniform electric field in the region where recoils travel. Due to the electric field, which accelerates positive Ar ions toward the recoil detector, we can separate in TOF different charge states of the Ar ions, created in $\beta^+$ decay. The higher charge states are the result of multiple electron shakeoff and have shorter TOF from the trap to the MCP.

### 2.5.1 The recoil detector.

The main part of our recoil detector is an assembly of three long life image quality MCPs, manufactured by Galileo Electro-Optics Corporation. Each microchannel plate itself is a wafer of lead glass 600 $\mu$m thick, 3.27 cm overall diameter with an active diameter not less than 25 mm. It is manufactured using thin solid-glass fibers which have a core glass, soluble in a chemical etchant, and a lead glass cladding which is not soluble in the core glass etchant, and which will eventually form the MCP matrix structure. The fibers are packed in the matrix, thermally fused within the lead glass envelope, and drawn into a boule which is then sliced into polished wafers with fiber orientation at 11° degrees to the normal of the plates. The soluble core glass is then removed by the etchant resulting in a microchannel plate with channels $10\,\mu$m in diameter and with $12\,\mu$m spacing. Then the plates are reduced in a hydrogen furnace, where the lead oxide at the glass surface is converted to semiconducting lead. Both surfaces of the MCP are covered by a thin Ni-Cr alloy electrode which penetrates inside the channels to a depth of $1-2$ channel diameters and allows the application of a potential difference between the MCP surfaces of typically $1000-1200$ V [81]. Typical resistance of the MCPs used is 150 MOhm between the surfaces. The open area of each MCP (i.e. area of the channels) is about 65% of the total active area of the plate.

When an electric field is applied between two MCP surfaces each channel acts as a miniature electron multiplier: if an energetic particle strikes the inner surface of the capillary it creates several $(2-3)$ secondary electrons. Each of those electrons, accelerated by the electric field inside the channel, in turn creates $2-3$ of the next generation and finally, an avalanche of $10^3-10^4$ electrons comes out of the channel. The total gain depends exponentially on the channel length and applied voltage. The penetration of the electrode material into the channel focuses the electric field and increases the fraction of the electrons involved in the multiplication process and hence the overall MCP detection efficiency. Depending on the application, the MCP surface may be treated with such materials as Au, Si or CsI to increase the quantum efficiency of the detector. We use uncoated plates to avoid sensitivity to light.

The gain of a single MCP is about $10^3-10^4$ which is not high enough to satisfy the needs of our experiment, where the detector must operate in the counting mode. It cannot be increased by enlarging the thickness of the MCP because positive space charge inside individual channels will cause gain saturation. Increase of the applied voltage is also not desirable because of possible high voltage break down. As a solution we use a well known technique of assembling three MCPs into a so called Z-stack. It is named this way because in cross-section the pattern of the microchannels resembles the letter Z (See Fig 2.13). In our detector, the plates are separated by a drift space of about $150\,\mu$m. Due to space charge effects inside this drift region, electrons originating from one channel of the preceding plate are spread over many channels of the next one, reducing the effects of channel saturation. The total electron gain of the detector is about $10^{10}-10^{12}$ which provides a well-peaked single electron pulse height distribution with relative width of about $70-80\,\%$.

In order to get the transverse coordinates of the primary hit we use a resistive

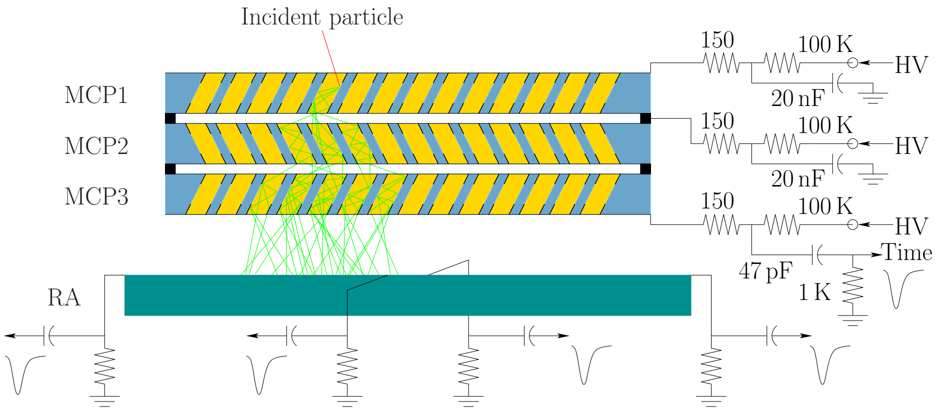

FIGURE 2.13: MCPs assembly in Z-stack configuration.

anode in conjunction with the MCP detector. The resistive anode is a rectangular plate, covered with a resistive layer, situated few mm's behind the last microchannel plate and biased positively with respect to it. After the electron avalanche from the MCP detector reaches the RA it starts to diffuse along the resistive surface. If one connects to each corner of the RA a charge sensitive detector, it is possible to measure the charge that reaches each corner. The measured division of charges depends on the resistance between the corners and the place of the center of gravity of the incident electron avalanche. A special shaping of the resistive layer allows one to make a linear combination of these charges which is proportional to the displacement of the center of gravity from the RA center (See [82] and references therein). The equivalent schematic of the resistive anode is shown in Fig 2.14. In Fig 2.15 is shown the MCP+RA assembly.

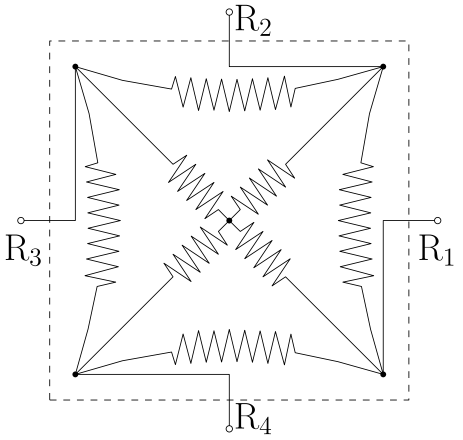

FIGURE 2.14: Equivalent schematic of RA.

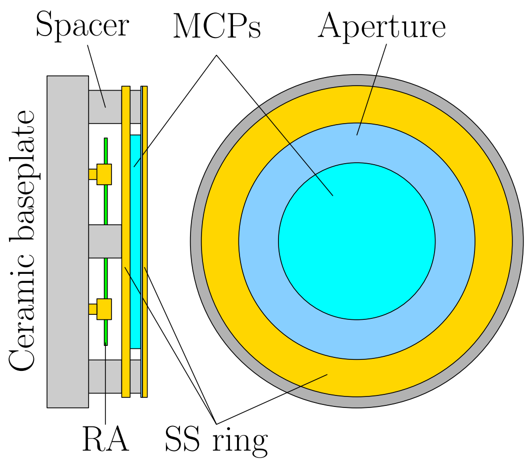

FIGURE 2.15: MCP+RA assembly.

### 2.5.2 The recoil detector spatial calibration.

The recoil detector has been calibrated with a mask mounted in place of the aperture shown in Fig 2.15 immediately adjacent to the front surface of the MCP (see left panel of Fig 2.16). The precision of the mask manufacturing allowed its installation with accuracy better than 0.1 mm. The MCP-RA assembly with the mask installed was irradiated by 3.183 MeV $\alpha$-particles from a $^{148}$Gd source situated on the detector axis approximately 50 cm away. Data collected should then mimic the mask hole pattern, but revealed some distortions.

The hit position on the RA can be calculated in the following way. If $c_1, \ldots, c_4$ are charges collected on appropriate outputs R1, ..., R4 of the resistive anode (see right panel of the Fig 2.16), then the hit coordinates are:

$$x_{hit} = (c_1 + c_2 - c_3 - c_4)/(c_1 + c_2 + c_3 + c_4)$$
$$y_{hit} = (c_2 + c_3 - c_1 - c_4)/(c_1 + c_2 + c_3 + c_4)$$

This expression is approximately valid if all electronic channels of the resistive anode readout have the same gain with no offset. Otherwise appropriate individual scaling of the output signals using a pulser has to be performed to eliminate the offsets and match the gains in each channel. This was done in our case.

In the Fig 2.17 are presented overlays of the mask pattern with its electronic images created by the direct RA signals (left panel), and by signals reduced to the the same gain and zero offset in each channel (right panel). The images are almost

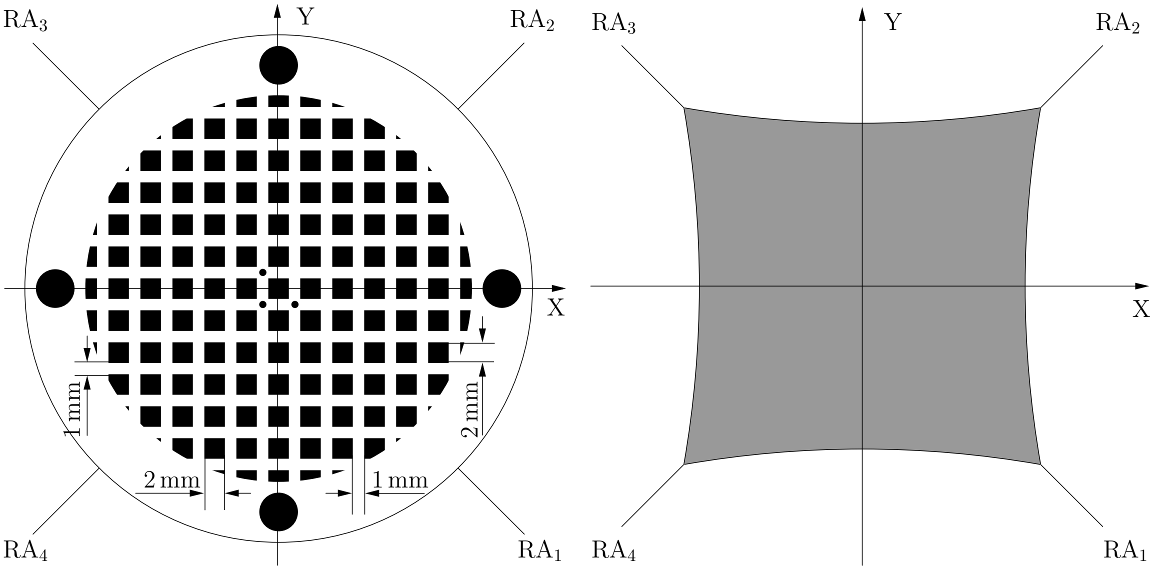

FIGURE 2.16: Mask for resistive anode calibration and calibration coordinates.

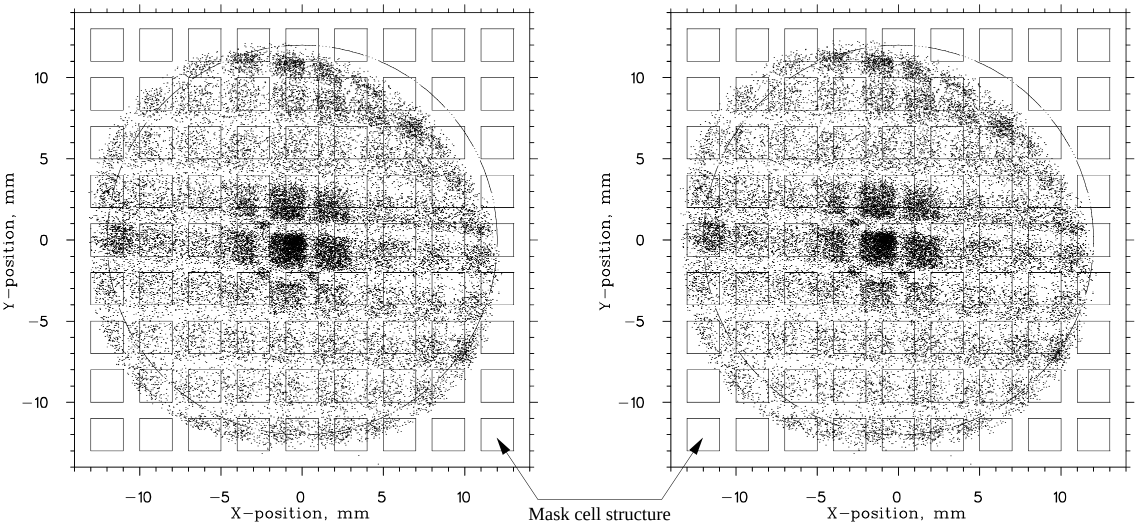

Figure 2.17: Non-calibrated (left) and pulser calibrated (right) electronic images of the mask.

identical. In both cases electronic images were scaled with the same factor to match as closely as possible the mask pattern. As a result we can see a cell structure that represents a distorted mask pattern. To eliminate or at least diminish distortions we have multiplied each individual reduced RA signals by its own scaling factor and applied a nonlinear frame transformation. The scaling factors and transformation coefficients were defined by the fitting of the electronic image to the mask pattern by the following method:

1. we have chosen a set of $5 \times 5$ central cells each $2 \times 2\,\mathrm{mm}^2$ and restricted our procedure to the data points that lie within these cells;
2. for each data point we have calculated coordinates as
   $x = x_0 + A\,(u_i \cos(\alpha) + v_i \sin(\alpha))$
   $y = y_0 + A\,(v_i \cos(\alpha) - u_i \sin(\alpha))$
   where $u_i$ and $v_i$ were defined by the expressions
   $u_i = (k_1 c_1 + k_2 c_2 - k_3 c_3 - k_4 c_4)/(k_1 c_1 + k_2 c_2 + k_3 c_3 + k_4 c_4)$
   $v_i = (k_2 c_2 + k_3 c_3 - k_1 c_1 - k_4 c_4)/(k_1 c_1 + k_2 c_2 + k_3 c_3 + k_4 c_4)$
3. in the first quadrant, where $x > 0$ and $y > 0$ we have calculated $r = \sqrt{x^2 + y^2}$, made the transformation $r \to r + \frac{4}{\pi^2}\phi(\frac{\pi}{2} - \phi)\varkappa r^2$ and calculated new coordinates $x = r\cos(\phi)$, $y = r\sin(\phi)$, where $0 < \phi < \pi/2$ is the polar angle;
4. for each cell we have calculated average values $\overline{x} = \frac{1}{N_i}\sum x_i$ and $\overline{y} = \frac{1}{N_i}\sum y_i$ with the index $i$ running through the data points which belong to one cell.

During the fit procedure we have minimized the function

$$\Phi(k_1, k_2, k_3, k_4, \alpha, A, x_0, y_0, \varkappa) = \sum \{(\overline{x}_{0j} - \overline{x}_j)^2 + (\overline{y}_{0j} - \overline{y}_j)^2\}$$

with $\overline{x}_{0j}$ and $\overline{y}_{0j}$ defining the centers of the cells in the mask and index $j$ running through all cells included in the fit. The fit resulted in the following parameter values:

$$\begin{array}{lrll} k_1 = 1, \text{ fixed in the fit} & A = & 16.84 \text{ mm} & \alpha = 0.0341\,\text{rad} \\ k_2 = 1.0607 & x_0 = & 1.20 \text{ mm} & \\ k_3 = 0.9780 & y_0 = & 0.53 \text{ mm} & \\ k_4 = 1.0290 & \varkappa = & 0.010\,\text{mm}^{-1} & \end{array} \tag{2.6}$$

The resulting images are presented in Fig 2.18. The left panel contains a full image and the right one is the central part of the mask. The second, third and fourth quadrants of the magnified figure contain images of the pinholes in the mask which have coordinates $(-1.5; 1.5)$ mm, $(-1.5; -1.5)$ mm and $(1.5; -1.5)$ mm respectively defined with manufacturing precision. On the top and bottom of this figure are coordinates of the centroids of the dots, contributing into pinhole images. Those coordinates differ from the coordinates of the centers of the pinholes by at most 0.05 mm. Considering all calibration information, we deduce that, within a radius of 10 mm from the center, the resulting nonlinear distortions in the electronic image of the mask pattern are less than 0.5 mm.

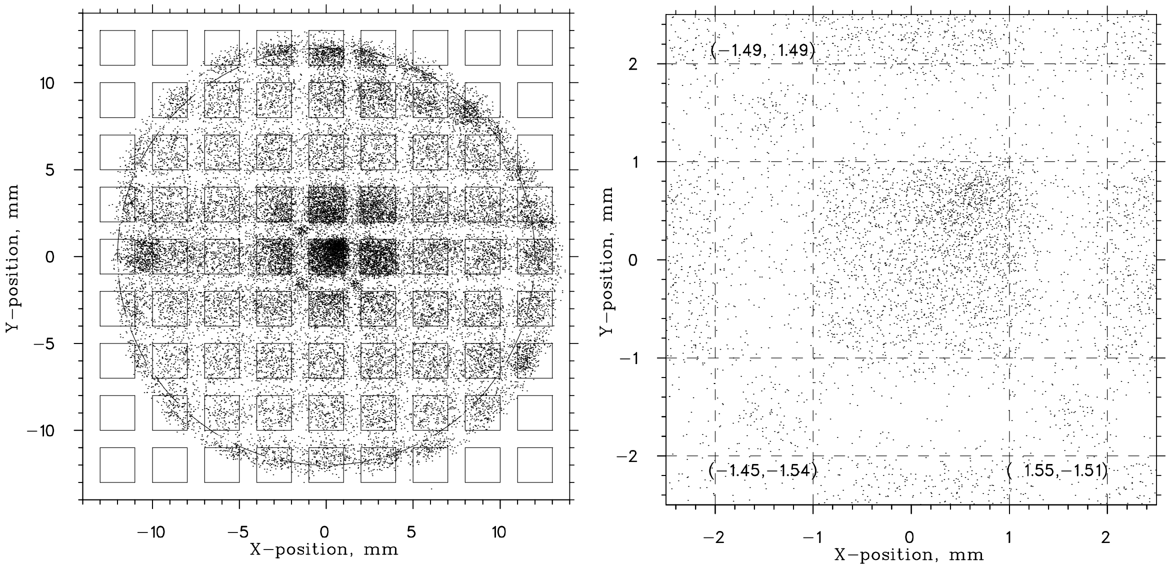

FIGURE 2.18: Fit-transformed electronic images of the mask.

### 2.5.3 The positron detector.

As a positron detector we have used a beta telescope (see Fig 2.19) consisting of a **d**ouble-sided **s**ilicon **s**trip $\Delta$E **d**etector (DSSD) followed by a plastic BC408 scintillator [83] 65 mm in diameter and 55 mm long, which was optically coupled through a Plexiglas light guide about 15 cm long to a Philips 4312/B 12-stage photomultiplier tube (PMT). The relatively low (compared to the silicon based detectors) energy resolution of the plastic scintillator (about 10% in the energy region $0-5\,\mathrm{MeV}$) is less important in the experiment than the time resolution and the much lower positron backscattering off the detector. A detailed description and analysis of the construction and operation of the beta telescope may be found in the Master's thesis of D.Melconian [84]. Here we just provide a brief overview of this device.

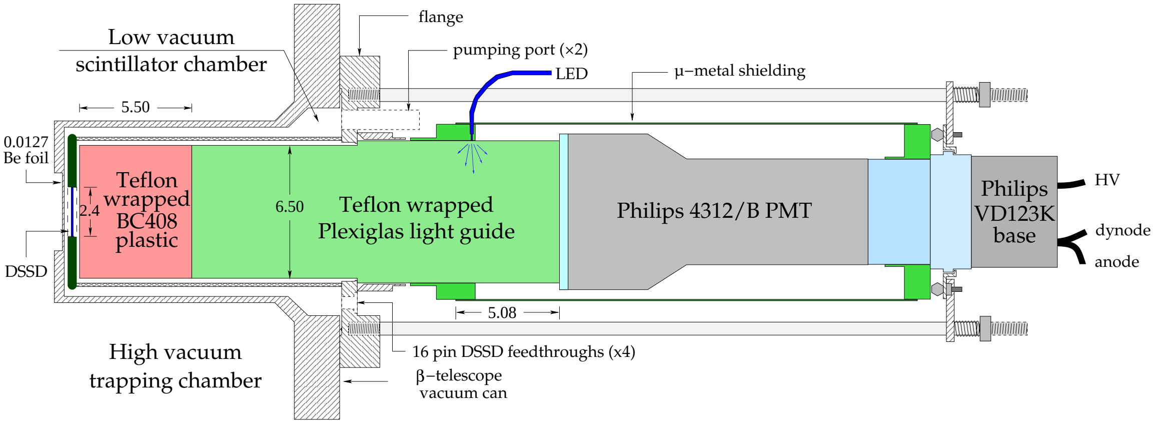

FIGURE 2.19: Beta telescope view: the DSSD-scintillator-lightguide-PMT assembly. The assembly is shown in the low vacuum can together with the elements of the telescope holder. All dimensions are given in cm.

The $\Delta$E detector, manufactured by Micron Semiconductor [85] is a silicon wafer 0.491 mm thick with a square active area $24\times24\,\mathrm{mm}^2$. Each side of the detector has 24 evaporated thin aluminum electrodes 0.9 mm wide separated by a gap of 0.1 mm. The strips on the opposite sides were orthogonal. If one applies a potential difference between the electrodes on each side of the detector (typically 100 V), the electrons and holes, created in the detector's body due to the traversing ionizing particle, will drift in the nearly uniform electric field toward the appropriate electrode. The resulting current pulse can be detected. This design allowed us a simple hit localization in the transverse plane. The view of the DSSD together with the mount is shown in Fig 2.20 under the working orientation. The signals from each strip were individually amplified to allow an amplitude analysis. In addition, Y-strips, grouped by six, provided timing

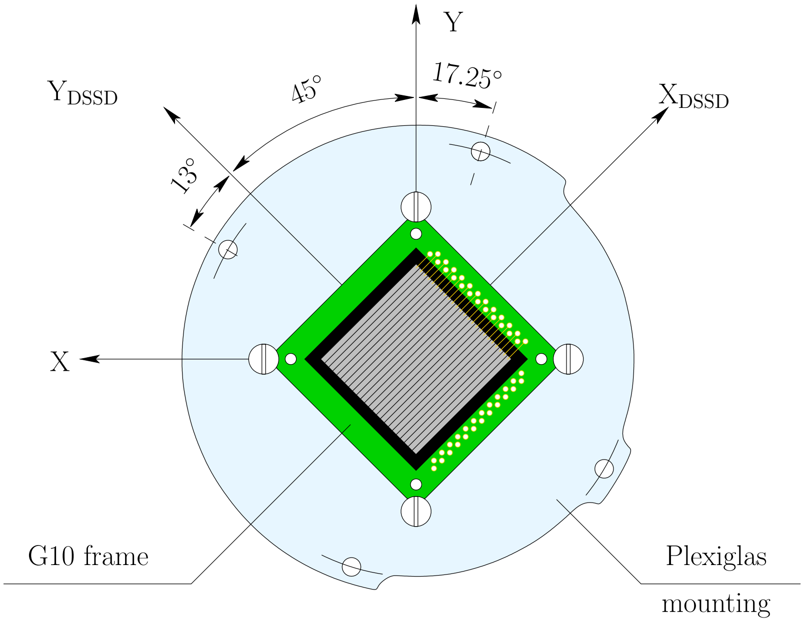

FIGURE 2.20: Schematic view of the DSSD. On the front side of the DSSD one can see the Y-strips which faced the positrons and provided both amplitude and time signals. The $X-$strips are hidden on the rear side of the DSSD and provided amplitude signals only.

signals to make a hardware coincidence with the scintillator. The $\Delta E$ detector was initially calibrated with low-energy photons from a source of $^{241}$Am and later on-line with the positrons from $^{38\mathrm{m}}$K $\beta^+$ decay. Only events which produced a single hit in each plane have been included in the analysis. Conditions on the amplitude of the DSSD signal were rather relaxed as we accepted practically all events which have had energy deposition in DSSD less than 1 MeV. [†] The details of the DSSD position analysis and energy calibration are provided in the M.Sc. thesis of D. Melconian [84].

After passing through the DSSD, ionizing particles enter the scintillator detector, which is situated just 2 mm behind the DSSD. A view of the scintillator-DSSD assembly (courtesy of D.Melconian) is presented in Fig 2.19. To ensure as uniform as possible light response of the scintillator, the scintillator itself and light guide were wrapped in a diffusive reflector, Teflon. The possible gain drift of the PMT was controlled by a stabilization unit [86]. By analyzing the PMT response to light pulses

---

[†] We have demanded the agreement between the signals from $X-$ and $Y-$planes: $|E_x - E_y| \leq 30\,\sigma$. Given the average energy deposition in the DSSD about 140 keV and $\sigma \simeq 8$ keV [84] this resulted in the acceptance of the overwhelming majority of the DSSD events. Cases when either $X-$ or $Y-$signal exceeded 1 MeV were considered to involve multiple, large-angle scattering of the positron in the DSSD and excluded from analysis.

from a blue light emitting diode (100 Hz repetition rate, pulse amplitude corresponding to an energy deposition of about 6 MeV) the stabilization unit corrected the voltage in the last dynode of the PMT to keep the gain constant. The LED was stabilized by varying its voltage to keep a constant pulse height in a temperature-stabilized photodiode detector. The light from the diode of 430 nm wavelength was delivered through an optical fiber to the body of the light guide that couples the scintillator and photomultiplier tube.

For temporal and amplitude analysis of the scintillator signals we have incorporated different PMT outputs. For timing we have used the anode output of the photomultiplier, which has highest gain and smallest time jitter. For amplitude analysis the output from the last dynode was used. Because of the smaller gain compared to the anode output, the last dynode is more linear as it is not affected by a variety of effects including the possible saturation of the PMT power supply.

### 2.5.4 Electrostatic focusing system.

The uniqueness of this experiment is based upon the fact that our group first suggested $\beta - \nu$ correlation measurements by means of simultaneous detection of the positrons and recoils [39, 44, 87]. The efficiencies of both the positron and recoil detectors play an extremely important role in the understanding of the experimental results. This is so because we are going to deduce the correlations by making comparison of the recoil time of flight spectra with that from Monte-Carlo simulations. Any efficiency dependence on recoil energy or on the hit position may induce significant systematic errors and decrease the precision of the experiment.

The known data about using microchannel plates for detection of atomic beams reveals that the detection efficiency depends on the species of atoms, their energy and charge. Neutral atoms have small detection efficiency, and it would vary up to atom energies of about 20 keV [88]. Partially ionized atoms are much more attractive. For instance, positive Ar ions have saturated detection efficiency $\simeq 60\,\%$ at energies $E_R > 3\,\mathrm{keV}$ [89].

From the $\beta^+$ decay we have expected in the detection chamber both neutral and charged Ar atoms. By comparing singles $\beta^+$ rates to coincidence rates, we determined that most of them, about 85 %, appear as either negative ions $\mathrm{Ar}^-$ or as neutral $\mathrm{Ar}^0$, with the rest as $\mathrm{Ar}^{+n}$ with n= $1, 2, 3, \ldots$ [41]. Due to the auto-ionization process, most of the $\mathrm{Ar}^-$ ions will convert into neutral atoms within a few picoseconds, although, in principle, some could remain as metastable $(\mathrm{Ar}^-)^*$ with lifetime 260 ns [90] (see below subsection 3.6.1). So, the application of an electric field which accelerates positive

Ar ions toward the recoil detector, increasing the impact velocity and accordingly their detection efficiency, significantly improves the experiment and simplifies data analysis. By doing this we at the same time enlarge the effective solid angle of the recoil detector and, hence, the overall efficiency. For instance, the geometric size of the recoil detector is about 0.01 of $4\pi$, while the application of an electric field 800 V/cm in our geometry allows one to direct onto the MCP about 30 % of the $Ar^{+1}$, 70 % of $Ar^{+2}$, 95 % of $Ar^{+3}$ and all $Ar^{+4}$ ions in coincidence with the corresponding positron. The electric field almost completely separates all these ions in time of flight and allows us to analyze them individually.

In order to simplify the future analysis, we have decided to apply a uniform electric field (parallel to the detection axis) in which the equations of motion of the charged particles are very simple and solvable analytically (see Fig 2.11). This decision gave us the possibility to accelerate the Monte Carlo analysis about 1000 times, as numerical integration was no longer needed.

The electrostatic focusing system (see Fig 2.21) consists of the the four hoops ($H_1 - H_4$), two split (inner/outer) plates ($P_1^i$, $P_1^o$, $P_2^i$, $P_2^o$), the MCP−RA assembly and the supporting structure. The hoops and plate $P_1$ were made of 1 mm thick glassy carbon – strong, light, low Z conductive material, compatible with the ultra high vacuum environment. Plate $P_2^o$ is glassy carbon 2 mm thick. The inner plate $P_2^i$ serves also as the positron collimator for the beta telescope . It is machined from a 2 mm thick Ta-W alloy plate. (See Fig 2.12 which also illustrates the construction used to achieve the split plate design.) Each of the hoops and plates is annular in

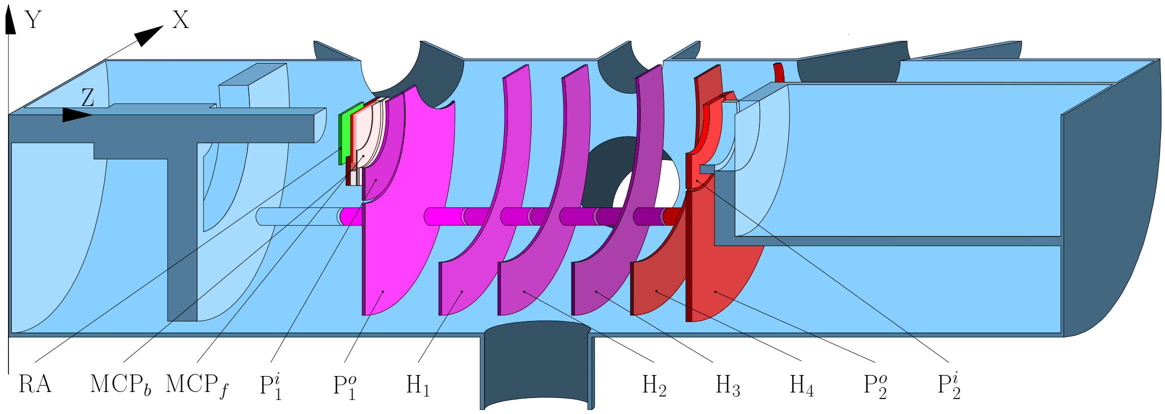

Figure 2.21: Three-dimensional view of the grid volume. The different colors represent elements under different potentials with blue color assigned to the ground: RA - resistive anode; $MCP_b$ - back MCP; $MCP_f$ - front MCP; $P_1^i$ - plate 1 inner; $P_1^o$ - plate 1 outer; $H_1$ - hoop 1; $H_2$ - hoop 2; $H_2$ - hoop 2; $H_3$ - hoop 3; $H_4$ - hoop 4; $P_2^o$ - plate 2 outer; $P_2^i$ - plate 2 inner (collimator).

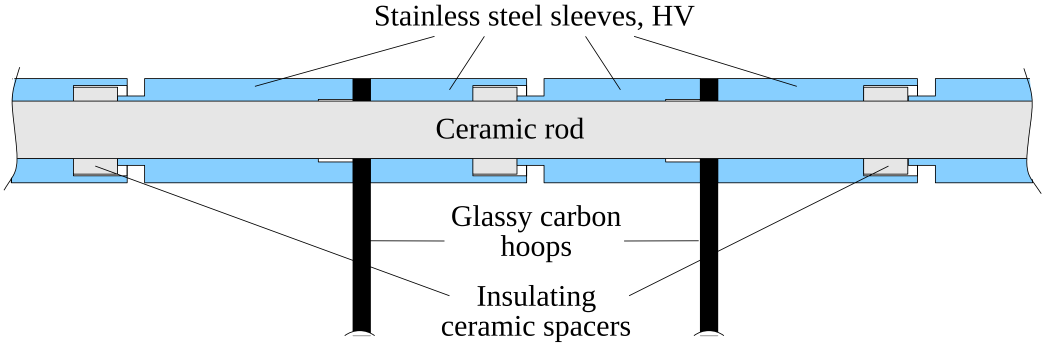

Figure 2.22: Element of the focusing system.

shape (preserving cylindrical symmetry of electric field) but both $P_1^o$ and $P_2^o$ required cutouts to allow for transmission of the four horizontal trapping laser beams. Special attention was paid to the presence of the insulators in the trapping volume. All ceramic parts were screened by conductive elements to exclude direct view from the trap and prevent charge build up on their surface. Glassy carbon was used to avoid oxide layers and patch effects. A cross section of part of the focusing system element illustrating the insulators can be seen in Fig 2.22.

Each element of the focusing system was biased to a specific potential, to provide a uniform electric field in the region of travel of the detected Ar ions. The values of the individual potentials were calculated by the relaxation method [91] using the modified RELAX3D code [92, 93], which allows electric field calculations on a three dimensional rectangular grid mesh. This package was chosen because of the availability of the source code, which was needed to make modifications. Modifying the program, we have incorporated a relaxation code into a fitting routine based on the Marquardt algorithm [94, 95]. With a given geometry, the electrode potentials are determined by specifying the desired value of the electric field, and then letting the program run.

As the detection chamber including the electrodes and vacuum apertures has up−down and left−right symmetry, it was enough to make calculations of the electric field just in one quarter of the volume, which was done using a grid mesh with 0.25 mm along the detection axis (Z) and $0.5\times0.5\,\mathrm{mm}^2$ in the transverse plane; $1425\times201\times201$ grid points altogether. A view of the grid volume can be seen in Fig 2.21. We were forced to use such a small grid size because the relaxation code allowed one to make the element boundaries only at the grid points, so the element sizes and the distances between them along the detection axis could only be specified with increments of 0.25 mm. The spacing in the transverse direction was not so critical, but, for the better convergence of the relaxation process, dimensions of the mesh along different axes should be similar and not differ more than by a factor of 3−4.

As a figure of merit, which was minimized during the fitting procedure, we have used a standard deviation of the calculated electric field strength from the desired value. The evaluation of the field standard deviation has been performed in each grid point along the detection axis between the MCP and the point 10 mm beyond the center of the chamber, 289 points altogether. As the relaxation code calculates the values of the potentials in each grid point, we have calculated an electric field in the separate routine using 5−point Lagrange interpolation.

In Fig 2.23 we present the distribution of the longitudinal component of the electric field at different radii in the central horizontal plane ($X$−axis). The values of the electrode potentials which resulted from the calculations are collected in the Tab 2.3.

### 2.5.5 Operation of the experimental apparatus.

The experimental apparatus worked in the following way. A mass-separated beam of mixed $^{38\text{gs}}$K and $^{38\text{m}}$K ions is stopped and released as neutral atoms from the Zr neutralizer. Only the $^{38\text{m}}$K is captured into the vapor-cell MOT in the collection chamber with a capturing efficiency about $10^{-3}$. Trapped $^{38\text{m}}$K atoms are resonantly transferred using a chopped laser beam with 75 % efficiency to the second, detection chamber, equipped with the nuclear detectors. The atoms are re-trapped there into the detection MOT directly from the atomic beam. The duty cycle in the second trap entails: push atoms from the first trap for 20 ms; wait 50 ms for transfer; change the second MOT laser frequency and the power to minimize the atomic cloud size; wait 1 ms to let the cloud reach equilibrium; collect data for 150 ms from the small unperturbed trap; repeat [40].

The operation of the trapping apparatus is controlled by a dedicated computer,

TABLE 2.3: Electrode potentials resulting from the fitting procedure. See Fig 2.21 for electrode notation.

| Electrode | $U$ [V] | Electrode | $U$ [V] | Electrode | $U$ [V] |
|---|---|---|---|---|---|
| RA | −500.0 | $P_1^o$ | −3864.4 | $H_4$ | +4172.0 |
| $MCP_b$ | −700.0 | $H_1$ | −1988.4 | $P_2^o$ | +4373.8 |
| $MCP_f$ | −4000.0 | $H_2$ | −6.0 | $P_2^i$ | +5715.1 |
| $P_1^i$ | −3754.8 | $H_3$ | +1859.7 | | |

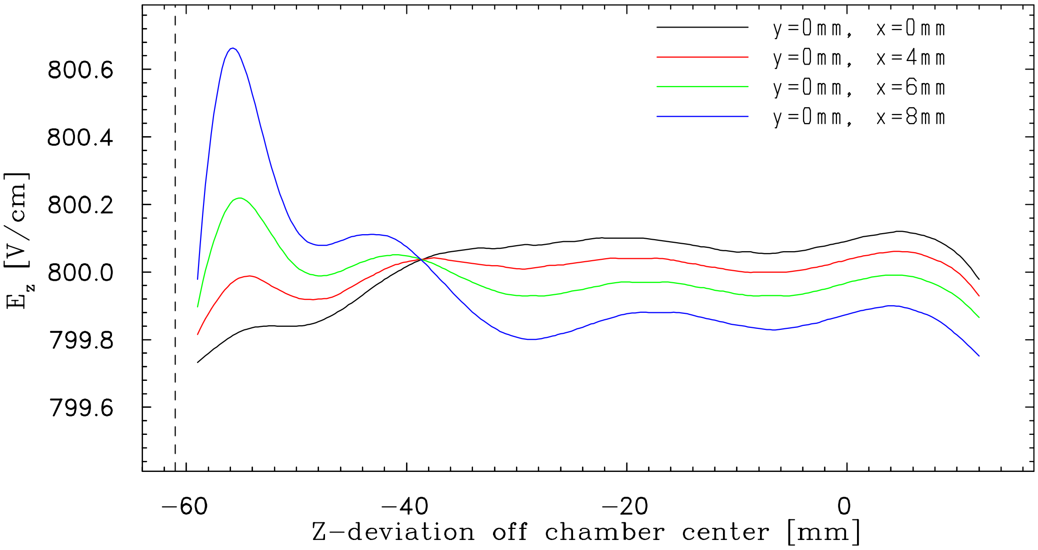

FIGURE 2.23: Longitudinal component of the electric field. Each curve represents the calculated value of $E_z$ along the line parallel to the $Z$-axis and displaced by some amount in the $X$−direction.

which continuously transfers the status of the trapping equipment to the acquisition system for nuclear data, which operates continuously. This gives us the possibility to sort the data depending on the condition under which they have been taken.

### 2.5.6 Data acquisition system of the experiment.

The Data Acquisition System (DAQS) of the experiment consists of two separate subsystems. The first one, which is governed by a PC running the DOS/Windows operating system (OS), controls the process of trapping and transmits the trapping conditions to the second one, an acquisition system for nuclear data based on MIDAS [96]. The signals from the front end electronics, optical DAQS and isotope yield monitors are fed into CAMAC hardware which is controlled by a VME processor running MIDAS under the VxWorks OS. All collected data is sent to a dual processor PC running Linux OS and are stored on hard disk. Both on-line and off-line analysis is done with the NOVA data analyzing program [97].

The operation of the relevant part of the nuclear data acquisition system is described below in some detail and illustrated in the the electronic schematic diagram, shown in the Fig 2.24. For each event DAQS reads and records the following values:

- integral of the signals from the last scintillator dynode and from the 48 strips of the DSSD with charge sensitive ADCs LC2249W and LC2249A respectively;
- amplitudes of the signals from the MCP and from the 4 outputs of the resistive anodes with peak sensing ADCs AD811A and AD413A;

- time of the first and second hits of the MCP with respect to the front edge of the event trigger pulse in the 5th and 6th channel of the multihit TDC LC408.
- state of the trapping apparatus (such as presence of the push beam, trap status) in the C212.

The event trigger (429A) can be initiated by either the positron detector, or the MCP, or pulsers used for on-line calibration, or a Nitrogen laser used for photoionization of the trapped $^{38m}$K. When the system is ready to accept an event, it will be triggered into an acquiring state by the first incoming signal from the mentioned sources. While in acquiring mode, DAQS won't accept any subsequent signal in the ET unit during the inspection time of about $100\,\mu$s while all data are recorded. The trigger generator is a Quad Mixed Logic Fan-In/Fan-Out LeCroy 429A (LC429A), which initiates an identical response to any first incoming pulse. It issues a logic pulse to strobe the *EG&G*/ORTEC C212 [98] unit, a logic COMMON pulse to the multihit TDC LeCroy 4208 (LC4208) and ADC's gates for digitizing the delayed analog signals from the dynode PMT output, multiple DSSD outputs, outputs of the MCP and the resistive anodes. Depending on the source of the trigger we distinguish between five types of events, the origin of which is explained below:

- beta event, when the event is triggered by a scintillator-DSSD hardware coincidence signal;
- scintillator event, when the event is triggered by a prescaled scintillator signal;
- scintillator pulser event, when the event is triggered by the scintillator stabilization system;
- MCP event, when the event is triggered by a MCP signal;
- photo event, when the event is triggered by the strobe of the Nitrogen gaseous laser;
- pulser event, when the event is triggered by a signal from a research pulser.

**Beta events**:

An amplified and discriminated signal from any Y-strip of the DSSD, along with a delayed Constant Fraction Discriminator (CFD) TC455 response to the PMT anode signal, are sent to a coincidence unit LeCroy 465 (LC465). If the signals are overlapped within a time window of 40 ns, a logic output signal from LC465, the front edge of which coincides with the front edge of TC455 pulse, is sent to the input of bit #6 of C212 and to the event trigger unit. Such events are considered as resulting from detection of a positron. They can be used for *in situ* calibration of the beta telescope and will be referenced as double coincident events or doubles.

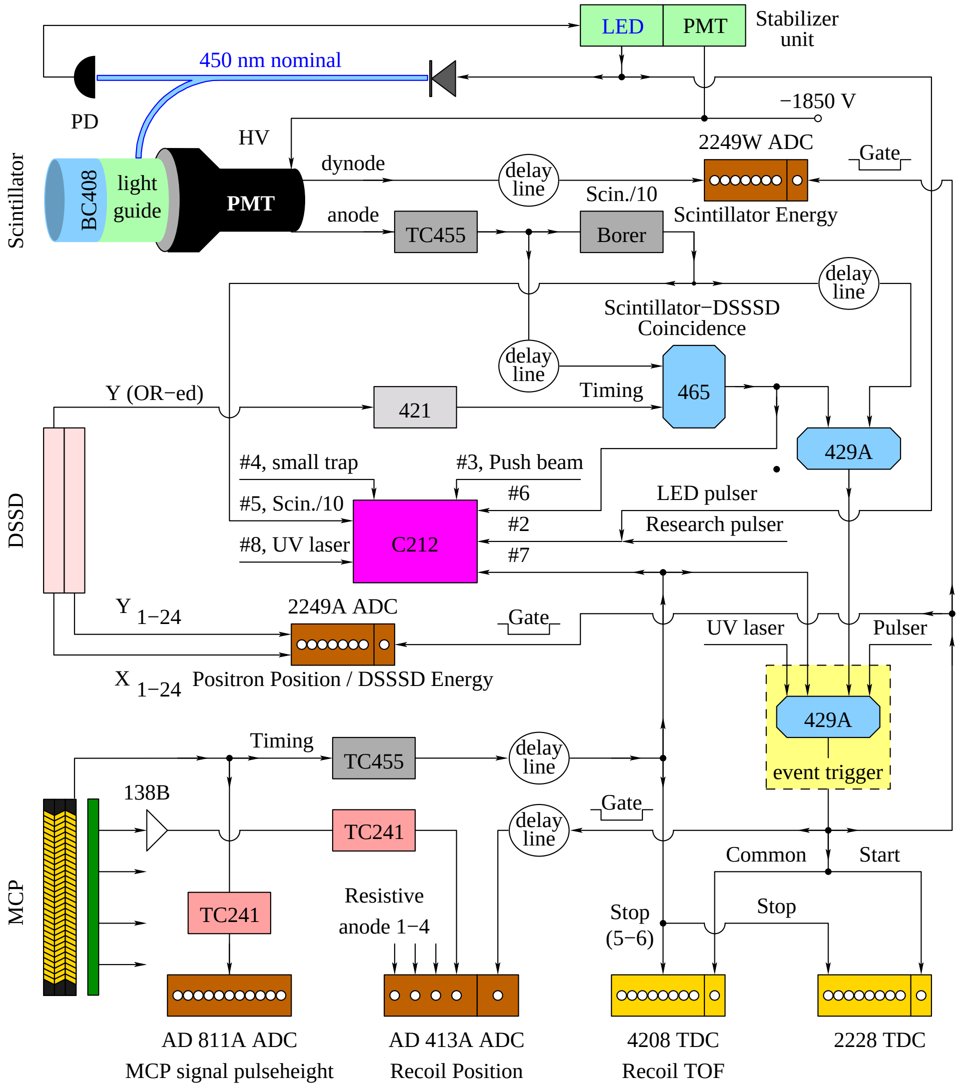

| | | | |
|---|---|---|---|
| LeCroy 2249W | charge−sensitive ADC | LeCroy 429A | quad logic fan−in/fan−out |
| LeCroy 2249A | charge−sensitive ADC | EG&G/Ortec AD 413A | peak−sensitive ADC |
| LeCroy 2228A | single hit TDC | EG&G/Ortec AD 811A | peak−sensitive ADC |
| LeCroy 4208 | 8−channel real time TDC | EG&G/Ortec C212 | coincidence buffer |
| LeCroy 465 | triple 4−fold logic unit | Tennelec 455 | constant fraction discriminator |
| LeCroy 421 | amplitude discriminator | Tennelec 241 | spectroscopy amplifier |

FIGURE 2.24: Electronic schematic diagram of the experiment. In the center of the diagram there is the C212 coincidence buffer, which allows one to store and record into the event stream the state of the nuclear and optical DAQS and distinguish between events taken under different conditions.

For these events the signal from the event trigger to the common input of the 4208 TDC initiates an inspection period of $12\,\mu$s during which the time of the first subsequent hit in the MCP is recorded in channel 5 (MHTDC5). Any second hit within the same period is recorded in channel 6. The MHTDC5 spectrum contains the time of flight data for the $^{38}$Ar recoils observed in coincidence with a positron detected in the beta telescope. These events are referred to as triple coincidences or triples and are used for the evaluation of the $\beta-\nu$ correlation parameter.

**Scintillator singles events**:

The second output of the PMT CFD TC455 is sent to the Borer prescaler, so every $10^{\text{th}}$ scintillator pulse gets passed through. The pulses, passed through the prescaler, are additionally delayed and sent to the input of bit #5 of the C212 and to the event trigger. The delay is adjusted to ensure the input to the event trigger arrives after a possible scintillator-DSSD coincidence (i.e. a $\beta^+$ input). Events, initiated by these prescaled scintillator pulses (Scin/10) without a hardware coincidence are mostly due to the detection of annihilation $\gamma-$quanta and 2.17 MeV $\gamma-$quanta from the $^{38}$K ground state decay. These events are used in the energy calibration of the scintillator and as a measure of the $\gamma-$background. There is no useful information expected from the LC4208 in these events.

**Scintillator pulser events**:

Approximately one tenth of the prescaled scintillator events are initiated by the Light Emitting Diode (LED) of the PMT stabilization system. In addition to the C212 input #5 these events have signal in the input of bit #2 of C212.

**MCP events**:

Discriminated with a TC455 CFD, the delayed MCP logic signal is split in two. One is sent to the input of bit #7 of the C212 and the other to the event trigger. The delay is adjusted in such a way that in the case of a simultaneous hit of scintillator and MCP, the signal from the MCP comes about 30 ns later than that from the scintillator and as a consequence the timing of the event trigger is defined by the leading edge of the scintillator TC455 CFD. MCP events with no coincident positron detected in the beta telescope have a characteristic feature in the LC4208. As the common input and the stop are derived from the same pulse, MHTDC5 exhibits a "self-triggered" peak. In cases when this trigger was caused by a $\beta^+$ incident on the MCP, there may be a second hit (recorded in MHTDC6) resulting from the coincident recoil emitted predominantly toward beta telescope.

**Photo ionization events**:

A Nitrogen laser strobe is split in two and sent to the input #8 of C212 and to the event trigger. MHTDC5 of LC4208 contains information about the TOF of trapped $^{38\mathrm{m}}$K atoms ionized and accelerated from the trap to the MCP. As such ions are born essentially at rest (with energy about 1 eV) they spend longer time in the trap volume before being accelerated and are used to probe the uniformity of the applied electric field in this region.

**Pulser events**:

A strobe from the *EG&G*/ORTEC 448 research pulser is sent to input #2 of C212 and the event trigger. The signal itself is sent to the RA preamps *EG&G*/ORTEC 138B and is used to monitor the stability of the preamps.

## CHAPTER 3

# Data Analysis.

From the data collected with the TRINAT apparatus, evaluation of the $\beta - \nu$ correlation parameter $a$ can be done in several ways. For instance, it is possible to study the shape of the energy spectrum of the detected Ar recoils [99, 100, 101] or study the shape of the positron-neutrino angular distribution. Both these approaches require evaluations, event by event, of the recoiling Ar atom momentum, while the second one also needs the same evaluations for the positron. We have decided to analyze the time of flight spectra of the Ar recoils detected in coincidence with the positrons, which are, of course, related to the recoil energy distribution. See Fig 3.1.

Such an approach gives us a possible way to avoid calculations event by event of the recoil transverse hit position for the data. Instead, we use spectra for all events, accepted by the recoil detector within an active area, well defined by a precisely manufactured aperture. This eliminates possible systematic errors caused by the spatial

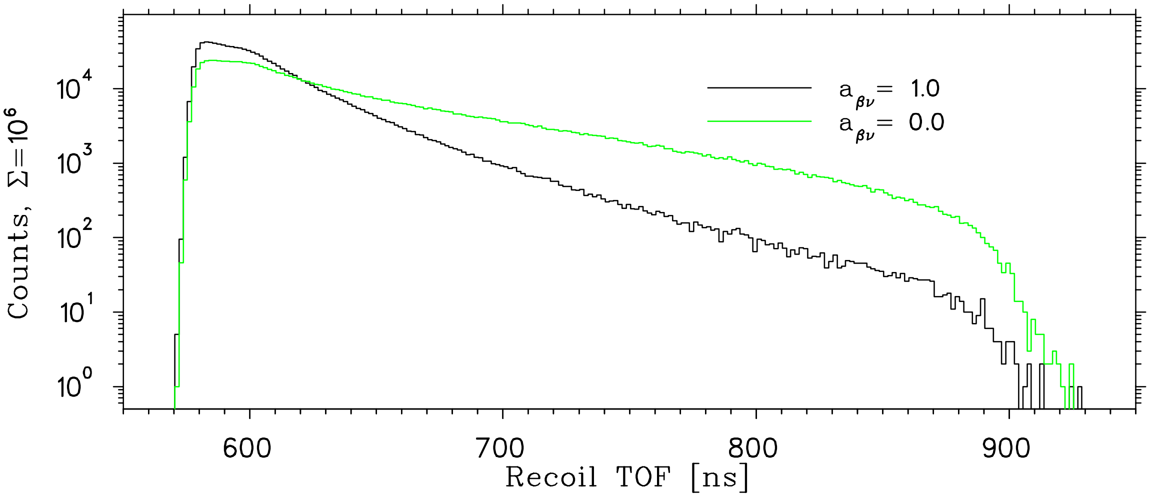

FIGURE 3.1: Monte Carlo simulation of $^{38}Ar^{+1}$ recoil TOF spectra with $a$ = 1.0 and $a$ = 0.0. Simulations are done under the present experimental conditions.

non-linearities of the recoil detector response, described in the Sec 2.5.2 but leaves uncertainties due to trap position and electric field strength. In principle, part of these errors caused by the finite size of the active area of the MCP vanishes too if all recoils coincident with positrons are collected, as has been done in the correlation experiment with trapped $^{21}$Na by the Berkeley group. Unfortunately, due to the physical constraints in the apparatus we were not able to work in such a regime and collect not all of the Ar$^{+1}$, Ar$^{+2}$ and Ar$^{+3}$ ions (See Sec 2.5.4 for numbers). In contrast, we use the dependence of the beta decay rate on the positron energy in the data analysis. This substantially increases the sensitivity to the correlation parameter though it requires a calibration of the beta detector and introduces additional systematic errors.

In this chapter we describe the Monte Carlo model of the experiment, present the collected experimental data, show how the data has been manipulated to define the energy calibration of the beta detector, the trap size and position inside the detection chamber, the electric field strength and some other parameters, which are necessary for careful Monte Carlo simulation of the experiment.

## 3.1 Monte Carlo simulations.

In designing the experiment and for the data analysis we have developed and used two Monte Carlo models of the experiment. Both of them employ a simulation of the positrons and neutrinos creation with the decay rate

$$\frac{d\Gamma}{dE_e d\Omega} \sim F(E_e, Z)\, p_e E_e E_\nu^2 \left[1 + b\frac{m_e}{E_e} + a\frac{p_e}{E_e}\cos\theta\right], \tag{3.1}$$

where $c = \hbar = 1$; $m_e$, $p_e$ and $E_e$ are the positron rest mass, momentum and the total relativistic energy; $E_\nu = E_0 - E_e$ is the neutrino energy; $E_0 = Q_\beta + m_e$ is the total energy released in the decay for positron and neutrino (5.5333 MeV in the case of $^{38\text{m}}$K); $\theta$ is the angle between positron and neutrino momenta; $F(E_e, Z)$ is the Fermi function, accounting for correction to the positron energy due to its Coulomb interaction with the daughter nucleus. The kernel of both Monte Carlo models is a FORTRAN program, which, taking into account radiative order$-\alpha$ corrections [51], generates initial momenta of positrons and neutrinos distributed in accordance with expression (3.1). We assume the initial $^{38\text{m}}$K atom was at rest at the time of decay, ignore the kinetic energy of the recoiling daughter nucleus (as $T_R < 430\,\text{eV}$) and thus calculate the initial recoil momentum

$$\boldsymbol{p}_{Ar} = -\boldsymbol{p}_e - \boldsymbol{p}_\nu \ .$$

and, given the knowledge of the initial coordinates and the applied electric field, trace the recoil and positron in the experimental apparatus.

One Monte Carlo model is a full GEANT3-based model of the experiment, developed mainly by D. Melconian and described in his M.Sc. thesis [84]. It includes a complete geometric and material description of the detection chamber (see section 2.5), allows one to track each primary and secondary particle from the decay through all physical volumes, to flag them in each volume and evaluate energy losses. The tracking of a particle is aborted when its kinetic energy becomes smaller then 0.5 keV. The annihilation of positrons and the interaction of the subsequent photons are included. These Monte Carlo simulations allow us to completely reproduce the experiment by calculating event by event such values as the energy, absorbed in the scintillator and in the DSSD; position of the impact of the positron on the DSSD; TOF of the recoiling Ar atoms and ions from the trap to the MCP and position of the impact of the recoil on the MCP. We use it to understand energy losses of the positrons in the scintillator and to build scintillator response functions for positrons with any given energy. Although this model is indispensable for understanding all physical processes in the detection chamber, it makes full analysis of the experimental data difficult because of very time consuming calculations.

To speed up calculations we have developed another, simplified model, which will be referred to as the "fast" Monte Carlo. In this model we produce events, in which positrons originate from the trap and propagate inside a solid angle, covering the DSSD. The act of positron detection including the energy left in the scintillator is evaluated using a response function derived with the full Monte Carlo program. Because there is no tracking of the positrons in the media, calculations are about three orders faster than in the GEANT-based MC. Here we take into account such parameters as trap position and size, electric field strength and the values of the $\beta - \nu$ angular correlation parameters $a$ and $b$. The propagation of the recoils is described as the motion of a charged or neutral particle in the uniform electric field (see Sec 2.5.4) and the recoiling Ar ion is considered as detected if it hits the MCP within a 12 mm radius (defined in the hardware by the aperture shown in the Fig 2.15). The detection efficiency of the MCP for Ar ions under experimental conditions is considered to be constant [89].

We have compared the events from the fast MC with those from the GEANT-based MC, produced under similar condition, i.e. the same trap size and position, electric field strength and the same active sizes of MCP and DSSD. The full MC includes positron interactions in the 127 $\mu$m Be foil between the trap and DSSD. We define as "response events" one class of positron trajectories within GEANT for which the positron emitted from the trap strikes first the Be foil and then the DSSD. For a given initial positron energy we define the corresponding scintillator energy response by the distribution of energies deposited in the scintillator averaged over all of the corresponding "response events" generated in GEANT (for example see Fig. 4.13 and 4.14). These response functions are then used in the fast MC to account for the response of the beta telescope to positrons incident directly from the trap. The recoil TOF spectra, produced for a wide energy range of coincident positrons with the fast MC and with "response" events from the GEANT-based program have been found to be indistinguishable.

Within GEANT there are a relatively small number of events that are not "response" but still result in significant energy loss in both the DSSD and the scintillator in coincidence with a recoil hit on the MCP. Most of these "not response" events involve positrons either scattered off the edge of the collimator ("scattered") or, being initially directed toward the recoil detector, were scattered back to the beta telescope from the MCP or surrounding elements ("backscattered", see Fig 2.12). The ratio of the "not response" to "response" events depends on the energy deposited in the scintillator, decreasing as that energy increases. The GEANT-based MC simulations show that for all events with detected positron energy above 500 keV this ratio is less than 0.018.

When building the Monte Carlo simulated spectra which were used in the analysis of the experimental data, we have mixed events, produced by both fast MC and "not-response" events from the full MC. The fraction of events added was defined by the "not-response" to "response" ratio which we have calculated using the full MC. On top of that we have added in a random coincidence background, evaluated from the collected triples data with events which have MHTDC5 reading in the channel range 3000−9000. This background we attribute to events which are triggered by a positron in the beta telescope from one decay followed by the detection of a hit in the MCP originating from another decay. During the analysis we have varied MC parameters such as the energy calibration of the scintillator, trap size/position, electric field strength or $\beta - \nu$ correlation parameters in the fast MC only, while "not response" events have been generated once, with our best estimates of these values. We consider this procedure to be legitimate because of the relatively small fraction of "not response" events.

## 3.2 The principles of the data analysis.

As a way to analyze the experimental data we have chosen a fitting of different kinds of experimental spectra with those produced with Monte Carlo simulations. Considering that errors of the count in each bin of experimental spectra obey a Poisson distribution, we have searched for a maximum of the Likelihood function, constructed with the data and MC simulations. All parameters of interest we evaluated at this point of maximization. To be more specific, we have minimized the quantity

$$\chi^2_\lambda(\mathbf{p}) = 2\sum_{i=1}^{N} f_i(\mathbf{p}) - y_i + y_i \ln \frac{y_i}{f_i(\mathbf{p})} \ , \tag{3.2}$$

where the summing is performed over the $N$ data points included in the fit; $y_i$ and $f_i(\mathbf{p})$ are the experimental count and fitting function (MC count plus small backgrounds) in the $i^{th}$ entry and $\mathbf{p}$ is the vector of parameters, subjected to optimization. It is shown [102], that (3.2) reaches a minimum at the same point of parameter space $\mathbf{p} = \mathbf{p}_0$ where the Likelihood function $\mathcal{L}(\mathbf{p})$ is maximized and gives unbiased estimates of the parameters $\hat{\mathbf{p}}_0$. A Maximum Likelihood fit has been chosen over Least Squares (where the counting statistics in each data bin is considered to obey to Gaussian distribution) for the following reason. In order to increase the sensitivity of the analysis to the fitting parameters we have created many bins in the experimental spectra. But it is known [103] that limited numbers of entries in bins can result in errors in normalization. Although the bias, introduced with each bin may be smaller than the corresponding statistical error, a result based on such a fit can be wrong by an amount larger than the overall statistical error. It is even recommended [104] that in the case of a Least Squares fit, the number of events in each bin should be at least 50.

Returning to the expression (3.2) one can say that the function $\chi^2_\lambda(\mathbf{p})$ has properties similar to a $\chi^2$ in a Least Squares fit. The value of $\chi^2_\lambda$ at the point of minimum indicates the quality of the fit and the curvature of the hyper surface $\chi^2_\lambda(\mathbf{p})$ at the point of minimum defines the errors of the estimates $\hat{\mathbf{p}}_0$, although one has to be careful when the average number of counts in a bin becomes small.

The search for the minimum of the $\chi^2_\lambda$ function from (3.2) has been performed using the Marquardt algorithm [94, 95], which allows for an effective search for the minimum even in the case of highly nonlinear dependence on the optimized parameters. In just a few cases, when we have encountered extremely high correlations between parameters, have we relied on mapping of the $\chi^2_\lambda(\mathbf{p})$ hyper surface.

## 3.3 Experimental data.

The correlation parameter analysis has been done with data collected during October-November of the year 2000. Using CCD camera images of the cloud fluorescence, we have selected runs with trap stability better than 0.05 mm along the detection axis. Overall we have recorded 508905 triple events (See section 2.5.6) with the detection of a positron in the beta telescope ($\Delta E{\cdot}E$ coincidence) producing the event trigger followed by a hit in the MCP recorded in MHTDC5. These have signals in the scintillator ADC channel range 50−1800 and MCP TDC range 0−11 $\mu$s (1 ns/channel). The part of this data in the time range 0−3 $\mu$s is shown in Fig 3.2 as a scatter plot, where each dot represents a detected event. The presented data appear in roughly three groups. The first group (from right to left) is concentrated near channel 1500 of the horizontal axis. It contains mostly events when a neutral recoiling Ar atom was detected in coincidence with a positron from the same $\beta^+$ decay. The data located between TDC channels 400 and 1200 is filled with events involving the detection of coincident $\mathrm{Ar}^{+1,+2,\ldots,+6,\ldots}$ ions. Near TDC channel 100 one can see two clusters. They contain events when both detectors have registered relativistic particles such as positrons, annihilation $\gamma$−quanta or UV photons. The 24265 events located near TDC channel 110 represent cases of near simultaneous detection of relativistic particles by both the beta telescope and the recoil detector (scintillator-MCP prompt). The 178 events in TDC channels 78 and 79 are the result of an MCP event trigger which occurs slightly before an unrelated positron is detected in the telescope. (The same signal results in both the TDC start and stop.) Across all TDC channels > 79 there are similar events

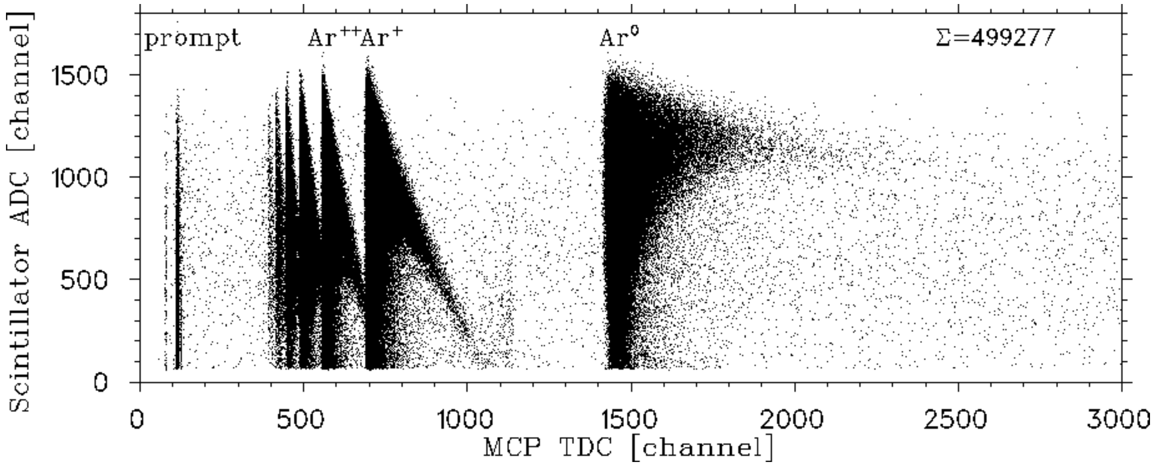

FIGURE 3.2: Triple coincident events from the runs, selected for the correlation parameter evaluation. 499277 events in the plot.

for which the positron provides the event trigger, in most cases (TDC $> 113$) followed by an unrelated hit in the MCP. As was indicated in the Sec 3.1, the spectrum of these events recorded in the range $3000 \leq$TDC$\leq 9000$ is used to estimate the contribution of accidental coincidences in the region of the real $\beta^+$–Ar coincidences. As expected, the random coincidences exhibit a scintillator ADC distribution essentially the same as that of the positron double coincident events.

The events, shown in the Fig 3.2 have additional conditions, which are listed below.

Beta telescope:
- The single hit in the DSSD must be within the central 22 mm in both $X$ and $Y$. This helps to exclude cases of multiple scattering of the positron off the DSSD mount. It is also vital as the effective size of the collection area of the outermost strips is poorly defined because of fringe field.

Recoil detector:
- There should be no hit in the second channel of the MCP TDC (MHTDC6), this removes event multiplicity in the recoil detector and allows undistorted RA amplitude analysis;
- there should be a nonzero reading in the MCP ADC;
- each of all four RA signals should be nonzero and below an upper threshold of 8600 to exclude saturation of the charge sensitive preamps, this makes possible reconstruction of the transverse recoil coordinates on the MCP.

This filtering has removed 118048 events from analysis. Among those removed are:

|  |  |  |
|---|---|---|
| 70236 | - | outer strips of DSSD fired |
| 34037 | - | double hit in recoil detector |
| 22565 | - | zero reading in the MCP ADC |
| 57 | - | RA preamp missing or saturation. |

(The total number of listed events is bigger than 118048 because some of them have met multiple conditions for removal.) These initially filtered data are shown in the Fig 3.3.

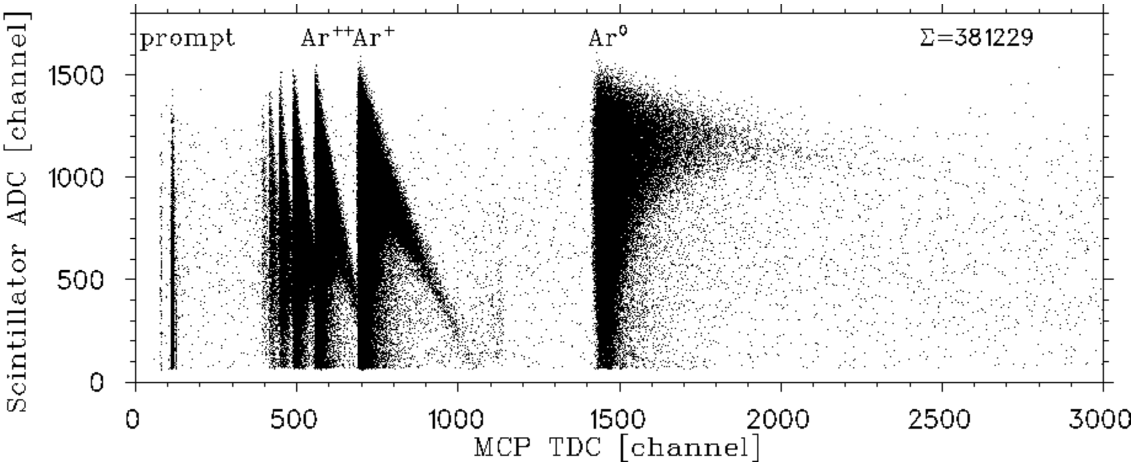

FIGURE 3.3: Preliminarily filtered triple events.

## 3.4 Energy calibration of the scintillator with double coincident events.

As mentioned above, using the observed dependence on positron energy in the data analysis has made necessary an energy calibration of the scintillator detector. Such a calibration had been performed with radioactive $\gamma-$sources after the manufacture of the detector [84]. This was based on fitting measured Compton spectra with Monte Carlo simulations. We have adopted the detector's energy resolution, determined this way.

$$\sigma_{scin} = \sqrt{(1.80\,\mathrm{KeV}) \times T_{scin}}$$

However, because of different backgrounds and known discrepancies between the calibration of such detectors with the $\gamma-$sources and charged particles [105] we have decided to recalibrate detector with the data collected in the correlation experiment.

To be consistent, we have chosen the same set of runs as in the analysis of the recoil TOF spectra. From these runs were selected scintillator data, corresponding to the double coincident events (See Sec 2.5.6 for definition) with the DSSD having single hits in the central $22{\times}22\,\mathrm{mm}^2$. The data from 7711727 events were binned to get an experimental spectrum of energies observed in the scintillator. The spectrum created with binning 5 ch/bin is shown in the Fig 3.4. It was fitted with a spectrum generated in the GEANT-based MC under the same conditions as the data. While simulating the MC events we have used Standard Model values of the $\beta$–$\nu$ correlation parameter $a = 1$ and Fierz term $b = 0$ in the expression for the beta decay rate (3.1). Because the Monte Carlo simulates only events originating from the beta decay of the $^{38\mathrm{m}}$K in

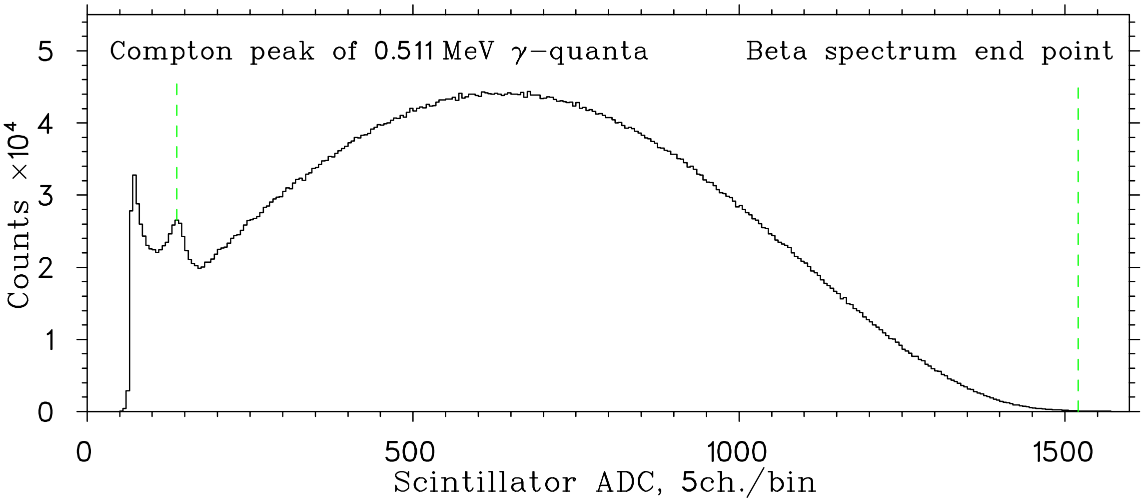

FIGURE 3.4: Experimental spectrum of energies detected in the scintillator from double coincident events.

the trap it did not reproduce contributions of the untrapped $^{38m}$K and ground state $^{38}$K atoms which decay both in the detection and collection chambers. We describe them as two backgrounds, which have been measured experimentally and added with appropriate normalization to the MC simulations. One of them, called "valve open" is created mostly by the decay of the ground state $^{38}$K which resides primarily in the collection chamber but also partially diffused into detection chamber through the connecting pipe (See Sec 2.1 for decay scheme of $^{38}$K). We have measured the valve open spectrum by switching off the isomerically selective transfer of the atoms between the chambers. Another type of background is created by the untrapped $^{38m}$K atoms decaying on the walls of the detection chamber and on the elements of the accelerating electrostatic system. This, so called "poof" background has been evaluated by switching off the trap in the second chamber, releasing trapped atoms and taking measurements while they are sitting on the surrounding construction elements. Because of the low count rate we were not able to collect an amount of background events, comparable with that in the double data. For this reason the background spectra have been smoothed using a fourth order Savitzky-Golay smoothing filter, which preserves the area under the data, the zeroth moment, but also the higher moments [106, 107]. Because of the fast changing slope of the spectra we have used a variable filter width $nw$ (see Fig 3.5).

Both background spectra have been normalized to unit count and used in the fitting expression:

$$F = Norm \times [MC] + B_{pw} \times [Backg_{pw}] + B_{vo} \times [Backg_{vo}] \tag{3.3}$$

where $[MC]$ is the Monte Carlo simulated spectrum of the energy deposited in the scintillator, $[Backg_{vo}]$ and $[Backg_{pw}]$ are normalized "valve open" and "poof" background spectra respectively. A $B_{pw}$, contribution of the "poof" background, has been estimated to be 0.01 of the double coincident events while the $B_{vo}$, contribution of the "valve open" background, and normalization factor $Norm$ have been considered as fitting parameters. We have adopted a linear detector calibration, transforming simulated scintillator observed energy $E_{sc}$ into ADC channels using expression

$$Channel = Offset + Slope \times E_{sc} \ , \tag{3.4}$$

with the parameters *Slope* and *Offset* being varied during the fitting procedure.

The observed scintillator energy spectrum shown in Fig 3.4 has two well defined points. The first one is a peak near channel 150, which is created by Compton

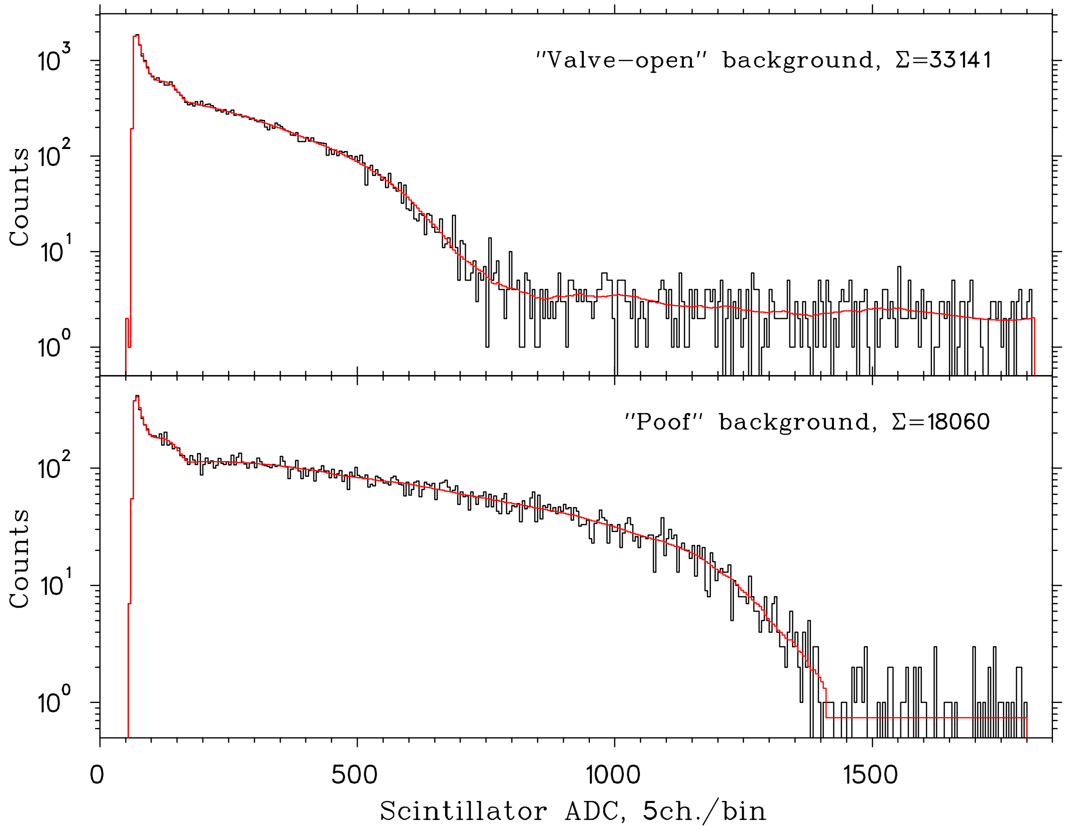

FIGURE 3.5: Experimentally measured double coincident background spectra: original data in black and smoothed ones in red. Upper panel: "valve open" background. ADC range 70−168: nw=98, 168−1800: nw=500. Lower panel: "poof" background. ADC range 70−172: nw=110, 68−1410: nw=520, 1410−1800: flat with average level value.

scattering in the scintillator of the 0.511 MeV $\gamma-$quanta from positrons annihilated in the DSSD. This peak corresponds to an observed energy of about 0.340 MeV. The second point is the end point of the beta spectrum, which results from positrons at the maximum kinetic energy available (5.022 MeV). and resides near channel 1500. This point is not so well defined because its position is affected by the Compton summing of the annihilation $\gamma-$quanta and by the preceding energy losses of positrons in the DSSD, in the Be window which separates high and low vacuum volumes and in the light-reflecting Teflon wrapping of the scintillator. The total energy loss amounts to about 0.180 MeV [84]. Both of these effects (Compton summing and preceding energy losses) are included in the GEANT simulations used in the fits of the scintillator spectra observed for double coincident events.

### 3.4.1 Direct fit of the double coincident energy spectrum.

Performing the calibration fit in the ADC channel range 90−1800 and 200−1800 we have obtained results which are shown in Tab 3.1 and in Fig 3.6 where one sees an overlay of the experimental and fitting spectra with both linear and logarithmic scales as well as residuals over the fit range. Residuals are in standard deviations and are calculated as

$$[Resid.] = ([Data] - [Fit]) / \sqrt{[Fit]}. \tag{3.5}$$

The 90−1800 fit, resulting in a $\chi^2$ per degree of freedom about 8 cannot be accepted. One sees particularly large disagreement between the data and simulations in the region of energies below channel 500. Setting the fitting range to be from just above the Compton peak resulted in a fit of considerably better quality with parameters and residuals, shown in the lower part of the Fig 3.6 and in the second line of Tab 3.1 respectively. The $\chi^2$ is still large, more than 2 per degree of freedom, but over the more limited range the residuals are generally smaller. However, the calibration parameters, extracted in these two cases are quite different, deviating by as much as 30 times the statistical errors and showing correlations with the evaluated amount of the "valve open" background $B_{vo}$.

TABLE 3.1: Energy calibration using double coincident events with binning 5 ch/bin for the two channel ranges 90−1800 and 200−1800. *N.f.* is the number degrees of freedom in the fit and *C.L.* is the resulting confidence level.

| Channels | *Offset* | *Slope* | *Norm* | $B_{vo}/10^4$ | *N.f.* | $\chi^2$ | *C.L.* |
|---|---|---|---|---|---|---|---|
| 90−1800 | 40.6(1) | 293.63(4) | 0.4164(2) | 31.2(2) | 337 | 2675.6 | 0 |
| 200−1800 | 43.0(2) | 293.36(5) | 0.4141(2) | 44.4(4) | 315 | 775.5 | 0 |

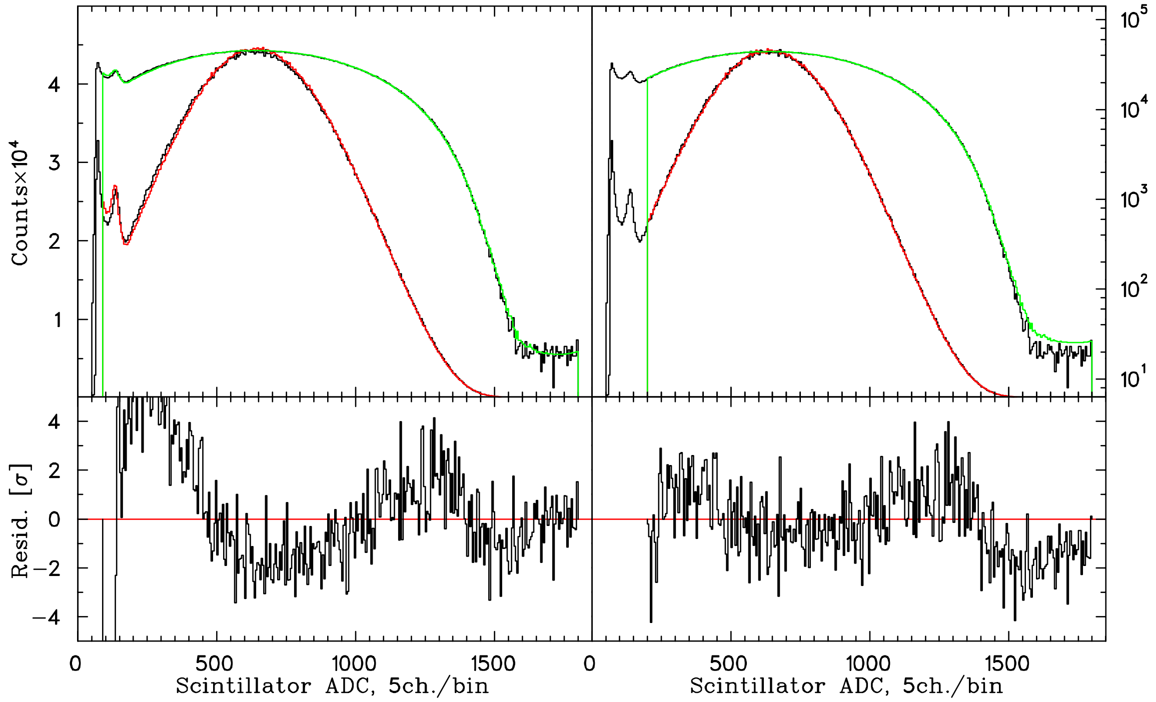

FIGURE 3.6: Energy calibrations over single continuous ranges of ADC channels. On the left side is shown the fit over the channel range 90−1800 and on the right one over channels 200−1800. On each side the upper panel contains an overlay of the data (black) and fit on linear (red) and logarithmic (green) scales. The lower panels contain residuals, measured in the standard deviations as defined by Eq 3.5.

### 3.4.2 Calibration fit over the two separated regions.

To reduce such correlations we have decided to decouple slope and offset by dividing the wider fitting region in two, one in the region of the Compton peak and the other at higher scintillator energies. The fitting procedure was an iterative process, in which we have fitted *Offset*, *Norm* and $B_{vo}$ over the channels around the Compton peak and then used the fitted value of the *Offset* as fixed to fit *Slope*, *Norm* and $B_{vo}$ over the range of channels near the end point of the beta spectrum. The resulting value of the *Slope* has then been used to refit the *Offset* and so on. The boundaries of the *Offset*'s fitting range (90−165) have been chosen to be near the bottoms of valleys, surrounding the Compton peak with binning 5 ch. per bin. For the higher energies at first we have chosen channels 650−1800 and have binned the data 50 ch. per bin. The final fitted values of the calibration parameters are collected in the Tab 3.2. Overlay of the fitting spectra and data and residuals are shown in the Fig 3.7. Using this approach produces considerably better residuals, although near the end point of the

Table 3.2: Energy calibration with double coincident events simultaneously fitting the two separated channel ranges 90−165 and 650−1800.

| *Channels* | *Offset* | *Slope* | *Norm* | $B_{vo}/10^4$ | *N.f.* | $\chi^2$ | *C.L.* |
|---|---|---|---|---|---|---|---|
| 90−165 | 45.1(2) | 293.14(0) | 0.435(4) | 22.1(9) | 11 | 9.48 | 0.58 |
| 650−1800 | 45.1(0) | 293.14(5) | 0.4116(2) | 26.8(1) | 19 | 94.0 | 0 |

beta spectrum there still exists a dip (channels 1400−1550 in the right panel of the Fig 3.7). The presence of this systematic deficit of counts cannot be explained by the uncertainties in backgrounds in the bin 1400−1450 because the evaluated background is a factor of 50 less than the beta induced events. Most probably the reason is in an inadequate account in the MC of the Compton summing of the photons produced by the positrons annihilated in the plastic scintillator or of the light collection from positrons and annihilation 0.511 Mev photons or some combination of both of these effects.

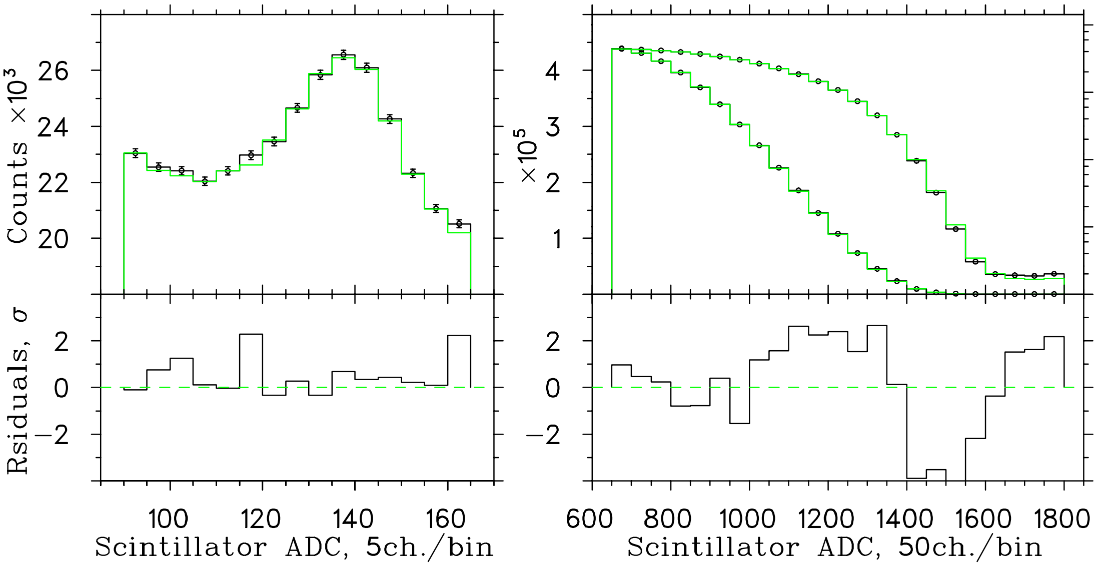

Figure 3.7: Energy calibration over two separated ranges of ADC channels. The region near the Compton edge of the 0.511 MeV photons is in the left panel and the energy range above 2.5 MeV is in the right one.

### 3.4.3 Calibration using the value of the pedestal in the scintillator ADC as an offset.

Despite the relatively good description in the MC of the energy spectrum of double coincident events in two separated regions (channels 90−165 and 650−1400) three comments have to be made:

- the agreement is reached with different normalizations of the GEANT3 generated spectrum and "valve open" background in each region;
- the data in the channel region 180−1600 are significantly under predicted by the fit;
- the discrepancy in channels 1400−1800 has not been accounted for in detail.

From the second statement it follows that, because the Compton peak of the 0.511 MeV photons appears on top of the rising edge of the beta spectrum, the net result of the fit with an underestimate in the MC produced beta spectrum can be an artificial shift of the *Offset* toward the low energies. In turn, an underestimate of *Offset* will result in the overestimate of *Slope*. So, it would be helpful to define one of the fitting parameters (*Offset* or *Slope*) using some additional subset of data which is not included directly in the evaluation of the correlation parameter.

Such a subset has been found and contains scintillator ADC data recorded for events triggered by the microchannel plate of the recoil detector. There are $\approx 5.5\times10^5$ of these events and nearly all of them appear in channels 78 and 79 of the MHTDC5 spectrum ("self" triggers). For these events the scintillator ADC spectrum is shown in Fig 3.8. The dominant peak near channel 50 is attributed to events for which there

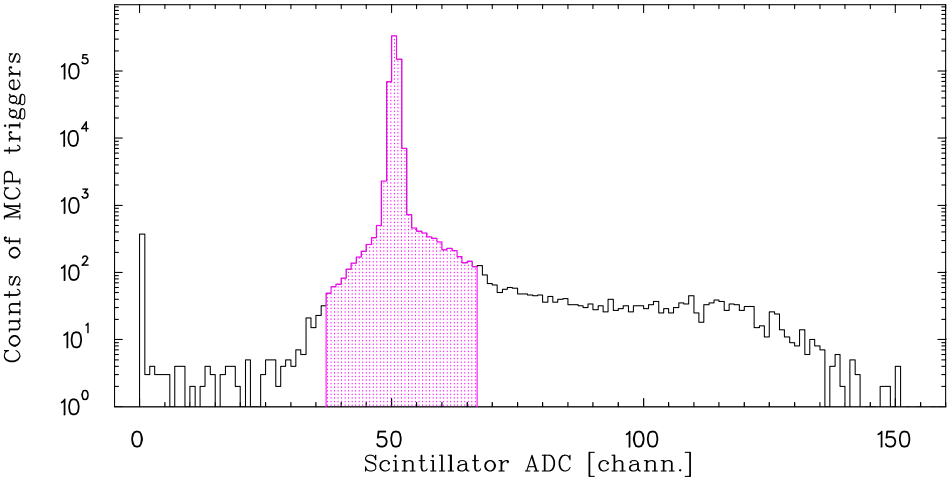

FIGURE 3.8: Pedestal in the scintillator ADC from MCP triggered events.

was no energy deposited in the scintillator (pedestal events). The width of this peak is the result of electronic noise but the average amplitude represents the integral (over the period of the ADC gate) of an intentional DC offset at the input to the charge integrating ADC. Since the width of the ADC gate is the same for both beta telescope and MCP triggered events the average amplitude of the pedestal observed in Fig 3.8 is used to estimate the *Offset* for the calibration of the scintillator energy spectra. The continuum of events extending approximately to channel 140 can be attributed to ≈1 % of the events for which the Compton scattering of annihilation photons deposits energy in the scintillator (but no signal in the DSSD).

The precise evaluation of the pedestal position has been done by fitting the spectrum over the region of channels 35−67 with the superposition of Gaussian, Lorentzian and $6^{th}$ order polynomial $P_6$ which represents background. The details of the fit and residuals are shown in Tab 3.3 and in Fig 3.9. The fit of the same data with the sum of Gaussian and polynomial $P_6$ has resulted in essentially the same pedestal value $x_0 = 50.6627(29)$ but with larger error and negligible confidence level. This shows that, while the peak shape is not perfectly Gaussian, its centroid is very well defined:

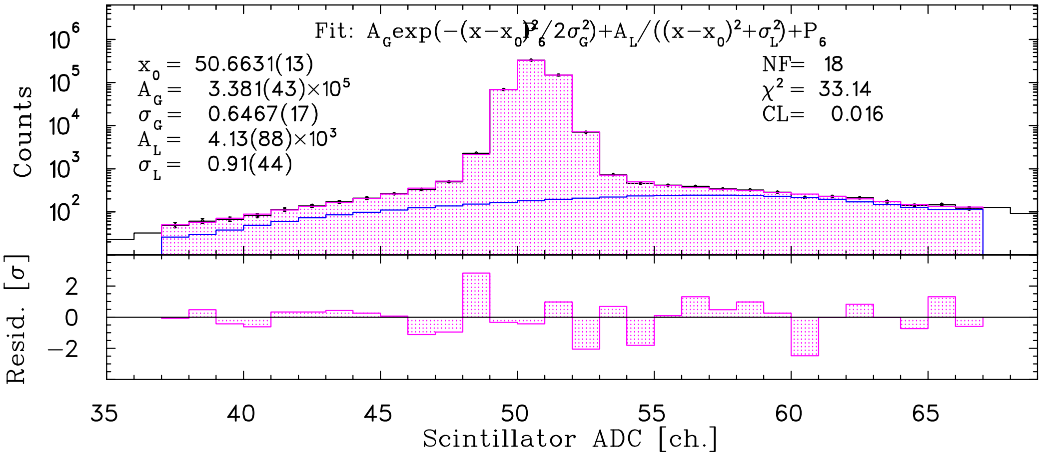

Figure 3.9: The pedestal in the scintillator ADC from MCP triggered events in the upper figure. The lower figure shows the fits and residuals in the expanded fitting range.

Table 3.3: Numerical results of the fit of the pedestal.

| $x_0$ | $A_G \times 10^5$ | $\sigma_G$ | $A_L \times 10^3$ | $\sigma_L$ | $NF$ | $\chi^2$ | $CL$ |
|---|---|---|---|---|---|---|---|
| 50.663(1) | 3.38(4) | 0.647(2) | 4.13(88) | 0.91(44) | 18 | 33.15 | 0.016 |

$$Offset = x_0 = 50.663(1)\ . \tag{3.6}$$

Given the deviations of the Monte Carlo model from the experimental data we have decided to perform calibration fits in the channel range where the data and MC simulations are in acceptable agreement. Fixing the high boundary of the fitting range in channel 1400 (when the MC starts to disagree with the data, see the right panel of the Fig 3.7), we have fitted MC to data for a set of low boundaries between the channels 600 and 900 with binning of spectra 50 ch/bin and varying in the fits MC normalization and calibration slope. The "valve open" background was fixed at the level defined by the counts in the channels 1650−1800 and the calibration offset was fixed as in Eq 3.6. Fig 3.10 illustrates the results of these fits. One sees in the upper panel the behavior of the calibration slope as function of the lower boundary of the fitting range. The lower panel shows the corresponding $\chi^2$ values and confidence levels of the fits.

We consider as acceptable a value of the confidence level corresponding to variations of $\chi^2$ within the natural limits

$$N - \sqrt{2N} < \chi^2 < N + \sqrt{2N} \ ,$$

where $N$ is the number of degrees of freedom. In the Tab 3.4 is shown the quality of the calibration fits as a function of the low fit boundary (with the high fit boundary

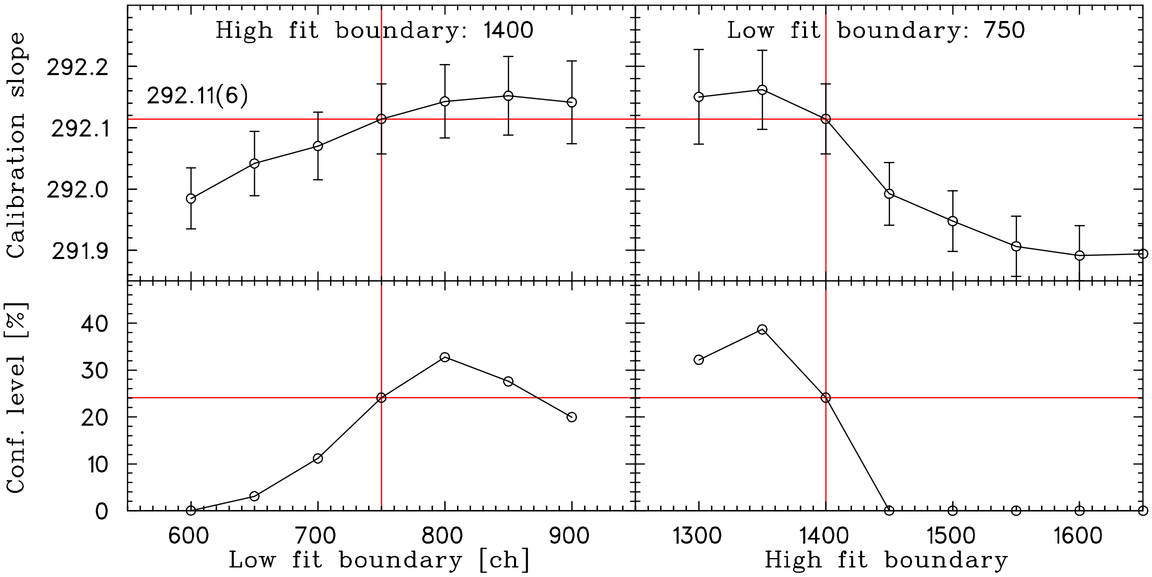

Figure 3.10: Calibration with double coincident events with fixed *Offset*. Upper left panel shows the dependence of the calibration slope on low boundary of the fitting region and lower one shows the confidence level of each fit. The right panel shows behavior of the *Slope* as a function of the high fit's boundary (top) and confidence level of the fits (bottom).

TABLE 3.4: Quality of the calibration fits when using ADC pedestal as *Offset* over the set of ADC channel ranges with fixed upper boundary in channel 1400. The first line shows the low boundary of the ranges; the second line gives the $\chi^2$ of the fit; and the third one shows the "acceptable" range in $\chi^2$ corresponding to the natural limits (see text).

| Low ADC | 600 | 650 | 700 | 750 | 800 | 850 | 900 |
|---|---|---|---|---|---|---|---|
| $\chi^2$ | 39.0 | 22.6 | 16.9 | 12.7 | 10.3 | 9.9 | 9.8 |
| $\chi^2$ range | 8–18 | 7–17 | 6–16 | 6–15 | 5–13 | 4–12 | 3–11 |

at the ch. 1400). The channel range 750–1400 is the highest for which the calibration fit is "acceptable". If we rely on the double coincident events for an energy calibration with an offset fixed by pedestal, the optimum parameters are those of this fit

$$Offset = 50.663(1)\,\mathrm{ch} \quad Slope = 292.11(6)\,\mathrm{ch/MeV}\ . \tag{3.7}$$

A comparison of the data and the fit (with this optimum value of the slope) is shown in Fig 3.11. Also shown are the contributions to the fit of the "valve open" and "wall" backgrounds which, in the region of the fit (ch 750–1400) are always ≤1% of the total. The plots of the residuals (data–fits) illustrate the quality of the fit. The parameters defined by this fit were then used to extrapolate the fit and compare with

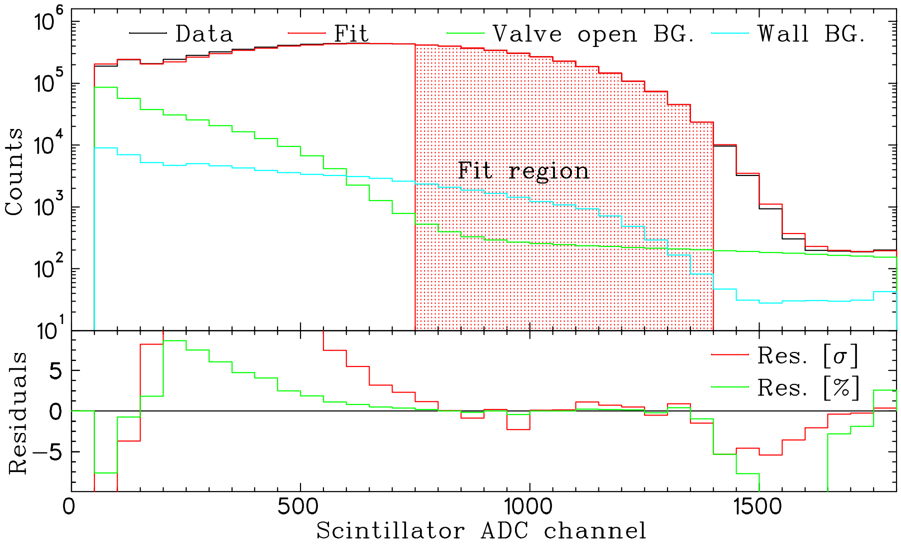

FIGURE 3.11: Fit of the scintillator observed energy spectrum with double coincident events. The fit is over the ADC channel range 750–1400 with fixed *Offset*=50.663. The upper panel shows the contribution of the constituent parts of fitting function. The lower panel shows residuals measured in per cent and standard deviations. The results of comparing the data with extrapolations of the fit beyond the fitting region are also shown.

data over the full range, ch 50−1800. The corresponding residuals are substantially larger outside the region of the fit. Fig 3.11, in the ADC channel range 200−750, suggest that the valve open background does not adequately account for source of background in this region. The deviation above channel 1400 is presumably of the same origin as observed in Fig 3.7.

## 3.5 Instant of the beta decay – reference point of the TOF measurements.

In order to define the time of the decay we consider "prompt" events. They can be seen in Fig 3.3 near the MCP TDC channel 110. We associate these data with events that produce nearly simultaneous hits in the beta detector (plastic scintillator) and in the recoil detector (MCP). Such events could be produced when a relativistic positron scatters off the MCP, causing a hit in that detector, and is subsequently detected in the beta telescope; when a positron is detected by the telescope and the MCP registers a $\gamma$-quantum from positron annihilation or a UV photon emitted by the excited recoil ion produced in the $\beta^+$ decay; or, when both the scintillator and the MCP detect 511 keV photons from positrons which annihilate in the DSSD. These events give us a measure of "zero" time. As the time resolution of the detecting system is defined by the mutual timing of the MCP and the scintillator, we explore correlations between the registered time and the amplitude of signals from both detectors. In this analysis of the prompt events we use the time measured by the single hit Time-to-Digit-Converter (SHTDC), LeCroy LC2228A TDC, with resolution 0.25 ns/ch. In the Fig 3.12 which contains $\mathrm{ADC_{mcp}}$−TDC and $\mathrm{ADC_{scin}}$−TDC scatter plots one sees deviations of a few nanoseconds of the time signals at lowest amplitudes of the scintillator and MCP signals. (The signs of the deviations are opposite because the scintillator provides a start and the MCP generates a stop). Both walks can be significantly reduced by the simultaneous application of thresholds for the scintillator ($\simeq$270 channel) and MCP ($\simeq$200 channel) signals.

As has been mentioned above, events of several different types contribute to the prompt peak. Particles responsible for such events may travel with different velocities and through different distances. This would broaden the prompt peak and, more significantly, change its centroid by an unknown amount and might result in significant errors in the zero time determination. To reduce such errors we have applied some conditions which helped us to better define the nature of the prompt events.

We have decided to use highly selected events that originated from decays when

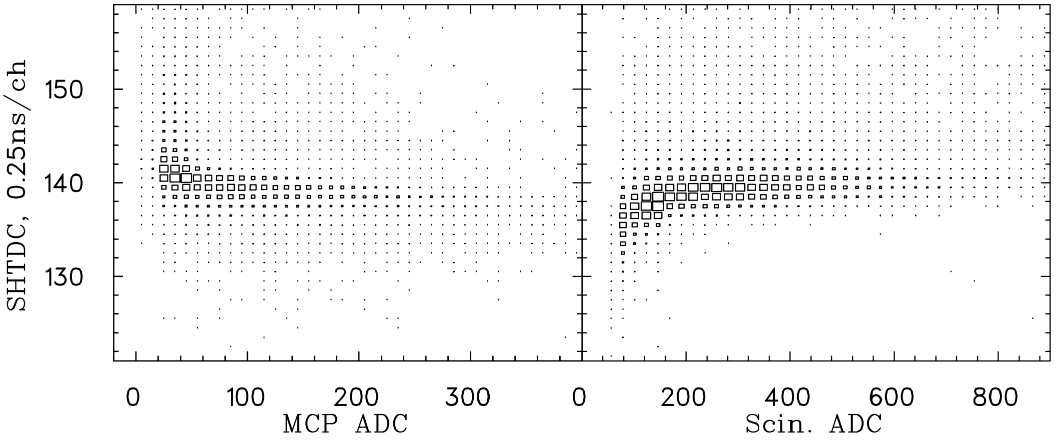

FIGURE 3.12: Distribution of the prompt events as function of the detected time and pulse amplitudes, observed in the MCP (left) or scintillator (right) ADCs. The TDC resolution is 0.25 ns/ch.

the positron initially has been directed toward the recoil detector, produced a hit in the MCP and, due to scattering in the MCP material, hit the beta telescope where they have also been detected. The corresponding $Ar^{+1}$ recoil, in turn, has also been detected. Such events we consider as scintillator events. They can be characterized by the MHTDC5 reading in channels 110–130 due to the positron and MHTDC6 (the time of a second MCP hit) reading in channels 1000–1150 due to the $Ar^{+1}$ recoil initially directed toward the beta telescope. Alternatively, the recoils from such "backscatter" events contribute to the MHTDC5 spectra if the positron has not been detected by the MCP (see Fig 3.13). In the scatter-plot we have shown the area containing the events of interest by the angle. They contribute predominantly to the

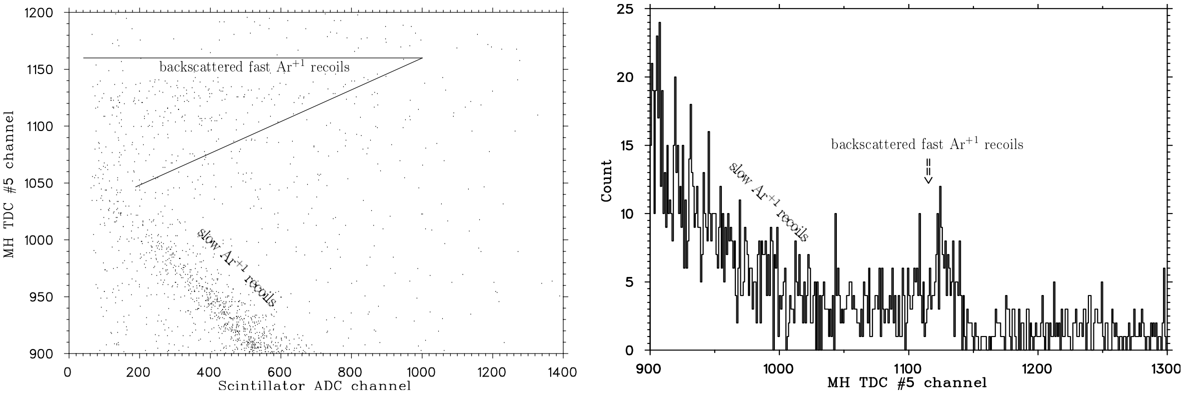

FIGURE 3.13: Scatter-plot (left) and TOF spectrum (right) of the events with positrons scattered off the recoil detector (but not detected by the MCP).

peak between channel 1100 and 1150 in the TOF spectrum. The same sort of events can be associated with the detection of $\mathrm{Ar}^{+2}$ ions as the second hit of MCP TDC in the channel region 740−790. We select such events in accordance with following conditions:

- first hit in MHTDC5 is between channels 110−130;
- second hit in MCP multihit TDC (MHTDC6) is between channels 740−790 ($\mathrm{Ar}^{+2}$) or 1100−1150 ($\mathrm{Ar}^{+1}$);
- RA signals are above threshold in channel 84 for all four RA ADCs;
- outer strips of the DSSD are not fired.

All together 138 events passed these conditions. We have fitted the corresponding prompt peak with the following expression:

$$\begin{aligned} f &= \sum_{i=1}^{N} \int_{t_{i-1}}^{t_i} \varphi dt \qquad (3.8) \\ \varphi &= \frac{A}{\sqrt{2\pi}\sigma} \exp\left[-\frac{(t-\eta)^2}{2\sigma^2}\right] + \frac{2B}{\tau} \operatorname{erfc}\left(\frac{\eta+\sigma^2/\tau - t}{\sqrt{2}\sigma}\right) \exp\left(\frac{\eta - t}{\tau}\right) + \\ & \frac{C}{2} \operatorname{erfc}\left(\frac{\eta + \sigma - t}{\sqrt{2}\sigma}\right), \end{aligned}$$

which is the linear combination of a Gaussian peak with width parameter $\sigma$ centered at t $= \eta$ (first term); the convolution of an exponential with time constant $\tau$ and the same Gaussian (second term); and a complementary error function (third term). The coefficients $A, B$ and $C$ give the contribution of each term. The first term describes events when the positron is detected in both detectors: first it strikes the MCP and then the beta telescope. The second term describes events in which the positron escapes detection in the MCP (because of the finite efficiency of the MCP to betas or because the positron scattered off nearby elements) but is detected in the beta detector and the MCP detects an UV photon from deexcitation of the $\mathrm{Ar}^{+1*}$ or $\mathrm{Ar}^{+2*}$ ions. This term may also describe some remaining walk in the scintillator timing. The third term describes accidental background.

We have fitted the selected data using function (3.8), applying different thresholds to the scintillator ADC signal (see left panel of Fig 3.12) and assuming no accidental background ($C \equiv 0$). Fit results are collected in the Tab 3.5 as functions of the applied threshold. As a prompt peak position we have adopted the value of $\eta$ from the fit with scintillator threshold in ADC channel 300, because for backscattered events the time walk in the scintillator under this condition becomes small (see Fig 3.14) while MCP timing does not exhibit any pulse height dependence.

TABLE 3.5: Fits of the prompt peak with different thresholds in the scintillator signal. The parameters are defined in Eq 3.9 with $C \equiv 0$.

| ADC min | $\eta$ | $\sigma$ | $\tau$ | A | B | $DF$ | $\chi^2$ | $CL$ |
|---|---|---|---|---|---|---|---|---|
| 50 | 112.97(12) | 0.62(09) | 2.21(43) | 91(16) | 47(14) | 15 | 16.37 | 0.36 |
| 100 | 112.97(12) | 0.58(09) | 2.16(39) | 80(15) | 49(14) | 15 | 16.05 | 0.38 |
| 150 | 113.09(12) | 0.48(10) | 2.27(43) | 66(13) | 43(12) | 15 | 16.33 | 0.36 |
| 200 | 113.13(13) | 0.49(10) | 2.33(47) | 60(12) | 41(11) | 15 | 16.90 | 0.32 |
| 250 | 113.14(14) | 0.51(10) | 2.45(52) | 52(11) | 35(10) | 15 | 16.10 | 0.38 |
| 300 | 113.21(17) | 0.52(10) | 2.54(58) | 44(10) | 31(10) | 15 | 16.33 | 0.36 |
| 350 | 113.18(18) | 0.53(12) | 2.67(64) | 38(10) | 29(9) | 15 | 16.15 | 0.37 |

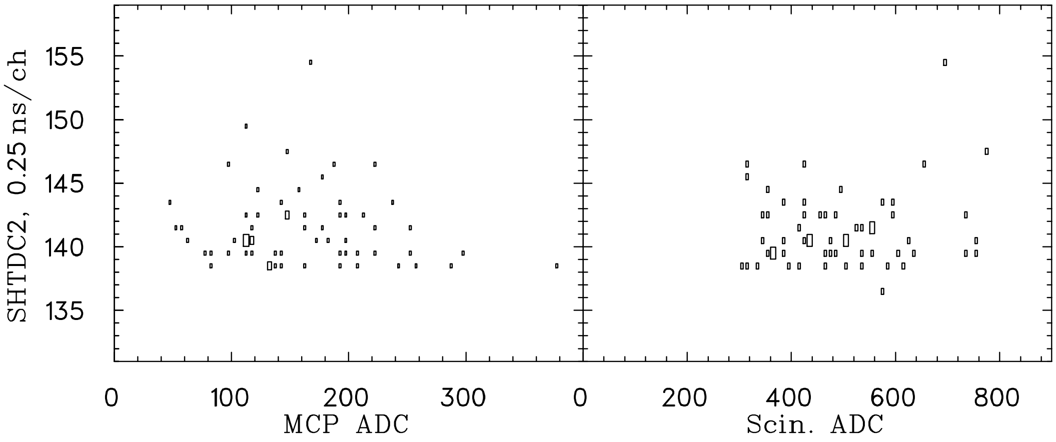

FIGURE 3.14: Distribution of the prompt events triggered by positron backscattered off MCP as function of the detected time and pulse amplitudes, observed in the MCP (left) or scintillator (right) ADCs. TDC resolution is 0.25 ns/ch. Scintillator threshold of 300 is applied.

The fitted value, $\tau = 2.54 \pm 0.58\,\text{ns}$, is in agreement with the lifetime of the $(\text{Ar}^0)^*$ reported in [108].The quality of this particular fit can be seen in Fig 3.15. The resulted value of $\eta$,

$$\eta = 113.21 \pm 0.17\,\text{ns} \tag{3.9}$$

now can be used to evaluate a $\Delta$, the intrinsic delay between the signals from positron and recoil detectors when they are simultaneously fired by detected particles. Recalling that we have considered events in which the positron hits the MCP first and then the beta telescope, one can conclude that for these prompt events the start is delayed by the positron travel time from MCP to beta telescope.

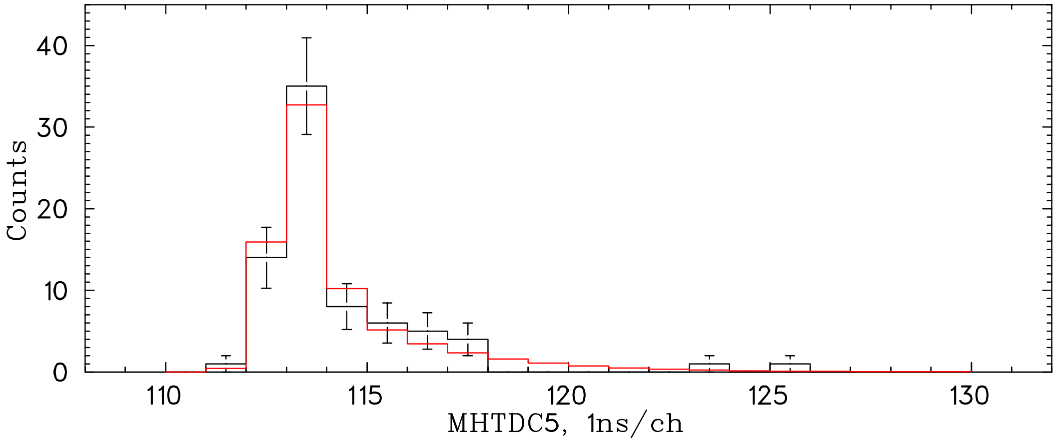

FIGURE 3.15: Fit of the prompt peak: Circles with error-bars denote TOF spectrum of the MHTDC5 prompt peak events with Scin.ADC>300 which have MHTDC6 reading in the channels 740−790 or 1100−1150, and histogram denotes resulting fitting function.

$$\eta = \Delta - \tau_{MCP} - \tau_{SCI} \quad \text{or} \quad \Delta = \eta + \tau_{MCP} + \tau_{SCI} = 113.66 \pm 0.17\,\text{ns} \tag{3.10}$$

Here $\tau_{MCP} \approx 0.21\,\text{ns}$ is the travel time of the relativistic particle from trap to MCP and $\tau_{SCI} \approx 0.24\,\text{ns}$ is its travel time from trap to scintillator.

The value of $\Delta = 113.66 \pm 0.17\,\text{ns}$ now can be used to evaluate a zero time value, which should be added to the Monte Carlo generated recoil time of flight. For events which are used to build the recoil TOF spectra, the *Start* signal comes delayed by the positron travel time from trap to beta detector. So for location of the "zero" time in the MHTDC5 or for addition to the Monte Carlo calculated recoil TOF time one can write:

$$t_0 = \Delta - \tau_{SCI} = 113.42 \pm 0.17\,\text{ns} \ . \tag{3.11}$$

Another important parameter is the width of the Gaussian in the fitting function. This parameter $\sigma = 0.52 \pm 0.10\,\text{ns}$ defines the time resolution of the apparatus and is of importance for evaluation of the trap size.

## 3.6 Evaluation of the trap position along the detection axis. Neutral recoils: analysis of the TOF and the detection efficiency.

During data collection the parameters of the MOT have been adjusted to locate the minimum of the trapping potential as close as possible to the center of the detection chamber. This required symmetry of the magnetic quadrupole field with respect to this point and power balance of the laser beams. Nevertheless, the exact trap position which is needed for the Monte Carlo model has been defined with collected data. For this purpose, we have selected events associated with the detection of neutral recoiling $Ar^0$ atoms in coincidence with positrons. These events can be seen in Fig 3.3 to the right of TDC channel 1400. Using $Ar^0$ atoms to define the trap position has a big advantage as trajectories of neutral atoms are not perturbed by the applied electric field. This allows a field-independent analysis with the results applicable to evaluation of the strength of the electric field. The trap position is measured relative to the nominal center of the detection chamber which is taken to be the origin of the coordinate system ($x=y=z=0$) at a distance of 61.25 mm from the surface of the MCP ($z=-61.25$ mm).

### 3.6.1 Shape of the $Ar^0$ TOF spectrum.

For the evaluation of the longitudinal trap position we have selected events with scintillator detected energy between channels 800−1800 (which corresponds to the positron energy above $T_\beta = 2.7$ MeV) and with the sum of resistive anode signal above channel 5000. A time of flight spectrum for such events is shown in Fig 3.16. The rising edge of the spectrum contains events in which the positron and neutrino are emitted in approximately the same direction. For this reason the corresponding fast recoils carry nearly the same momentum (about 5.5 MeV/c) and kinetic energy (0.430 keV). The shape of the rising edge in this spectrum is defined by both the trap position and trap size. These values can be extracted by fitting the spectrum

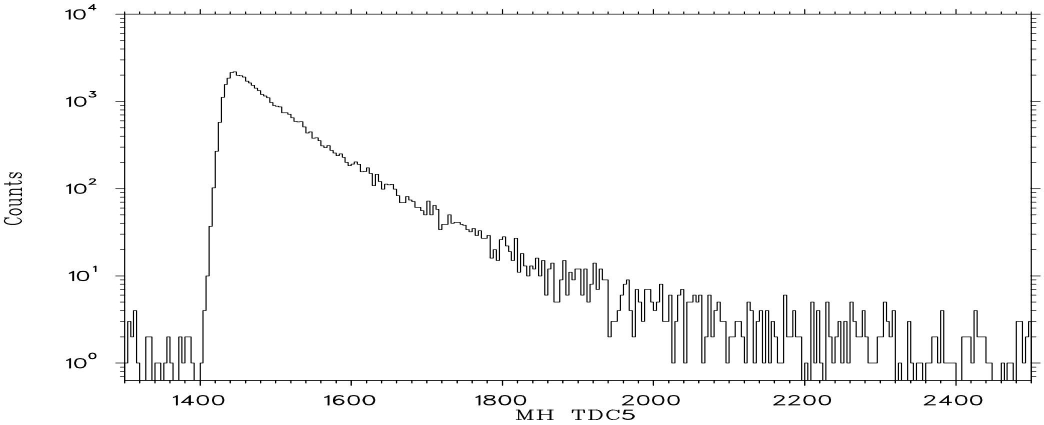

FIGURE 3.16: TOF spectrum of the $Ar^0$ recoiling atoms, detected in coincidence with the positron detector (Scin.ADC>800). These data have been used to extract the longitudinal trap position.

with one from the Monte Carlo while varying trap position and size as independent parameters. Here the MC naturally includes the effects of finite detector size and we assume a Gaussian density distribution of $^{38\mathrm{m}}$K atoms in the trap. A Gaussian distribution is consistent with the optical measurements [41]. For better specification of these parameters, the fitted part of the TOF spectrum has to include not only the rising edge but the peak itself and some amount of data beyond the maximum. To minimize the effect of the high TOF cut one needs to understand the physics involved in formation of the falling part of the TOF spectrum. Besides the $\beta - \nu$ angular correlation, one should consider such factors as the possible influence of the Ar$^{-*}$ metastable state with life time $\tau_e = 260\,\mathrm{ns}$ [90] which decays by auto-ionization to the Ar$^0$ ground state [109], and the dependence of the MCP detection efficiency on recoil energy [88].

The Ar$^{-*}$ metastable, if produced and detected, might distort the Ar$^0$ TOF spectrum, because, in the presence of the electric field, these ions will be decelerated before auto-ionization in flight thus altering the shape of the Ar$^0$ TOF spectrum. We have searched for these by changing the accelerating field from 800 V/cm to 400 V/cm and found the possible initial contamination of Ar$^{-*}$ in Ar$^0$ to be small ($-0.007 \pm 0.039$). Monte Carlo analysis of the TOF spectra revealed that an admixture of metastables up to 10% of the total in the Ar$^0$ would not change the shape of the spectra enough within first 260 ns to make any detectable distortion in the trap position or size. One can expect a considerably stronger effect due to the dependence of the MCP detection efficiency on recoil energy.

### 3.6.2 MCP detection efficiency of Ar$^0$.

Neutral Ar atoms bombard the MCP with kinetic energies from zero up to 430 eV, and it is known [88] that in this impact energy range the detection efficiency may significantly degrade with decrease of the recoil energy. This alters the shape of the TOF spectrum, shown in (Fig 3.16). The effect increases with increasing TOF. It is most likely that $\beta^+$ decay of the potassium isotopes makes neutral argon atoms in both the atomic ground state, Ar$^0$, and metastable states with known lifetimes of 40 s [110, 111]. Atoms striking an MCP detector can produce secondary electrons resulting in detection due to two different mechanisms [112, 113]. The first one ("potential") is applicable to metastable states only and depends on the excitation energy of the atom with respect to the work function of the material in the MCP surface. This contribution is roughly independent of the incident recoil velocity. For the other mechanism ("kinetic") the efficiency is approximately proportional to the atom's impact energy once above some threshold. In our efficiency we define a residual efficiency $\varepsilon_0$ and minimal recoil energy (velocity) $E_{min}$ ($v_{min}$) at which the "kinetic" term vanishes. As we are not trying to deduce absolute numbers, the efficiency can be normalized to that for maximum available recoil impact energy $E_{max} = 430\,\mathrm{eV}$ and written as a function of impact velocity in the following form:

$$\varepsilon(v) = \begin{cases} \varepsilon_0 & \text{if } v < v_{min} \\ \varepsilon_0 + (1-\varepsilon_0)\frac{v^2 - v_{min}^2}{v_{max}^2 - v_{min}^2} & \text{if } v_{min} < v < v_{max} \end{cases} \tag{3.12}$$

Quantitatively, the MCP efficiency for $\mathrm{Ar}^0$ atoms has been defined in a search for heavy neutrino mixing [44, 77] with the same data as is used in this experiment. The data sample has been selected from events with coincident scintillator observed energy in channels 1100−1300, corresponding to positron energy 3.7−4.3 MeV. This high $\beta^+$ energy range has been chosen to avoid a possible interference with an admixture of a heavy neutrino. We have binned the multihit TDC data between channels 1250−2350 into 550 bins, 2 ns/bin, and fitted the resulting spectrum with one simulated with Monte Carlo. Appropriately normalized experimental accidental background, measured in the MHTDC5 range of channels 3000−9000, has been added to the Monte Carlo simulations. Several rounds of fits were performed. Initially, to get starting values, we fitted data varying four parameters, namely trap size and position, residual efficiency $\varepsilon_0$ and minimum "kinetic" detection velocity $v_{min}$. Then the resulting values of $\varepsilon_0$ and $v_{min}$ have been fixed and used, as described in Sec 3.6.3, in the fits of the front edge of the $\mathrm{Ar}^0$ TOF spectrum to obtain improved fits to the trap position ans size. We have then used these corrected (and now fixed) trap parameters to get final value of the MCP efficiency. We have found

$$\begin{array}{lllllllll} v_{min} & = & (3.5 \pm 0.8) \times 10^6\,\mathrm{cm/s} & \chi^2 & = & 583.33 & DF & = & 547 \\ \varepsilon_0 & = & 0.33 \pm 0.05 & C.L. & = & 0.14 & & & \end{array}$$

The value of $v_{min}$ is reasonable compared to available data [88]. In Fig 3.17 we present an overlay of the experimental $\mathrm{Ar}^0$ TOF data with Monte Carlo simulations with both constant and recoil energy dependent MCP detection efficiency. It can be added, that during analysis of the detection efficiency, effects of possible deviation of the $\beta - \nu$ angular correlation parameter from the Standard Model value and the presence of $\mathrm{Ar}^{-*}$ metastables have been included.

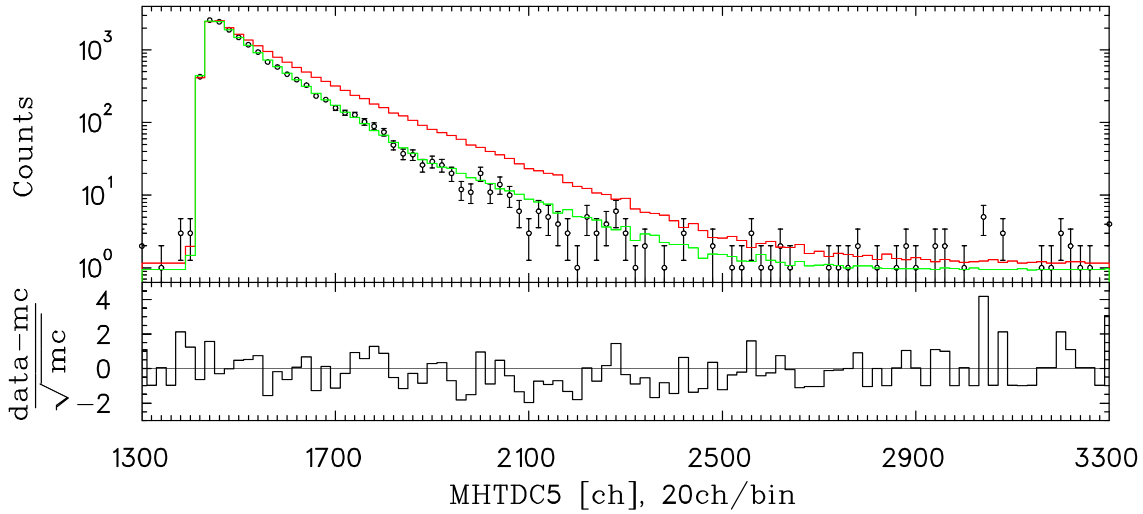

Figure 3.17: Upper panel: Fit of the MCP detection efficiency with $\mathrm{Ar}^0$ TOF data. Collected data are plotted with error bars. The red histogram is the MC simulations with recoil energy independent MCP detection efficiency. There is an excess of events in the falling part of the spectra. The green line represents MC simulations with the recoil energy dependent MCP detection efficiency. Lower panel: Residuals of the fit, measured in the units of standard deviation.

### 3.6.3 Fit of the neutral Ar TOF spectrum for longitudinal trap position and size.

The trap position $z_0$ and size (FWHM) have been determined by fitting TOF spectra in four MHTDC5 intervals 1404−1496, 1408−1496, 1412−1496 and 1416−1496 for each of three overlapping ranges of coincident scintillator energy with ADC channels 600−1200, 700−1200 and 800−200. Examples (for the range 700−1200) of data, fitting functions and residuals, measured in standard deviations is shown in Fig 3.18, while complete results of the fits are contained in Tab 3.6. The consistency of the results is very good, as the scattering of the fitted parameters around appropriate mean values is less than errors of the individual fits. Because most of the data is common to all fits the final estimates of the uncertainties are those of individual fits.

$$\begin{array}{lcc} & \mathrm{z_0}\,[\mathrm{mm}] & \mathrm{FWHM}\,[\mathrm{mm}] \\ \mathrm{mean:} & -0.168(7) & 0.620(19) \\ \mathrm{r.m.s.:} & 0.002 & 0.012 \end{array} \tag{3.13}$$

Thus the distance measured between the trap and surface of the MCP is 61.08 mm.

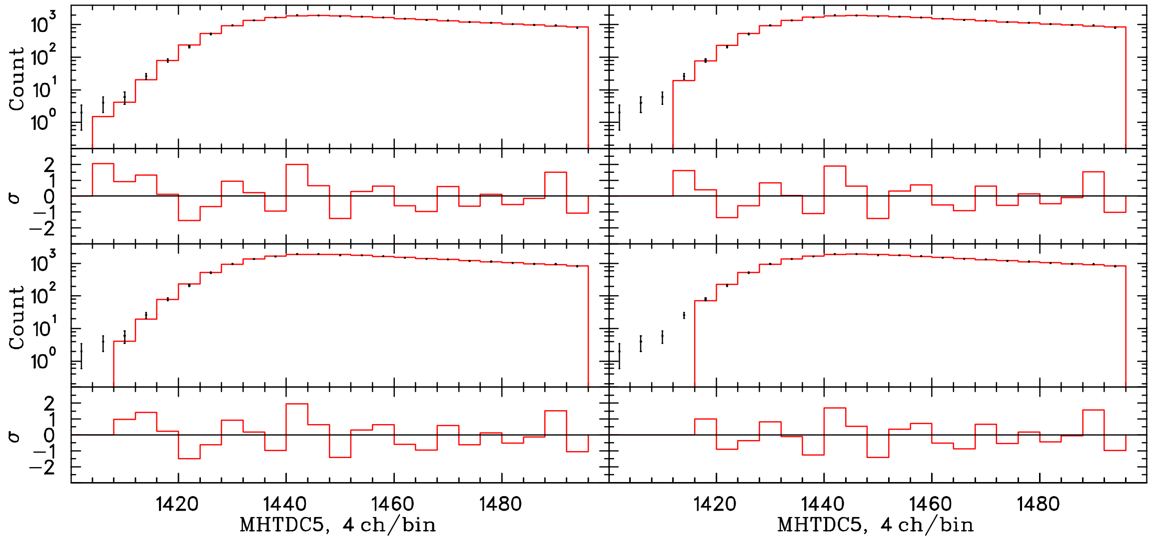

FIGURE 3.18: Fit of trap size and position in $Z$−direction with $\mathrm{Ar}^0$ TOF data. Overlay of data (error-bars) and fitting function (red histogram). The range of the scintillator observed energy of coincident positrons is chosen between ADC channels 700 and 1200.

TABLE 3.6: Fitting of the trap position with $\mathrm{Ar}^0$ TOF spectra over three scintillator ADC overlapping ranges. Results are tabulated for 4 values of the minimum MHTDC5 channel included in the fit. In each case the maximum is 1496 and the TDC data is binned 4 ns/bin. The correlation parameter values used in Monte the Carlo simulations are $a = 0.99$, $b = 0$; $N_{MC} = 10^7$.

| Low ADC ch. | Low TDC ch. | $z_0$ mm | FWHM mm | $N$ | $\chi^2$ | $\chi^2/N$ | $CL$ |
|---|---|---|---|---|---|---|---|
| 600 | 1404 | −0.167(6) | 0.628(16) | 20 | 29.07 | 1.45 | 0.086 |
| | 1408 | −0.168(6) | 0.627(16) | 19 | 27.18 | 1.43 | 0.101 |
| | 1412 | −0.168(6) | 0.624(17) | 18 | 26.25 | 1.46 | 0.094 |
| | 1416 | −0.169(6) | 0.606(19) | 17 | 21.37 | 1.26 | 0.210 |
| 700 | 1404 | −0.164(7) | 0.630(18) | 20 | 22.37 | 1.12 | 0.321 |
| | 1408 | −0.165(7) | 0.627(18) | 19 | 19.55 | 1.03 | 0.422 |
| | 1412 | −0.166(7) | 0.620(19) | 18 | 18.65 | 1.04 | 0.414 |
| | 1416 | −0.167(7) | 0.604(21) | 17 | 15.46 | 0.91 | 0.563 |
| 800 | 1404 | −0.169(8) | 0.631(20) | 20 | 27.71 | 1.39 | 0.116 |
| | 1408 | −0.169(8) | 0.628(20) | 19 | 23.67 | 1.25 | 0.209 |
| | 1412 | −0.170(8) | 0.621(21) | 18 | 22.43 | 1.25 | 0.214 |
| | 1416 | −0.172(8) | 0.593(24) | 17 | 17.67 | 1.04 | 0.410 |

## 3.7 Evaluation of the electric field strength.

As a tool to probe the strength of the applied electric field we have used Ar ion TOF spectra. The general idea of this analysis is to fit the parts of the TOF spectra which contain the fastest recoils only, simultaneously varying field strength and longitudinal trap size. Variations of the trap size allow us to check the consistency of the resulting values with that from analysis of the neutrals while exclusion of the slow recoils practically removes any possible dependence of the results on the angular correlation parameter $a$. In the analysis we have used triple events triggered by the beta telescope corresponding to detection of the $\mathrm{Ar}^{+1}$, $\mathrm{Ar}^{+2}$ and $\mathrm{Ar}^{+3}$. These fits assume the existence of a uniform electric field along the $Z-$axis, accelerating $\mathrm{Ar}^{+}$ ions from the trap ($z = -0.17\,\mathrm{mm}$) to the MCP ($z = -61.25\,\mathrm{mm}$). Also, we have we have used $\mathrm{Ar}^{+1}$ MCP events triggered by the recoil detector in which TOF information was recorded in MHTDC6. In these last events we have detected fast recoils which were emitted predominately towards the beta telescope and probed the uniformity of the electric field strength in the region about 1 cm beyond the trap (towards the beta telescope).

### 3.7.1 Evaluation of the electric field strength and longitudinal trap size by fitting the front edges of the $\mathrm{Ar}^{+1}$, $\mathrm{Ar}^{+2}$ and $\mathrm{Ar}^{+3}$ TOF spectra.

The electric field strength has been tested by fitting the TOF spectra of $\mathrm{Ar}^{+1}$, $\mathrm{Ar}^{+2}$ and $\mathrm{Ar}^{+3}$ ions both simultaneously and separately, over two sets of the MHTDC5 ranges:

| | Narrow | Wide |
|---|---|---|
| $\mathrm{Ar}^{+1}$: | TDC channels 688 – 720 and | 688 – 760 |
| $\mathrm{Ar}^{+2}$: | TDC channels 555 – 576 and | 555 – 592 |
| $\mathrm{Ar}^{+3}$: | TDC channels 488 – 500 and | 488 – 511 |

To maintain maximum sensitivity to the parameters of the fit we have analyzed the TDC data as recorded (1 ns/bin). The wider ranges of the TDC channels have been chosen to include all fast recoils for each Ar ion charge state. The narrower ranges covered just the front edge of the TOF spectra. The coincident positron energy has been taken in three intervals with low scintillator ADC threshold in channels 600, 700 and 800 and high threshold in channel 1200. The resulting values are collected in the Tab 3.7. Fig 3.19 overlays data (with error-bars) and fits (solid lines) as well as residuals, measured in standard deviations for the energy bin with ADC channels 700−1200 for both TDC ranges. In selecting the data for fitting, we have made a

TABLE 3.7: Simultaneous fitting of the electric field strength and trap size along the detection axis with $\mathrm{Ar}^{+1}$, $\mathrm{Ar}^{+2}$ and $\mathrm{Ar}^{+3}$ TOF spectra over three scintillator ADC overlapping ranges. The "narrow" and "wide" TDC channel ranges are defined in the text. The value of the correlation parameter used is $a = 0.99$, $b = 0$. Monte Carlo simulated spectra contain $N_{MC} = 10^8$ events.

| ADC ch. | TDC range | $-U_0$ V/cm | FWHM mm | $N$ | $\chi^2$ | $\chi^2/N$ | $CL$ |
|---|---|---|---|---|---|---|---|
| 600–1200 | narrow | 807.66(10) | 0.621(13) | 63 | 92.26 | 1.46 | 0.010 |
| | wide | 807.61(09) | 0.624(13) | 130 | 195.08 | 1.50 | 0.000 |
| 700–1200 | narrow | 807.70(11) | 0.622(14) | 62 | 83.83 | 1.35 | 0.034 |
| | wide | 807.62(10) | 0.629(14) | 130 | 182.86 | 1.41 | 0.002 |
| 800–1200 | narrow | 807.82(12) | 0.616(17) | 62 | 69.08 | 1.11 | 0.251 |
| | wide | 807.71(12) | 0.626(16) | 130 | 164.63 | 1.27 | 0.022 |

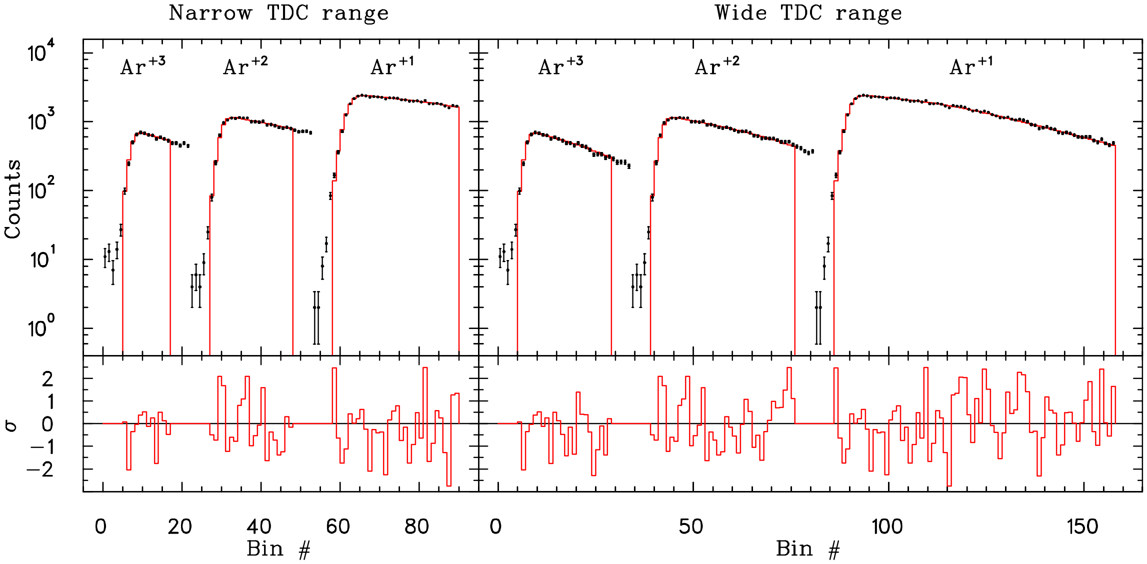

FIGURE 3.19: Overlay of data (error-bars) and fitting function (solid) from fits of the longitudinal trap size and electric field strength using ions $\mathrm{Ar}^{+1}$, $\mathrm{Ar}^{+2}$ and $\mathrm{Ar}^{+3}$ simultaneously. The range of the scintillator observed energy of coincident positrons is chosen between ADC channels 700 and 1200. The narrow and wide TDC ranges are defined in the text. Data outside regions of the solid lines are not included in the fit.

cut by excluding from the fit for each ion charge state those bins in the rising edge of the TOF spectrum, where the count is less than 5% of the maximum for that charge state. This has been done because at a beta energy, which corresponds to channel 700 in scintillator ADC, TOF spectra of $\mathrm{Ar}^{+2}$, $\mathrm{Ar}^{+3}$ are overlapping. As the population of the tails in the TOF spectra is sensitive to the value of the angular correlation parameter, we have reduced the sensitivity to these tails to avoid possible correlations with the values of $a$ and $b$. A simple averaging over all relevant entries in the Tab 3.7 gives $U = -807.67\,\mathrm{V/cm}$ and FWHM=0.623 mm. Averaging over wide and narrow TOF range separately results in: for the narrow range $U = -807.72\,\mathrm{V/cm}$, FWHM=0.620 mm; and, for wide one, $U = -807.64\,\mathrm{V/cm}$, FWHM=0.626 mm.

### 3.7.2 Separate fits of $\mathrm{Ar}^{+1}$, $\mathrm{Ar}^{+2}$ and $\mathrm{Ar}^{+3}$ TOF spectra.

The quality of the electric field evaluation has been tested also by fitting the TOF spectra of the $\mathrm{Ar}^{+1}$, $\mathrm{Ar}^{+2}$ and $\mathrm{Ar}^{+3}$ ions separately, over the same TOF ranges as used for the simultaneous fits (See Sec 3.7.1). The results are collected in Tab 3.8. From this table one can see that the $\mathrm{Ar}^{+2}$ ions give a slightly stronger electric field and smaller trap size compared to the other ions, with $\mathrm{Ar}^{+1}$ results being in the middle. The uncertainties in the resulting parameters from the fits with $\mathrm{Ar}^{+2}$ and $\mathrm{Ar}^{+3}$ data are considerably larger because of the smaller number of counts. The scattering of the fitted values is comparable to the statistical uncertainties in the fits for each charge state. Simple averaging over all entries in the Tab 3.8 gives an effective electric field and trap size $\overline{U} = -807.69\,\mathrm{V/cm}$, $\overline{\mathrm{FWHM}} = 0.620\,\mathrm{mm}$.

One can see that this average value of the trap size is completely compatible with that evaluated from the $\mathrm{Ar}^0$ ions (Tab 3.6) and by simultaneous fit of the TOF spectra of $\mathrm{Ar}^{+1}$, $\mathrm{Ar}^{+2}$ and $\mathrm{Ar}^{+3}$ (Tab 3.7). So we have decided to fix a trap size and refit the electric field strength with each available ion TOF spectrum. These fits have been performed using different values of $a$, the correlation parameter in the Monte Carlo (See Tab 3.9). The variations with $a$ of the resulting field strength are much smaller than the statistical errors of the fits. For the future use of the electric field strength and trap size and position along the detection axis we shall use following:

$$\begin{array}{rcll} U & = & -807.70(12) & \mathrm{V/cm} \\ z_0 & = & -0.168(7) & \mathrm{mm} \\ \mathrm{FWHM} & = & 0.62(2) & \mathrm{mm} \end{array} \qquad (3.14)$$

TABLE 3.8: Separate fitting of the electric field strength and trap size along the detection axis with $\mathrm{Ar}^{+1}$, $\mathrm{Ar}^{+2}$ and $\mathrm{Ar}^{+3}$ TOF spectra over three overlapping scintillator ADC ranges. The values of the correlation parameters used are $a = 0.990$, $b = 0$. $N_{MC} = 10^7$. The narrow and wide TDC ranges are defined in the text.

| Ar ion | ADC ch. | TDC range | $-U_0$ V/cm | FWHM mm | $N$ | $\chi^2$ | $\chi^2/N$ | $CL$ |
|---|---|---|---|---|---|---|---|---|
| +1 | 600– | narrow | 807.62(13) | 0.630(16) | 29 | 50.53 | 1.74 | 0 008 |
| | 1200 | wide | 807.59(12) | 0.635(15) | 69 | 118.66 | 1.72 | 0.000 |
| | 700– | narrow | 807.64(14) | 0.633(18) | 29 | 46.03 | 1.59 | 0.023 |
| | 1200 | wide | 807.49(13) | 0.647(17) | 69 | 107.97 | 1.56 | 0.002 |
| | 800– | narrow | 807.80(16) | 0.626(20) | 29 | 36.84 | 1.27 | 0.150 |
| | 1200 | wide | 807.61(15) | 0.641(20) | 69 | 94.93 | 1.38 | 0.021 |
| +2 | 600– | narrow | 807.95(19) | 0.573(28) | 18 | 27.99 | 1.55 | 0.062 |
| | 1200 | wide | 807.83(18) | 0.584(27) | 34 | 54.66 | 1.61 | 0.014 |
| | 700– | narrow | 808.07(20) | 0.566(31) | 18 | 24.32 | 1.35 | 0.145 |
| | 1200 | wide | 807.97(19) | 0.578(31) | 34 | 44.18 | 1.30 | 0.114 |
| | 800– | narrow | 808.12(22) | 0.565(36) | 18 | 19.54 | 1.09 | 0.360 |
| | 1200 | wide | 808.02(21) | 0.573(35) | 34 | 38.78 | 1.14 | 0.263 |
| +3 | 600– | narrow | 807.37(27) | 0.604(50) | 9 | 6.90 | 0.77 | 0.648 |
| | 1200 | wide | 807.39(25) | 0.603(49) | 21 | 16.23 | 0.77 | 0.756 |
| | 700– | narrow | 807.31(30) | 0.642(55) | 9 | 6.65 | 0.74 | 0.673 |
| | 1200 | wide | 807.43(28) | 0.630(54) | 21 | 20.83 | 0.99 | 0.469 |
| | 800– | narrow | 807.40(33) | 0.623(61) | 9 | 8.51 | 0.95 | 0.484 |
| | 1200 | wide | 807.51(31) | 0.612(59) | 21 | 24.66 | 1.17 | 0.262 |

### 3.7.3 Fit of $\mathrm{Ar}^{+1}$ TOF spectrum from MCP triggered events.

In Sec 3.4.3 we discussed the use of the MCP triggered events to estimate the offset in the energy calibration of the scintillator ADC. As previously mentioned, these self-triggered events appear in channels 78 and 79 in MHTDC5 with a centroid at $t_p = 78.27$. If one assumes they are produced by the emission of a fully relativistic $\beta^+$ (or photon) from the trap 6.1 cm away, the time of that decay can be assumed to be $t_0 = 78.07$ ns. If, following this decay, the associated Ar recoil ion "hits" the MCP the timing is recorded in MHTDC6. This spectrum is shown in Fig 3.20. Not all the features of this complex spectrum are understood, but the origin of three seems clear. If the center of the MCP is triggered by a $\beta^+$ of maximum energy there are well-defined TOFs for the $\mathrm{Ar}^{+1}$, $\mathrm{Ar}^{+2}$ or $\mathrm{Ar}^{+3}$ ions that are produced with kinetic energy 0.430 keV initially recoiling away from the MCP. They represent the maximum TOF

TABLE 3.9: Fits of the electric field strength with $Ar^{+1}$, $Ar^{+2}$ and $Ar^{+3}$ TOF spectra over three scintillator ADC overlapping ranges for 3 values of the angular correlation parameter. The trap width is assumed to be 0.62 mm. The narrow and wide ranges are defined in the text. The values of $\chi^2$ and the *CL* shown belong to the fits with $a = 0.990$ but are typical for all fits. $N_{MC} = 1\times10^7$. The last line of the table contains average values of the electric field strength for each value of the correlation parameter.

| Ar ion | ADC ch. | TOF range | $-U_0$,V/cm $a = 0.980$ | $-U_0$,V/cm $a = 0.990$ | $-U_0$,V/cm $a = 0.999$ | $N$ | $\chi^2$ | *CL* |
|---|---|---|---|---|---|---|---|---|
| +1 | 600–1200 | narrow | 807.68(11) | 807.66(11) | 807.65(11) | 30 | 50.83 | 0.010 |
| | | wide | 807.69(10) | 807.65(10) | 807.65(10) | 70 | 118.24 | 0.000 |
| | 700–1200 | narrow | 807.71(12) | 807.70(12) | 807.69(12) | 30 | 46.41 | 0.028 |
| | | wide | 807.65(11) | 807.65(11) | 807.57(11) | 70 | 110.03 | 0.002 |
| | 800–1200 | narrow | 807.83(13) | 807.83(13) | 807.82(13) | 30 | 36.81 | 0.183 |
| | | wide | 807.74(13) | 807.71(13) | 807.71(13) | 70 | 96.01 | 0.021 |
| +2 | 600–1200 | narrow | 807.79(16) | 807.78(16) | 807.78(16) | 19 | 30.66 | 0.044 |
| | | wide | 807.73(16) | 807.71(16) | 807.68(16) | 35 | 56.33 | 0.013 |
| | 700–1200 | narrow | 807.88(18) | 807.88(18) | 807.88(18) | 19 | 26.92 | 0.107 |
| | | wide | 807.85(17) | 807.85(17) | 807.83(17) | 35 | 46.25 | 0.097 |
| | 800–1200 | narrow | 807.94(20) | 807.93(20) | 807.92(20) | 19 | 21.75 | 0.297 |
| | | wide | 807.88(19) | 807.86(19) | 807.84(19) | 35 | 40.52 | 0.240 |
| +3 | 600–1200 | narrow | 807.30(24) | 807.32(24) | 807.32(24) | 10 | 7.00 | 0.726 |
| | | wide | 807.33(23) | 807.35(23) | 807.34(22) | 22 | 16.42 | 0.794 |
| | 700–1200 | narrow | 807.37(25) | 807.37(25) | 807.37(25) | 10 | 6.80 | 0.744 |
| | | wide | 807.46(24) | 807.46(24) | 807.45(24) | 22 | 21.00 | 0.521 |
| | 800–1200 | narrow | 807.41(28) | 807.41(28) | 807.40(28) | 10 | 8.54 | 0.577 |
| | | wide | 807.50(27) | 807.48(27) | 807.47(27) | 22 | 24.70 | 0.312 |
| | | | 807.70 | 807.69 | 807.67 | | | |

for each charge state and are shown on Fig 3.20 (assuming a uniform electric field of −807.7 V/cm). One expects (and detailed simulations confirm) that, for MCP events triggered by a positron, there will be relatively sharp peaks in the distributions of TOF for each Ar ion charge state just below these maximum possible values. These features are observed in Fig 3.20 and, in the case of $Ar^{+1}$, the "peak/background" appears to be >10. The data in the channel range 1050–1150 are shown in Fig 3.21 and, as is discussed below, analyzed to provide complementary information regarding the electric field strength and trap size.

To simulate these events the fast MC has been used with the assumption that

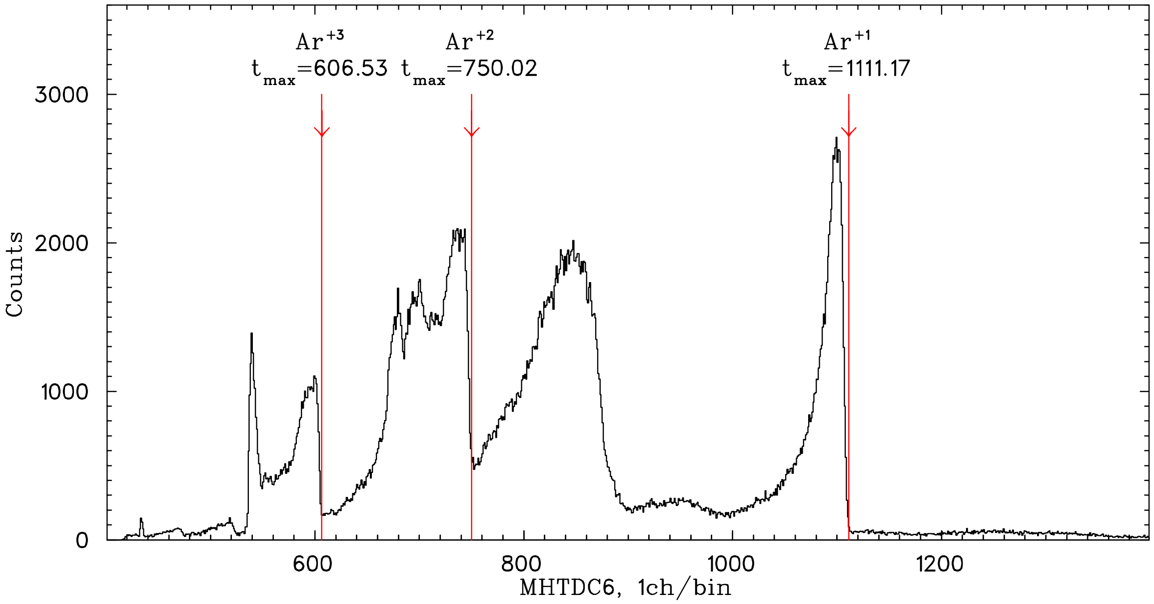

Figure 3.20: MHTDC6 spectrum of MCP triggered events. The three values of $t_{max}$ represent the values of TOF for $\mathrm{Ar}^{+1}$, $\mathrm{Ar}^{+2}$ or $\mathrm{Ar}^{+3}$ recoils assuming the MCP has been triggered by a $\beta^+$ of maximum kinetic energy (5.023 MeV) and that there is a uniform electric field $U = -807.7\,\mathrm{V/cm}$.

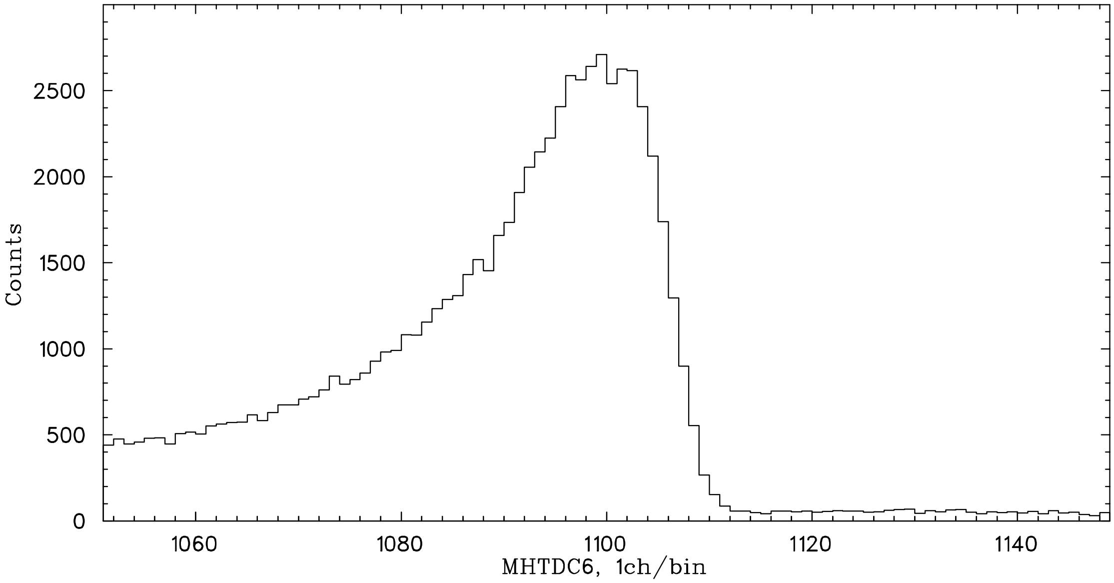

Figure 3.21: TOF spectrum of the $\mathrm{Ar}^{+1}$ ions in the MHTDC6 selected for electric field evaluation and triggered by the MCP.

the $\beta^+$ emerging directly from the trap strikes the MCP anywhere (within the 12 mm radius defined by the aperture) and is detected with an efficiency that is independent of $E_\beta$. Further, it is assumed that $a = 0.99$ and that the recoil is $\mathrm{Ar}^{+1}$. The trajectory of that ion is tracked in the uniform electric field and if it impacts the active area of the MCP the TOF is used to simulate the event in MHTDC6. The free parameters varied in the fits are the strength of the field ($U$), the FWHM of the trap and the magnitude of a "background" which is assumed to be independent of TOF. The results of fits with four different channel ranges are collected in Tab 3.10 and illustrated in Fig 3.22.

The analysis of these data indicates that the magnitude of the electric field is $\simeq 0.15\,\%$ greater than that in Eq 3.14. In all cases, however, the quality of the fit is very poor and for all but the fit with the widest channel range the fitted trap size is quite inconsistent with 0.62 mm.

Because the events shown in Fig 3.20 and Fig 3.21 involve two hits in the MCP (separated $\simeq$1.05 $\mu$s) there is no useful pulse height information in either the MCP ADC or the sum of RAs specific to the amplitude of the first one (attributed to a backscattered $\beta^+$). In this case this pulse is responsible for the event trigger and hence the start of the MHTDC. As is shown in Fig 3.12 for the prompt triple coincident events and in Fig 3.25 for the prompt photoion events, a significant number of events associated with the MCP ADC $< 50$ trigger the TDC "late" by as much as 4 ns. Numerically one can show that for the data presented in Fig 3.21 an "average" delay of the event trigger by 1.2 ns could account for an apparent increase in the magnitude of the electric field by 0.15%. Under these circumstance, one would also expect significant broadening of peaks observed in MHTDC6, perhaps accounting for the increase in the fitted trap width. Recoil ions striking the MCP produce more robust timing pulses (see Fig 3.26) and hence timing distortions in Fig 3.21 are much more likely to be associated with the TDC start.

TABLE 3.10: Results of the fits of MCP triggered $\mathrm{Ar}^{+1}$ TOF spectrum over the several TDC channel ranges, with simultaneous variations of the trap size, electric field strength and background level. $N_{MC} = 1\times10^5$.

| TDC range | $-U$, V/cm | FWHM, mm | Back-ground | $N$ | $\chi^2$ | $\chi^2/N$ | $CL$ |
|---|---|---|---|---|---|---|---|
| 1050−1150 | 808.82(3) | 0.650(12) | 52(1) | 96 | 242.23 | 2.52 | 0.000 |
| 1080−1120 | 808.95(5) | 0.742(19) | 50(2) | 36 | 67.73 | 1.88 | 0.001 |
| 1080−1130 | 808.95(5) | 0.738(19) | 53(2) | 46 | 74.52 | 1.62 | 0.005 |
| 1090−1130 | 808.96(4) | 0.734(18) | 53(2) | 36 | 54.01 | 1.50 | 0.027 |

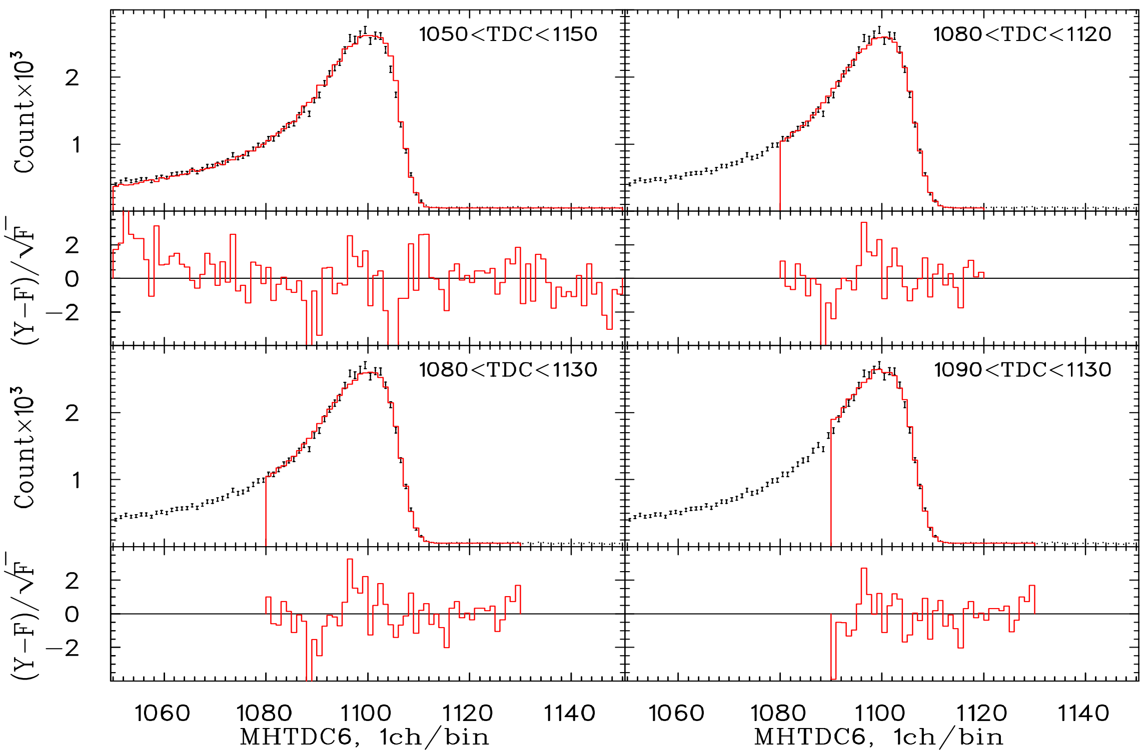

FIGURE 3.22: Fits and residuals of the MHTDC6 spectrum of MCP triggered events in the region of the $Ar^{+1}$. $Y$ is for data and $F$ is for fit. The corresponding fitting parameters are shown in the Tab 3.10.

Lacking the vital information regarding the amplitude of the MHTDC start pulse, no quantitative conclusions can be drawn from the results presented in Tab 3.10. The analysis is presented here in part to motivate possible modifications to the electronics for a future upgrade to the present experiment. In this regard it must be noted that there are unexplained features of the MHTDC6 spectrum in Fig 3.20 and that there may be a component of "background" within the fitting regions that is larger than the nearly constant background observed above channel 1100. It must be also added that the assumption that the efficiency of the MCP is independent of $E_\beta$ has not been verified.

### 3.7.4 $^{38m}K^+$ photoions as a probe of the electric field.

Analysis of the data collected during photoionization of the trapped $^{38m}$K atoms (see Sec 2.5.6 for a description of DAQS operation) gives a tool to test the quality of the electric field independent of beta decay. As $^{38m}K^+$ ions are created nearly at rest (the thermal velocity of atoms in the trap is less then 100 cm/sec and the additional kick due to ionization is about 400 cm/sec) the detection times of photoions must be well localized with a peak width defined by the trap size along the detection axis. This should allow a very precise measurement of the average ion TOF and hence the effective electric field strength.

Ionization of the trapped $^{38m}$K from the $4P_{3/2}$ state populated in the MOT has been produced with a commercial gaseous nitrogen laser which emits light at 337 nm wavelength in pulses with 600 ps duration. With this laser we had the possibility to ionize trapped atoms and detect potassium ions accelerated in the applied electric field toward the MCP in coincidence with the laser synchropulse.

We have detected about 40,000 events triggered by the UV laser. The TOF information for $^{38m}$K$^+$ ions has been recorded with the single hit TDC SHTDC and in channel MHTDC5 of the multihit TDC. SHTDC was set to have 0.25 ns/ch, 512 ns range. SHTDC1 and MHTDC5 have both been triggered by the CFD directly. Both TDCs spectra have peaks corresponding to the STOP generated by the UV light (prompt peak) and the MHTDC5 spectrum has a peak due to the arrival of the $^{38m}$K ions. The TOF distribution in MHTDC5 is shown in Fig 3.23. The peak near TDC channel 385 (prompt peak) is produced by 337 nm photons scattered from material near the trap and then interacting with the MCP and the peak near channel 1155 is due to ion detection. The separation of these peaks defines the time of flight for $^{38m}$K$^+$ ions following detailed analysis of the events associated with both peaks.

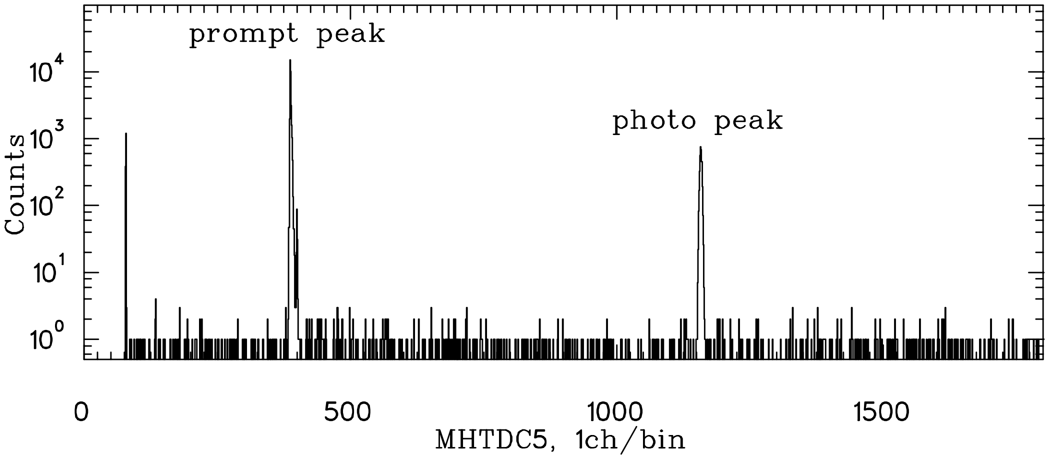

FIGURE 3.23: TOF distribution of the photoionization events. The photoion peak contains events in which MHTDC5 has been stopped by the detection of an ion, while in the prompt events stops were generated by scattered UV light. The separation between the prompt and photoion peaks defines the time of flight of the $^{38m}$K$^+$ ions.

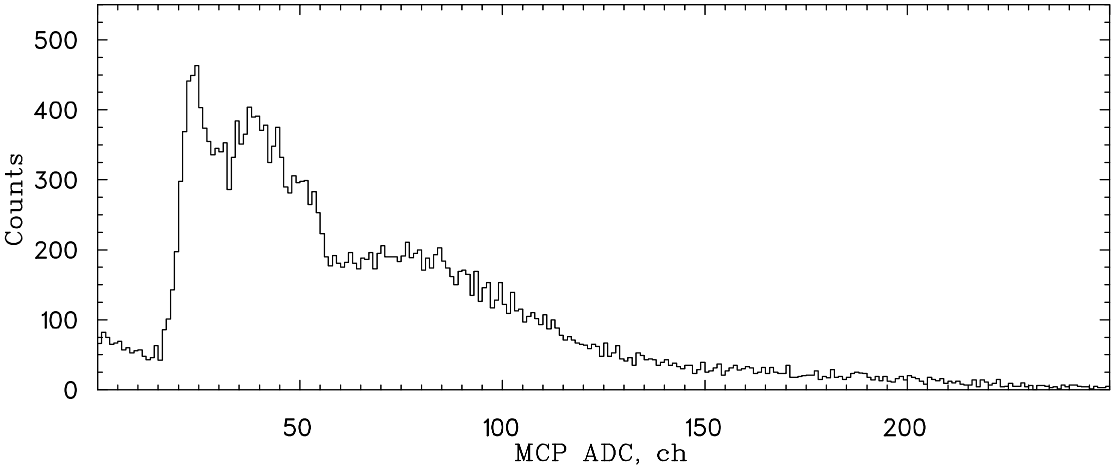

FIGURE 3.24: MCP signal pulse height distribution of the prompt events.

The events contributing to the prompt peak have a quite wide MCP pulse height distribution (see Fig 3.24) which results in significant variation in timing with amplitude. This "slewing" is clearly visible in the 2D Time−Amplitude scatter plot of MCP signals associated with the prompt events which is shown in the Fig 3.25. From the left panel one sees that the application of a threshold of 70 to the MCP ADC significantly reduces the variation in the timing. Nevertheless even for events with ADC>70 there is a dependence of the prompt peak position on ADC amplitude. This dependence is shown in the Tab 3.11 where we collect the centroids of the prompt peak evaluated in subsequent ADC pulse ranges.

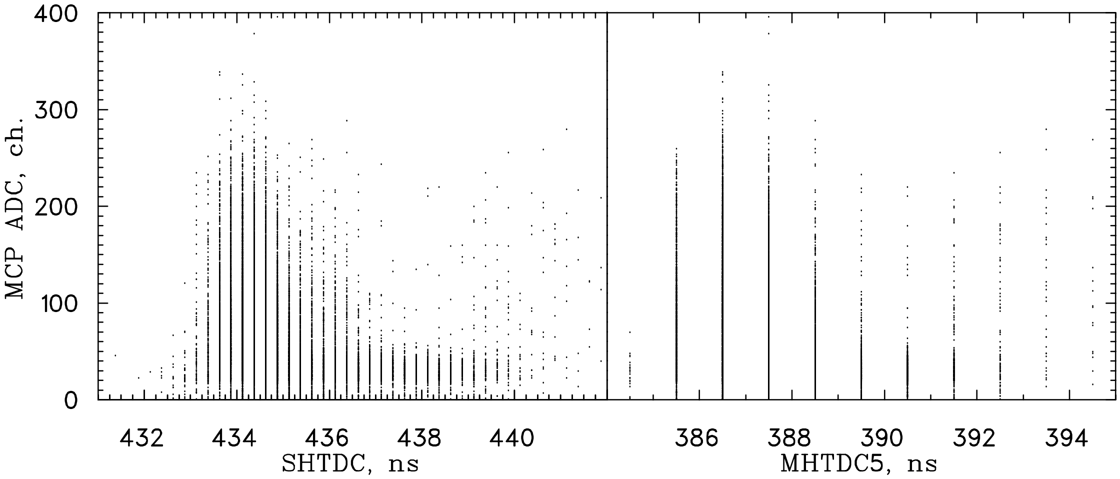

FIGURE 3.25: TOF−MCP two-dimensional distributions of the prompt peak events.

Table 3.11: Centroids of the prompt peak in Fig 3.23 (with statistical errors) as a function of the MCP pulse amplitude for 384<MHTDC5<390. One sees a weak dependence of the centroid position on the MCP pulse amplitude.

| ADC range | 70−90 | 90−110 | 110−130 | 130−150 |
|---|---|---|---|---|
| $t_{prompt}$ | 386.778(12) | 386.752(14) | 386.707(19) | 386.664(25) |
| ADC range | 150−170 | 170−190 | 190−210 | 210−230 |
| $t_{prompt}$ | 386.688(31) | 386.608(35) | 386.578(38) | 386.568(60) |

The events associated with photoions produce in MHTDC5 a peak with a noticeable tail on the left side which is shown in the Fig 3.26 together with the MCP signal pulse height distribution. The shape of the peak is not Gaussian and there is no model to explain the asymmetry of the peak. To exclude a possible bias due to fitting the wrong model we have calculated the arrival time as the peak's centroid. Following the same procedure as in the analysis of the prompt events we have evaluated peak centroids for the photoions as a function of the amplitude of the MCP signal. These results are collected in Tab 3.12.

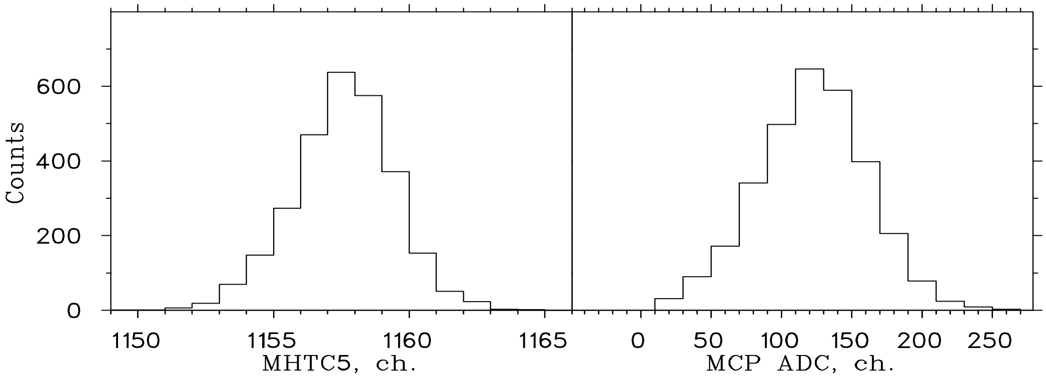

Figure 3.26: Peak events of the photoions. Left panel: MHTDC5 data, 1 ns/ch ($ADC_{MCP} > 70$). Right panel: $ADC_{MCP}$ data, 20 ch/bin (1150<MHTDC5<1165).

Table 3.12: Centroids of photoion peak (with statistical errors), evaluated for as a function of the amplitude of the MCP signal.

| ADC range | 70−90 | 90−110 | 110−130 | 130−150 |
|---|---|---|---|---|
| $t_{photo}$ | 1157.49(10) | 1157.54(9) | 1157.58(8) | 1157.69(8) |
| ADC range | 150−170 | 170−190 | 190−210 | 210−230 |
| $t_{photo}$ | 1157.66(10) | 1157.67(14) | 1157.20(22) | 1157.45(34) |

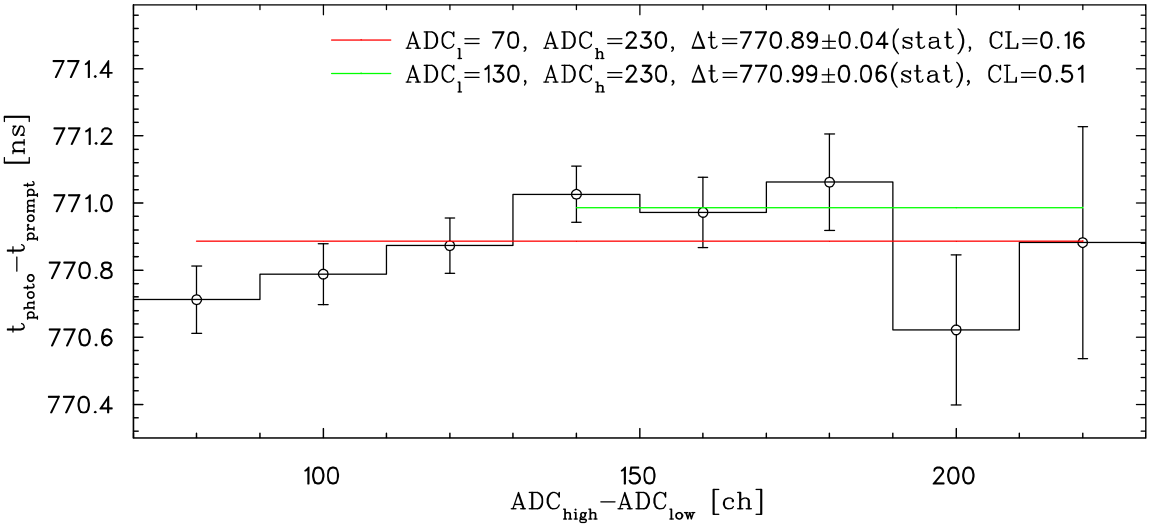

FIGURE 3.27: Measured $\Delta t = t_{photo} - t_{prompt}$) for the photoions as function of the MCP signal amplitude.

The average TOF of the photoions is derived from $\Delta t$, the difference of the centroids $t_{photo} - t_{prompt}$. The difference, as a function of the MCP amplitude, is plotted in Fig 3.27. If the ADC for the MCP precisely defines the amplitude of the timing pulse and if the timing variation, seen in Tab 3.11 are simply related to that amplitude, the time difference plotted in Fig 3.27 should be constant with an average value that can be used to define the photoion TOF. Fits to the data with these assumptions for the ADC channel ranges 70−230 and 130−230 are shown in Fig 3.27 together with the corresponding confidence levels. There are indications of some unexplained variations below ADC channel 130 and hence the adopted average is

$$t_{photo} - t_{prompt} = 770.99 \pm 0.06(stat)\, ns \ . \tag{3.15}$$

To complete this analysis and estimate the strength of an effective uniform electric field, $U$, one needs to define the dominant source of scattering of laser photons that produce the prompt peak. The UV laser beam enters the detection chamber through the pumping port (see Fig 2.10) and is centered on the trap. We assume that the detected photons are scattered from the horizontal fringe of the laser beam after passing the trap and striking the inner edges of the electrostatic hoop closest to the beam. As a consequence, on average the prompt peak is produced by photons that travel a distance ($r_h + \sqrt{z_0^2 + r_h^2}$, see below) further than those producing photoions.

We estimate the strength of a uniform electric field

$$U = \frac{2 z_d M_K}{c^2 \tau^2} \times 10^6 \, ,$$

where

$M_K = 35367.58$ : $^{38\mathrm{m}}$K ion rest mass, MeV/c$^2$
$c = 29.979245$ : velocity of light in vacuum, cm/ns
$z_0 = 6.125$ : nominal drift distance, cm
$\delta z = -0.017$ : trap displacement, cm
$z_d = z_0 + \delta z$ : actual drift distance, cm
$r_h = 5.00$ : hoop inner radius, cm
$t_d = (\sqrt{z_0^2 + r_h^2} + r_h)/c$ : prompt peak delay, ns
$\tau = t_{photo} - t_{prompt} + t_d$ : actual drift time, ns

The assumption regarding the dominant source of the prompt peak implies an average delay of the prompt peak, $t_d = 0.43\,\mathrm{ns}$. An independent measurement of this delay made after the experiment was consistent with this estimate with a statistical uncertainty of 0.07 ns. We assign this uncertainty to our estimate of $t_d$ and hence

$$\begin{aligned} \tau &= 771.42 \pm 0.09\,\mathrm{ns} \\ U &= 807.83 \pm 0.18\,\mathrm{V/cm}\ . \end{aligned} \tag{3.16}$$

This result is consistent with the value defined from the fits to the front edges of the $\mathrm{Ar}^{+1}$, $\mathrm{Ar}^{+2}$ and $\mathrm{Ar}^{+3}$ TOF spectra (Eq 3.14).

### 3.7.5 Constraints on electric field non-uniformity.

The TOF analysis for both the front edges of the $\mathrm{Ar}^{+1}$, $\mathrm{Ar}^{+2}$ and $\mathrm{Ar}^{+3}$ ions and the $^{38\mathrm{m}}\mathrm{K}^+$ photoions are consistent with the existence of a uniform electric field with a magnitude about 1% larger than the design goal (800 V/cm, see Sec 2.5.4). Given this discrepancy it is prudent to use the same data to place limits on the possible size of a gradient in the electric field.

We have assumed the simplest model of non-uniformity, a constant field gradient along the detection axis. In this case the longitudinal component of the electric field (transverse components are neglected) strength can be written as

$$U(z) = U_0 + \frac{dU}{dz}z = U_0 + U_z z\ . \tag{3.17}$$

The motion of ions in such a field is defined by the equation of motion of the mathematical pendulum. One can calculate analytically the ion's TOF from the trap to the recoil detector for any initial longitudinal velocity of the ion and given values of

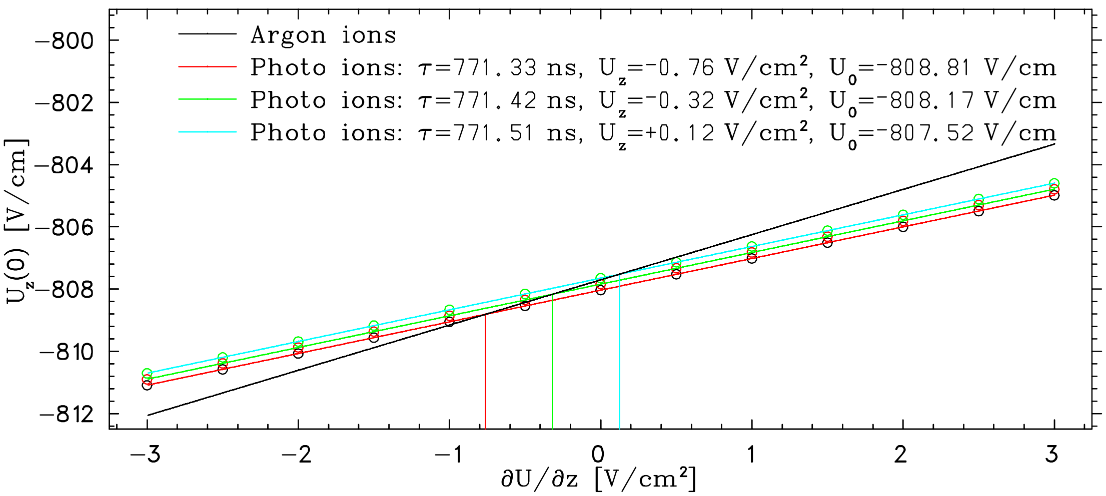

FIGURE 3.28: Relations between the field strength in center of the chamber and its gradient conserving TOF for photo- and Ar ions.

$U_0$ and $U_z$. Similarly given specific values for the initial velocity and the gradient $U_z$ one can calculate numerically the value of $U_0$ which results in a specific TOF.

The relations between $U_0$ and $U_z$ required to reproduce a TOF, $\tau = 771.42\,\mathrm{ns}$ for the photoions is shown in Fig 3.28. Simultaneous fitting the front edges of the $\mathrm{Ar}^{+1}$, $\mathrm{Ar}^{+2}$ and $\mathrm{Ar}^{+3}$ ions TOF spectra (as in Sec 3.7.1) requires for small values of the field gradient ($|U_z| < 3\,\mathrm{V/cm^2}$) a linear dependence given by

$$U_0 = -807.704 + 1.454\,U_z\ . \tag{3.18}$$

As is shown in Fig 3.28 the values

$$U_z = -0.32\,\mathrm{V/cm^2} \quad U_0 = -808.17\,\mathrm{V/cm} \tag{3.19}$$

simultaneously satisfy both conditions. Adopting the lower and upper limits for the photoion TOF together with (3.19) results in the following:

$$\begin{array}{lll} \tau = 771.33\,\mathrm{ns}: & U_z = -0.76\,\mathrm{V/cm^2} & U_0 = -808.71\,\mathrm{V/cm} \\ \tau = 771.51\,\mathrm{ns}: & U_z = +0.12\,\mathrm{V/cm^2} & U_0 = -807.52\,\mathrm{V/cm} \end{array} \tag{3.20}$$

In the subsequent analysis we use the original values (3.14) for a uniform field ( $U_z = 0\,\mathrm{V/cm^2}$, $U_0 = -807.70\,\mathrm{V/cm}$) but consider the influence of a possible gradient in estimating the systematic uncertainties.

## 3.8 Transverse trap size and position.

A straightforward way to determine the transverse trap size and position is using data associated with the detection $^{38\mathrm{m}}\mathrm{K}^{+}$ photoions. Due to the very small initial velocities ($\simeq 400\,\mathrm{cm/s}$) the photoions travel practically along the electric field and the image in the recoil detector created by the detected ions coincides with the initial transverse trap projection (in our experimental conditions with photoions TOF about 770 ns the resulting broadening is about $3\,\mu$m).

### 3.8.1 Application of the mask calibration to photoions.

In order to calculate the transverse coordinates where the potassium ion strikes the MCP we have used initially the RA calibration described in Sec 2.5.2. The position information was extracted for the photoion events, which we define as events which have no second hit in the multihit TDC (MHTDC6 = 0) and with the first hit being near the photoion peak (see Fig 3.23):

$$1149\,\mathrm{ch} \leqslant \mathrm{MHTDC5} \leqslant 1166\,\mathrm{ch}\ . \tag{3.21}$$

The RA pulse height distribution (PHD) and the transverse position evaluated with the MCP calibration defined in Sec 2.5.2 is shown in Fig 3.29. The plots on the left involve no restrictions on the value of MHTDC5 while those on the right include the cut (Eq 3.21) on the photoion peak. One sees a much better defined PHD and spatial trap localization using these events. The trap positions in the $X$ and $Y$ directions ($\delta_x = \overline{x}$ and $\delta_y = \overline{y}$) were evaluated as centers of gravity of the spatial coordinate distributions, while the trap size (FWHM) in the transverse directions ($\Delta_x$ and $\Delta_y$) are the measured standard deviations ($\sigma_x$ and $\sigma_y$) multiplied by $\sqrt{8\ln(2)}$).

$$\begin{array}{llllll} \delta_x = & 1.153(6)\,\mathrm{mm} & \sigma_x = & 0.323\,\mathrm{mm} & \Delta_x = & 0.759\,\mathrm{mm} \\ \delta_y = & 0.041(8)\,\mathrm{mm} & \sigma_y = & 0.468\,\mathrm{mm} & \Delta_y = & 1.100\,\mathrm{mm} \end{array} \tag{3.22}$$

The uncertainties in the trap position were estimated from standard deviations reduced by the square root of number of the observed events in the photoion peak.

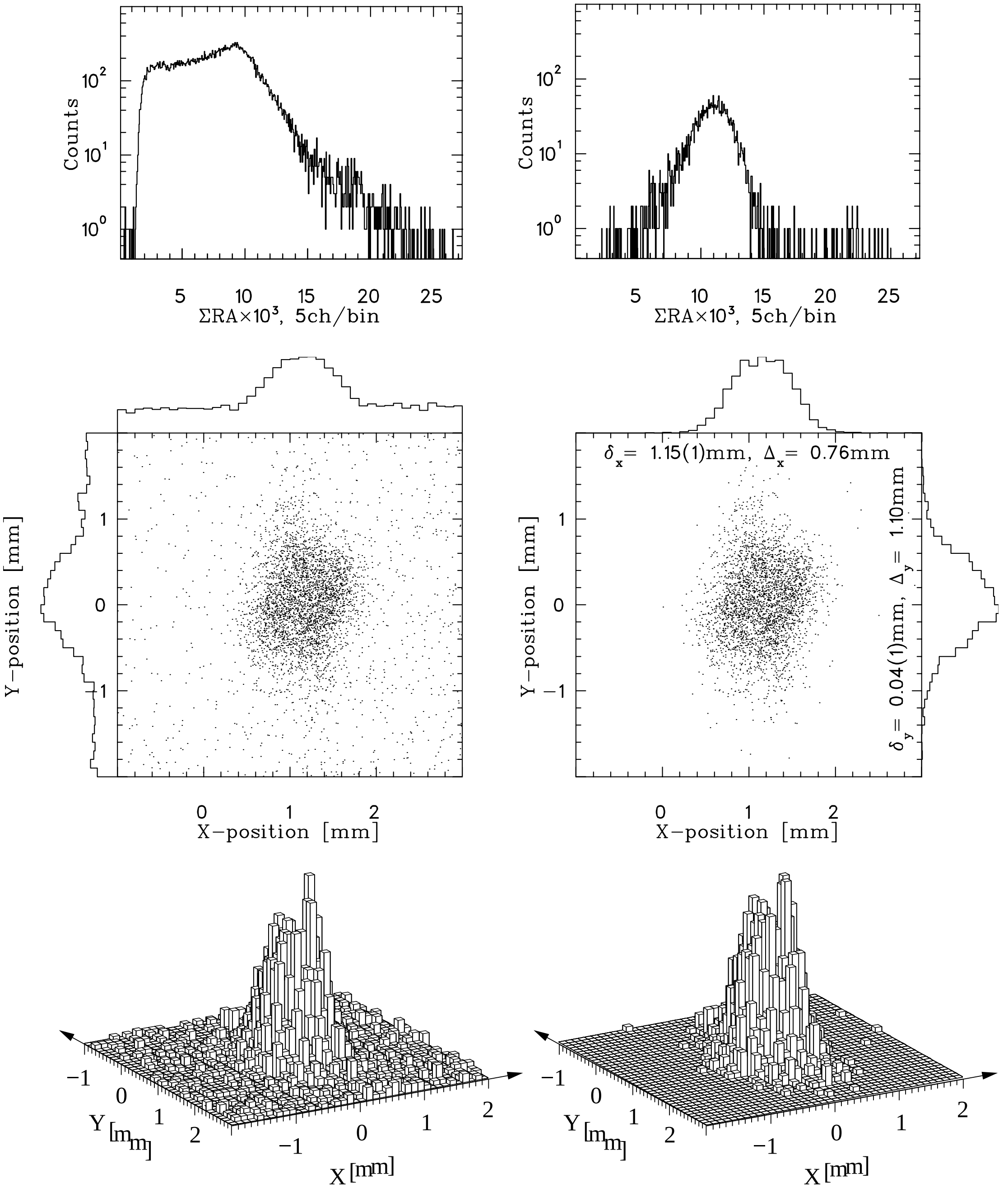

FIGURE 3.29: RA pulse height distribution, spatial scatter plot of events in the MCP and transverse density distribution in the MCP for events, triggered by the UV laser. Left: all detected events. Right: events ( $\sum = 3067$), corresponding to the detection of $^{38\mathrm{m}}\mathrm{K}^+$ ions in the photoion peak (selected as described in the text).

### 3.8.2 Spatial calibration of the RA with MCP hits by fast $\mathrm{Ar}^{+1}$ ions.

During the data collection the front side of the recoil detector has been covered with a 24 mm ID aperture to better define the detector's active area (See Fig 2.15 in Sec 2.5.1). Monte Carlo simulations of the experiment have shown that triple events with scintillator observed energy 300<Scin.ADC<750 and measured $\mathrm{Ar}^{+1}$ TOF 688<MHTDC5<770 should produce a near uniform hit distribution on the MCP inside a circle of 12 mm radius and that this distribution should not depend significantly on the trap size and position. These distributions are shown in the upper panel of Fig 3.30. Here the Monte Carlo simulations were generated with the $\beta-$decay source placed at the nominal center of the detection chamber, e.g. $x{=}y{=}z{=}0$ †. The distribution of the $\mathrm{Ar}^{+}1$ recoil events on the surface of the MCP is considered in terms of the radius ($r = \sqrt{x^2+y^2}$) and the angle $\phi$ ( $\tan\phi = y/x$ ). There are eight angular bins centered at 45°, 90°, . . . , 360° (which is along the $X-$axis). There are 27 bins in the range ($0 \le r \le 12.0$ mm) with widths chosen to keep the MCP area constant for each angle−radius bin (the outer radius for bin $n$, $r_n = 12.0\sqrt{n/27}$ mm). For the Monte Carlo, the distribution of events as a function of radius is identical for each angular bin, as it should be for zero or small transverse $(x, y)$ displacement of the trap. With the radial bins used the predicted distributions decrease $< 10\,\%$ between bin 1 and bin 27. The predicted events in bin 28 results from the gap of 0.25 mm between the rear surface of the aperture and the front surface of the MCP.

In the lower panels of the Fig 3.30 we show the data selected as described above with the applied mask calibration (Eqs (2.6) and (3.22)). There are serious discrepancies between the MC and the data. At certain angles there is compression of the data near the MCP edge and deviations of the total count in some angular bins from the average are far from that due to the statistics. In addition, one can see that the calculated maximum radius of the MCP active area is not constant and depends on azimuthal angle. So, at the angle $\phi = 180\,°$, (i.e. in the negative $X-$direction), this radius is about 11.6 mm while in the positive $X-$direction (at the angle $\phi = 360\,°$) the calculated MCP radius is about 13.0 mm.

In order to resolve the observed discrepancy we have recalibrated the resistive anode of the recoil detector. We have used the a transformation similar to that described in subsection 2.5.2:

---

† Uniformity of the MCP illumination is independent of trap displacement if this displacement is about 1 mm

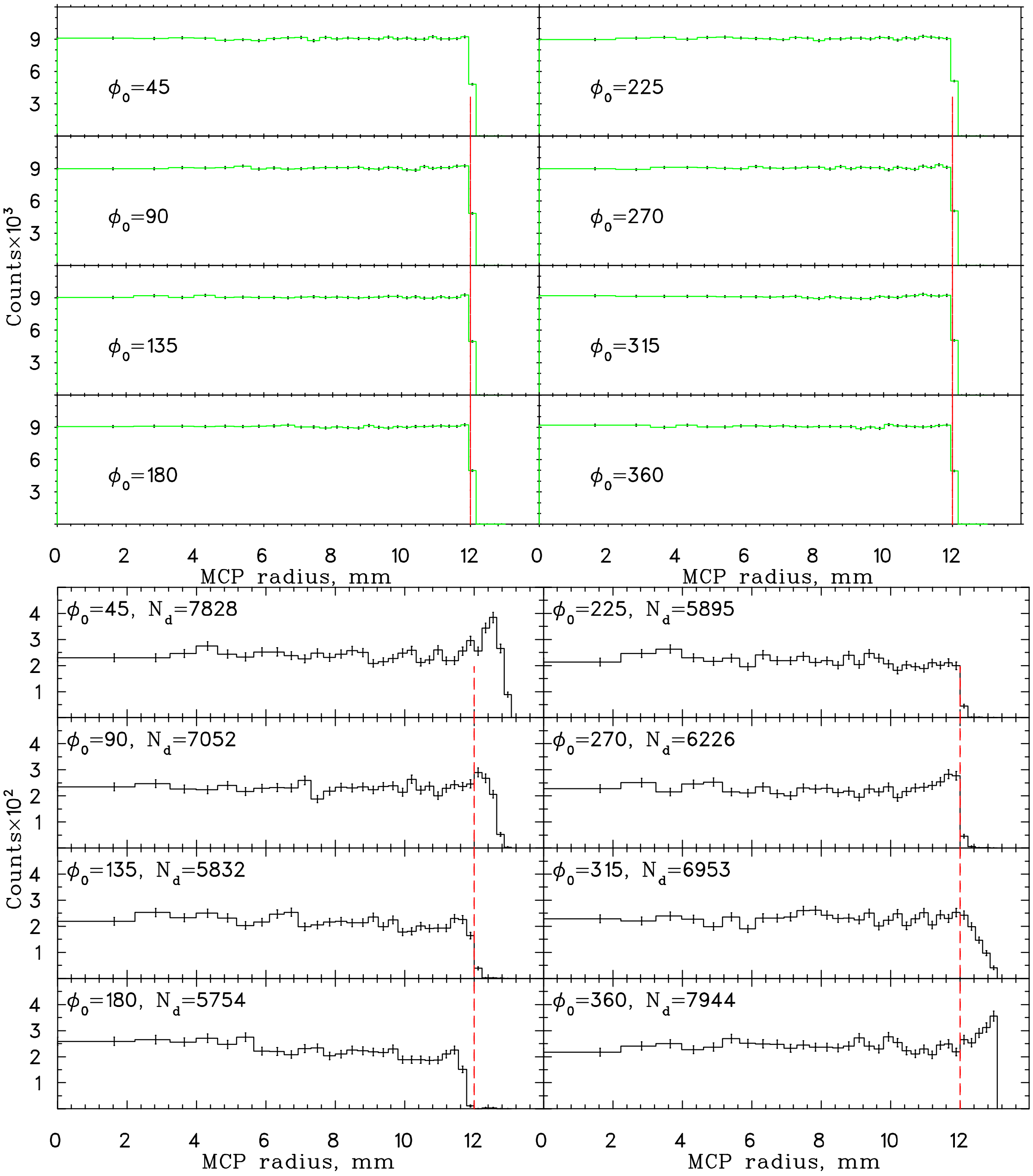

FIGURE 3.30: Radial and angular distribution of the MCP hits by the $Ar^{+1}$ ions for triple coincident events. The angular bin width is $\Delta\phi = 45^\circ$. The radial bins result in elements of equal area (see text). The selection conditions applied are $300 < \mathrm{Scin.ADC} < 750$, $688 < \mathrm{MHTDC5} < 770$. Upper panel: Monte Carlo simulations. Lower panel: data with the mask spatial calibration in the RA given by Eq (2.6).

$$\begin{aligned}
&x = x_0 + A\,u_i \\
&y = y_0 + A\,v_i \\
&u_i = (k_1c_1 + k_2c_2 - k_3c_3 - k_4c_4)/(k_1c_1 + k_2c_2 + k_3c_3 + k_4c_4) \\
&v_i = (k_2c_2 + k_3c_3 - k_1c_1 - k_4c_4)/(k_1c_1 + k_2c_2 + k_3c_3 + k_4c_4) \\
&r \to r(1 + \varkappa r \cos(\phi - \phi_0))\,,
\end{aligned}$$

During evaluation of the transformation coefficients we have compared spectra as in the Fig 3.30, transforming data and minimizing function $\chi^2(\mathbf{p})$ of Eq 3.2, where $f_i(\mathbf{p})$ represented the data and $y_i$ referred to the MC. The Monte Carlo simulation has been performed once and normalized to the same total number of events as the data. After optimizing the fit we have obtained the following set of transformation coefficients, that differ from those derived with the "mask" (2.6):

$$\begin{array}{llll}
k_1 = 1.0000 & A = & 16.32\ \text{mm} & \phi_0 = 11.7^\circ \\
k_2 = 1.1072 & x_0 = & 0.116\ \text{mm} & \\
k_3 = 1.0265 & y_0 = & -0.032\ \text{mm} & \\
k_4 = 1.0096 & \varkappa = & 0.0022\,\text{mm}^{-1} &
\end{array} \tag{3.23}$$

Application of this calibration, based on the predicted uniformity of the MCP illumination, resulted in the radial-angular spectra shown in Fig 3.31. The quality of the fit ($\chi^2$ per degree of freedom about 6.77 for 208 degrees of freedom) does not allow quantitative conclusions about the uncertainties in the definition of the fit parameters. Nevertheless, comparing the lower part of Fig 3.30 with Fig 3.31, one sees that the filling of each angular bin in the latter is considerably more uniform than in the previous. The calculated radius of the MCP active area is practically constant and coincides with the nominal 12.0 mm. At the same time some data compression near the MCP edge is still visible in the first quadrant ( $0^\circ < \varphi < 90^\circ$).

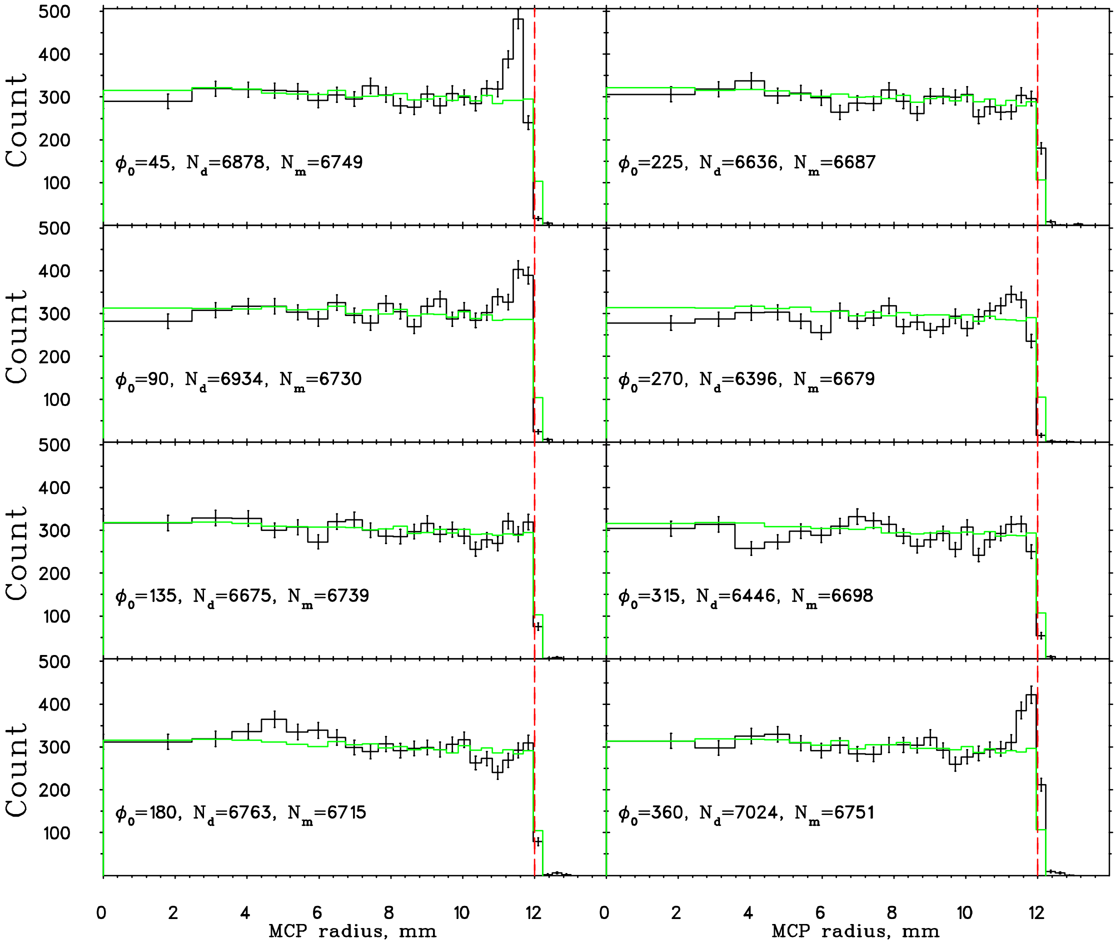

FIGURE 3.31: Radial and angular distribution of the MCP hits by the $\mathrm{Ar}^{+1}$ ions for triple coincident events. The angular bin width is $\Delta\phi = 45\,^{\circ}$. The radial bins result in elements of equal area (see text). The conditions are $300 < \mathrm{Scin.ADC} < 750$, $688 < \mathrm{MHTDC5} < 770$. The data transformed using the refitted calibration of the RA (3.23) are compared to the Monte Carlo simulations normalized to the same total count. The MC spectrum was generated with $N_{MC} = 2\times10^6$ entries.

### 3.8.3 Application of the "fast $\mathrm{Ar}^{+1}$" calibration to the photoions. Transverse trap size and position.

The spatial calibration (3.23) has been applied to the photoionization data, selected as in Sec 3.8.1. Using the same procedure as in that subsection we have evaluated the first and the second moments of the hit's spatial distributions and found for the trap size ($\Delta_x$ and $\Delta_y$) and position ($\delta_x$ and $\delta_y$) in $X$ and $Y$ directions:

$$\begin{array}{llllll} \delta_x = & 0.10(1)\,\mathrm{mm} & \sigma_x = & 0.31\,\mathrm{mm} & \Delta_x = & 0.74\,\mathrm{mm} \\ \delta_y = & 0.06(1)\,\mathrm{mm} & \sigma_y = & 0.46\,\mathrm{mm} & \Delta_y = & 1.06\,\mathrm{mm} \end{array} \qquad (3.24)$$

The image of the trap with photoionized trapped $^{38m}K^{+1}$ is shown in Fig 3.32.

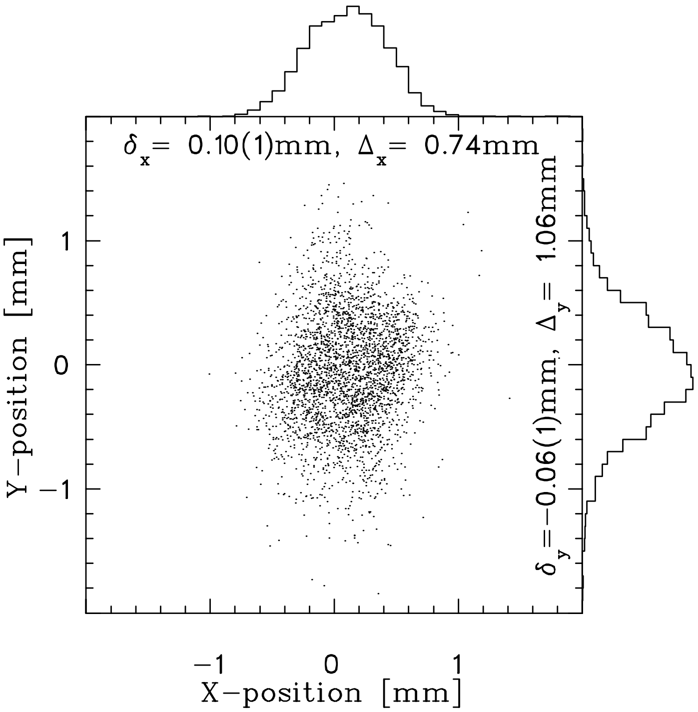

FIGURE 3.32: The scatter plot of the photoion events using the "fast Ar$^{+1}$" spatial RA calibration (Eq 3.23). $\delta_x = \overline{x}$ and $\delta_y = \overline{y}$ are mean values of the evaluated hit coordinates, while $\Delta_x$ and $\Delta_y$ are respective standard deviations ($\sigma_x$ and $\sigma_y$) multiplied by $\sqrt{8\log(2)}$.

### 3.8.4 Recoil impact energy and spatial dependencies of the MCP detection efficiency.

In the data analysis presented we have assumed that, for the recoil ions, the MCP detection efficiency does not depend on energy and does not depend on the impact angle on the MCP. The first assumption is justified by data presented in Ref [89] from which one concludes (see Fig 3.33) that for Ar$^{+1}$ ion impact energy above 3 keV the detection efficiency dependence on energy is very weak. In our case the Ar$^{+1}$ ion impact energy is between 4.9 and 5.4 keV and hence the energy dependence of the recoil detection efficiency can be neglected.

A spatial dependence could arise due to variations across the recoil detector of the average recoil impact angle with respect to the microchannels in the front plate of the detector. Initially, our assumption of spatial uniformity of the detection efficiency might look as if it contradicts known data. Indeed, in the Refs [114, 115] authors report

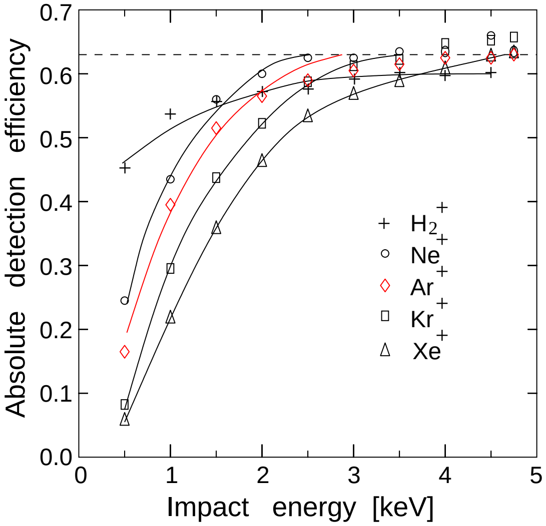

FIGURE 3.33: Absolute MCP detection efficiency as a function of the ion impact energy. Compilation of Fig 3 from Ref [89]. We have highlighted in red data for $Ar^{+1}$ ions.

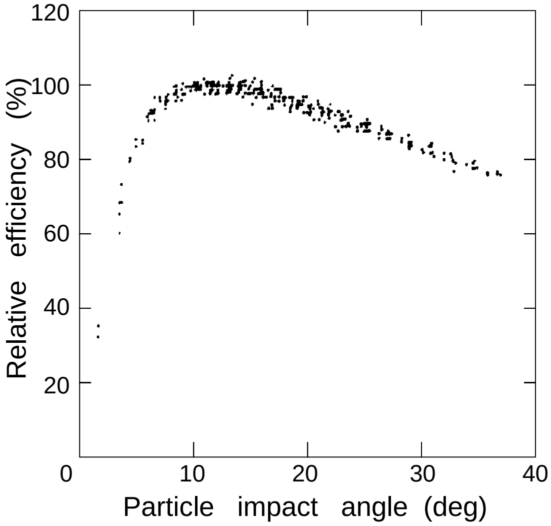

FIGURE 3.34: MCP detection efficiency as function of the angle between the channel and velocity of the incident ions $H^+$, $He^+$ and $O^+$ (original Fig 7 published in Ref [115]).

significant variations of the MCP based detector efficiency when the angle of incident charged particles with respect to the microchannel changes from 0 ° to 40 °. In Fig 3.34 we show such dependence as is presented in the original article [115]. The maximum efficiency authors find to be at 13 °. The degradation of the efficiency at smaller and larger incident angles is attributed to weaker secondary electron production or quantum efficiency [113]. Additional detection efficiency reduction at smaller incident angles may occur due to the deeper penetration of the primary particle along the channel and hence smaller final gain, which leads to fewer counts at a fixed registration threshold [115]. It should be noted that all measurements in this paper were done with a detector consisting of two MCPs in a chevron configuration.

Our detector consists of three MCPs in Z-stack configuration (see description in Sec 2.5.1 and Fig 2.13) and has considerably higher gain. In addition we have run the front plate, which interacts with the incident particles, in a saturated mode where the gain is almost insensitive to the penetration depth. For this reason we suggest that in our case the efficiency reduction at smaller incident angles is similar to that for angles larger than 13 °, although we did not have the opportunity to test this assumption by independent calibration. Detailed Monte Carlo simulations have shown that, under experimental conditions, the incident angle spread of even $Ar^{+1}$ ions with respect to the microchannels is $11 \pm 5$ ° which is relatively small. Nevertheless, we have tested different possibilities for the angular efficiency dependence in the the fits of radial-angular distributions of the events across the recoil detector (Fig 3.31) and found that the best fit corresponds to the uniform case. The higher ion charge states have smaller angle spread. Based on this test with the beta decay data, we have assumed a uniform charged recoil detection efficiency across all the active area of the detector.

## 3.9 Data selection and binning for analysis of the $\beta$–$\nu$ correlation.

To optimize the useful signal and reduce the possible backgrounds, only selected portions of the triple coincidence data presented in Fig 3.3 have been considered in the analysis of the $\beta$–$\nu$ correlation. This includes the $\mathrm{Ar}^{+1}$, $\mathrm{Ar}^{+2}$ and $\mathrm{Ar}^{+3}$ data with observed scintillator energies corresponding to the range 200<Scin.ADC<1550. To simplify the analysis and facilitate display the scintillator data in this range is divided into 27 bins each 50 channels wide. The lower ADC limit completely removes the Compton edge for 0.511 MeV photons which is very prominent in the double coincidence data (see Fig 3.7) and is attributed to positrons which annihilate in the DSSD. There are essentially no triple coincidence events with Scin.ADC>1550.

In the analysis to estimate the strength of the electric field presented in Sec 3.7 it has been noted that there are well-defined minimum values of the TOF for $\mathrm{Ar}^{+1}$, $\mathrm{Ar}^{+2}$ and $\mathrm{Ar}^{+3}$ ions corresponding to events in which both the beta and neutrino we emitted along the positive $Z$ axis and that these minima are nearly independent of positron energy. In the $\beta - \nu$ correlation analysis we choose to bin the MHTDC5 data in 4 channel (i.e. 4 ns) bins and observe the following limits (see Fig 3.35):

| Ar ion charge | +1 | +2 | +3 |
|---|---|---|---|
| MHTDC ch. | ≥688 | ≥556 | ≥488 |

These observed limits include any bin at the fast edge with at least 5% of the counts observed in in the next higher 4 ns bin.

As is evident in Fig 3.35, the distance traveled by the ions under the electric field applied in this experiment was not sufficient to fully separate the $\mathrm{Ar}^{+1}$, $\mathrm{Ar}^{+2}$ and $\mathrm{Ar}^{+3}$ charge state distributions at the lower values of scintillator observed energy. The counts observed in the 4 ns bins just below those listed above would be sensitive to even a very weak non-Gaussian tail in the spacial distribution of trapped atoms in the $\hat{z}$ direction (specifically in the $-\hat{z}$ direction). To avoid this uncertainty the bins corresponding to 552≤MHTDC5<556 (with an observed total of 31 events) and 660≤MHTDC5<668 (with 96 events) were excluded from the analysis.

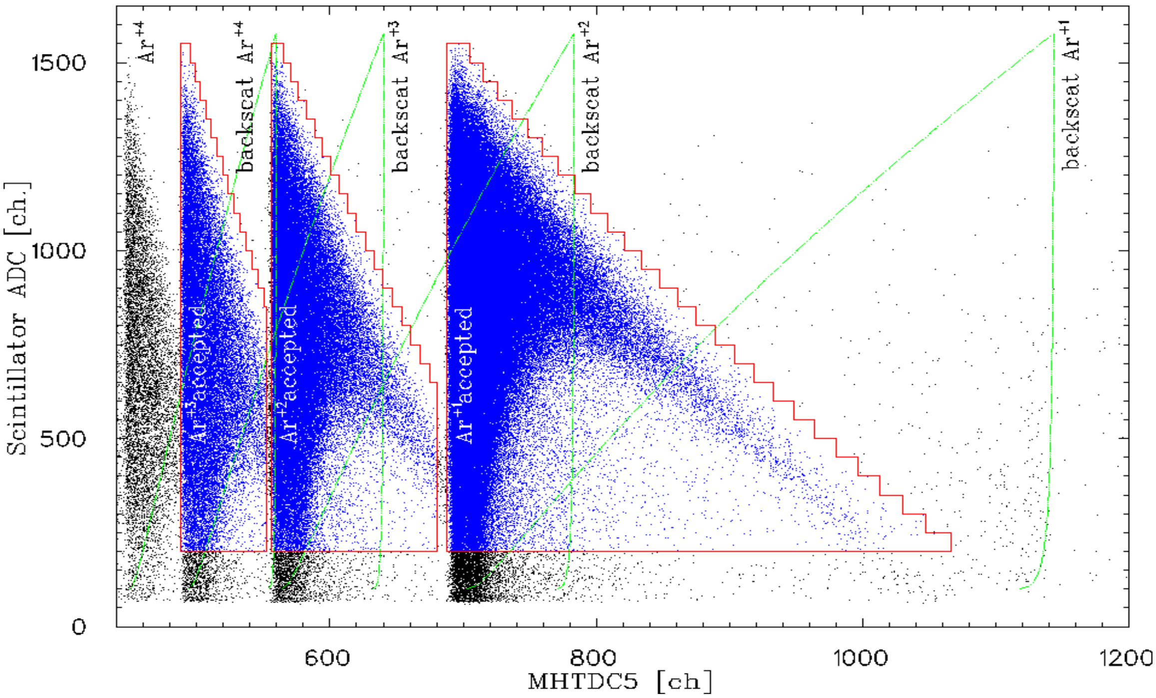

FIGURE 3.35: The events considered for the $\beta$–$\nu$ correlation analysis (shown in blue). Green lines define the regions where one can expect the presence of backscattered events. The cuts used to select the data for analysis are shown in red and are discussed in the text.

For each Ar ion charge state observed in coincidence with a positron emitted at 0 ° there is a well defined maximum TOF (when the neutrino is emitted at 180 °) that increases (nearly linearly) as $E_\nu$ increases from 0 to 5.023. MeV. This fact leaves substantial regions in the ADC–TDC scatter plot which contain only background (including random $\beta$–MCP coincidences and events following the backscattering of positrons). For each 50 channel bin of the ADC these regions in the TDC were systematically removed by the application of the kinematic cuts shown in Fig 3.35 and defined below.

For a given positron total relativistic energy, $E$, the maximum TOF, $t_{max}$, occurs when the initial Ar ion recoil velocity has its maximum possible value in the $+\hat{z}$ direction (away from the MCP).

$$\begin{aligned} v_{max} &= [(E_0 - E) - \sqrt{E^2 - m^2c^4}]/Mc \\ t_{max} &= v_{max}/a_i + \sqrt{(v_{max}/a_i)^2 + 2S/a_i} + t_0 \end{aligned} \tag{3.25}$$

where

$c = 29.9792$ – velocity of light in vacuum cm/ns
$m = 0.511$ – electron rest mass MeV/c$^2$
$E = T_\beta + mc^2$ – positron relativistic energy MeV
$E_0 = 5.5344$ – total energy available for leptons MeV
$M = 35362.05$ – $^{38}$Ar atom rest mass MeV/c$^2$
$U = 807.70\times10^{-6}$ – electric field strength MV/cm
$i = (1,2,3)$ – ion charge state number
$a_i = i\,Uc^2/M$ – acceleration of the ion Ar$^{+i}$ cm/ns$^2$
$S = 6.108$ – distance from the trap to MCP cm
$t_0 = 113.42$ – time shift (see section 3.5) ns

In order to define an "inclusive" kinematic cut for each ADC bin $t_{max}$ was defined using a value of $T_\beta$ chosen to represent a suitable minimum value for the bin with minimum channel:

$$T_\beta = \frac{Min.channel - Offset}{Slope} - 0.200\,\text{MeV}\ .$$

The 0.200 MeV term accounts for the fact that the observed scintillator energy is sometimes increased by as much as 0.340 MeV by the hard Compton scattering of an annihilation photon but that this energy is also decreased by at least 0.140 MeV by energy losses in the beryllium foil, DSSD and Teflon wrapping of the scintillator. The actual values of the linear calibration used were $Offset = 42.00$, $Slope = 294.08$ (MeV$^{-1}$). The cuts defined in this way are plotted in Fig 3.35. They remove from the analysis a total of 169 observed events (from a total of $\simeq$270,000). For the ADC range 200–1550 without the kinematic cuts a total of 3834 bins (50 ch×4 ns) would have been included in the analysis. With the cuts the total is 2113 bins.

The values of the slope and offset used to define the kinematic cuts were values adopted at an early stage of the analysis. A subsequent test with the final calibration parameters revealed that this change would have removed only 3 additional observed events. Since as with all the cuts shown in Fig 3.35, the same cuts are applied in the Monte Carlo simulations, a change in the kinematic cuts to account for the change in calibration was deemed unnecessary.

The analysis of the $\beta$–$\nu$ correlation presented in the Chap 4 is discussed in terms of three different ADC channel ranges. These are listed below together with the total number of 50 ch×4 ns bins which would have been included in the analysis without kinematic cuts and those remaining after the cuts:

| Channel range | Without cuts | With cuts |
|---|---|---|
| 200−1550 | 3834 | 2113 |
| 550−1550 | 2840 | 1213 |
| 750−1550 | 2272 | 791 |

## 3.10 Scintillator energy calibration with triple coincident events.

Addressing the problems of the scintillator energy calibrations with double coincident events (Sec 3.4), we have performed such a calibration with the events in which both the positron and the charged recoil were detected, which means that the same data subset was used to calibrate the scintillator and to evaluate the correlation parameter $a$. Such data selection practically eliminates the influence of the backgrounds originating from decays of untrapped $^{38\mathrm{m}}$K and $^{38\mathrm{gs}}$K atoms because the detection chamber has been designed to have no surfaces from which decays could result in recoil ions striking the MCP in the TOF range of interest. In this section we describe this analysis.

The triple coincident data included in this analysis is the same as that used for the $\beta{-}\nu$ correlation analysis, i.e. those within the cuts (shown in red) on the ADC−TDC scatter plot in Fig 3.35. As for $\beta{-}\nu$ correlation analysis, the ADC data was divided into 50 channel bins starting at channel 200. To suppress the sensitivity of the result to the value of $a$ the data for all 3 charge states was summed over all values of the TOF within the cuts shown in Fig 3.35. The result for the full ADC range $200 \leq$Scin.ADC$\leq 1550$ is the 27 channel spectrum shown at the top of Fig 3.36.

The simulation of these data used to define the energy calibration of the scintillator was based primarily on the fast Monte Carlo simulation described in Sec 3.1. The *Offset* in the calibration was assumed to be 50.663 as determined from the "pedestal" (see Sec 3.4.3). The fast MC could then be used to simulate, for any specific value of the *Slope*, the data in Fig 3.36 that could be attributed to positrons emitted from the trap, impinging directly on the central $22{\times}22\,\mathrm{mm}^2$ of the DSSD which are observed in coincidence with Ar recoil ions observed in the MCP. All the TOF cuts discussed in Sec 3.9 were also imposed on the MC−simulated data. Although these cuts select primarily the $\mathrm{Ar}^{+1}$, $\mathrm{Ar}^{+2}$ and $\mathrm{Ar}^{+3}$ recoils, examination of Fig 3.35 indicates that for ADC channels $\leq 750$ there is a contribution from the "slow tail" of the $\mathrm{Ar}^{+4}$ recoils. These are included in the fast MC.

As is discussed in Sec 3.1 the fast MC does not account for the relatively small

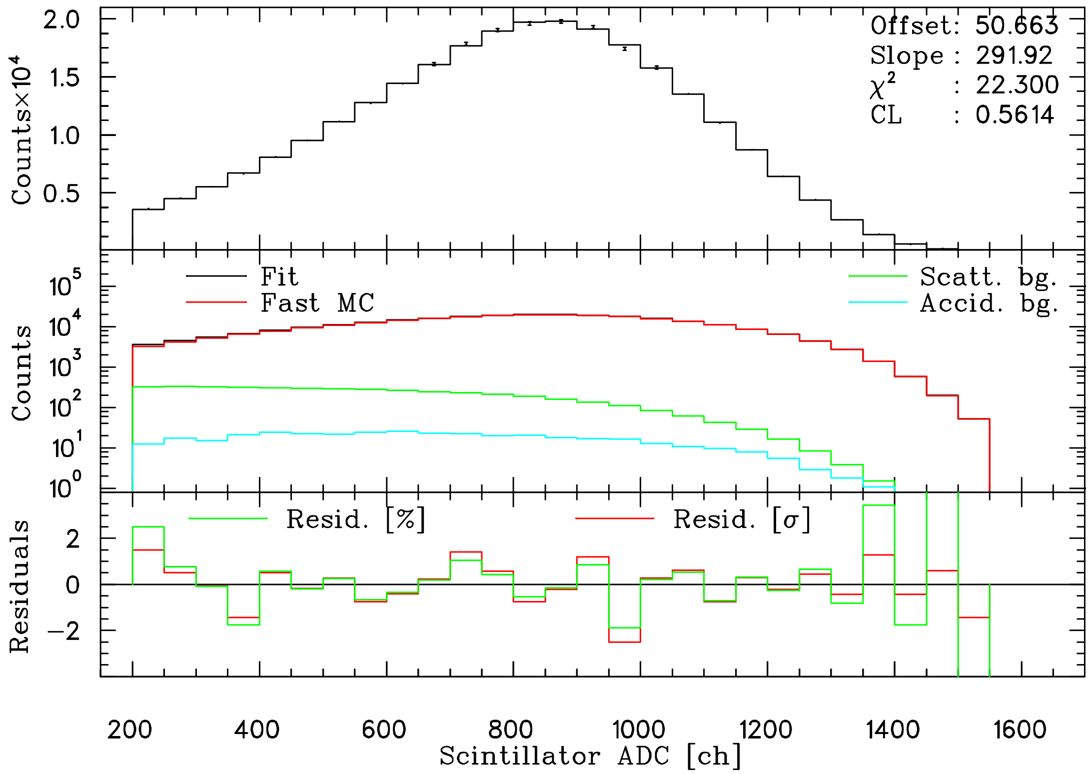

FIGURE 3.36: Energy calibration with triple coincident events. Upper panel shows data (with error-bars) and fitting function (with solid line). Middle panel shows constituents of the fitting function such as appropriately normalized spectra from the fast MC and those from scattered and accidental backgrounds. Lower panel shows fit residuals measured in per cent and in standard deviations which are small and flat over whole fitting range.

number of events in which a recoil ion is observed in coincidence with a positron penetrating the scintillator after significant scattering in the MCP structure, in the edge of the collimator or elsewhere in the detection chamber. The contribution of this component relative to that of the fast MC was calculated for each bin from the ratio "not response"/"response" predicted by the full GEANT simulation.

A third component, included in the simulation presented in Fig 3.36 are the random coincidences which are triggered by a positron from one decay observed in the beta telescope which is followed by an unrelated hit in MCP. These events have a uniform distribution of stops in MHTDC5 and are estimated for each bin on the basis of the data observed in the TDC range 3000−9000. Our account of the origin of these events is supported by Fig 3.37 in which the ADC spectrum for all random events with $3000 \leq \mathrm{TDC} \leq 9000$ is compared with that of the positron double coincident events.

In the full simulations of data shown in Fig 3.36 (fast MC + scattered background

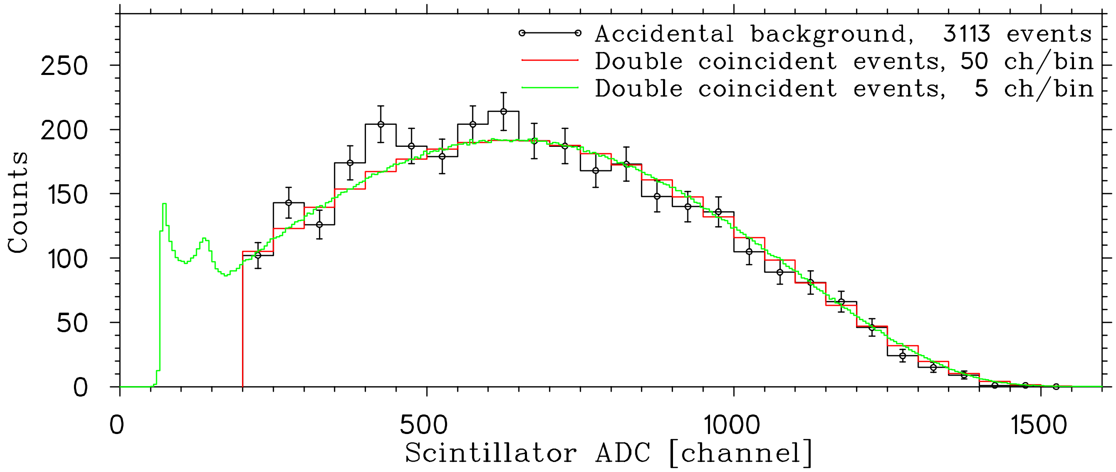

FIGURE 3.37: Energy spectrum of accidental background events for 3000≤TDC≤9000 (histogram with errors). The double coincident positron energy spectrum is normalized over the channel range 200−1550 to the same sum (3113) as is observed in the accidental background spectrum.

+ accidental background) the total count in the simulation is equated to that observed in the data over the ADC range that is fitted. As an example, the best fit for the channel range 200−1550 resulting in the $Slope = 291.92$ is shown in the Fig 3.36. The data and the full Monte Carlo simulation are compared in the upper panel. The three components included in the simulation are shown in the middle panel. It should be emphasized that in each bin the number of accidentals is fixed and the ratio $Scattered/Fast\ MC$ is is defined from full GEANT based simulations. The scattered background contributes $\sim 10\%$ to the total in the lowest energy bin included in the fit. The residuals $(Data - Fit)$ are shown both in % and $\sigma$ ($\sigma = (Data - Fit)/\sqrt{Fit}$). The quality of the fit is excellent. For comparison with the fits to the double coincident data (see Sec 3.4), fits to the data shown in Fig 3.36 but including the data in more limited ranges are compared in Tab 3.13. The results are consistent and within the more limited statistics available ( c.f. "doubles") reveal no systematic deviations with observed scintillator energy. For further use we adopt the calibration of expression (3.4) with

$$Offset = 50.663(1) \quad Slope = 291.92(16)\ . \tag{3.26}$$

We considered the parameters of the energy calibration of the scintillator to be most reliably defined by (3.26). In the case of the double coincident spectra fitted with $Offset = 50.663$ (see Fig 3.10) acceptable fits could only be obtained by restricting the scintillator energy range 750≤Scin.ADC≤1400. In that data there is clearly a source of background below channel 750 that is not adequately represented in the

Table 3.13: Evaluation of the calibration slope from the triple coincident events over different scintillator ADC channel ranges. The Standard Model values $a = 1.0$ and $b = 0.0$ have been used in the Monte Carlo.

| Channel range | *Slope* | $NF$ | $\chi^2$ | $CL$ |
|---|---|---|---|---|
| 750−1400 | 291.98(21) | 12 | 11.86 | 0.46 |
| 750−1450 | 291.94(19) | 13 | 12.19 | 0.51 |
| 750−1500 | 291.97(19) | 14 | 12.49 | 0.57 |
| 750−1550 | 291.92(18) | 15 | 14.85 | 0.46 |
| 550−1550 | 291.88(16) | 19 | 17.40 | 0.56 |
| 200−1550 | 291.92(16) | 26 | 22.30 | 0.67 |

simulations. In contrast, the relatively small backgrounds simulated in the analysis shown in Fig 3.36 are accounted for with no "free" parameters.

It has previously been noted that the fits to the double coincident data cannot account for the energy region 1400≤Scin.ADC≤1600 and that no reasonable background has been identified to account for this discrepancy. It may be that there is a deficiency in the GEANT description of events involving partial absorption in the scintillator of the annihilation photons. If such a deficiency exists it appears to be not evident with the smaller statistics of the triple coincident data (Fig 3.36). It is perhaps relevant to notice that if the "doubles" fit is extended to channel range 750≤Scin.ADC≤1550, the central value of the fitted *Slope* $= 291.90 \pm 0.04$ is in very good agreement with that given in Eq 3.26. Although this agreement may suggest it is better to include rather than exclude the discrepant region, it will not be used to suggest that uncertainty in the *Slope* is less than that given in Eq 3.26.

## 3.11 Recoiling ion charge state distribution and effects of recoil energy dependent electron shakeoff corrections.

In the previous parts of the data analysis, such as the energy calibration with triple coincident events or the evaluation of the electric field strength, we have fitted simultaneously TOF or beta energy distributions for the events associated with detection of the $\mathrm{Ar}^{+1}$, $\mathrm{Ar}^{+2}$ and $\mathrm{Ar}^{+3}$ recoiling ions. The relative charge state distribution of these ions has been determined experimentally from data recorded in April 1999 and initially reported in Ref [41]. Using the GEANT3 based Monte Carlo simulation we have produced equal numbers (few million) of events associated with the detection of

$\mathrm{Ar}^{+1}$, $\mathrm{Ar}^{+2}$, $\mathrm{Ar}^{+3}$ and $\mathrm{Ar}^{+4}$ ions. Applying to the MC events the same conditions as to the data we have built recoil TOF spectrum keeping just events with coincident positron energy above 2.5 MeV. This high threshold ensured a separation in TOF of $\mathrm{Ar}^{+1}$, $\mathrm{Ar}^{+2}$, $\mathrm{Ar}^{+3}$ and $\mathrm{Ar}^{+4}$ ions and eliminated almost all backscattered events. (For the separation see Fig 3.35, in which ADC channel 750 corresponds to a positron emitted with a kinetic energy of 2.5 MeV.) Fitting the Monte Carlo simulated spectra to data by varying the normalization of each constituent part we have defined that the relative ion creation probabilities of $\mathrm{Ar}^{+1}$, $\mathrm{Ar}^{+2}$, $\mathrm{Ar}^{+3}$ and $\mathrm{Ar}^{+4}$ are in the ratios

$$p_1 : p_2 : p_3 : p_4 = 0.3743 : 0.1023 : 0.0427 : 0.01\,. \tag{3.27}$$

We have assumed there that the MCP detection efficiency is independent of recoil impact energy and angle [113, 89]. Also, for this initial analysis we have assumed that the charge state distribution results from orbital mismatch of initial and final atomic wave functions and is independent of both the positron and recoil energies.

The values of the relative ion creation probabilities given above were determined by restricting the scintillator ADC range to a region where the result was very insensitive to the details of the Monte Carlo simulations. A sensitive test of these simulations can be obtained by considering the entire channel range $200-1550$. The data for each of the 27 50ch bins ($i$) was summed over the three TOF ranges, "$\mathrm{Ar}^{+1}$ accepted", "$\mathrm{Ar}^{+2}$ accepted" and "$\mathrm{Ar}^{+3}$ accepted" defined in Fig 3.35 to obtain $D_1^i$, $D_2^i$ and $D_3^i$. The results of the simulations (with $a = 1$ and $b = 0$) were binned in the same way to provide $F_1^i$, $F_2^i$ and $F_3^i$. The simulation was normalized such that

$$\sum_i F_1^i + F_2^i + F_3^i = \sum_i D_1^i + D_2^i + D_3^i \ .$$

For each bin the ratio

$$\mathcal{R}^i = \frac{D_1^i}{F_1^i} \times \frac{F_2^i + F_3^i}{D_2^i + D_3^i}$$

is a test of the accuracy of the Monte Carlo in predicting the fraction of the $\mathrm{Ar}^{+1}$ recoils that "miss" the recoil detector relative to that for the sum of the $\mathrm{Ar}^{+2}$ and $\mathrm{Ar}^{+3}$ recoils. Since the fast Monte Carlo is generated with typically 2000 times the statistics of the data the fractional uncertainty in $\mathcal{R}^i$ is simply given by

$$\Delta\mathcal{R}^i = \left[\frac{1}{D_1^i} + \frac{1}{D_2^i + D_3^i}\right]^{1/2} \ .$$

The values of $\mathcal{R}^i$ and these uncertainties are plotted in Fig 3.38.

Clearly the observed ratios are consistent with the simulations over the entire energy range. This analysis, in contrast to the scintillator energy calibration with the

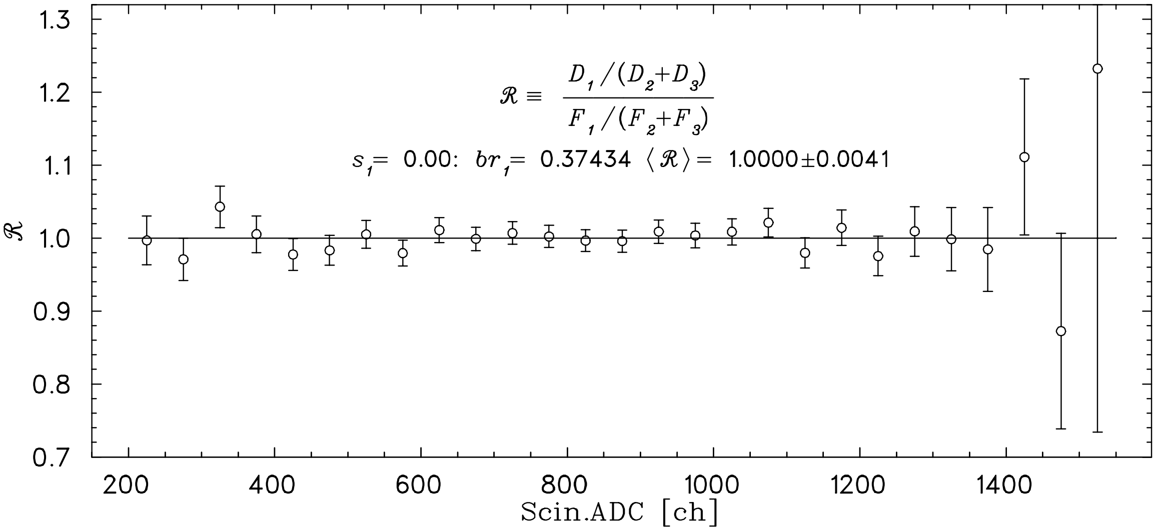

FIGURE 3.38: Test of the production and geometric acceptance of $\mathrm{Ar}^{+1}$ ions at the MCP relative to that of $\mathrm{Ar}^{+2}$+ $\mathrm{Ar}^{+3}$. The simulations are for $a = 1,\ b = 0,\ s_1 = 0$ and the relative ion creation probabilities given by (3.27).

triple coincident events (Fig 3.36), does not depend significantly on the adequacy of the Monte Carlo simulation of the scintillator energy response. The weighted average, $\langle\mathcal{R}\rangle = 1.0000(41)$ indicates an optimum value for the $p_1/(p_2+p_3)$ production ratio given by (3.27). The statistical uncertainty in the result can be interpreted as defining the $\mathrm{Ar}^{+1}$ relative creation probability to be

$$p_1 = 0.3743(15) \tag{3.28}$$

The known dependence of the ionization cross section on the energy of the emitted positron (direct collision) for low $Z$ atoms such as Ar is only significant at very low energy, below 1 keV [116], and has very little impact on the correlation parameter $a$ in superallowed transitions [117]. The recoil energy dependent effects, however, are considerably stronger and might play a significant role in charge state distribution of recoiling ions in beta decays of light atoms with relatively high $Q-$value (several MeV). The theoretical estimates which use semi-empirical values of oscillator strength [118] predict that in the case of $^{38\mathrm{m}}$K the recoil energy dependent correction to the $\mathrm{Ar}^{+1}$ creation probability is about a 3% effect [119]. The corrections for $\mathrm{Ar}^{+2}$ and $\mathrm{Ar}^{+3}$ should be smaller than this by factors ∼9 and ∼20 respectively and can be neglected [43].

We have adopted a simple model with a linear dependence of the $\mathrm{Ar}^{+1}$ creation probability on the recoil kinetic energy $T$

$$p_1(T, s_1) = p_1(0, s_1) \cdot (1 + s_1 \frac{T}{T_{max}}) \ . \tag{3.29}$$

The creation probabilities of higher ion charge states are still assumed to be energy independent with the ratios given by (3.27). The function $p_1(0, s_1)$ has been defined by repeating the analysis of $\mathcal{R}^i$ with the modified simulations and imposing the condition $\langle R \rangle = 1$. Direct numerical calculation with values of $s_1$ in the range $0 < s_1 < 0.1$ shows that this condition is satisfied provided

$$p_1(0, s_1) = p_1(0, 0) \cdot (1 - 0.76\, s_1) \ . \tag{3.30}$$

Moreover, with this simple modification, the consistency of the values of $\mathcal{R}^i$ is unchanged from that shown in Fig 3.38. This result is not altered significantly if the values of $a$ or $b$ are varied over the ranges considered in this experiment.

# Chapter 4

# Fits, Results and Systematic Errors.

## 4.1 Evaluation of the angular correlation parameters.

The good quality of the calibration fits with triple coincident events described in Sec 3.10 prompted us to attempt to simultaneously evaluate the $\beta - \nu$ correlation parameters $a$ and $b$ for positrons depositing energy in the scintillator corresponding to the ADC channel range 200−1550 (0.51−5.14 MeV). For convenience let us write again the expression for the decay rate in the case of a $0^+ \rightarrow 0^+$ decay by positron emission:

$$\frac{d\Gamma}{dE_e d\Omega_e d\Omega_\nu} \sim F(E_e, Z)\, p_e E_e E_\nu^2 \left(1 + b\frac{m_e}{E_e} + a\frac{p_e}{E_e}\cos\theta\right), \tag{4.1}$$

with correlation coefficients $a$ and $b$ as defined in Ref. [33]

$$\begin{aligned} a &= \frac{2 - |\tilde{C}_S|^2 - |\tilde{C}'_S|^2 + 2\alpha\, Z(m_e/p_e)\mathcal{I}m(\tilde{C}_S + \tilde{C}'_S)}{2 + |\tilde{C}_S|^2 + |\tilde{C}'_S|^2} \\ b &= \frac{-2\sqrt{1-\alpha^2 Z^2}\mathcal{R}e(\tilde{C}_S + \tilde{C}'_S)}{2 + |\tilde{C}_S|^2 + |\tilde{C}'_S|^2}, \end{aligned} \tag{4.2}$$

where we define $\tilde{C}_S = C_S/C_V$ and $\tilde{C}'_S = C'_S/C'_V$ and assume as in the Standard Model $C_V = C'_V$ and $\mathcal{I}m(C_V) = \mathcal{I}m(C'_V) = 0$. Equation (4.2) includes Coulomb corrections involving the energy of the positron interacting with the daughter nucleus of charge $Z$.

The expressions for $a$ and $b$ above make it convenient to introduce the (in general complex) quantities

$$L = \tilde{C}_S + \tilde{C}'_S \text{ and } R = \tilde{C}_S - \tilde{C}'_S$$

which define the strength of the scalar coupling to the left and right handed neutrinos.

In terms of these quantities

$$\begin{aligned} a &= \frac{4-|L|^2-|R|^2+4\alpha Z\,(m_e/p_e)\,\mathcal{I}m(L)}{4+|L|^2+|R|^2} \\ b &= \frac{-4\sqrt{1-\alpha^2Z^2}\,\mathcal{R}e(L)}{4+|L|^2+|R|^2}\;. \end{aligned} \tag{4.3}$$

The analysis of the present experiment involves a search for deviations from the predictions of the Standard Model ($C_S = C'_S = L = R = b = 0$, $a = 1$) resulting from a possible contribution of the scalar interaction. Although, in general, this interaction is defined in terms of the real and imaginary parts of two complex numbers, the expressions for $a$ and $b$ in (4.3) indicate that this experiment is sensitive to only 3 quantities: $\mathcal{R}e(L)$, $\mathcal{I}m(L)$ and $|R|$. There is no sensitivity to a possible complex phase of $R = |R|e^{i\phi}$.

In this chapter the analysis of the present experiment is made with the additional assumption that the scalar interaction does not involve time-reversal violation, i.e. $\mathcal{I}m(C_S) = \mathcal{I}m(C'_S) = \mathcal{I}m(L) = \mathcal{I}m(R) = 0$. We shall analyze data in terms of $L$ and $R$ with

$$\begin{aligned} a &= \frac{4-|L|^2-|R|^2}{4+|L|^2+|R|^2} \\ b &= -\frac{4\sqrt{1-\alpha^2Z^2}\,L}{4+|L|^2+|R|^2}\;. \end{aligned} \tag{4.4}$$

The possible implications of $\mathcal{I}m(L) \neq 0$ are considered in App D.

The evaluation of the angular correlation parameters has been performed with the triple coincident data selected as described in Sec 3.9. After application of the kinematic cut we have considered events in the MHTDC5 channel ranges of 488−552, 556−680 and 688−1080, which are predominantly $\mathrm{Ar}^{+1}$, $\mathrm{Ar}^{+2}$ and $\mathrm{Ar}^{+3}$ ions respectively. Considering the scintillator ADC region of channels 200−1550 we have binned the data into 2D spectra with 50 and 4 channels per bin in energy and time respectively.

As an example, a detailed comparison of the data and the simulation for the scintillator range 200≤Scin.ADC≤1550 is presented in Figs 4.1−4.5 for the Standard Model values of the parameters $a = 1$ and $b = 0$ ($L = R = 0$). (Fits for other values of $L$ and $R$ are discussed in Sec 4.1.1). A summary of the input parameters for the simulations, determined as discussed in Chap 3, is given in Tab 4.1. These initial fits are made assuming that the MCP efficiency is independent of the angle of incidence of the ion and that there is no recoil energy dependent shakeoff correction ($s_1 = 0$ in

TABLE 4.1: Standard input parameters for the simulations used to evaluate the angular correlation parameters. The determination of these parameters is described in Chap 3 with the results given by the reference indicated. Where relevant, the uncertainties ($1\sigma$) in these values are shown.

| Parameter | | Value | Unit | Equation |
|---|---|---|---|---|
| Scintillator energy calibration | *Offset* | 50.663(1) | ch | 3.6 |
| Scintillator energy calibration | *Slope* | 291.92(16) | ch/MeV | 3.26 |
| MHTDC5 zero time | $t_0$ | 113.42(17) | ns | 3.11 |
| Trap position | $z_0$ | −0.168(7) | mm | 3.13 |
| | $x_0$ | 0.10 | mm | 3.24 |
| | $y_0$ | 0.06 | mm | 3.24 |
| Trap size | $\mathrm{FWHM}_z$ | 0.62(2) | mm | 3.13 |
| | $\mathrm{FWHM}_x$ | 0.74 | mm | 3.24 |
| | $\mathrm{FWHM}_y$ | 1.06 | mm | 3.24 |
| Uniform electric field strength | $U_0$ | −807.70(12) | V/cm | 3.14 |
| Relative Ar ion charge state distribution | $\mathrm{Ar}^{+1}$ | 0.3743(15) | | 3.28 |
| | $\mathrm{Ar}^{+2}$ | 0.1023 | | 3.27 |
| | $\mathrm{Ar}^{+3}$ | 0.0427 | | 3.27 |
| | $\mathrm{Ar}^{+4}$ | 0.0100 | | 3.27 |

Eq 3.29). Since the simulation shown is for the specific values $L = R = 0$, the only remaining free parameter is the overall normalization of the simulation which is fixed by requiring that the total number events included in the Fit is equal to the total number of events in the Data (268973 for the data shown in Figs 4.1−4.5).

As is discussed in Sec 3.10 for the scintillator energy calibration with triple coincident events, for each bin (here 4 ns in MHTDC5 by 50 ch in scintillator ADC) the fit is given by the sum of contributions from the "fast" Monte Carlo (response function events), the scattered background and the random coincidence background. The summing is done over all bins included in the fit. The 27 plots shown in Figs 4.1−4.5 are the TDC spectra for each of the (50 channels wide) bins for the scintillator ADC. The individual data points are shown and compared with the fits. Also shown are the contributions to the full simulations of the scattered and random backgrounds. For each of the 2113 bins (4 ns×50 ADC channels) the contribution to $\chi^2$ is calculated according to Eq 3.2.

For the fit shown the total $\chi^2$ is 2344.6. Such a fit would be acceptable at a

Confidence Level of only 0.025%. The contribution to the this total $\chi^2$ arising from each of the 27 ADC bins is shown in Figs 4.1−4.5 along with the number of MHTDC5 bins involved. A comparison of these quantities suggests that there is a dramatic

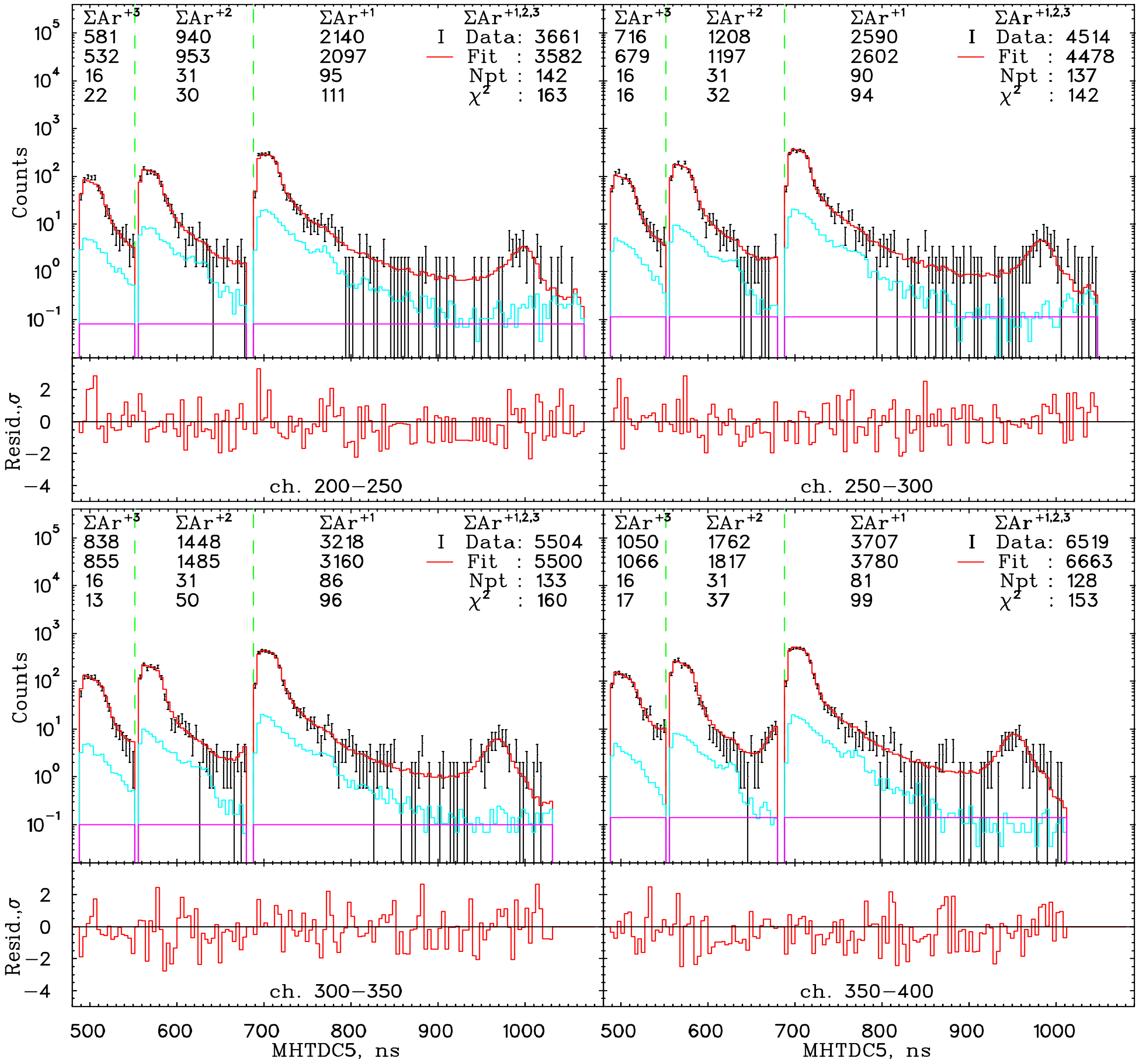

FIGURE 4.1: An example of the recoil TOF spectra (4 ns/bin) comparing the data and simulation in each of 27 energy bins (50 ADC ch/bin) over the channel range 200−1550. The full simulation is plotted as a histogram ("Fit") for comparison with the data in the upper portion of each segment. Also shown are the contributions to the fit of the Scattered Background (cyan) and Random Coincidence Background (magenta). The three TOF regions dominated by $\mathrm{Ar}^{+1}$, $\mathrm{Ar}^{+2}$ and $\mathrm{Ar}^{+3}$ ions are shown together with sums of *Data*, *Fit*, *Npt* and $\chi^2$. In the lower portion of each panel are plotted the residuals measured in standard deviations ($(Data - Fit)/\sqrt{Fit}$). The simulations shown are for $L = R = 0$ ($a = 1$, $b = 0$). Shown here is the ADC channel range 200−400.

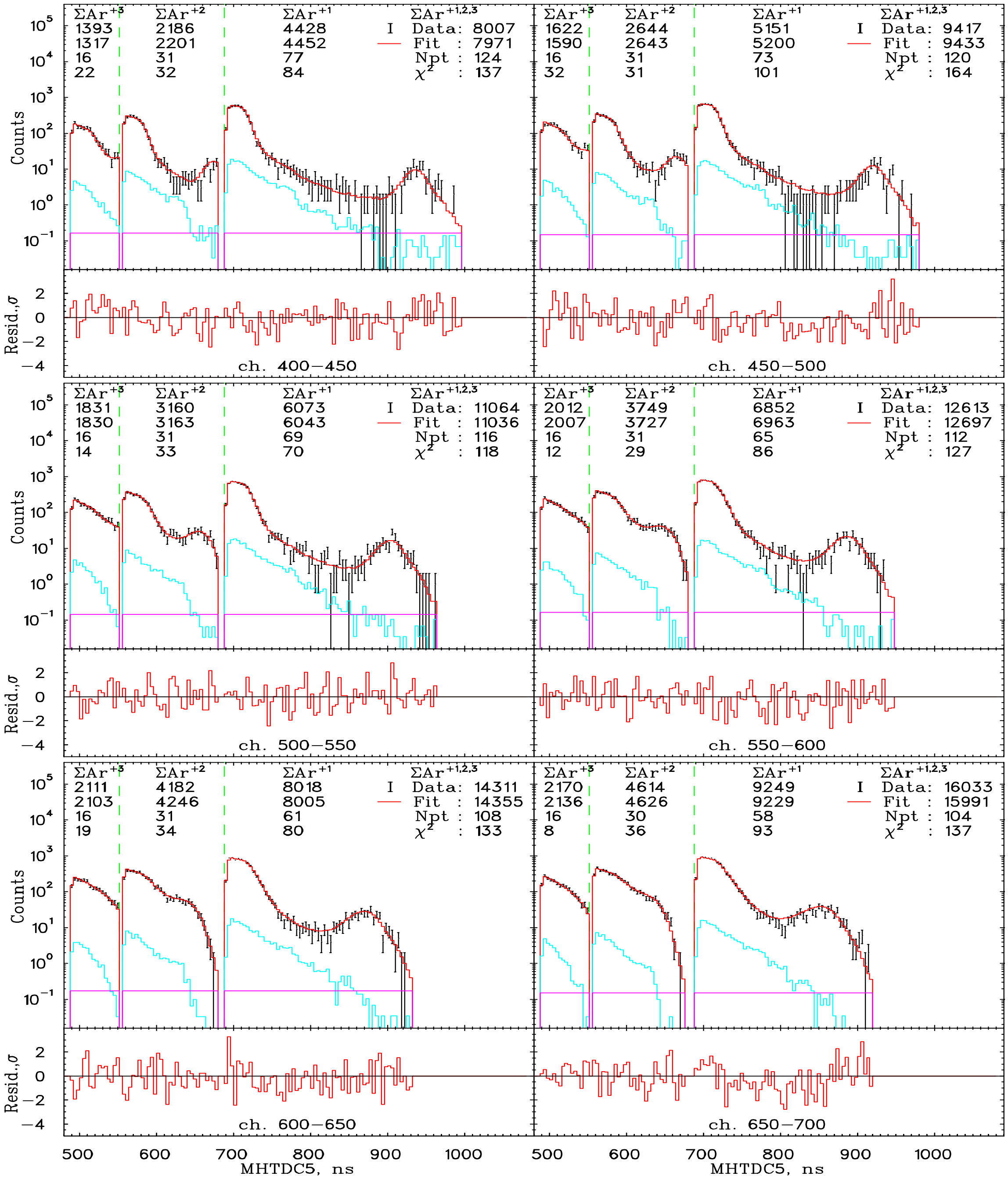

FIGURE 4.2: An example of the recoil TOF spectra comparing data and simulation for the ADC channel range 200−1550 with $L = R = 0$ continued (see Fig 4.1 caption). Shown here is the ADC channel range 400−700.

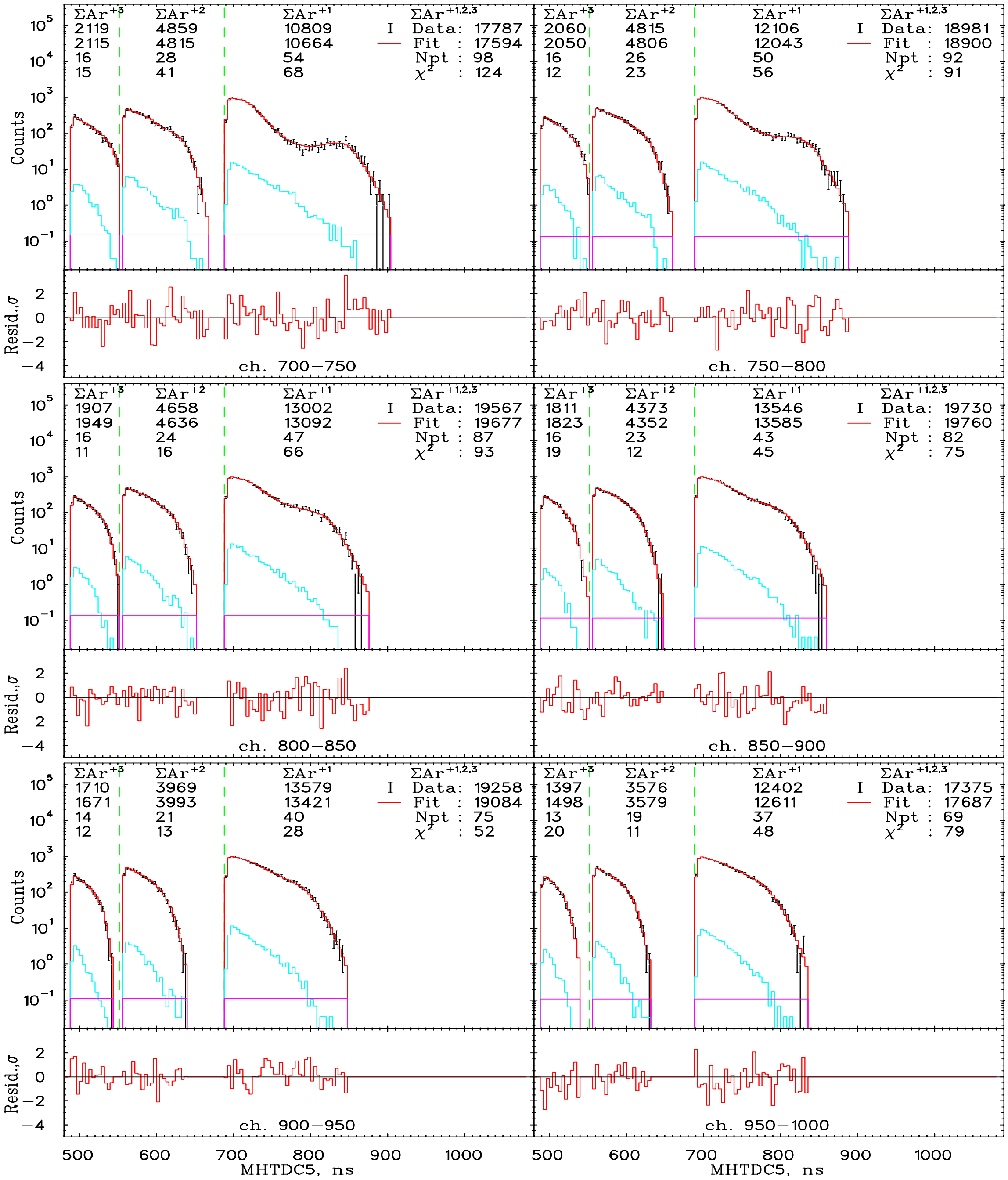

FIGURE 4.3: An example of the recoil TOF spectra comparing data and simulation for the ADC channel range 200−1550 with $L = R = 0$ continued (see Fig 4.1 caption). Shown here is the ADC channel range 700−1000.

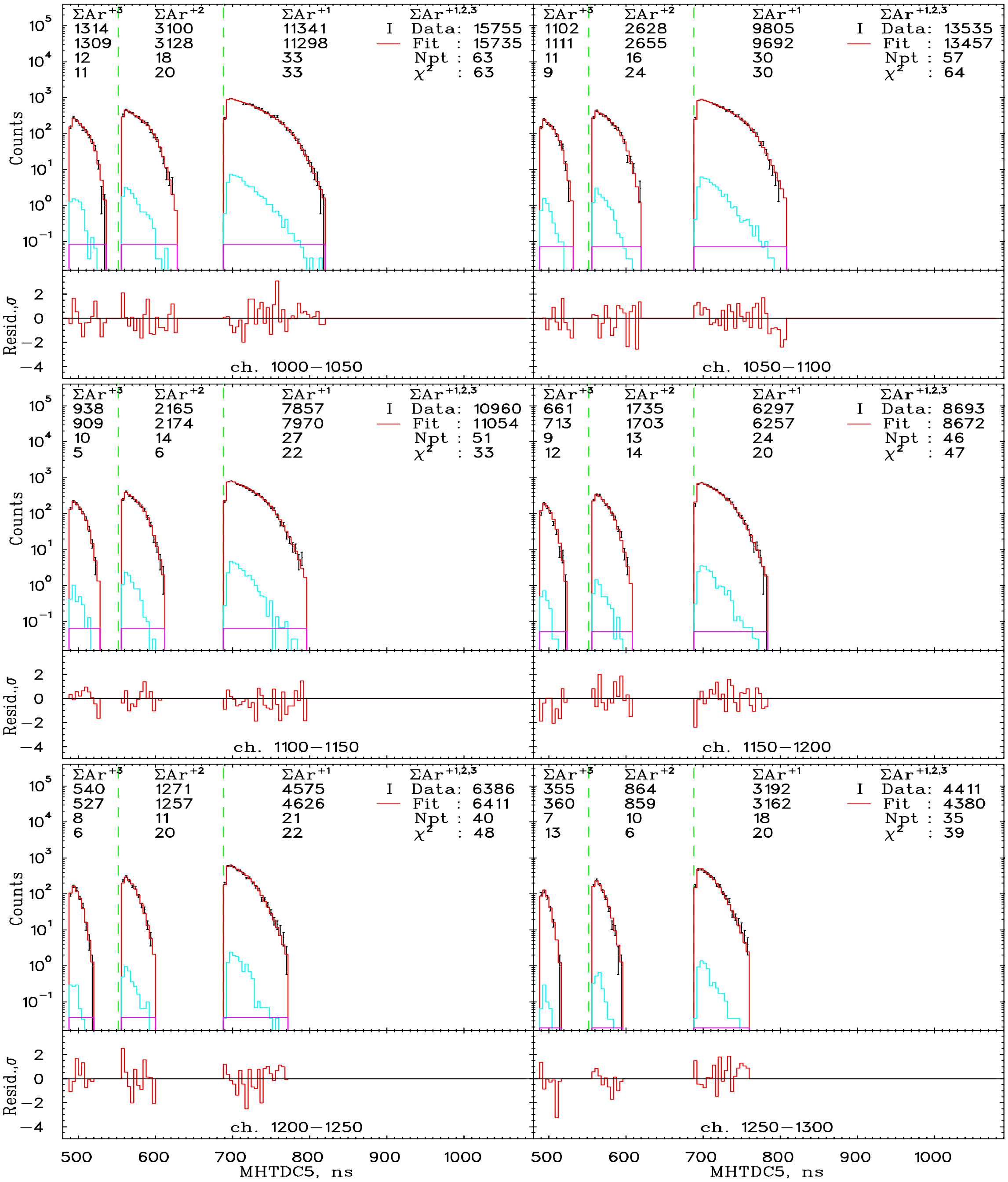

Figure 4.4: An example of the recoil TOF spectra comparing data and simulation for the ADC channel range 200−1550 with $L = R = 0$ continued (see Fig 4.1 caption). Shown here is the ADC channel range 1000−1300.

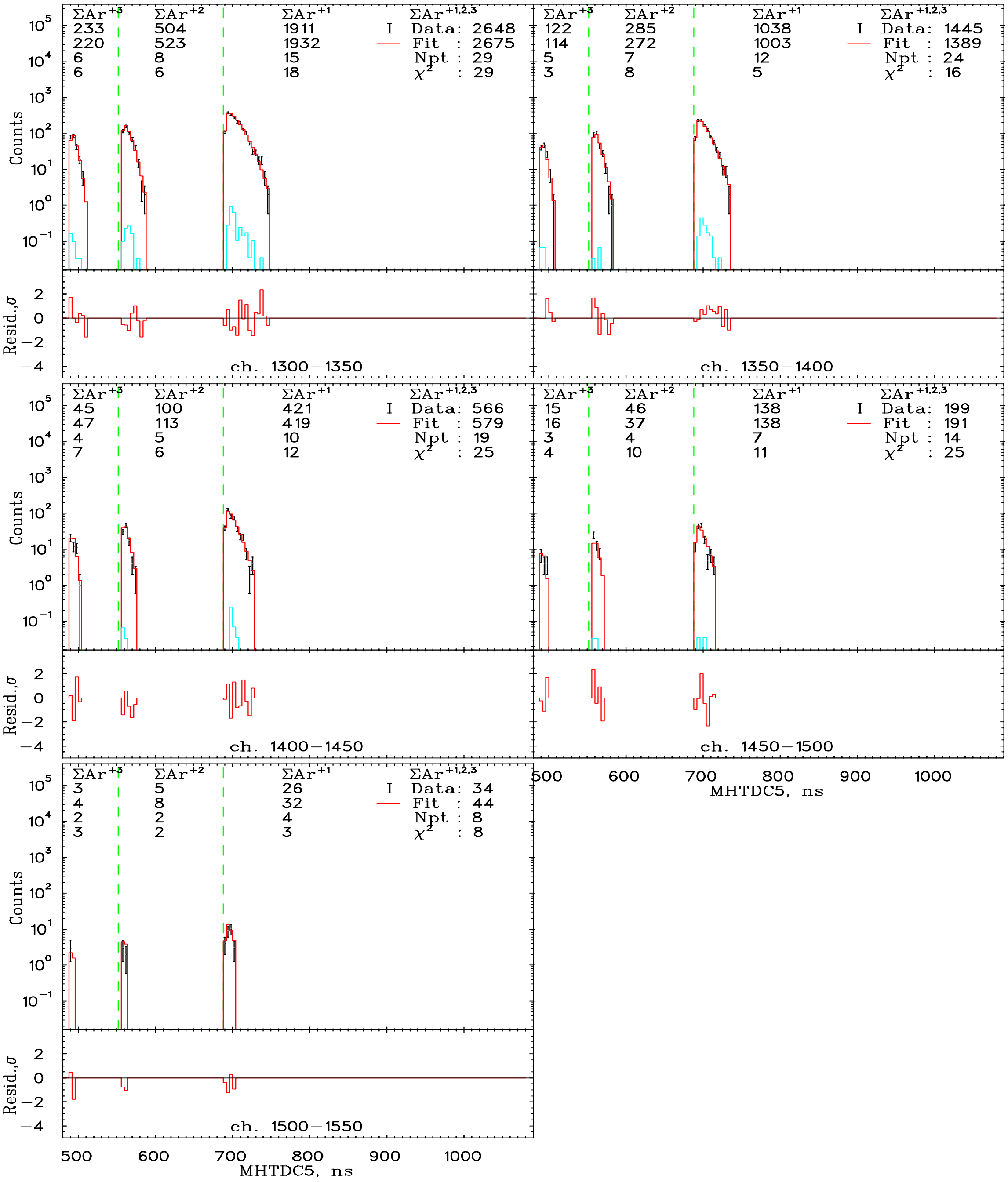

FIGURE 4.5: An example of the recoil TOF spectra comparing data and simulation for the ADC channel range 200−1550 with $L = R = 0$ continued (see Fig 4.1 caption). Shown here is the ADC channel range 1300−1550.

improvement in the quality of the fit for those ADC bins with Scin.ADC$\geq$750. To quantify this observation we show in Tab 4.2 the contributions to the total $\chi^2$ arising from the ADC channel ranges 200−550, 550−750 and 750−1550. Further discussion of these results follows the account of searches for the optimum values of the $R$ and $L$ for the scintillator channel ranges 200−1550.

TABLE 4.2: Partial values of $\chi^2$ for the indicated ADC channel range from the fit presented in Figs 4.1−4.5 ($L = R = 0$).

| Channels | *Npt* | $\Sigma\chi^2$ | $CL$ |
|---|---|---|---|
| 200−550 | 900 | 1037 | ∼0.1% |
| 550−750 | 422 | 521 | ∼0.07% |
| 750−1550 | 791 | 787 | ∼50% |

### 4.1.1 $\chi^2(L, R)$ for scintillator ADC channel range 200−1550.

Simulations of the data presented in Figs 4.1−4.5 were repeated as a function of $L$ and $R$. (The decay rate (4.1) depends only on $|R|$, results are presented for $R \geq 0$.) The resulting values of $\chi^2$ are illustrated in the contour plot presented in Fig 4.6 based on fits at each of the points shown. The minimum value of $\chi^2$ is 2340.9 which occurs at $L = -0.022$ and $R \simeq 0.000$. The corresponding Confidence Level is 0.032% for 2111 degrees of freedom. If one uses the $\chi^2 + 1$ contour to define the $1\sigma$ limits then $L = -0.022(9)$ and $|R| < 0.048$. The corresponding limits on the correlation parameters are

$$a \geq 0.9987, \ b = 0.022(9) \tag{4.5}$$

Although in Fig 4.6 $\chi^2_{min}$ is lower than $\chi^2(L = R = 0)$ by 4.5 a detailed comparison of the Data and Fit with $L = -0.022$ and $R = 0$ is hardly distinguishable from that shown in Figs 4.1−4.5 and provides no additional insight. The contributions to $\chi^2_{min}$ from the scintillator ADC channel ranges 200−550, 550−750 and 750−1550 are 1034.7, 519.5 and 786.6 respectively which differ only marginally from those given in Tab 4.2.

We choose to reject the result presented in Fig 4.6 on the basis of the unacceptable quality of the fit ($CL = 0.032\%$) together with a clear indication that there is some systematic discrepancy between the simulation and the data for the scintillator ADC channels < 750.

It is possible that the deficiency is in the GEANT3 based Monte Carlo simulations of the beta telescope response which becomes increasingly sensitive to the "tail" of the response at lower beta energies. This problem might account for the failure to obtain an acceptable fit for the energy of the scintillator with double coincident events when including events with the scintillator ADC channels < 750. (As mentioned in Sec 3.4, however, the "doubles" in this region may also be distorted by an inadequate account of the backgrounds.)

Inspection of Figs 4.1−4.5 also indicates that for the higher beta energies the separation of the $Ar^{+1}$, $Ar^{+2}$ and $Ar^{+3}$ recoil distributions is complete and that, even for $Ar^{+1}$ ions, all recoils coincident with the betas in the telescope are collected. Increasingly with lower observed beta energy the recoil distributions overlap and, particularly for the $Ar^{+1}$ ions, a "dip" forms in the middle of the recoil TOF distribution as the result of ions passing outside the 12.0 mm radius defined by the collimator on the MCP. Although these effects are included in the Monte Carlo, the consequences are regions in the MHTDC5 distributions where the simulations are particularly sensitive to both the contribution of the scattered background and the tail of the beta response.

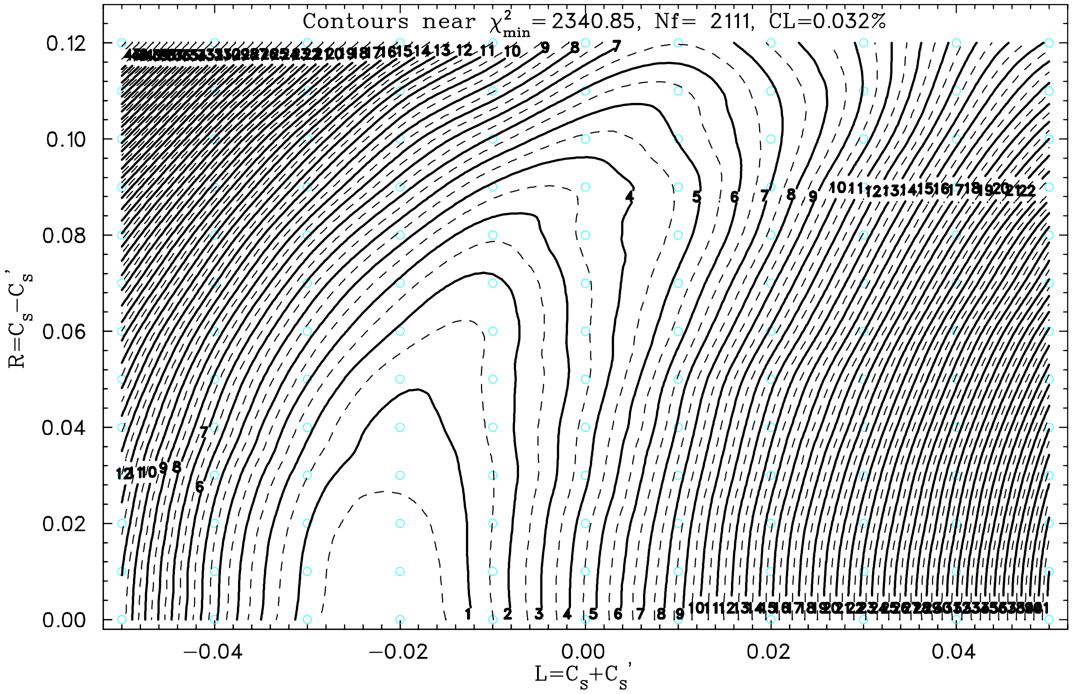

FIGURE 4.6: Contour plot of $\chi^2$ as a function of $L$ and $R$ for the ADC channel range 200−1550. The contours are labeled with respect to the minimal value of $\chi^2_{min} = 2340.85$. The $\chi^2$ changes by 1 between the solid contours and by 1/2 between solid and dashed.

### 4.1.2 $\chi^2(L, R)$ for scintillator ADC channel range 550−1550.

The contour plot of $\chi^2$ as a function of $L$ and $R$ for the ADC channel range 550−1550 is shown in Fig 4.7. The best fit occurs at $L = -0.015$ and $|R| = 0.011$ with $\chi^2_{min} = 1306.0$ which, for 1211 degrees of freedom, corresponds to a Confidence Level of 3.0%. The $\chi^2 + 1$ contour would define the limits $-0.026 \leq L \leq 0.016$ and $|R| \leq 0.097$ with significant mutual correlation of these two parameters. As in the case of the fits for the ADC channel range 200−1550, the quality is excellent ($CL \sim 50\%$) in the range 750−1550 but notably worse ($CL \sim 0.1\%$) below ch. 750. On this basis we choose to also reject the result presented in Fig 4.7.

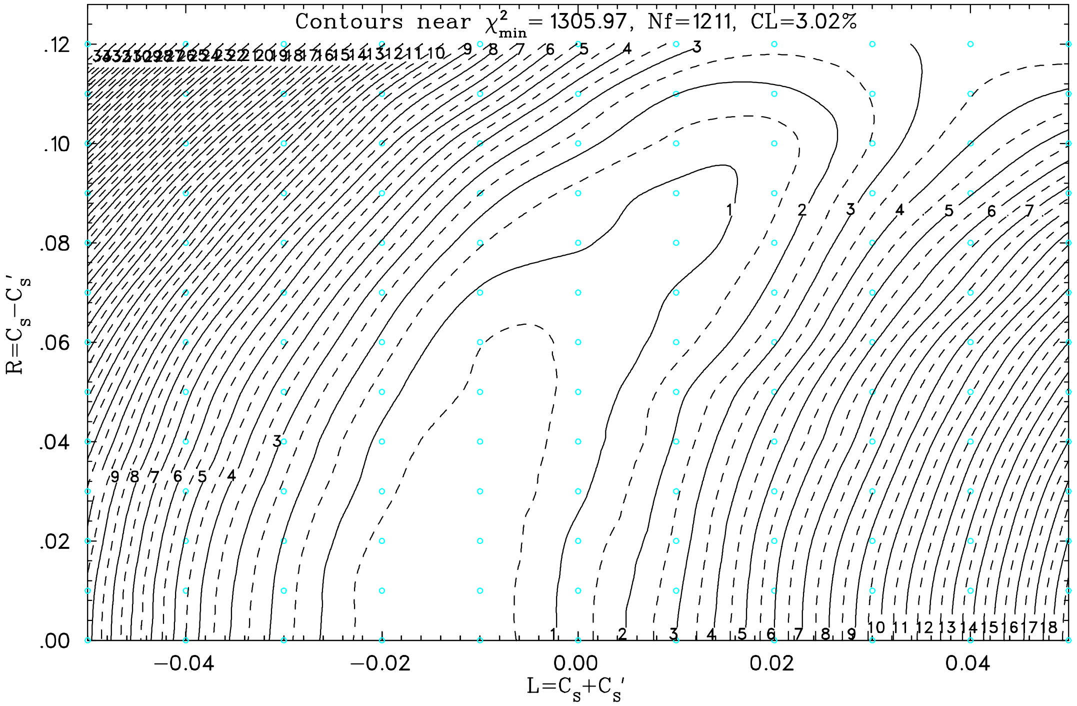

FIGURE 4.7: Contour plot of $\chi^2$ as a function of $L$ and $R$ for the ADC channel range 550−1550. The contours are labeled with respect to the minimal value of $\chi^2_{min} = 1305.97$. The $\chi^2$ changes by 1 between the solid contours and by 1/2 between solid and dashed.

### 4.1.3 $\chi^2(L, R)$ for scintillator ADC channel range 750−1550.

The contours of equal $\chi^2$ as functions of $L$ and $R$ for ADC channels 750−1550 (which corresponds to observed beta energies higher than 2.4 MeV) are shown in Fig 4.8 for the limited range $-0.05 \leq L \leq 0.05$ and $|R| \leq 0.12$. In contrast to the situation shown in Figs 4.6 and 4.7, the quality of the fit is excellent ($\chi^2_{min} = 787.51$ for 789 degrees

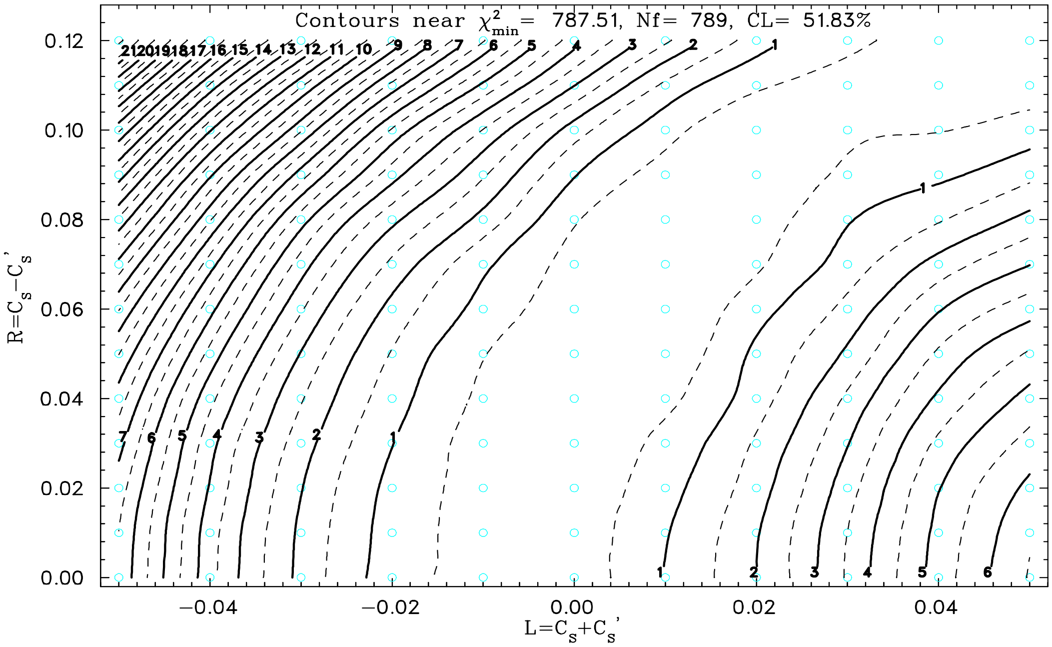

FIGURE 4.8: Contour plot of $\chi^2$ as a function of $L$ and $R$ for the ADC channel range 750−1550. The contours are labeled with respect to $\chi^2_{min} = 787.51$. The $\chi^2$ changes by 1 between the solid contours and by 1/2 between solid and dashed.

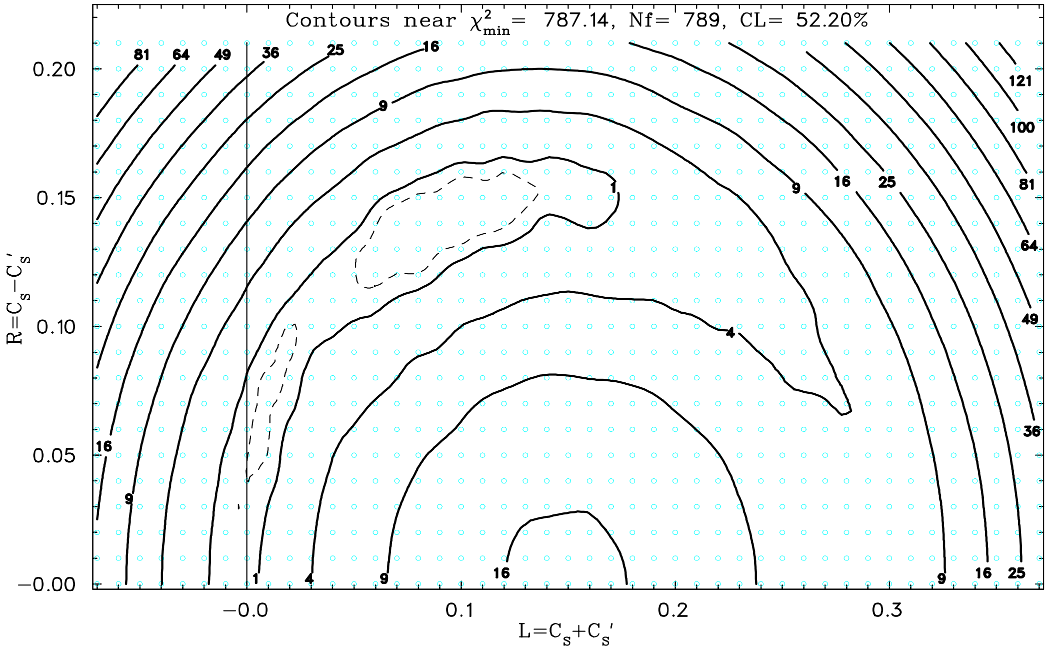

FIGURE 4.9: Contour plot of $\chi^2$ as a function of $L$ and $R$ for the ADC channel range 750−1550 over an extended range of $L$ and $R$.

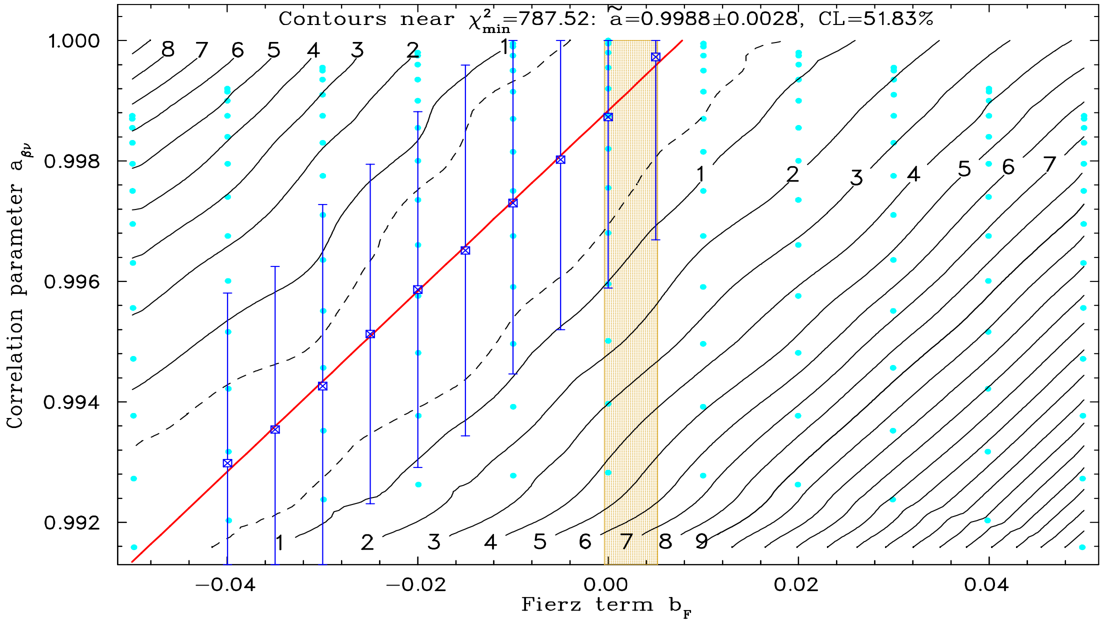

Figure 4.10: Contours of $\chi^2$ as function of $b$ and $a$ labeled with respect to the $\chi^2_{min} = 787.51$. The $\chi^2$ changes by 1 between the solid contours and by 1/2 between solid and dashed. The red line exhibits the correlations between the optimum values of $a$ and $b$ with $\tilde{a} = 0.9988$ (see text). The error bars plotted along this line correspond to the limits $\tilde{a} = 0.9988 \pm 0.0028$. The yellow band corresponds to the limits given by Savard [120], $b = 0.0024(28)$.

of freedom, $CL = 51.8\%$).

Eliminating the lower positron energies from the analysis, however, results in very strong correlations between the optimum values of $L$ and $R$ with acceptable fits extending well beyond the range shown in Fig 4.8. A similar (but weaker) correlation has been mentioned with reference to Fig 4.7 and is also evident for higher $\chi^2$ contours in Fig 4.6. The full extent of these correlations is exhibited in Fig 4.9. Over this wider range in the parameters $\chi^2_{min} = 787.14$ (which is marginally lower) and occurs for $L = 0.09$ and $R = 0.14$. The $\chi^2$ contours shown in Fig 4.9 ($\chi^2_{min} + 1,\ +4,\ +9\ \ldots$) define the $1\sigma$, $2\sigma$, $3\sigma$ statistical uncertainties in the limit that systematic uncertainties are neglected. The $1\sigma$(stat) contour clearly includes the region near $\chi^2 = 787.5$ shown in Fig 4.8.

It should be emphasized that the fits shown in Fig 4.9 are all based on the standard input parameters listed in Tab 4.1. Although most of these parameters were obtained from analysis of the $\beta -$ Ar recoil coincidence data assuming values of the $\beta - \nu$ correlation parameters very close to the Standard Model values ($a = 1.0,\ b = 0.0$), care was taken to choose conditions for which the sensitivity of the parameters to modest changes in these values is negligible. If, however, one considers the point

$L = 0.30$, $R = 0.00$ (hence, $a = 0.956$, $b = -0.29$) and repeats with these values the fit of the slope of the energy calibration from the data shown in Fig 3.36 the result is a *Slope* $= 291.38(15)\,\mathrm{ch/MeV}$ obtained with $\chi^2 = 43.5$. Serious consideration of the full $(L, R)$ parameter space shown in Fig 4.9 cannot be based on the single value of $291.92\,\mathrm{ch/MeV}$ for the *Slope*. In fact, (for $L = 0.30, R = 0$) the data shown in Fig 3.36 is compatible with the "best" linear calibration at a confidence level of only 1.2%. Even for the point ($L = 0.09$, $R = 0.14$, e.g. $a = 0.986$, $b = -0.089$) the data shown in Fig 3.36 gives a slope of 291.75(15) with $\chi^2 = 24.9$.

As is discussed below in connection with Fig 4.10, a reanalysis of the present data for the ADC channel range 750−1550 to accommodate the full $(L, R)$ parameter space shown in Fig 4.9 is not attempted because of the existing limits on the value of $b$ derived from analysis of superallowed $0^+ \rightarrow 0^+$ beta decay within the Conserved Vector Current hypothesis for nuclei from $^{10}$C to $^{74}$Rb [37, 120].

The correlations between the optimum values of $L$ and $R$ evident in Fig 4.8 are also seen in Fig 4.10 showing $\chi^2(a, b)$ for the equivalent range in these parameters. The sensitivity to the parameter $b$ (or $L$) is dramatically reduced by essentially restricting $T_\beta > 2.5\,\mathrm{MeV}$ and hence $m_e/E_e < 0.20$. The correlation between $a$ and $b$ can be exhibited by defining a "reduced" correlation parameter [34]:

$$\tilde{a} = a/(1 + b\,\langle\frac{m_e}{E_e}\rangle), \tag{4.6}$$

where $\langle E_e\rangle$ is effectively an average of the positron total energy for the events included in the fit.

In Fig 4.10 the red line corresponds to $\tilde{a} = 0.9988$ and $\langle E_e\rangle = 3.40\,\mathrm{MeV}$ where these values are chosen to best correspond to $\chi^2_{min}$ as a function of $a$ and $b$. Also shown in Fig 4.10 are the limits

$$\tilde{a} = 0.9988 \pm 0.0028,\ \langle E_e\rangle = 3.40\,\mathrm{MeV},\ \langle\frac{m_e}{E_e}\rangle = 0.1503, \tag{4.7}$$

which coincide well with the contours $\chi^2 = \chi^2_{min} + 1$ and hence define the $1\sigma$ statistical error.

The results presented in Fig 4.10 are consistent with a range of negative values for $b$. The data do impose a limit, however, on positive values of $b$ because of the upper limit on the allowed values of $a$ (Eq 4.3). From Fig 4.10 the $1\,\sigma$ limit is

$$b < 0.023\ . \tag{4.8}$$

(This limit is also evident in Fig 4.8 and corresponds to $L > -0.023$.)

The most recent published limits, $b = 0.0024(28)$ [120] derived from analysis of superallowed $0^+ \rightarrow 0^+$ beta decay within the Conserved Vector Current hypothesis are shown in Fig 4.10. The specific values are likely to change both as a result of ongoing experimental measurements and further analysis of the isospin-symmetry breaking corrections [121]. In terms of the analysis presented in Fig 4.10, however, it would seem reasonable to conclude that values of $|\, b \,| > 0.05$ can be neglected. Moreover, combining specific limits on $b$ from other sources with the analysis presented in Fig 4.10 is straightforward. As an example, if the limits in Fig 4.10 are combined with the result (4.7) one would obtain

$$\begin{aligned} a &= \tilde{a}\,(1 + b\,\langle \frac{m_e}{E_e} \rangle) \\ &= (0.9988 \pm 0.0028)[1 + 0.1503\,(0.0024 \pm 0.0028)] \\ &= 0.9992 \pm 0.0028\ . \end{aligned} \tag{4.9}$$

## 4.2 Evaluation of the systematic errors.

Our method of analysis of the angular correlations relies on knowledge of several observables which have been defined independently, included in the Monte Carlo model and used in the simulations. From all of them we have selected those which have the strongest effect on the angular correlation evaluation:

- electric field strength and uniformity;
- parameters of the energy calibration of the beta telescope;
- shape of the response function of the beta telescope;
- MCP efficiency as a function of the recoil incident angle and energy;
- uncertainties in defining the MHTDC5 reference time ($t_0$) and the transverse trap location ($x_0, y_0$);
- dependence of the ionization probability on initial recoil energy.

By assuming these systematic effects where independent, we evaluate them using:

$$\sigma_a^i = \frac{da}{dp_i}\,\sigma_{p_i}\ , \quad \frac{da}{dp_i} = \frac{a(p_i + \sigma_{p_i}) - a(p_i - \sigma_{p_i})}{2\sigma_{p_i}} \tag{4.10}$$

where $da/dp_i$ is the derivative of the angular correlation on the particular $i^{th}$ parameter included in the MC, and $\sigma_i$ is the accuracy of definition of this parameter.

### 4.2.1 Effects due to electric field strength uncertainties.

We have estimated the electric field strength using the fits of the front edges of $\mathrm{Ar}^{+1}$, $\mathrm{Ar}^{+2}$ and $\mathrm{Ar}^{+3}$ TOF spectra in the Sec 3.7.1. These values are defined independently of angular correlation parameter, because in this analysis we considered just fast recoils and ignored slow ones. The resulting value $U = 807.70\,\mathrm{V/cm}$ has been defined with accuracy $\sigma_U = 0.12\,\mathrm{V/cm}$ (3.14). In order to evaluate the effects of the electric field strength uncertainties on the angular correlation estimate, we have changed the field by $\sigma_U$ in both directions and fitted the 2D spectra in the ADC channel range $750-1550$ with the Fierz term fixed at $b=0$ and varying the correlation parameter $a$ to obtain the best fit values shown in the Tab 4.3.

TABLE 4.3: The best fit values of the angular correlation parameter $a$ evaluated for the extreme values of the electric field strength with $b = 0$.

| $E$-field [V/cm] | Correlation parameter $a$ |
|---|---|
| $U - \sigma_U = -807.82$ | $0.9976 \pm 0.0030(stat)$ |
| $U + \sigma_U = -807.58$ | $0.9999 \pm 0.0030(stat)$ |

The systematic error is evaluated according expression (4.10) as

$$\sigma_a^U = \frac{a(U+\sigma_U) - a(U-\sigma_U)}{2\sigma_U}\,\sigma_U = 0.0012 \tag{4.11}$$

### 4.2.2 Effects due to electric field non-uniformity.

In Sec 3.7.5 we have found values of the electric field strength and gradient which simultaneously satisfy measured TOFs of both photoionized K atoms and Ar ions (Eq 3.19). In order to evaluate the effects of possible field non-uniformity on the angular correlation estimates we fitted 2D TOF−Scin.ADC data spectra with a Monte Carlo which has a shape of the electric field from Eq 3.17 with a set of field gradients (the relationship between $U_0$ and $U_z$ is defined by Eq 3.18) and found, as shown in Fig 4.11, the derivative of the correlation parameter $a$ on the field gradient (with $b = 0$):

$$\partial a / \partial U_z = 0.0021\,\mathrm{cm}^2/\mathrm{V}\ .$$

In Tab 4.4 we show the fitted value of $a$ for value of $U_z$ that best accounts for the $^{38\mathrm{m}}\mathrm{K}^{+1}$ photoions (3.19) and for the estimated limits on $U_z$ (3.20). One sees that, considering the statistical errors, the value of the correlation parameter corresponding

FIGURE 4.11: Derivative of the correlation parameter as function of the electric field gradient evaluated with $b = 0$.

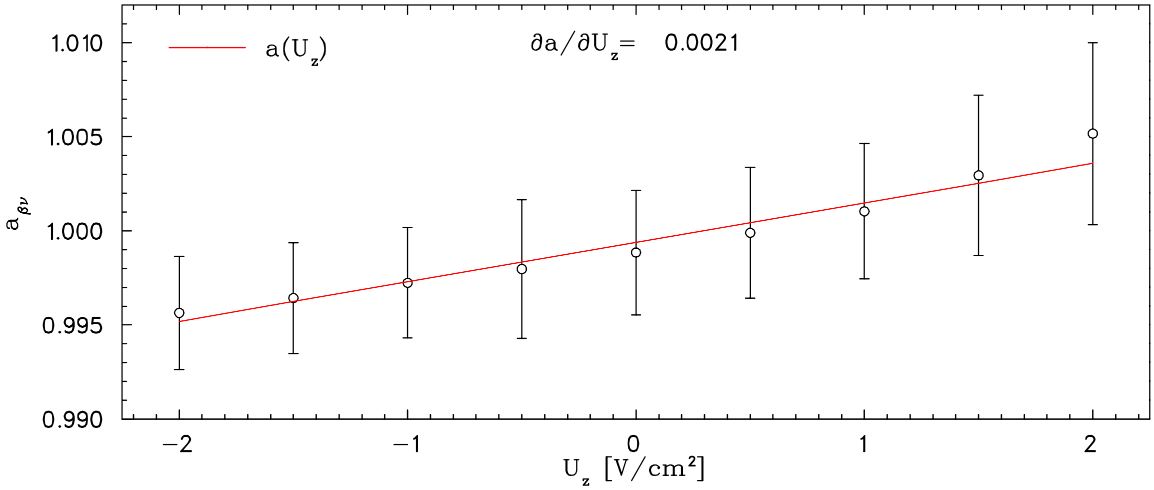

TABLE 4.4: The best fit value of $a$ in the presence of an electric field gradient with $b = 0$ (see text).

| $U_z$ [V/cm$^2$] | $U_0$ [V/cm] | $a$ |
|---|---|---|
| $-0.76$ | $-808.71$ | $0.9978 \pm 0.0029(stat)$ |
| $-0.32$ | $-808.17$ | $0.9987 \pm 0.0028(stat)$ |
| $+0.12$ | $-807.52$ | $0.9997 \pm 0.0028(stat)$ |

to the central values of the field and field gradient from this table is practically indistinguishable from the estimate with uniform field $U_0 = -807.70\,\mathrm{V/cm}$. This allows us to write for the error due to the possible field non-uniformity:

$$\sigma_a^{U_z} = \pm 0.0010 \tag{4.12}$$

### 4.2.3 Systematic errors due to the scintillator energy calibration.

The accuracy of determination of the parameters of the beta detector energy calibration namely *Offset* $= 50.663(1)$ and *Slope* $= 291.92(16)$ allowed us to neglect uncertainties in the *Offset* because its relative error is less than $10^{-5}$. The effects of uncertainties in the *Slope* were estimated by evaluating the $\beta - \nu$ angular correlation parameter for zero Fierz term using the nominal *Offset* $= 50.663$ and extreme values of the calibration slope. The numerical results are collected in the Tab 4.5, with which the systematics due to the calibration uncertainties can be calculated as

$$\sigma_a^{cal} = (1.0004 - 0.9972)/2 = 0.0016 \tag{4.13}$$

TABLE 4.5: Angular correlations for extreme values of calibration slope.

| *Slope* | $a$ | *DF* |
|---|---|---|
| 291.76 | 0.9972 | 789 |
| 292.08 | 1.0004 | 789 |

### 4.2.4 Positron detector response function shape: low energy tail.

As we have calibrated our beta detector with the data collected in the experiment, adequate modeling of the beta detector response function plays an important role in both the calibration and then in the evaluation of the angular correlation coefficient. We have had a possibility to verify the shape of the response function using the triple coincident events associated with slow $\mathrm{Ar}^{+1}$ recoils when fast and slow recoils are completely separated in TOF. These events can be seen in the Fig 3.35 in the region with MHTDC5>800. Most of the events below the slow recoil ridge represent cases of positron back scattering off the plastic scintillator surface and belong to the so called low energy tail of the scintillator response function (see for instance the parametrization in Ref [122], where the authors studied a very similar detector).

The TOF interval between the channels 800 and 920 has been divided into three and the corresponding scintillator detected positron energy spectra are shown in Fig 4.12. These spectra represent response functions integrated over a positron energy range of about 450 keV. (A narrower energy range could have been achieved with $\mathrm{Ar}^0$ recoils but this would involve their poorly known MCP detection efficiency.) These spectra are compared with the corresponding spectra from the simulations used in the correlation analysis. (The data and simulations are normalized to the same total over the full ADC channel range 200−1550 and TDC range 480−1080.)

We have defined the tails of the response as the part of the spectra with the condition

$$E = E_{bnd} < E_{max} - 2\sigma \ , \tag{4.14}$$

where $E_{max}$ corresponds to the energy at the maximum of the spectrum and $\sigma$ is evaluated by fits of the central part of the peaks with a Gaussian. The comparisons of

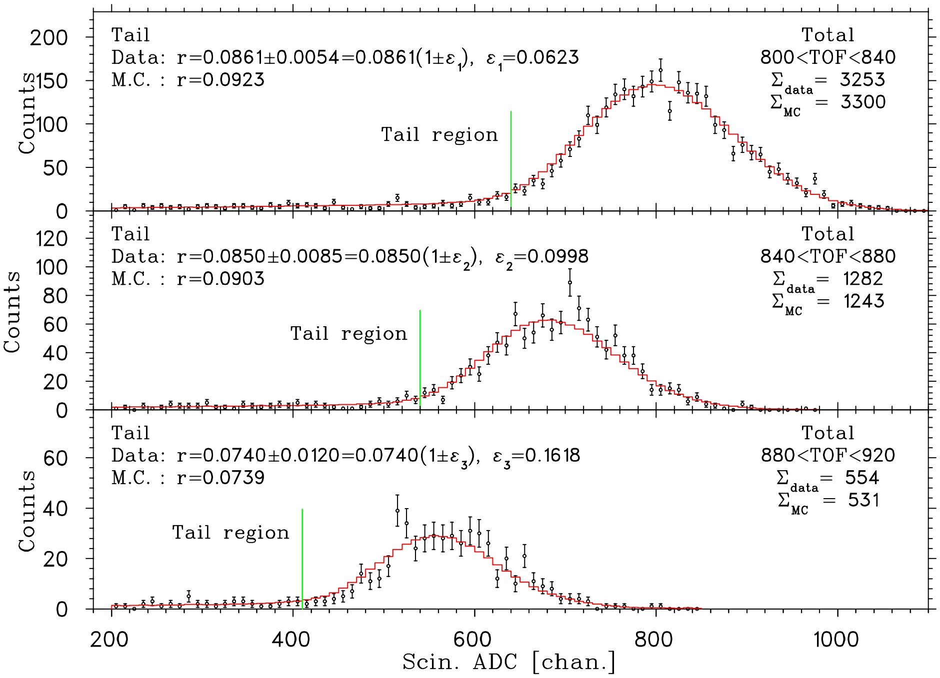

FIGURE 4.12: Comparison of the data and simulation for slow $Ar^{+1}$ recoil events. The relative contribution in the tail region is used to test the adequacy of the GEANT3 based response functions in this region (see text).

data and MC for each of the three MHTDC5 ranges are shown in Fig 4.12. Combining all three ranges with the weights defined by the data we obtain for the weighted average of the ratio of the data and simulations:

$$\left\langle \frac{(Tail/Total)_{data}}{(Tail/Total)_{MC}} \right\rangle = 0.943 \pm 0.047 \ . \tag{4.15}$$

The systematic error associated with the low energy tail of the GEANT generated response function can be evaluated as a product of the derivative of the angular correlation as function of the amplitude of the tail and the uncertainty in that amplitude. In order to evaluate the derivative we have artificially modified response functions by varying the amplitude in the region of the tail (4.14) by factors of 1.1, 1.05, 0.95 and 0.90. Examples of the response functions, generated by the GEANT based simulation program are shown on the upper panel of the Fig 4.13 with a normalization to unit area under the curves. The response modified in this way exhibits a "step" and needs to be smoothed. This has been done using a second order Savitzky-Golay filter with width of 15 data points (this filter conserves the area under the curve) in the region $E_{bnd} - 150\,\text{keV} < E < E_{bnd} + 100\,\text{keV}$ (10 keV between data points). In order to con-

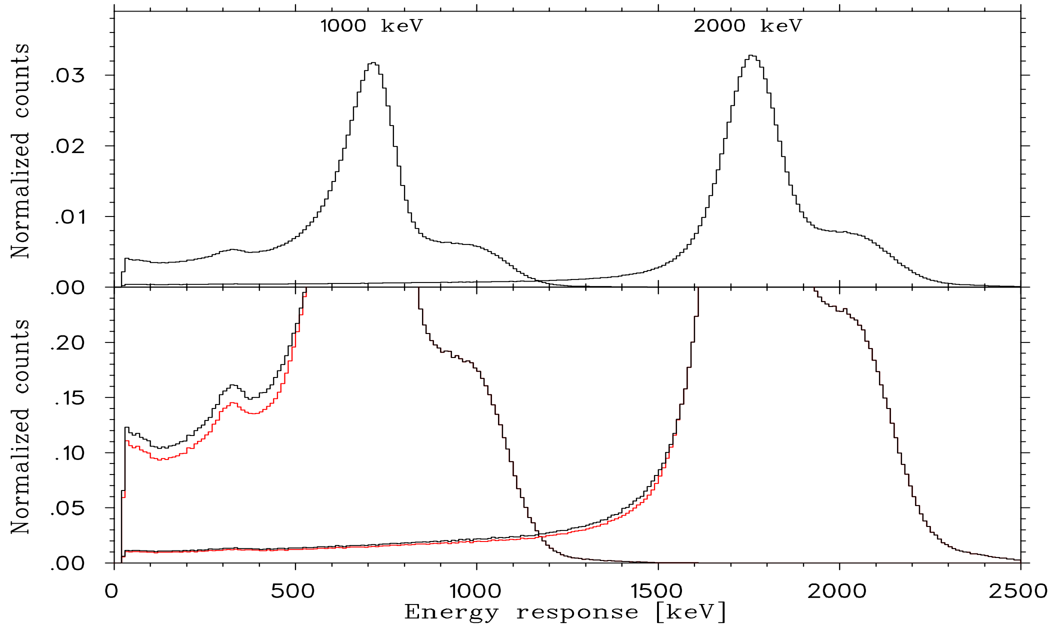

FIGURE 4.13: Upper panel: GEANT generated response of the scintillator for "non scattered" positrons of incident energies 1000 and 2000 keV. Lower panel: Original response functions (black) and those with the low energy tail reduced by 10% (red).

serve the efficiency defined in GEANT we have renormalized the resulting responses to the same area as the initial ones. In the lower panel of Fig 4.13 we depict the original GEANT scintillator responses and those with the tail reduced by 10% for positrons of incident energies 1000 keV and 2000 keV. (For plotting convenience we have normalized the responses to the same maximum value.)

The scintillator energy calibration used in the analysis of the triples data (Eq 3.26) is based on the fits to that data in 27 energy bins over the channel range 200−1550 including $\text{Ar}^{+1}$, $\text{Ar}^{+2}$ and $\text{Ar}^{+3}$ in a single time bin for $488 \leq \text{MHTDC5} \leq 1080$ (actually the kinematic cut removes the time bins 488−552, 680−688 and above 1068). As is shown in Fig 3.36 the dominant component in this fit results from the simulations of the fast Monte Carlo for the "response function" events.† Any modification of the response functions requires a refit of the data in Fig 3.35 to obtain an optimum value of the *Slope*. The results of such fits with *Tail* values 0.90, 0.95, 1.00, 1.05 and 1.10 are shown in columns 2−5 of Tab 4.6.

The same data (791 bins) for the scintillator channel range 750−1550 that resulted in value $\tilde{a} = 0.9988 \pm 0.0028(\text{stat})$ (Eq 4.7) using the original response functions is

---

† These events involve positrons emitted from the trap in the direction of the DSSD which pass through the Be window and then enter the central $22 \times 22\,\text{mm}^2$ area of the DSSD.

TABLE 4.6: Evaluation of the correlation parameter $a$ with modified response function tails. Calculations are performed with propagation of the tail changes through the linear calibration with $a = 1$ and $b = 0$. The results of calibration fits over ADC channels 200−1550 with modified tails are shown in the left side of the table. The calibration offset is fixed by the pedestal value *Offset* = 50.663.

| Calibration fits ($a = 1,\ b = 0$) | | | | | Evaluation of $a$ ($b = 0$) | | | |
|---|---|---|---|---|---|---|---|---|
| *Tail* | *Slope* | *DF* | $\chi^2$ | *CL* | $a$ | *DF* | $\chi^2$ | *CL* |
| 0.90 | 291.51(16) | 26 | 45.14 | 0.011 | 0.9962(25) | 790 | 791.26 | 0.481 |
| 0.95 | 291.72(16) | 26 | 29.38 | 0.294 | 0.9975(29) | 790 | 789.02 | 0.503 |
| 1.00 | 291.92(16) | 26 | 22.21 | 0.677 | 0.9988(29) | 790 | 789.09 | 0.502 |
| 1.05 | 292.12(16) | 26 | 23.04 | 0.631 | 1.0002(29) | 790 | 789.57 | 0.498 |
| 1.10 | 292.31(16) | 26 | 31.58 | 0.207 | 1.0014(29) | 790 | 792.51 | 0.468 |

used to estimate $da/dT$ from the analysis presented in columns 6−9 of Tab 4.6. For each value of the modified tail with the corresponding value of the *Slope* the quality of the fit ($\chi^2$) was calculated as function of $a$ with $b = 0$. The optimum value of $a$ is essentially a linear function of the relative amplitude of tail ($T$) with

$$\frac{da}{dT} = 0.026\ . \tag{4.16}$$

The analysis of the triples data with $800 \leq$ MHTDC $\leq 920$ presented in the Fig 4.13 is consistent with a modified *Tail/Total* ratio of 0.943±0.047. If the quality of the calibration fits ($488 \leq$ MHTDC5 $\leq 1068$) listed in column 4 of Tab 4.6 is used to estimate $T$, the result is

$$T = 1.020 \pm 0.025\ ,$$

and is rather insensitive to $b$. The lower estimate of $T$ is based on limited statistics and is in a kinematic region where the scattered background contributes ~10% to the fit. The region of the "tail" is, however clearly separated from the "peak". We conservatively combine the two estimates to suggest

$$T = 1.00 \pm 0.05\ ,$$

which together with (4.16) results in the error

$$\sigma_a^{tail} = 0.0013\,. \tag{4.17}$$

### 4.2.5 Positron detector response function shape: Compton summing of the 0.511 MeV annihilation gamma quanta.

In tests of Compton summing effects we have used an approach different from that for the low energy tail. That is because the behavior of the additional peak due to the Compton summing of the annihilation $\gamma-$quanta significantly differs from the low energy tail. Problems with separation of the low energy tail and full absorption peak occur for incident positron energies less than 1000 keV and detected energies less than 500 keV, i.e. in the range which is not very important in our analysis. The situation with Compton summing is opposite. Fig 4.14, where we present GEANT simulated normalized responses of the scintillator to mono-energetic positrons, shows that for incident energies above 2 MeV contributions from Compton and full absorption peaks are overlapping and the possibility to decrease or increase the contribution of the Compton summing into the response function (as was done for the low energy tail in the section 4.2.4) is very difficult.

In order to analyze the systematics due to possible uncertainties in accounting for Compton scattering of positron annihilation quanta we have parametrized the GEANT simulated scintillator response function in a way similar to reported in Ref [122] with components:

$$\begin{aligned} f(E) &= A_1 f_1(E, E_g, \sigma) + A_2 f_2(E, E_g, \sigma) + A_3 f_3(E, E_g, \sigma, k) \\ &\quad + A_4 f_4(E, E_g, \sigma, W) + A_5 f_5(E, E_g, \sigma, W) \end{aligned} \tag{4.18}$$

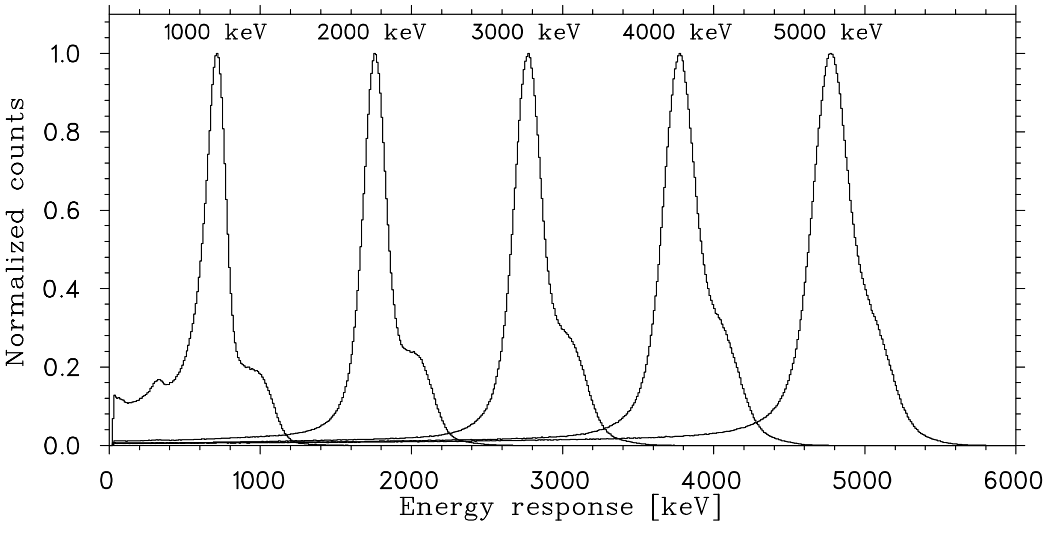

FIGURE 4.14: GEANT generated response lines of the scintillator for mono-energetic positrons (positron energy is shown above each graph). Lines are normalized to unit amplitude.

where the functions $f_{1,\ldots,5}$ are normalized to unit area and the coefficients $A_{1,\ldots,5}$ define the intensity of each component to best simulate the GEANT response. The functions $f_{1,\ldots,5}$ given in Appendix A are the same as in Ref [122]$^{\dagger}$.

We have fitted the GEANT simulated response functions with the expression (4.18) for a set of incident positron energies above 1.0 MeV and found the values of the coefficients $A_{1,\ldots,5}$, $\sigma$, $k$, and $W$ all as functions of $E_g$ which reproduce the best standard scintillator response functions. As is outlined in App A, the component $A_4 f_4$ is attributed to coincident summing between fully stopped positrons and energy deposited by Compton scattering of one of the subsequent annihilation quanta. The values of $A_4$ were increased (and reduced) by 5% and 10% to modify responses (which were renormalized to the original overall number of entries) resulting in the modified response functions.

Using these newly constructed response functions we have performed fits to to both the energy calibration data (ch. 200−1550) and the angular correlation data (ch. 750−1550) to find new calibration slopes and the corresponding values of $a$ (for $b = 0$) as shown Tab 4.7. There is a difference in the values of $a$ from the table and our best evaluation $a = 0.9988$ because the entries in the table are calculated using parametrized positron detector response functions (4.18). This parametrization was used to study changes of the angular correlation parameter only. The essential conclusion from Tab 4.7 is that if one includes the influence on the energy calibration, the effects of modest changes in the Compton summing on the fitted value of $a$ are very small. To be specific

$$\frac{da}{dC} = -0.002\ . \tag{4.19}$$

The very weak sensitivity of $a$ to the influence of Compton summing reduces the requirement for a stringent test of the GEANT simulation of this feature. Fig 4.15 shows the same "slow recoil" data as was used to test the low energy tail. For each spectrum we have calculated the ratio ($Toe/Total$) where $Toe$ has been defined by the conditions $E_{scin} > E_{bnd}$, $Count(E_{bnd}) = \exp(-1/2)\cdot MAX(Count)$ as is shown in Fig 4.15. The regions of $Toe$ are shown there in green. Combining all these ranges we obtain for the weighted average

$$\left\langle \frac{(Toe/Total)_{data}}{(Toe/Total)_{MC}} \right\rangle = 1.05 \pm 0.04\ .$$

---

[†] Despite the same form of parametrization of the functions $f_{1,\ldots,5}$ as in Ref [122] the parameters $E_g$ and $\sigma$ are somewhat different. In our case $E_g$ defines the centroid of the Gaussian component of the scintillator response and does not include the average energy loss (∼ 180 keV) in the preceding elements (Be foil, silicon DSSD and Teflon wrapping). The parameter $\sigma$ defines the width of the Gaussian which includes the influence of both the scintillator resolution and energy straggling of the positrons in the preceding elements.

TABLE 4.7: Calibration ($a = 1,\ b = 0$) of the scintillator ADC and evaluation of the correlation parameter $a$ with a modified Compton summing intensity and propagation of these modifications through the linear calibration (3.4) and (3.26).

| Calibration fits ($a = 1,\ b = 0$) | | | | | Evaluation of $a$ ($b = 0$) | | | |
|---|---|---|---|---|---|---|---|---|
| *Comp* | *Slope* | *DF* | $\chi^2$ | *CL* | $a$ | *DF* | $\chi^2$ | *CL* |
| 0.90 | 292.43(15) | 26 | 25.28 | 0.503 | 0.9967(26) | 790 | 789.01 | 0.503 |
| 0.95 | 292.14(15) | 26 | 28.75 | 0.323 | 0.9966(26) | 790 | 789.38 | 0.500 |
| 1.00 | 291.86(15) | 26 | 34.24 | 0.129 | 0.9966(25) | 790 | 789.98 | 0.493 |
| 1.05 | 291.59(15) | 26 | 41.33 | 0.029 | 0.9965(25) | 790 | 790.80 | 0.485 |
| 1.10 | 291.32(16) | 26 | 49.98 | 0.003 | 0.9963(25) | 790 | 792.17 | 0.472 |

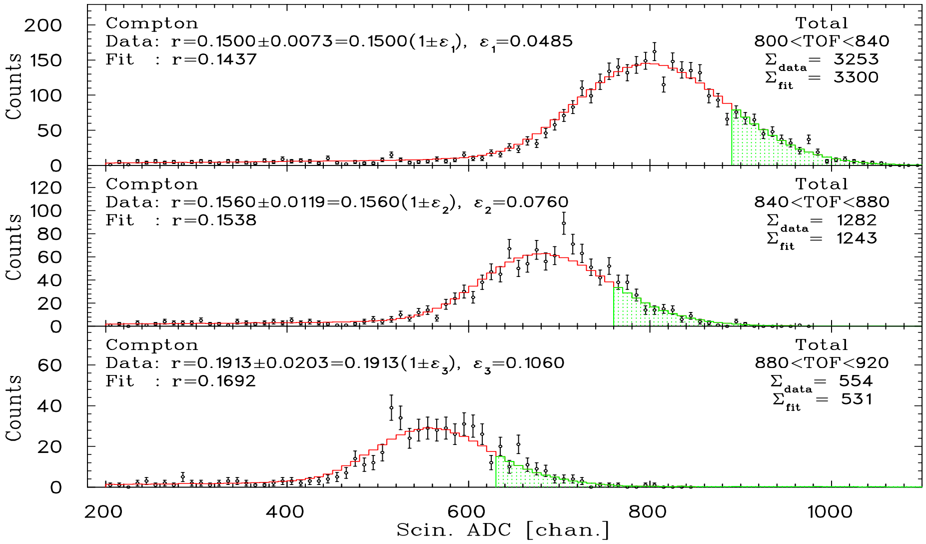

FIGURE 4.15: Comparison of the data and simulation for slow $\mathrm{Ar}^{+1}$ recoil events. The relative contribution of the highest energies is used to test the prediction of the Compton toe in the response functions (see text).

As was mentioned previously, the region of the toe is not well separated from the peak but we conclude that Compton summing is accounted for to within a factor of $\sim$10% and hence from (4.19) follows

$$\sigma_a^{toe} = 0.0002 \tag{4.20}$$

### 4.2.6 Effects of MCP efficiency dependence on incident recoil angle.

As was mentioned in Sec 3.8.4 in the data analysis we have assumed that the MCP detection efficiency for Ar ions does not depend on recoil impact angle. In order to check what systematic error may be associated with this assumption we have evaluated the correlation parameter $a$ for the case of angular dependence as described in Ref.[115] and shown in Fig 3.34. Introducing such a recoil impact angle efficiency dependence we have evaluated $\chi^2$ comparing the 2D TOF spectra from data and MC for a set of correlation parameter values (see Tab 4.8). The dependence of the $\chi^2$ as a function of the correlation parameter $a$ was fitted (see Fig 4.16) by a second order polynomial in both cases to find a minimizing value of correlation parameter $a = 0.9975$ in the presence of angular dependence. The shift $\Delta a = 0.0013$ we have

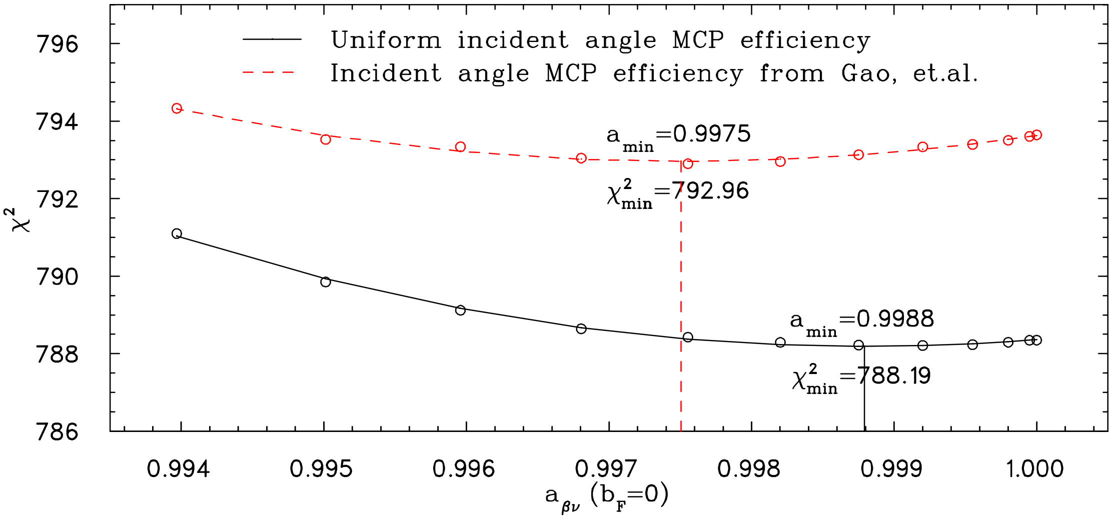

FIGURE 4.16: $\chi^2$ as function of $a$ $(b = 0)$ with uniform MCP detection efficiency as function of recoil impact angle and with the variation reported by Gao *et al.* in Ref [115] and shown in Fig 3.34.

TABLE 4.8: The dependence of $\chi^2$ on the correlation parameter (with $b = 0$) in the absence and presence (Ref [115]) of MCP detection efficiency $\varepsilon$ dependence on Ar ion impact angle shown in Fig 3.34.

| $a$ | $\chi^2$ $(\varepsilon_\theta = 0)$ | $\chi^2$ $(\varepsilon_\theta \neq 0)$ | $a$ | $\chi^2$ $(\varepsilon_\theta = 0)$ | $\chi^2$ $(\varepsilon_\theta \neq 0)$ |
|---|---|---|---|---|---|
| 0.99501 | 789.85 | 793.53 | 0.99920 | 788.21 | 793.33 |
| 0.99681 | 788.64 | 793.04 | 0.99980 | 788.29 | 793.50 |
| 0.99820 | 788.29 | 792.96 | 1.00000 | 788.35 | 793.64 |

considered as a systematic effect with simultaneous rise of $\chi^2$ by $\Delta\chi^2 = 4.77$ from 788.19 to 792.96. The reduction of the change of the correlation parameter to unit change in $\chi^2$ results in an estimate of the systematic error

$$\sigma_a^{\theta} = 0.0006 \ . \tag{4.21}$$

### 4.2.7 Effects of MCP efficiency dependence on incident energy.

The well known MCP detection efficiency dependence on the energy of incident charged particles [89, 123] may introduce bias in the evaluation of the correlation parameter. Indeed, such a dependence would change a detected ratio of fast (higher energy) and slow (lower energy) Ar ions with respect to the natural. We measured the MCP detection efficiency in the $\mathrm{Ar}^{+1}$ ion energy range 4.8−5.3 keV by comparing the rate of beta−recoil coincidences for four values of applied electric field and taking into consideration only events where fast recoils in the front edge of the $\mathrm{Ar}^{+1}$ TOF spectrum were detected. The resulting values were corrected for the corresponding recoil collection efficiency and measured beta decay rate. The measured MCP detection efficiency was found to be constant to accuracy 0.0060 and defines a statistically limited systematic error of the correlation parameter of

$$\sigma_a^{E_{Ar^{+1}}} = 0.0010 \ . \tag{4.22}$$

This error was found as a difference of best fit values of the correlation parameter $a$ $(b = 0)$ for constant and linearly dependent on recoil energy MCP detection efficiencies

$$\frac{d\varepsilon}{dE} = \frac{0.060}{5.3 - 4.8}\ \mathrm{keV}^{-1}.$$

The fits were performed using the MHTDC5−Scin.ADC 2D spectra of $\mathrm{Ar}^{+1}$, $\mathrm{Ar}^{+2}$ and $\mathrm{Ar}^{+3}$ ions simultaneously in the Scin.ADC range of channels 750−1550.

An alternative evaluation of an energy dependence of the MCP detection efficiency has been done using data known from the literature [89] and shown in Fig 3.33. We have fitted the points for Ar with an expression similar to that from [113] (results are depicted in the Fig 4.17) and found the relative change of detection efficiency for $\mathrm{Ar}^{+1}$ ions for incident energies of 4.8 keV and and 5.3 keV to be $\Delta\varepsilon/\varepsilon = 0.0011(50)$ which is compatible with our own evaluations.

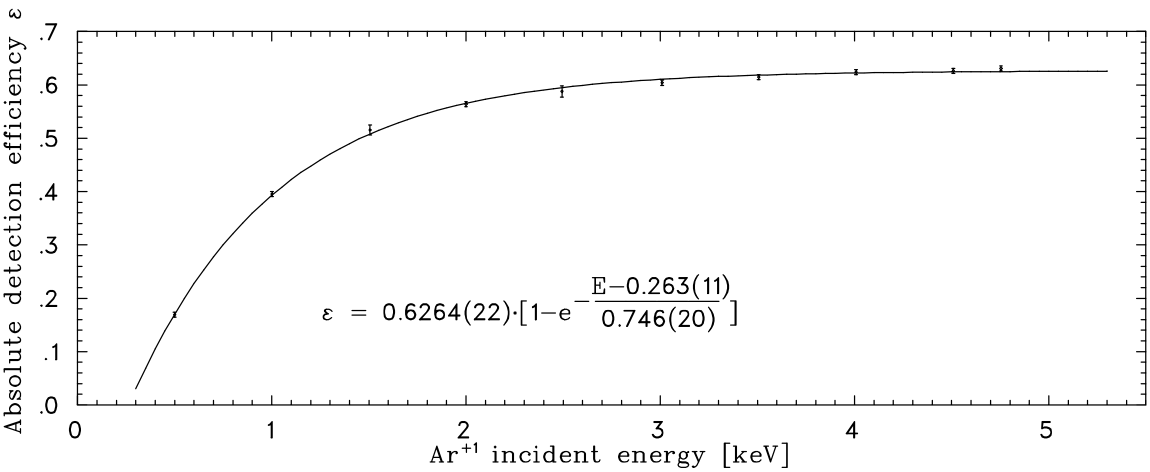

FIGURE 4.17: Fit of the $Ar^{+1}$ MCP detection efficiency as function of impact energy. Data are taken from Ref [89].

### 4.2.8 Systematic error due to the prompt peak position uncertainties.

The instant of the beta decay for each detected triple coincident event has been defined from an analysis of the prompt peak in Sec 3.5 as

$$t_0 = 113.42 \pm 0.17\,\text{ns} \ .$$

In order to evaluate effects of this uncertainty we have propagated it by re-evaluating for extreme values of $t_0$ the longitudinal trap position $z_0$ (using data with detection of $Ar^0$) and subsequently the effective uniform electric field strength $U_0$ (with ions $Ar^{+1}$, $Ar^{+2}$ and $Ar^{+3}$). The best fitting values of the correlation parameter $a$ ($b = 0$) are shown in Tab 4.9 and define its systematic error $\sigma_a^{t_0}$ as:

$$\sigma_a^{t_0} = 0.0009 \tag{4.23}$$

TABLE 4.9: Influence of the prompt peak uncertainties on $z_0$, $U_0$ and hence the correlation parameter.

| $t_0$ | $z_0$ | $U_0$ | $a$ |
|---|---|---|---|
| 113.25 | −0.0160 | −807.16 | 0.9997(30) |
| 113.42 | −0.0168 | −808.70 | 0.9988(30) |
| 113.59 | −0.0176 | −808.25 | 0.9979(30) |

### 4.2.9 Systematic errors due to the transverse trap position uncertainties.

The effect of the transverse trap position on the correlation parameter $a$ in our experiment arises due to the incomplete collection of the recoiling Ar ions. Monte Carlo simulations predict that, in coincidence with positrons of energies above 2.5 MeV with the trap on the detection axis, 84.53% of the $\mathrm{Ar}^{+1}$ ions hit the recoil detector. Any displacement of the trap off the axis results in a reduction of the percentage of $\mathrm{Ar}^{+1}$ ions collected. For example, for a displacement 0.5 mm this drops to 84.34%. We might expect that the fitted value of the correlation parameter would depend on the transverse trap position because of the different angular distributions of fast and slow recoils.

Despite the small errors in the transverse trap location obtained in Sec 3.8.3 one has to remember that the accepted RA calibration is done with a method which is not very sensitive to the calibration at the center of the MCP. For this reason we have decided to be conservative and estimate the uncertainty in the defined trap position to be $\sigma_r = 0.5\,\mathrm{mm}$. The systematic error due to the transverse trap position uncertainty was estimated as the difference between the value of $a$ for nominal trap location (see Tab 4.1) and its value evaluated with trap displaced by $\sigma_r = 0.5\,\mathrm{mm}$ radially. A fit of the correlation parameter for displaced trap resulted in $a = 0.9984$ which defined the corresponding systematic error

$$\sigma_a^{r_0} = \pm \left\{ \begin{array}{c} 0.0000 \\ 0.0004 \end{array} \right\} . \tag{4.24}$$

### 4.2.10 Electron shakeoff correction uncertainties.

The influence of a possible electron shakeoff correction on the angular correlation parameter has been evaluated using the same triple coincident data that was used to define the result $a = 0.9988(28)$ for a value of $b = 0$. The modifications to the simulations to include an electron shakeoff correction of the form (3.29) are described in Sec 3.11. They include defining the $\mathrm{Ar}^{+1}$ relative creation probability to be

$$p_1(T, s_1) = 0.3743 \cdot (1 - 0.76\, s_1) \cdot (1 + s_1 \frac{T}{T_{max}})$$

where $T$ is the initial recoil kinetic energy and $T_{max}$ is the maximum value (430 eV). With these modifications new fits of $a$ (with $b = 0$) were made for values of $s_1$ from 0.02 to 0.10. For each value of $s_1$ the values of $\chi^2(a, s_1)$ was fitted with a second order polynomial to obtain values of $\chi^2_{min}(s_1)$ and the corresponding values of $a_{min}$ which appear in Tab 4.10.

TABLE 4.10: Values of the fitted angular correlation parameter $a_{min}$ as a function of the shakeoff correction value $s_1$ for $\mathrm{Ar}^{+1}$ ($b = 0$).

| $s_1$ | $a_{min}$ | $\chi^2_{min}$ | $s_1$ | $a_{min}$ | $\chi^2_{min}$ |
|---|---|---|---|---|---|
| 0.00 | 0.9988(28) | 787.51 | 0.06 | 0.9918(28) | 801.60 |
| 0.02 | 0.9963(29) | 789.95 | 0.08 | 0.9894(29) | 809.89 |
| 0.04 | 0.9939(29) | 795.13 | 0.10 | 0.9873(28) | 819.86 |

The results presented in Tab 4.10 can be used to provide the only available direct experimental estimate of $s_1$. Fitting the values of $\chi^2_{min}(s_1)$ provides the estimate $s_1 = -0.028(22)$. This result is within $1.3\,\sigma$ of 0 but we regard negative values to be beyond the physically allowed range. Using the standard procedure for the estimate of an uncertainty when the best fit lies beyond the physically allowed region [124] we obtain a constraint on the value of the shakeoff correction.

$$s_1 = 0.000 \pm \left\{ \begin{array}{c} 0.013 \\ 0.000 \end{array} \right\} . \tag{4.25}$$

Considering the tabulated values of $a$ as a function of the corresponding values of $s_1$ we have calculated the derivative $da/ds_1 = -0.116$ which combined with (4.25) results in the systematic error due to the electron shakeoff correction uncertainties

$$\sigma_a^{s_1} = \pm \left\{ \begin{array}{c} 0.0000 \\ 0.0015 \end{array} \right\} . \tag{4.26}$$

The analysis presented in Fig 3.38 indicates that $\mathrm{Ar}^{+1}$ ions are created relative to the sum of $\mathrm{Ar}^{+2}$ and $\mathrm{Ar}^{+3}$ in the ratio $p_1/(p_2 + p_3) = 0.3743/0.1450$. The statistical uncertainty in this ratio is 0.41%. To estimate the influence of this uncertainty on the determination of $\tilde{a}$ the fits of $a$ (with $b = s_1 = 0$) were repeated with $p_1 = 0.3743 \pm 0.0015$. The result is an estimated contribution to the systematic error $\sigma_a^{p_1} = 0.00003$ which is considered negligible. The ratio of the relative creation probabilities of $\mathrm{Ar}^{+2}$ and $\mathrm{Ar}^{+3}$ ($p_2/p_3$) is determined (from the data shown in Fig 4.1−4.5) with a statistical precision of 0.7%. It is estimated that this uncertainty also has a negligible effect in the determination of $\tilde{a}$.

### 4.2.11 Summary of the systematic errors of the experiment.

As a result of the precision of the triple coincident data included in the analysis presented in Fig 4.10 the quantity $\tilde{a}$ is determined with a statistical uncertainty:

$$\tilde{a} = 0.9988 \pm 0.0028 .$$

For the range in the values of $b$ included in Fig 4.10, the systematic uncertainties in $\tilde{a}$ have been evaluated assuming $b = 0$. A summary of the contributions of all of the systematic errors discussed in this section is presented in Tab 4.11 where the independent errors are grouped in accordance with the source of the error. The last line of the table represents a quadratic sum of all entries and gives an estimate of the total systematic error.

TABLE 4.11: Summary of the significant uncorrelated systematic errors.

| Source of error | Value | Equation |
|---|---|---|
| **Applied electric field:** | | |
| field strength/trap width | ±0.0012 | 4.11 |
| field non-uniformity | ±0.0010 | 4.12 |
| **Beta Detector Response:** | | |
| energy calibration | ±0.0016 | 4.13 |
| line shape tail/total | ±0.0013 | 4.17 |
| 511 keV Compton summing | ±0.0002 | 4.20 |
| **Recoil detector efficiency:** | | |
| MCP incident recoil angle | ±0.0006 | 4.21 |
| MCP incident ion energy | ±0.0010 | 4.22 |
| **Prompt peak:** | ±0.0009 | 4.23 |
| **Transverse trap position:** | $^{+0.0000}_{-0.0004}$ | 4.24 |
| **Electron shakeoff dependence on $p_{\text{recoil}}$** | $^{+0.0000}_{-0.0015}$ | 4.26 |
| **Total systematic error** | $^{+0.0030}_{-0.0034}$ | |

The total systematic error given in Tab 4.11 is slightly asymmetric (essentially as a result of the "unphysical" estimate of the electron shakeoff correction). For the purposes of the future discussion we adopt the simpler (and in practice equivalent) result

$$\Delta\tilde{a} = \pm 0.0034(\text{syst}) \tag{4.27}$$

## 4.3 Results of the present experiment (assuming $\mathcal{I}m(L) = 0$).

The analysis of the experimental data and related systematics has revealed that in the evaluation of the beta−neutrino correlation parameter $a$ for the $^{38\mathrm{m}}\mathrm{K} \rightarrow {}^{38}\mathrm{Ar} + \mathrm{e}^{+} + \nu$ decay we can obtain a reliable result only if we restrict the analysis to events associated with the detection of positrons emitted with kinetic energies above 2.5 MeV. In this region of beta energies the sensitivity of the experiment to the Fierz term is suppressed by the factor $m_e/E \leq 0.16$ and as a result the recoil time of flight analysis keeps a sensitivity only to the reduced correlation parameter $\tilde{a}$ (Eq 4.7). The definition of $\tilde{a}$ reflects the measured correlations between $a$ and $b$ as shown in Fig 4.10.

Combining the results of the statistical analysis of the data (Eq 4.7) and the systematic uncertainties of the experiment listed in Tab 4.11 one derives for the reduced correlation parameter:

$$\tilde{a} = 0.9988 \pm 0.0028\,(\mathrm{stat}) \pm 0.0034(\mathrm{syst}) = 0.9988 \pm 0.0044 \tag{4.28}$$

In addition to the correlation between the values of $a$ and $b$ defined by (4.28), the data in Fig 4.10 can be used to place an upper limit on the value of $b$. Taking account of the statistical error only, that limit is $b < 0.023$. Including the systematic error on $\tilde{a}$ that result becomes

$$b < 0.035\ . \tag{4.29}$$

## Chapter 5

# Discussion of Present Results and Future Development.

### 5.1 Present Results.

The final result of the present experiment, as presented in Chap 4, can be expressed as

$$\tilde{a} \;=\; 0.9988 \pm 0.0028\,(\mathrm{stat}) \pm 0.0034(\mathrm{syst}) = 0.9988 \pm 0.0044$$

$$\text{where} \qquad \tilde{a} = \frac{a}{1 + 0.1503\,b} \tag{5.1}$$

This is the primary result of the experiment. In addition the data, when combined with the estimates of the systematic errors, can be used to place a limit on the value of $b$

$$b < 0.035 \; . \tag{5.2}$$

All of the quoted limits correspond to a 68% confidence level. These results are consistent with the predictions of the Standard Model ($a = 1, b = 0$) and, when statistical and systematic errors are combined, the primary result is ~33% more restrictive than the best previous $\beta - \nu$ experiment, the Seattle/Notre Dame/ISOLDE collaboration's study of the $\beta-$delayed proton decay of $^{32}$Ar [34] with the published result [†]

$$\tilde{a} = 0.9989 \pm 0.0052 \pm 0.0039, \; \tilde{a} = \frac{a}{1 + 0.1913\,b} \; . \tag{5.3}$$

Some care is needed in combining the results (5.1) and (5.3) because of the different values of $\langle m_e/E \rangle$ (0.1503 and 0.1913). In Tab 5.1 we present the estimates of $a$ for the two experiments for 3 values of $b$. For the range of values of $b$ included in Tab 5.1,

---

[†] This method depends strongly on the $Q-$value of the decay and mass re-measurements mean it should be re-evaluated [125]

TABLE 5.1: Combining the results of the present experiment and those of Adelberger *et al.* [34]. The values of $a$ (including systematic errors) are given for 3 values of $b$.

| $b$ | $a$ (68% $CL$) | | |
|---|---|---|---|
| | Adelberger *et al.* [34] | Present work | Combined |
| 0.00 | 0.9989(65) | 0.9988(44) | 0.9988(36) |
| −0.02 | 0.9951(65) | 0.9958(44) | 0.9956(36) |
| −0.04 | 0.9913(65) | 0.9928(44) | 0.9923(36) |

the results of the two experiments are completely compatible and there would appear to be no reason that the systematic error should be correlated. Hence, it is legitimate to quote the combined results presented in the table. The combined results can be expressed as

$$\tilde{a} = 0.9988(36) \quad \text{with} \quad a = \tilde{a}\,(1 + 0.1622\,b)\ . \tag{5.4}$$

This also implies an upper limit on the value of $b$

$$b < 0.027\ . \tag{5.5}$$

As is mentioned in connection with Fig 4.10, a value of $b$ beyond the range $|b| < 0.05$ would seem completely incompatible with a value derived from analysis of $0^+ \rightarrow 0^+$ beta decay. Tab 5.1 indicates that (5.4) is a valid combined result in this range.

The most recent published limit derived from the analysis of superallowed beta decay is $b = 0.0024(28)$ [120]. If this result is combined with the present result (5.1) we obtain

$$a = 0.9992 \pm 0.0044 \tag{5.6}$$

and if combined with (5.4) we obtain

$$a = 0.9992 \pm 0.0036\ . \tag{5.7}$$

The error quoted in (5.1, 5.4, 5.6 and 5.7) each corresponds to the total error at the 68% confidence level. We estimate that increasing each of these errors by the factor 1.645 provides an estimate of the total error at the 90% $CL$.

If one assumes $\mathcal{I}m(L) = 0$, the expression for $a$ and $b$ (4.3) together with an experimental value of $\tilde{a}$ can be used to determine a value of $|R|$ that depends on $b$. The maximum value of $|R|$ is derived from the minimum value of $\tilde{a}$ together with the assumed value of $b$. As has been noted in connection with (4.3) the limit applies to

$|R|$ and is independent of any possible complex phase $R = |R|e^{i\phi}$. In Tab 5.2 we show these limits for $b = -0.01$, 0.00 and $b = 0.01$ derived from $\tilde{a} = 0.9944$ and 0.9916, the minimum values (including systematic errors) from the present experiment at the 68% and 90% confidence levels. Also shown are the corresponding limits for $\tilde{a} = 0.9952$ and 0.9929 associated with (5.4), the combined results of the present experiment and that of Adelberger *et al.* [34].

In (5.6) and (5.7) we quote the value of $a$ which is obtained by combining the result of Savard *et al.* [120] for $b$ with either the result of the present experiment or that combined with the $^{32}$Ar results. The corresponding upper limits on the value of $|R|$ are:

$$\text{Present experiment} \ : \ |R| < 0.102 \ (68\% \ CL) \quad |R| < 0.127 \ (90\% \ CL) \qquad (5.8)$$

$$\text{Including [34]} \ : \ |R| < 0.093 \ (68\% \ CL) \quad |R| < 0.116 \ (90\% \ CL) \qquad (5.9)$$

The analysis presented above is based on the assumption that $\mathcal{I}m(L) = 0$. The possibility that $\mathcal{I}m(L) \neq 0$ is considered in App D. Finite values of $\mathcal{I}m(L)$ would only decrease the limits on $|R|$ and hence the limits presented above remain generally valid.

Similarly, the least restrictive limits on the $\mathcal{I}m(L)$ that can be derived from the present experiment follow the assumption that $|R| = 0$. As for the limits on $|R|$ in Tab 5.2, the limits on $\mathcal{I}m(L)$ depend on the value of $\mathcal{R}e(L)$ (see Tab D.1). If one accepts the value $b = 0.0024(28)$ [120], the present experiment implies (for $|R| = 0$) :

TABLE 5.2: Upper limits of $|R|$ that can be derived from the present experiment and from the present results combined with the $^{32}$Ar result [34]. The limits are given for $b = -0.01$, 0.00 and $b = 0.01$ at both the 68% and 90% confidence levels. It is assumed that $\mathcal{I}m(L) = 0$

| | Maximum value of $\lvert R\rvert$ | | | |
|---|---|---|---|---|
| | Present result | | Including [34] | |
| $b$ | 68% $CL$ | 90% $CL$ | 68% $CL$ | 90% $CL$ |
| 0.01 | 0.090 | 0.117 | 0.079 | 0.105 |
| 0.00 | 0.106 | 0.130 | 0.098 | 0.119 |
| -0.01 | 0.119 | 0.141 | 0.113 | 0.132 |

$$\mathcal{I}m(L) = 0.020(106) \quad 68\% \ CL \qquad (5.10)$$

$$\mathcal{I}m(L) = 0.019(132) \quad 90\% \ CL \ . \qquad (5.11)$$

The limits presented above are completely compatible with $\mathcal{I}m(L) = 0$. As is outlined in App D, the non-zero "central" value ( $\mathcal{I}m(L) \simeq 0.020$ ) is the result of the

"Coulomb correction", the term linear in $\mathcal{I}m(L)$ in the expression for $a$ in (D.1). This term results from the "external" interaction of the decay positron in Coulomb field of the daughter nucleus which modifies the influence of the time reversal violating component. Reasonable estimates of the limits placed on $\mathcal{I}m(L)$ that can be attributed directly to the weak interaction are (for $b = 0.0024(28)$ ):

$$|\mathcal{I}m(L)_{\text{weak}}| < 0.106 \quad 68\% \; CL$$
$$|\mathcal{I}m(L)_{\text{weak}}| < 0.132 \quad 90\% \; CL \; .$$

## 5.2 Physics Impact of the Present Experiment.

The result of the present experiment

$$\tilde{a} = 0.9988 \pm 0.0044 \quad \text{where} \quad \tilde{a} = \frac{a}{1 + 0.1503\, b}$$

represents the most precise determination of the beta−neutrino correlation for a superallowed $0^+ \rightarrow 0^+$ decay for which there are no contributions from axial vector (or tensor) interactions. Recoil order corrections are small and have been included in the simulations. The result is consistent with the predictions of the Standard Model and can be used to place limits on the properties of a non-SM weak scalar interaction.

The limit on $b$ that can be derived from the present experiment ($b < 0.035,\; 68\% \; CL$ including systematics) is not very "competitive" (see Fig 4.10). But when the present results are combined with a separate determination of $b$ (and hence $\mathcal{R}e(L)$) the results are the best direct limits on the remaining coupling constants that define the strength of a scalar interaction. Defining (as in Sec 4.1) $L = \tilde{C}_S + \tilde{C}'_S$ and $R = \tilde{C}_S - \tilde{C}'_S$, these limits at the 90% $CL$ are

$$|R| < 0.13 \quad \text{and} \quad \mathcal{I}m(L) = 0.02(13) \; .$$

(As is explained in the previous section, the non-zero central value in the latter result represents the influence of the "external" Coulomb correction.)

The present result is 33% more restrictive than the best previous determination of the positron−neutrino correlation for a $0^+ \rightarrow 0^+$ transition derived from a detailed analysis of the energy spectrum of protons emitted following the beta decay of $^{32}$Ar [34]. The two experiments involve completely different techniques and consequently independent systematic errors. The results of combining the two experiments, both in terms of $\tilde{a}$ and a slightly more restrictive limit on $|R|$ are presented in the previous section.

Within this decade there have been two extensive reviews of tests of the standard electroweak model with an emphasis on experiments involving nuclear beta decay [30, 31]. Also included in these reviews are discussions of the indirect limits on many extentions to the Standard Model that are based on other considerations. Concerning scalar interactions these include constraints on scalar coupling deduced from analysis of charged pion decay [126] and upper limits on neutrino masses [127] and on electric dipole moments [128]. Both of these reviews [30, 31] emphasize the importance of direct experimental limits and, in the context of scalar interactions, studies of beta−neutrino correlations in $0^+ \rightarrow 0^+$ beta decays.

## 5.3 Systematic Limitations on the Present Experiment.

The present results are derived from an analysis of the triple coincident data limited to the scintillator ADC range 750−1550. The direct contribution of counting statistics to the uncertainty in the result is comparable to the estimate of the combined systematic uncertainties. In most cases the estimates of the possible systematic errors are defined by analysis of data recorded during experiment and could be reduced in a future experiment with significantly better statistics.

The result of the $\beta - \nu$ correlation analysis of triple coincident events for the scintillator ADC range 200−1550 are presented in Fig 4.6. The result in terms of the central values for $a$ and $b$ was rejected on the basis of the quality of the fit in in the ADC range 200−750. The analysis can be used, however, to provide an indication of the statistical precision with which $a$ and $b$ could have been determined if the undefined "systematic effect" had not been present. The $1\,\sigma$ statistical limits in terms of $a$ and $b$ were

$$\Delta a \sim 0.0013,\ \Delta b \sim 0.009\ .$$

The analysis of the present experiment revealed several factors that limited the precision of the result in a manner such that simply improving the statistics of a future experiment would not resolve. These are discussed in the following section.

### 5.3.1 Quality of the fits $\chi^2(L, R)$ for Scin.ADC$<$ 750.

The problems associated with extending the analysis of the $\beta - \nu$ correlation data below scintillator ADC channel 750 are mentioned above and discussed in detail in Secs 4.1.1 and 4.1.2. The consequences are a final result which provides no useful restrictions on the value of $b$ and a statistical precision in the determination of $\Delta a$ reduced by a factor of 2.

Two possible sources of this discrepancy have been proposed:

a) the relative amplitude of the low energy tail of the response function of the detector;

b) the intensity of the triple coincident events involving a positron emitted from the trap but scattered before striking the DSSD detector relative to the intensity of the "response function" events.

The triple coincident data above scintillator ADC channel 200 shown in Fig 4.12 has been used to place limits on the uncertainty of the relative amplitude of the tail. Examination of the recoil TOF spectra shown in Fig 4.1–4.5 reveals the increasing significance of the scattered background for the lower scintillator ADC channel bins.

### 5.3.2 Incomplete collection of the recoil ions and TOF separation of the $\mathrm{Ar}^{+1}$, $\mathrm{Ar}^{+2}$ and $\mathrm{Ar}^{+3}$ ion distributions.

Fig 3.35 clearly reveals that for the higher detected positron energies, recoil ions for all values of $\vartheta_{\beta\nu}$ strike the MCP while at the lowest energies this is true for only those with $\vartheta_{\beta\nu}$ near $0^\circ$ or $180^\circ$. This same Fig. also illustrates the overlap in TOF of different charge states for lower values of the detected positron energy. Although these "kinematic" effects are accounted for in both the full GEANT and Fast (response function) Monte Carlos they have, as outlined below, a negative impact on the analysis.

In those regions in Fig 3.35 for which most recoils "miss" the MCP the small number of recorded events is particularly sensitive to both the relative amplitude of the low energy tail and the contribution of scattered positrons mentioned above. The dramatic degradation in the quality of the fits, $\chi^2(L,R)$ for ADC channels less than 750 may well reflect this enhanced sensitivity. In general, the fraction of recoil Ar ions missing the MCP decreases as the ion charge increases ($\mathrm{Ar}^{+1} \rightarrow \mathrm{Ar}^{+3}$). If this was not the case, a comparison of the simple spectrum of $E_{scin}(\mathrm{Ar}^{+1})$ obtained by summing over the values of TOF within the kinematic cut with the corresponding $E_{scin}(\mathrm{Ar}^{+2})$ could be used to estimate the size of the $\mathrm{Ar}^{+1}$ electron shakeoff correction.

The overlap of the $\mathrm{Ar}^{+1}$ and $\mathrm{Ar}^{+2}$ TOF distributions evident in Fig 3.35 means that the $\mathrm{Ar}^{+2}$ recoils with $\mathrm{MHTDC5} > 660$ could not contribute in a determination of $a$. (And similarly for $\mathrm{Ar}^{+3}$ recoils with $\mathrm{MHTDC5} > 552$.) In terms of the TOF separation of ion charge states, it would also help to have the maximum TOF for "backscattered" $\mathrm{Ar}^{+2}$ to be less than the TOF for all $\mathrm{Ar}^{+1}$ events and similarly for "backscattered" $\mathrm{Ar}^{+3}$ and the $\mathrm{Ar}^{+2}$ events.

### 5.3.3 Discrepancy between the predicted and measured strength of the electric field.

As is discussed in Sec 3.7.5, the electrostatic focusing system was designed to achieve a uniform electric field of $-800\,\mathrm{V/cm}$ along the axis between the center of the detection chamber ($x = y = z = 0$) and the center of the MCP ($z = -61.25\,\mathrm{mm}$). From an early stage in the analysis it was realized that the data shown in Fig 3.3 allowed for precise measurements of the distance between the center of the cloud of trapped $^{38\mathrm{m}}\mathrm{K}$ atoms and the MCP (hence $z_0$), the FWHM of the cloud in the $z$-direction and an "average" value of the electric field strength (designated $U_0$ in Sec 3.7). Following this procedure resulted in a value $U_0 = -807.70(12)$ (Eq 3.14). Even with this precision in the estimate of the field, the corresponding uncertainty in the fitted value of $a$ (for $b = 0$) is $\sigma_a^U = 0.0012$ (Eq 4.11). This analysis reveals that the use of the triple coincident data to determine the precise strength of the field is essential. The initially unexplained surprise was the 1% discrepancy between the predicted and measured strengths of the field.

Given this it was thought to be essential to have some estimate of the possible influence of non-uniformity in the field. As is discussed in Sec 3.7 the measured TOF of the $^{38\mathrm{m}}\mathrm{K}^+$ photoions, 771.42(09) ns, was used for this purpose. This TOF is very nearly identical to that of the slowest $\mathrm{Ar}^{+1}$ recoils observed in coincidence with positrons with Scin.ADC$\,>750$ (Fig 4.3) and is, within the statistics of the measurements, consistent with the existence of a uniform field of $-807.70(12)\,\mathrm{V/cm}$ (as determined from the fastest Ar recoil ions). The statistical precision of the measurements allows one to put limits on the influence of a possible non-uniformity in the field (defined in terms of an "effective" linear gradient $U_z = \partial U/\partial z$). From the analysis presented in Sec 4.2.2 for the present result $\sigma_a^{U_z} = 0.0010$.

After the analysis presented in this thesis was completed a coding error was discovered in the program used to optimize the electric field. All of the stainless steel sleeves (see Fig 2.22) had been assigned to be at 0 V although (as is shown in the Fig 2.21) they were actually at the same potential as the nearest glassy carbon hoop. The best estimate of the field for the voltages given in Tab 2.3 (with the error corrected) is shown in App B (Fig B.2). The field is quite non-linear, especially near the MCP, but is much more nearly uniform in the region of the trap with its strongest value $E_z = -808.4\,\mathrm{V/cm}$ at $z = -7\,\mathrm{mm}$. To test how well the actual field is predicted in Fig B.2 the motion of the $^{38\mathrm{m}}\mathrm{K}^+$ photoions was tracked numerically from the trap to the MCP. The calculated TOF is 771.9 ns which is to be compared with the measured value of 771.4 ns and a value 775.2 ns which is predicted for a uniform field of $-800.0\,\mathrm{V/cm}$. An apparent TOF discrepancy of 0.49% is reduced to 0.06%.

### 5.3.4 Failure to account for the positron double coincident energy spectrum.

It was known from the outset that precise calibration of the positron energy spectrum would be of crucial importance in the present analysis. The total number of events in the energy spectrum of the scintillator for $\Delta E - E$ (double) coincident events (Fig 3.4) exceeds that for $\Delta E - E - MCP$ (triple) coincident events (Fig 3.3) by a factor of 20. The potential advantage for calibration can only be realized if the additional sources of background are understood.

As is discussed in Sec 3.4, an acceptable fit to the double coincident spectrum was achieved only over a limited range (channels $750-1400$) for the scintillator ADC. Estimates of the backgrounds present above channel 1000 (Fig 3.11) suggest that these are not the source of the discrepancy above channel 1400. In Sec 3.4.2 it is suggested that this discrepancy may indicate a failure of the GEANT Monte Carlo to completely account for Compton summing of annihilation photons possibly related to spatial variations in light collection from the scintillator. A failure to accurately define the backgrounds, particularly that associated with the decays of untrapped $^{38\mathrm{gs}}\mathrm{K}$ may dominate the failure to fit the channel region $200-750$ in Fig 3.11. It must be added, however, that in this region account must also be taken of uncertainties in the low energy tail of the response function and the contribution of positrons scattered before reaching the DSSD.

### 5.3.5 Spatial calibration of the recoil detector.

The spatial calibration of the resistive anode used to provide the $(x, y)$ coordinates of the Ar recoils striking the MCP was initially based on the hit pattern observed when an $\alpha-$particle source was used to illuminate a precisely manufactured grid mounted adjacent to the front surface of the MCP. The pattern observed defined the calibration particularly well in the central $4\times4\,\mathrm{mm}^2$ region (Fig 2.18).

For the present experiment the grid was replaced by a circular aperture of radius 12.0 mm. As is described in Sect. 3.8.2, the nearly uniform illumination of the area within this aperture by a selected group of $\mathrm{Ar}^{+1}$ recoils produced a test of the initial calibration which was particularly sensitive at $r = 12.0\,\mathrm{mm}$. Since the two calibrations were incompatible the one obtained during the experiment was adopted. For the analysis presented in this thesis, the spatial calibration of the recoil detector was used only to define the $(x, y)$ coordinates of the trap ($\delta_x = 0.10\,\mathrm{mm}$ and $\delta_y = -0.06\,\mathrm{mm}$) defined by the hit pattern of the $^{38\mathrm{m}}\mathrm{K}^+$ photoions (Fig 3.32). Fortunately, the sensitivity of $a$ to the precise location of the trap near $\delta_x = \delta_y = 0$ is very weak (see Sec 4.2.9).

## 5.4 Future Prospects.

The results presented in this thesis involve a thorough investigation of a new technique to measure the $\beta - \nu$ angular correlation $W(\vartheta_{e\nu})$ in a pure Fermi transition as a function of $E_\beta$ in order to determine both coefficients $a$ and $b$. Despite the limitations outlined in the previous section, the final result, consistent with the Standard Model, is more restrictive of possible scalar contributions to the derived parameter $\tilde{a}$ than the best previous experiment. As is outlined below, with the insight gained from the analysis presented in this thesis and an anticipated increase in the rate of data acquisition, it is suggested that an upgrade [129] to the present experiment would lead to a very substantial improvement in the results. The original goal of directly determining both $a$ and $b$ should be achieved. While it is difficult to be precise about the extent of the anticipated improvement, goals in terms of the uncertainties $\Delta a = 0.001$ and $\Delta b = 0.004$ would seem realistic.

### 5.4.1 Increased population of trapped $^{38\mathrm{m}}$K.

Recent improvements in the techniques associated with the production and delivery of radioactive beams at TRIUMF [78] suggest that one could anticipate the delivery of $\sim 5\times10^7\,\mathrm{s}^{-1}$ of $^{38\mathrm{m}}\mathrm{K}^+$ ions to the TRINAT neutralizer. This intensity, utilizing a TiC target and a proton beam current of $45\,\mu\mathrm{A}$ would be an increase of by a factor of $\sim$5. The trapping efficiency has also been improved by a factor of 3 using additional laser power.

### 5.4.2 Larger MCP-based recoil detector with delay-line anode readout.

In order to overcome the limitations discussed in Sec 5.3.2, a new experiment would utilize both a larger MCP and a stronger electric field. As an example, in Fig 5.1 we show Monte Carlo simulations of TOF spectra of the first four charge states of

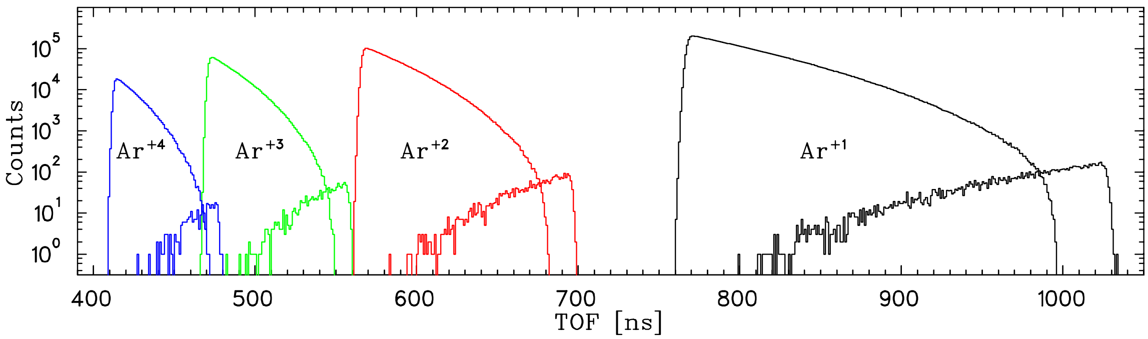

FIGURE 5.1: TOF spectra of Ar ions in upgraded geometry (see text).

Ar ions (together with backscattered events) for an applied uniform electric field of 1400 V/cm and trap-to-MCP distance of 140 mm. All ions coincident with betas of kinetic energy greater than 350 keV strike the MCP within a diameter of 75 mm.

We have already acquired a position sensitive recoil detector using 3 MCP's each with a minimum active diameter of 75 mm. The three MCP are mounted in a Z-stack configuration (as before) but the channels have an angle of 19° to the normal eliminating events when ions hit the MCP at angles within 5° of the axis of a channel. This provision should significantly reduce the possible uncertainties associated with the angle of incidence (see Fig 3.34 and Sec 4.2.6).

The new MCP is used with a DL80 ($80\times 80\,\text{mm}^2$) delay-line anode readout produced by RoentDek Handels GmbH [130]. The specifications include spatial resolution of $\leq 0.15$ mm and variations from linearity not to exceed 0.15 mm over the entire active area of the MCP [131]. Measurements to confirm that the recoil detector meets these specifications have been initiated. Tests will be made to verify the stability of the spatial calibration over the entire period of the experiment. In the analysis scheme detailed in this thesis the spatial calibration of the recoil detector is used directly only to define the $(x, y)$ location and the extent of the trap. The precision (including stability) of the spatial calibration is of crucial importance, however, in the "alternate" analysis scheme which will be used to dramatically reduce the uncertainties associated with the energy response of the positron telescope (see App C).

### 5.4.3 Stronger, more uniform electric field.

The detailed design of the electrostatic focusing system needed to achieve the uniform 1400 V/cm field assumed in Fig 5.1 has not been done. As before, care must be taken to avoid surfaces on electrodes where $^{38\text{m}}$K atoms, escaping from the trap might collect and then provide possible sources of $\beta^+-$ recoil coincidences. Tests will be needed to confirm that the considerably stronger field can be reliably achieved.

As is shown in App B, the electric field used in the present experiment was significantly less uniform than anticipated. By combining the TOF information for the fastest Ar ion recoils and the $^{38\mathrm{m}}\mathrm{K}^{+}$ photoions an adequate characterization of the field was achieved. Moreover, once the original coding error was corrected, the revised calculation of the electric field accounted for the observed photoion TOF with a precision of 0.06%. We anticipate that it will still be necessary to measure a precise value for the effective average value of the new field but that any correction for the non-uniformity will be negligible.

### 5.4.4 Beta detector: response and calibration.

For now there are no plans for major changes to the positron telescope hardware. An attempt will be made, however, to improve the quality of the fast timing pulse from the PMT anode in order to reduce the "time slewing" which is evident in Fig 3.12 and contributes to the error associated with the prompt peak position (Sec 4.2.8). The telescope provides an energy response that is useful for $T_\beta \geq 0.5\,\mathrm{MeV}$ and the $\Delta E \cdot E$ coincidence requirement is an important factor in essentially eliminating triple coincident events involving detection of the 2.17 MeV photons associated with untrapped $^{38\mathrm{gs}}\mathrm{K}$.

Improvements are planned in the Monte Carlo simulations of the energy response of the telescope. In order to improve the accuracy of tracking positrons prior to annihilation, the GEANT3 portion of the detailed Monte Carlo will be reworked to incorporate the PENELOPE code [132, 133, 134] which is reported [135, 136] to be more accurate in its description of electron scattering at large angles and in accounting for electron energy losses at low energy. Another improvement in the Monte Carlo may involve describing light propagation from the scintillator through the light guide. This could lead to a response function slightly dependent on the location $(x, y)$ of the hit in the DSSD and differences in the average efficiency of the light collection for positrons and annihilation photons.

In addition to the changes mentioned above a critical test will be made by trapping $^{37}\mathrm{K}$ with careful analysis of the double coincident $(\Delta E \cdot E)$ positron spectrum. The maximum positron kinetic energy of 5125.46(23) MeV [137] is very similar to that of $^{38\mathrm{m}}\mathrm{K}$. There is no intense $\gamma$-ray background (as in the case of $^{38\mathrm{m}}\mathrm{K}$). In a detailed analysis, however, care must be taken to account for the 2% branch to the level at 2.80 MeV in $^{37}\mathrm{Ar}$ [138]. $^{37}\mathrm{K}$ has been successfully trapped previously in the TRINAT apparatus [45].

### 5.4.5 Measurements of electron shakeoff dependence on recoil momentum.

Complete collection and separation in TOF of the coincident $\mathrm{Ar}^{+1}$, $\mathrm{Ar}^{+2}$ and $\mathrm{Ar}^{+3}$ recoils, together with reliable $(x, y)$ readout of the larger MCP, should provide a means of measuring $s_1$, the electron shakeoff correction parameter in an analysis that is independent of values of the parameters $a$ and $b$. For each coincident event , the $(x, y)$ coordinates from the MCP together with the Ar ion TOF can be used to determine the initial recoil energy. Therefore, for each of the charge states ($\mathrm{Ar}^{+i}$) one can generate the spectrum of events $N_i(T_{rec})$. If $s_1 = 0$, these three spectra should differ by only the normalization factors $(p_1,\ p_2,\ p_3)$. For values of $s_1 > 0$, the spectrum $N_1(T_{rec})$ should be linearly enhanced at higher recoil energies when compared with $N_2(T_{rec})$ and $N_3(T_{rec})$ (3.29).

A recent measurement of the $\beta - \nu$ correlation in the decay of optically trapped $^{21}$Na is based on the observation of charged $^{21}$Na recoils in coincidence with shakeoff electrons [139]. The basic geometry of that experiment is very similar to the one described in this thesis except for the replacement of the beta-telescope with a second MCP used to detect the atomic electrons. A significant advantage of this technique is the much larger detection efficiency of the electron MCP (by a factor of between 10 and 50) that results from the focusing of the electrons in the strong electric field. The application of this technique in the future upgrade of the present experiment will be considered on the basis of detailed simulations and experience gained as part of the ongoing TRINAT experiment S956 [140]. Of particular interest in the context of electron shakeoff would be the possibility of determining $s_1$ from high statistics measurements of the distributions of the $\mathrm{Ar}^{+1}$ and $\mathrm{Ar}^{+2}$ recoils as functions of $T_{rec}$ (although in this case there would not be complete separation in TOF of the Ar ions for the conditions illustrated in Fig 5.1). The observation Ar recoils in coincidence with shakeoff electrons might also provide more precise results for tests of variations in the efficiency of the recoil detector.

# CHAPTER 6

# Summary.

The first experiment initiated to measure positron-neutrino correlations in the beta decay of optically trapped neutral atoms is described. We have studied the $0^+ \rightarrow 0^+$ superallowed Fermi transition in the isomer $^{38\mathrm{m}}$K which makes our measurements uniquely sensitive to possible scalar contributions to the weak interaction. The online isotope separator of the TRIUMF ISAC facility provided the radioactive species. By selectively confining the neutral alkali atoms of the isomer in a magneto-optical trap, we prepared a point-like pure, cold and completely backing-free source. This allowed the measurements of the initial momentum of the recoiling $^{38}$Ar nucleus observed in coincidence with positrons for which the kinetic energy and direction were also measured. Since the positron decay populates only the ground state, these measurements defined the momentum of unobservable neutrino for each coincident event.

In order to increase the sensitivity of the experiment we have arranged the positron and recoil detectors facing each other along a common axis with the trap located on that axis near the midpoint. Detection of the positrons has been provided by a $\Delta E - E$ telescope consisting of a position sensitive Si $\Delta E$ detector backed by a plastic scintillator. To estimate the energy response of the telescope we have used a detailed GEANT3-based Monte Carlo simulation which included the full geometry of the detection chamber. Energy calibration of the plastic scintillator used to measure $E$ was derived directly from the energy of the positrons emitted in the decay of $^{38\mathrm{m}}$K, avoiding possible effects of differences in the calibration and data collection phases of the experiment. Ar recoils have been observed in coincidence with positrons with an MCP-based position sensitive recoil detector. The detected position together with the measured TOF provided an estimate of the initial recoil momentum. By application of a uniform electric field we have accelerated charged recoils towards the MCP, substantially increasing the detection efficiency, the effective solid angle and separating in TOF the different charge states created in the decay (Ar$^{+1}$, Ar$^{+2}$, Ar$^{+3}$ etc.). The precise distance between the trap and the MCP was deduced from the TOF of the fastest $\mathrm{Ar}^0$ observed in the MCP while the TOFs of the fastest $\mathrm{Ar}^{+1}$, $\mathrm{Ar}^{+2}$ and $\mathrm{Ar}^{+3}$ were used to deduce the strength of the uniform electric field. A small fraction of trapped $^{38\mathrm{m}}\mathrm{K}$ atoms was photoionized on-line by a pulsed laser. The TOF of $^{38\mathrm{m}}\mathrm{K}^+$ ions was used to measure the uniformity of the electric field. The coordinates of the impact on the MCP were used to deduce location and size of the trap in the directions transverse to the common axis defined by the detectors.

The angular correlation between the positron ($e$) and the neutrino ($\nu$) is defined in terms of the parameters $a$ and $b$:

$$W(\theta_{e\nu}) = 1 + a\,\frac{p_e}{E_e}\cos(\theta_{e\nu}) + b\,\frac{m_e}{E_e}$$

In the Standard Model this $0^+ \rightarrow 0^+$ transition is the result of a purely vector interaction producing only left-handed neutrinos with $a = 1$ and $b = 0$.

We have recorded about 500,000 $\beta -$ Ar coincident events. The final analysis has been limited to events in which the kinetic energy of the positron was greater than 2.5 MeV. Detailed comparison of the data and simulations over this limited range revealed that the Fierz term $b$ is not usefully determined but that the angular correlation can be expressed in terms of a "reduced correlation parameter" $\tilde{a}$, defined by the statistical precision of the data to be

$$\tilde{a} = 0.9988 \pm 0.0028\,(\mathrm{stat}), \quad \text{where} \quad \tilde{a} = \frac{a}{1 + 0.1503\,b}\ .$$

The quality of the fit is excellent ($\chi^2 = 787.5$ for 789 degrees of freedom).

We found that results of the fit are sensitive to a number of the experimental parameters (most of them mentioned above). Detailed analysis of the precision with which these parameters were determined together with the sensitivity of $\tilde{a}$ to these parameters provides estimates of the possible systematic errors and results in

$$\tilde{a} = 0.9988 \pm 0.0028\,(\mathrm{stat}) \pm 0.0034\,(\mathrm{syst})\,,$$

i.e.

$$\tilde{a} = 0.9988 \pm 0.0044\,(\mathrm{total})$$

These results are all given for a confidence level of 68%. The lower limit on the value of $\tilde{a}$ at the 90% $CL$ is

$$\tilde{a} \geq 0.9916\ .$$

This result is consistent with Standard Model of the weak interaction and is 33% more restrictive than best previous measurement of the beta−neutrino correlation for the $0^+ \rightarrow 0^+$ decay of $^{32}\mathrm{Ar}$ [34]. If the present result is combined with the recent estimate $b = 0.0024(28)$ [120] from an analysis of the systematics of superallowed $0^+\rightarrow 0^+$ decay assuming CVC, then the estimate of the angular correlation parameter is

$$\begin{array}{rcll} a & = & 0.9992 \pm 0.0044 & (68\%\ CL) \quad \text{or} \\ a & > & 0.9920 & (68\%\ CL) \quad . \end{array}$$

In the most general form the strength of a possible scalar contribution to beta decay can be specified in terms of two (complex) numbers: $C_S$ and $C'_S$. With the assumption that the vector interaction is described by the Standard Model (i.e. $C_V = C'_V$ and both are real) the (generally complex) quantities $L = (C_S + C'_S)/C_V$ and $R = (C_S - C'_S)/C_V$ define the strength of the scalar coupling to left- and right-handed neutrinos. The present experiment does not usefully define $b$ or $\mathcal{R}e(L)$, but if these are taken from the analysis mentioned above, then the present experiment provides the most restrictive direct limits on the possible values of the other parameters:

| | | | |
|---|---|---|---|
| $\lvert R\rvert$ | $<$ | 0.10 | (68% $CL$) |
| | | 0.13 | (90% $CL$) |
| $\mathcal{I}m(L)$ | $=$ | 0.02(11) | (68% $CL$) |
| | | 0.02(13) | (90% $CL$) |

(The weak dependence of these limits on the actual value of $\mathcal{R}e(L)$ is defined in Chap 5.)

The detailed analysis of this initial experiment suggests many ways in which improvements could be made. These are briefly discussed and it is estimated that, with modest software and hardware development, a total uncertainty of 0.1% in the value of $a$ would be a reasonable goal.

## APPENDIX A

# Parametrization of the Beta Detector Response.

In Ref [122] the authors fitted the response of a plastic scintillator telescope used for beta detection with a superposition of functions each of which described a physical phenomenon in the interaction of the positrons with the material of the detector

$$\begin{aligned} f(E) &= A_1 f_1(E, E_i, \sigma) + A_2 f_2(E, E_i, \sigma) + A_3 f_3(E, E_i, \sigma, k) \\ &\quad + A_4 f_4(E, E_i, \sigma, W) + A_5 f_5(E, E_i, \sigma, W) \ , \end{aligned} \tag{A.1}$$

where

$f_1$ - the full energy (Gaussian) peak;
$f_2$ - a flat low energy tail, produced by beta particles leaving the scintillator without having deposited their full energy;
$f_3$ - an exponential low energy tail;
$f_4$ - a high energy plateau, due to coincident summing between fully stopped positrons and the energy deposited by Compton scattering of one of the subsequent annihilation quanta;
$f_5$ - a high energy tail above the plateau which originates from a similar process, where both annihilation quanta are Compton scattered.

The functions $f_{1,\ldots,5}$ define the probability of observing an energy $E$ for a specific incident energy $E_i$. The parameters $\sigma$ and $W$ define the width of of the Gaussian peak and of the Compton plateau (and are functions of $E_i$). $k$ (units of $\mathrm{MeV}^{-1}$ ) defines the width of the exponential tail. The five functions $f_{1,\ldots,5}$ are each normalized to unit area and hence the parameters $A_{1,\ldots,5}$ define the fraction of the total response attributed to each process.

Expressions are given below for the functions $f_{1,\ldots,5}$. First, for convenience, one defines the functions $g(x)$ and $e(x)$

$$\begin{aligned} g(x) &= \exp(-x^2/2\sigma^2)/\sqrt{2\pi\sigma^2} \\ e(x) &= \mathrm{erf}(x/\sqrt{2\sigma^2}) \end{aligned}$$

and using them the functions $f_{1,\ldots,5}$ from (A.1) can be defined as

$$\begin{aligned} f_1 &= g\left(E-E_i\right) \\ f_2 &= \left[1-e\left(E-E_i\right)\right]/2E_i \\ f_3 &= \left[1-e\left(E-E_i+\sigma^2k\right)\right]\exp\left[k(E-E_i)+\sigma^2k^2/2\right]/(2/k) \\ f_4 &= \left[e\left(E-E_i\right)-e\left(E-E_i-W\right)\right]/2W \\ f_5 &= \{(E-E_i)\left[e\left(E-E_i\right)-2e(E-E_i-W)+e\left(E-E_i-2W\right)\right] \\ &\quad +2W\left[e\left(E-E_i-W\right)-e\left(E-E_i-2W\right)\right] \\ &\quad +2\sigma^2\left[g\left(E-E_i\right)-2g\left(E-E_i-W\right)+g\left(E-E_i-2W\right)\right]\}/2W^2\ . \end{aligned}$$

# APPENDIX B

# Electric field by Comsol 3.2.

The coding error in the RELAX3D simulation that resulted in an electric field measured (when assumed to be uniform) to be $E_z = -807.7\,\mathrm{V/cm}$ is mentioned in Sec 5.3.3. As part of the investigation of the original discrepancy ($-807.7\,\mathrm{V/cm}$ rather than predicted $-800.0\,\mathrm{V/cm}$) it was also noted that the RELAX3D code is not ideal for the present circumstances. This code has two main drawbacks: *i)* boundaries of physical volumes can be assigned only to the nodes of the mesh grid and *ii)* this mesh is uniform and rectangular. For this reason, in order to accurately describe elements of our electrostatic focusing system one has to use a very small mesh grid size (about 0.1 mm). This leads to an enormous growth of the array size and makes the convergence of the relaxation process hard to achieve in a reasonable calculation time. Because of this we were forced to use electrode potentials obtained without full convergence of the relaxation code.

Contemporary codes which utilize a triangle mesh and a variable size grid starting from a given electrode are free from the problems mentioned above and provide a result with the required accuracy.

The entire geometry of the detection chamber was modeled using Comsol 3.2 [141] and the electrostatic problem was solved with the electrode potentials as in the experiment (Tab 2.3). The color density plot of the potential distribution is presented in the Fig B.1. The quantitative estimates of the electric field are done using the numerical output from the package. We present these estimates graphically in the Fig B.2. The upper panel shows that the field in the $z$-direction varies by more than $30\,\mathrm{V/cm}$ over the distance from the trap to the MCP with the strongest field $E_z = -808.4\,\mathrm{V/cm}$ at $z \simeq -7\,\mathrm{mm}$. But, what is important, from the trap ($z = -0.17\,\mathrm{mm}$) up to $z = -25\,\mathrm{mm}$, where ions are slow and spend a large portion of their drift time, the field is quite uniform and its value is nearly consistent with the evaluations with triple coincident and photo events. Tracking of ${}^{38\mathrm{m}}\mathrm{K}^{+}$ photoions, initially at rest, from the trap center to the MCP resulted in a $\mathrm{TOF} = 771.9\,\mathrm{ns}$ which is quite similar to the observed value

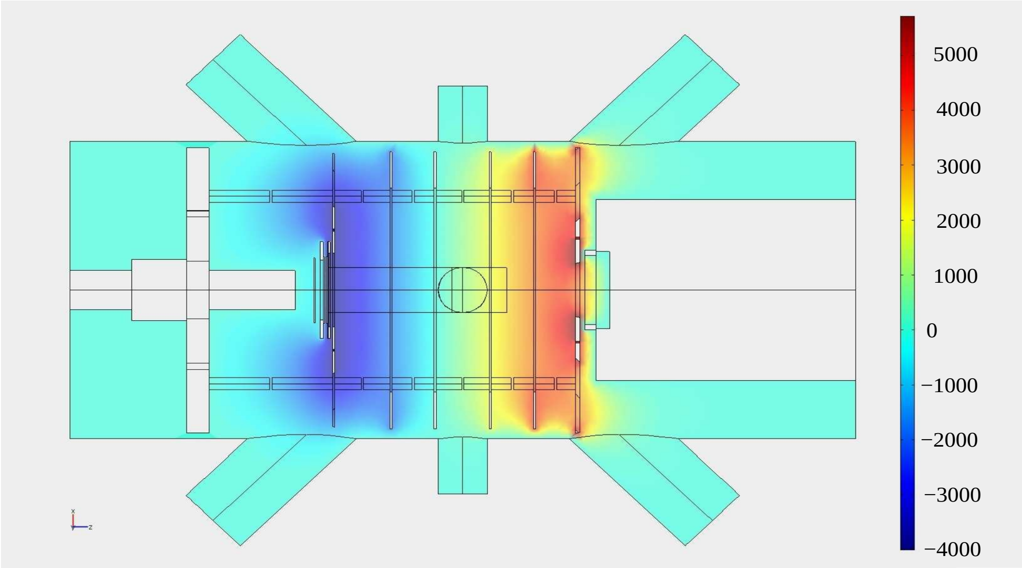

FIGURE B.1: Potential distribution in the $X - Z$ plane. The gradual change in the color from dark blue to dark red reflects growth of the electric potential from the minimum of $-4000$ V on the front MCP surface to the maximum of $+5715$ V on the inner plate near the collimator.

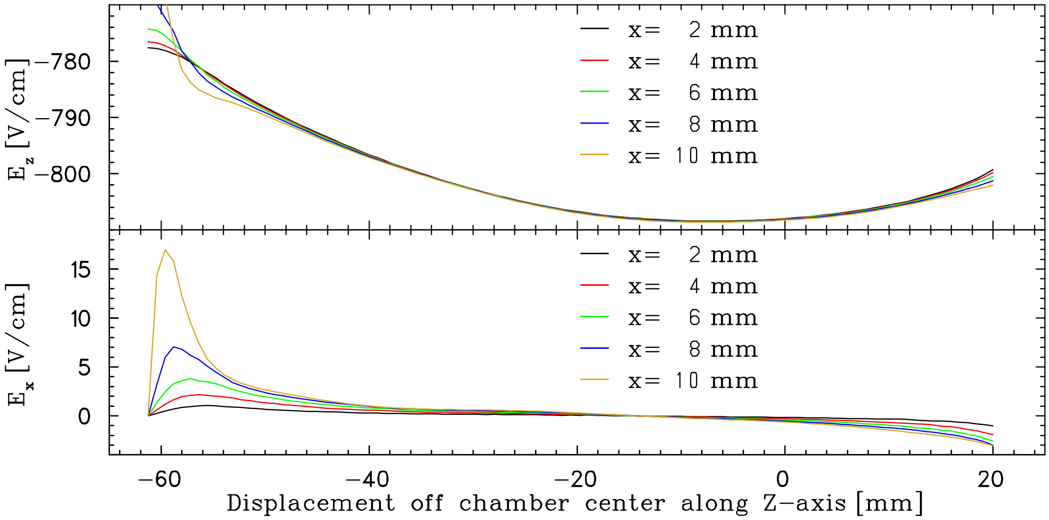

FIGURE B.2: Axial and radial electric field along the detection chamber. Plotted are both $z$ (upper panel) and $x$ (lower panel) components of the electric field taken for a set of transverse distances $x$ off the detection axis ($y = 0$)). These are the results of the simulations using Comsol 3.2, the applied voltages given in Tab 2.3 and the correct voltages for the "sleeves" (see Sec 5.3.3).

771.4 ns obtained in Sec 3.7.4.

The transverse electric field resulting from these calculations are shown in the lower panel of Fig B.2. It produces a negligible effect on the motion of the ions. We have compared the motion of the ions in the full calculated field and in one where the transverse field components were artificially zeroed. For ions which landed on the MCP at 11 mm off the center (the maximum detection radius in the experiment was 12 mm) the difference in the landing radii was found to be less than 10 $\mu$m.

# Appendix C

# Kinematic Reconstruction: Measurements of the Beta Detector Response.

The detectors used in the present experiment are designed to measure all three components of the momentum of both the positron and the Ar recoil. If all detectors were ideal (including the spatial calibration of the recoil detector and the energy response of the beta telescope), $\boldsymbol{p}_\nu$ could be obtained from these measurements as

$$\boldsymbol{p}_\nu = -(\boldsymbol{p}_\beta + \boldsymbol{p}_R)$$

But since the magnitude of $\boldsymbol{p}_\nu$ can also be determined from

$$|\boldsymbol{p}_\nu c| = Q_\beta - T_\beta$$

the the kinematics would be "overdetermined".

In the analysis of the triple coincident data presented in this thesis we have chosen to ignore the $(x, y)$ information from the recoil detector and rely on the energy response of the positron detector produced by a detailed GEANT3 simulation. As an alternative approach, one can use all the information (including the MCP $x, y$) except the measured $T_\beta$ to estimate this quantity [101]. As long as

$$|\boldsymbol{p}_R| < Q_\beta \tag{C.1}$$

a unique value of $T_\beta$ is obtained. (These events are referred to as the "slow events".)

This "alternative analysis" has been applied to the triple coincident data shown in Fig 3.35 with the following restrictions

$$\begin{aligned} 800 \leq \mathrm{MHTDC5} &\leq 1000 \\ 200 \leq \mathrm{Scin.ADC} &\leq 1550 \\ \mathrm{R_{MCP}} &\leq 10\,\mathrm{mm} \end{aligned} \tag{C.2}$$

For each of these events the difference between the measured beta energy and the energy calculated as outlined above is used to generate the "data" in the differential energy spectrum shown in the upper portion of Fig C.1. The data points represent an experimental determination of detector's energy response averaged over the rather wide energy energy range included. This response is then fitted using the parameters and functions defined in App A following the approach of Clifford *et al.* [122]. The fit is superimposed on the data in Fig C.1 (upper) and the values of the fitted parameters are shown in the "Data" column in Tab C.1.

For comparison the events produced by the full GEANT simulation and selected using the same cuts (C.2) are used to generate the differential energy spectrum shown in the lower portion of Fig C.1. This spectrum is also fitted as shown in the figure with the parameters listed in Tab C.1 (GEANT). The quality of the fits to both differential

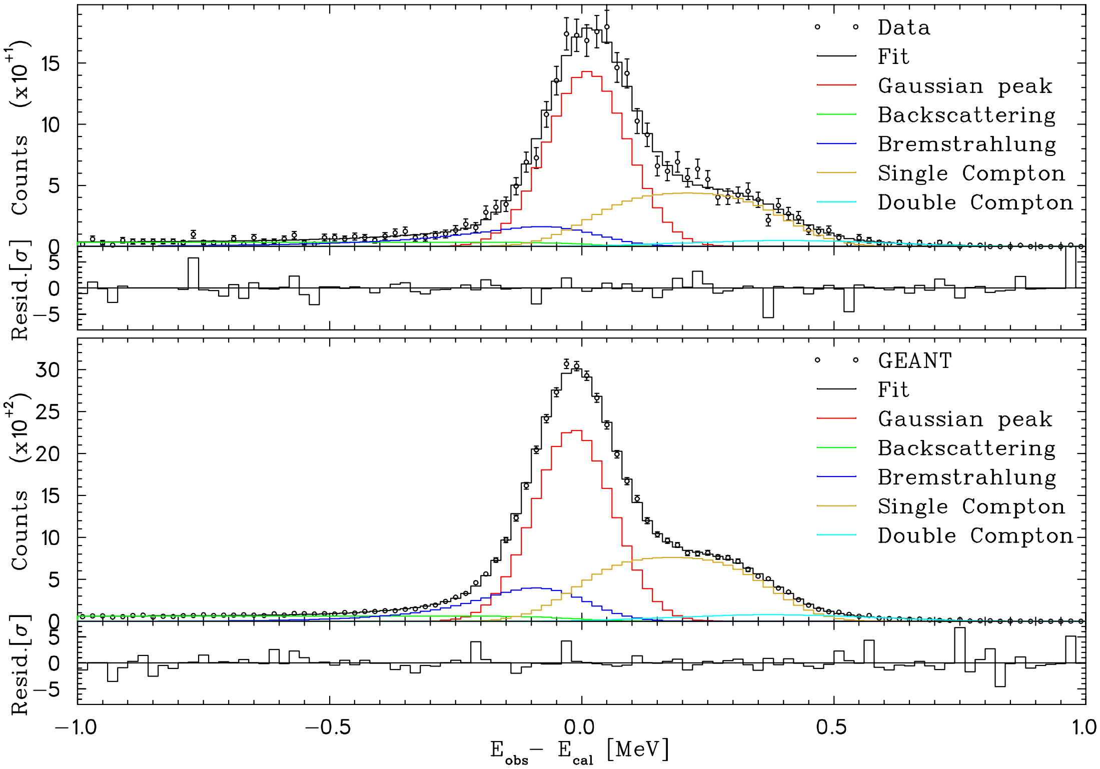

FIGURE C.1: The differential energy spectra generated by comparing the "observed" positron energy with that calculated from the remaining kinematic variables (see text). The "data" shown in the upper portion are derived from the triple coincident events observed in the experiment. For comparison the full GEANT simulation is used to generate the corresponding spectrum shown below. Both differential spectra are fitted as outlined in App A (see [122]) with the parameters shown in Tab C.1.

energy spectra is good. The smaller uncertainties for the GEANT parameters reflect the significantly better statistics in the GEANT sample. One parameter in the fit to the data that differs significantly from GEANT is $k$, the decay constant associated with the exponential tail. The significance of the 28 keV shift in the centroid of the two Gaussians is uncertain. The agreement in the parameters defining the width of the Gaussian and Compton edge as well as the single and double Compton plateau's is excellent. The large uncertainties for the Data in the amplitudes of the low energy and exponential tails reflect strong correlations between parameters. In this case the simpler analysis of the tail presented in Fig 4.12 is more informative.

Table C.1: Quality of the fits to the differential energy spectra shown in Fig C.1 and values of the fitted parameters. The functional form is defined in App A (see [122]).

| | | | Data | GEANT |
|---|---|---|---|---|
| $NF$ | | | 91 | 91 |
| $\chi^2$ | | | 85.90 | 90.59 |
| $\chi^2/NF$ | | | 0.944 | 0.996 |
| $CL$ | | | 0.631 | 0.492 |
| Full energy peak | | $A_1$ | 0.494(23) | 0.461(8) |
| Low energy tail | | $A_2$ | 0.060(27) | 0.063(5) |
| Exponential tail | | $A_3$ | 0.106(52) | 0.125(19) |
| Single Compton plateau | | $A_4$ | 0.301(17) | 0.313(4) |
| Double Compton plateau | | $A_5$ | 0.040(11) | 0.038(3) |
| Central energy | [MeV] | $E_0$ | 0.011(4) | −0.017(1) |
| Compton edge | [MeV] | $W$ | 0.394(11) | 0.392(3) |
| Energy resolution | [MeV] | $\sigma$ | 0.080(3) | 0.078(1) |
| Decay constant | [MeV$^{-1}$] | $k$ | 4.93(85) | 7.53(22) |

# Appendix D

# Coupling constants. Limits from the present experiment.

We repeat here the expressions for the angular correlation coefficients $a$ and $b$ if no assumption is made regarding time-reversal violation for a possible scalar interaction:

$$\begin{aligned} a &= \frac{4-|L|^2-|R|^2+4\alpha Z\,(m_e/p_e)\,\mathcal{I}m(L)}{4+|L|^2+|R|^2} \\ b &= \frac{-4\sqrt{1-\alpha^2 Z^2}\,\mathcal{R}e(L)}{4+|L|^2+|R|^2}\;. \end{aligned} \tag{D.1}$$

In the analysis of the positron-neutrino correlation in the $0^+ \rightarrow 0^+$ decay of $^{32}$Ar [34], the authors derive constraints on the scalar coupling constants based only on the observations of that experiment. For the present experiment such an analysis would include values of $\mathcal{R}e(L)$ extending over the range $-0.1 \leq \mathcal{R}e(L) \leq +0.4$ (as in Fig 4.9). As is noted in Sec 4.1.3, a fully consistent analysis of the present experiment over such a wide range in $\mathcal{R}e(L)$ cannot be based on the energy calibration given in Tab 4.1. Instead of attempting to derive limits on $\mathcal{I}m(L)$ independent of other experiments, we choose the other extreme: we consider the restrictions on $\mathcal{I}m(L)$ assuming $\mathcal{R}e(L) = 0$ and then explore briefly the sensitivity of this result to other values of $\mathcal{R}e(L)$.

Shown in the Fig D.1 are the values of $\chi^2(\mathcal{I}m(L))$ for the scintillator ADC channel range 750−1550 assuming $|R| = \mathcal{R}e(L) = 0$. The analysis is of the same data as is included in Sec 4.1.3 with the "fast Monte Carlo" altered to include the $\mathcal{I}m(L)$ term in (D.1). A sixth order polynomial fit (in powers of $\mathcal{I}m(L)$) accounts well for for the variation over a wide range in $\mathcal{I}m(L)$. The estimated value $\chi^2_{min} = 787.6$ is essentially the same as that shown in Fig 4.10, $\chi^2_{min} = 787.5$.

The lower portion of Fig D.1 indicates that for $-0.073 \leq \mathcal{I}m(L) \leq 0.112$ the fitted value of $\chi^2$ is less than $\chi^2_{min} + 1$ and hence these limits correspond to a 68% $CL$ taking account of only the statistical errors in the data. The asymmetry of this result (with respect to $\mathcal{I}m(L) = 0$) reflects the influence of the term linear in $\mathcal{I}m(L)$ in (D.1).

For small values of $|R|$ (for example $|R| = 0.05$) the limits on $\mathcal{I}m(L)$ corresponding to $\chi^2 = 788.6$ are somewhat more restrictive than those shown in Fig D.1 (as one would expect from (D.1)). In quoting limits on $\mathcal{I}m(L)$, it is therefore appropriate to use those derived assuming $|R| = 0$.

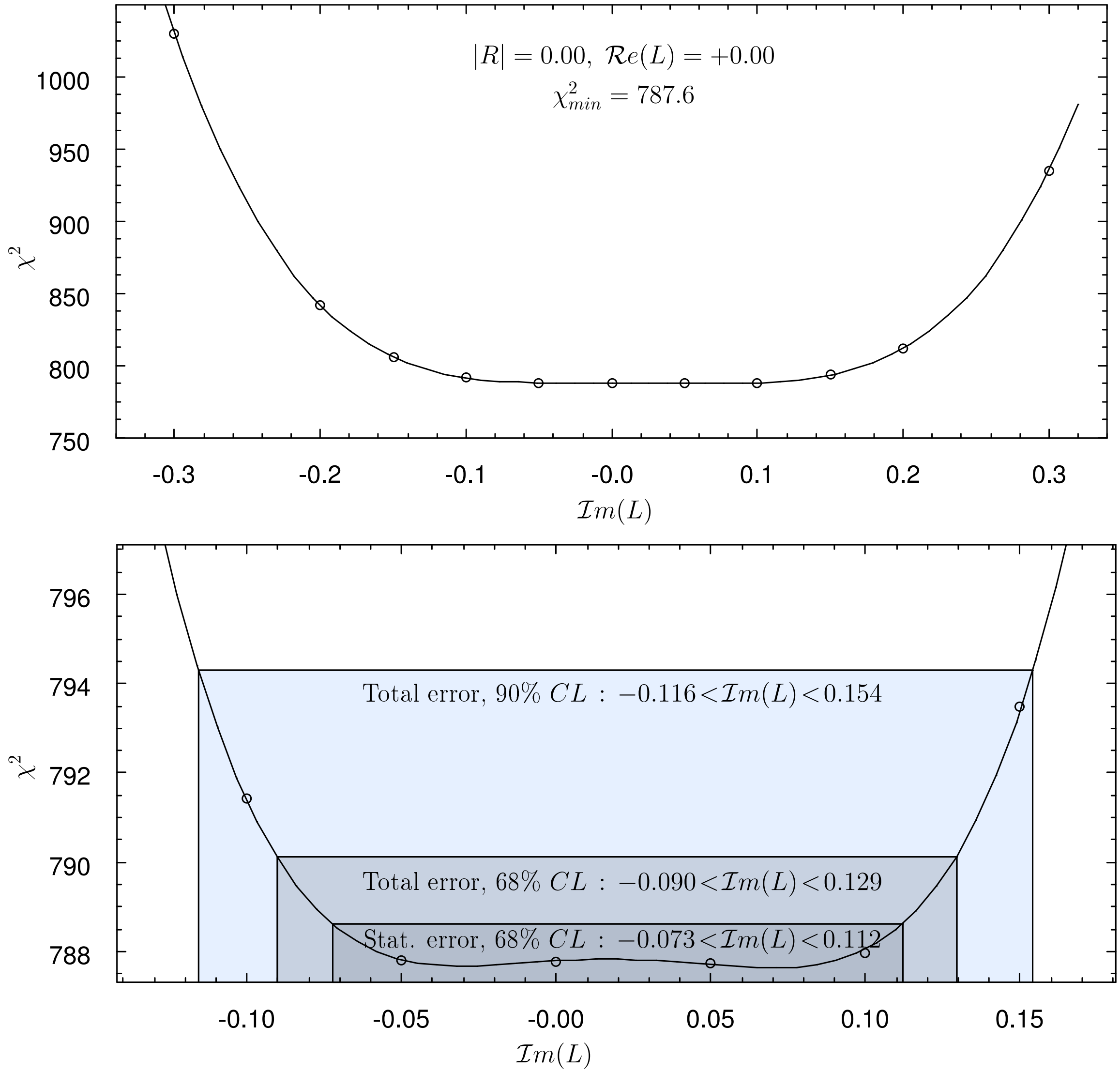

FIGURE D.1: $\chi^2$ as function of the imaginary part of $L$ for the scintillator ADC channel range 750−1550, assuming $|R| = \mathcal{R}e(L) = 0$. The fit over the wider range in $\mathcal{I}m(L)$ is shown in the upper portion and the limits derived are illustrated in the lower portion.

TABLE D.1: Limits on $\mathcal{I}m(L)$ that can be derived from the present experiment for specific values of $\mathcal{R}e(L)$ assuming $|R| = 0$. These limits are based on the total (stat.+syst.) uncertainties at the 68% and 90% confidence levels.

| $\mathcal{R}e(L)$ | $\mathcal{I}m(L)$ (68% $CL$) | $\mathcal{I}m(L)$ (90% $CL$) |
|---|---|---|
| $-0.01$ | $0.019 \pm 0.096$ | $0.019 \pm 0.124$ |
| $0.00$ | $0.020 \pm 0.110$ | $0.019 \pm 0.135$ |
| $+0.01$ | $0.019 \pm 0.123$ | $0.020 \pm 0.146$ |

The detailed analysis including the systematic uncertainties in Sec 4.2 indicated that for $\mathcal{R}e(L) = \mathcal{I}m(L) = 0$ the results of the present experiment can be expressed as

$$\begin{array}{lcll} a & \geq & 0.9960 & \text{Stat. error, } 68\%\ CL \\ a & \geq & 0.9944 & \text{Total error, } 68\%\ CL \\ a & \geq & 0.9916 & \text{Total error, } 90\%\ CL \end{array}$$

where the latter two limits would correspond to the minimum value of $a$ consistent with the data at $\chi^2 = \chi^2_{min} + 2.5$ and $\chi^2 = \chi^2_{min} + 6.7$. Using these same increments and $\chi^2_{min} = 787.6$ the corresponding limits on $\mathcal{I}m(L)$ are shown in Fig D.1.

The same analysis as is presented in Fig D.1 can be made for other values of $\mathcal{R}e(L) \neq 0$. In Tab D.1 we show for $\mathcal{R}e(L) = -0.01$, $0.00$ and $+0.01$ the limits on the $\mathcal{I}m(L)$ for the total error (stat.+syst.) in the present experiment at both 68% $CL$ and 90% $CL$. Direct calculations showed that when combining the present result for $\tilde{a}$ with the latest estimate of $b$ [120] the resulting uncertainty in the value of $a$ is completely dominated by the uncertainty in $\tilde{a}$ (4.9). Combining the result $b = 0.0024(28)$ with the present experiment we obtain using Tab D.1:

$$\mathcal{I}m(L) = 0.020(106) \quad 68\%\ CL \tag{D.2}$$

$$\mathcal{I}m(L) = 0.019(132) \quad 90\%\ CL\ . \tag{D.3}$$

In the analysis presented in Fig 4.10 it is shown that, although the beta-neutrino correlation (4.1) includes the term $b\,(m_e/E_e)$, it is sufficient to approximate this term by $b\,\langle m_e/E_e\rangle$ where $\langle E_e\rangle = 3.40\,\text{MeV}$ is the average of $E_e$ for the data included in the fit. Similarly, for the term linear in the $\mathcal{I}m(L)$ (D.1), if one replaces $p_e$ by

$\langle p_e \rangle = 3.37\,\mathrm{MeV/c}$, the expression for $a$ takes the simple form (for $\mathcal{R}e(L) = |R| = 0$):

$$\begin{aligned} a &= \frac{1 + 0.020\,\mathcal{I}m(L) - 0.25\,\mathcal{I}m(L)^2}{1 + 0.25\,\mathcal{I}m(L)^2} \\ &\simeq 1 + 0.020\,\mathcal{I}m(L) - 0.50\,\mathcal{I}m(L)^2 \qquad (\text{ for } \mathcal{I}m(L) \simeq 0\,) \\ &= 1.0002 - \frac{1}{2}\,(\mathcal{I}m(L) - 0.020)^2 \end{aligned}$$

This approximate expression could be used to obtain essentially the same results as those presented in Tab D.1 (which do not involve the approximations).

The Coulomb correction [33] that is responsible for the linear in $\mathcal{I}m(L)$ in (D.1) is not explicitly the result of time reversal violation in the weak interaction. It alters the impact of a value of $\mathcal{I}m(L) \neq 0$ on the correlation. In terms of the limits that can be placed on $\mathcal{I}m(L)$ that could be attributed directly to time reversal violation in the weak interaction it would seem appropriate to quote the values (for $b = 0.0024(28)$):

$$|\mathcal{I}m(L)_{\mathrm{weak}}| < 0.106 \quad 68\%\ CL \tag{D.4}$$

$$|\mathcal{I}m(L)_{\mathrm{weak}}| < 0.132 \quad 90\%\ CL \tag{D.5}$$

These limits are only marginally larger than those obtained from the present experiment for $|R|$ (see Tab 5.2).

# Bibliography

[1] C. .L. Cowan, Jr., F. Reines, F. .B. Harrison, *et al.*, *Detection of the Free Neutrino: a Confirmation*, Science **124**, 103 (1956)

[2] Frederick Reines and Clyde L. Cowan, Jr., *The neutrino*, Nature **178**, 446 (1956)

[3] E. Fermi, *Tentativo di una teoria dell'emissione dei raggi "Beta" (An Attempt at a Theory of Beta-Ray Emission)*, Ric. Scient. **4**, 491 (1933)

[4] E. Fermi, *Tentativo di una teoria dei raggi Beta. (An Attempt at a Theory of Beta Rays.)*, Nuovo Cim. **11**, 1 (1934)

[5] E. Fermi, *Versuch einer Theorie der $\beta$-Strahlen*, Z. Physik **88**, 161 (1934)

[6] Particle Physics Group, *Review of Particle Physics. Constants, Units, Atomic and Nuclear Properties.*, Phys. Lett. B **592**, 91 (2004)

[7] Sargent, Proc. Roy. Soc. **A139**, 659 (1933)

[8] G. Gamow and E. Teller, *Selection Rules for the $\beta$–Disintegration*, Phys. Rev. **49**, 895 (1936)

[9] W. Pauli, *Die Allgemeinen Prinzipen der Wellenmechanik*, Handbuch der Physik , 83-272 (1933)

[10] B. M. Rustad and S. L. Ruby, *Gamow-Teller Interaction in the Decay of $He^6$*, Phys. Rev. **97**, 991 (1955)

[11] C. H. Johnson, F. Pleasonton, and T. A. Carlson, *Precision Measurement of the Recoil Energy Spectrum from the Decay of $He^6$*, Phys. Rev. **132**, 1149 (1963).

[12] F. Glück, *Order-$\alpha$ radiative correction to $^6He$ and $^{32}Ar$ decay recoil spectra*, Nucl. Phys. A **628**, (1998) 493.

[13] T. D. Lee and C. N. Yang, *Question of Parity Conservation in Weak Interactions*, Phys. Rev. **104**, 254 (1956)

[14] C. S. Wu, and E. Ambler, R. W.Hayward, D. D. Hoppes and R. P. Hudson, *Experimental Test of Parity Conservation in Beta Decay*, Phys. Rev. **105**, 1413 (1957)

[15] E. Ambler, R. W. Hayward, D. D. Hoppes, and R. P. Hudson and C. S. Wu, *Further Experiments on $\beta$ Decay of Polarized Nuclei*, Phys. Rev. **106**, 1361 (1957)

[16] Richard L. Garwin, Leon M. Lederman, and Marcel Weinrich, *Observations of the Failure of Conservation of Parity and Charge Conjugation in Meson Decays: the Magnetic Moment of the Free Muon*, Phys. Rev. **105**, 1415 (1957)

[17] H. Frauenfelder, R. Bobone, E. von Goeler, et al., *Parity and the Polarization of Electrons from $Co^{60}$*, Phys. Rev. **106**, 386 (1957)

[18] Lorne A. Page, and Milton Heinberg, *Measurements of the Longitudinal Polarization of Positrons Emitted by Sodium-22*, Phys. Rev. **106**, 1220 (1957)

[19] S. S. Hanna and R. S. Preston, *Positron Polarization Demonstrated by Annihilation in Magnetized Iron*, Phys. Rev. **106**, 1363 (1957)

[20] M. Goldhaber L. Grodzins, and A. W. Sunyar, *Helicity of Neutrinos*, Phys. Rev. **109**, 1015 (1958)

[21] A. Salam, *On Parity Conservation and Neutrino Mass*, Nuovo Cim. **5**, 299 (1957)

[22] L. Landau, *On the Conservation Laws for Weak Interactions*, Nucl. Phys. **3**, 127 (1957)

[23] T. D. Lee and C. N. Yang, *Parity Nonconservation and a Two-Component Theory of the Neutrino*, Phys. Rev. **105**, 1671 (1957)

[24] W. B. Herrmannsfeldt, D. R. Maxson, P. Stähelin, and J. S. Allen, *Electron-Neutrino Angular Correlation in the Positron Decay of Argon 35*, Phys. Rev. **107**, 641 (1957)

[25] W. B. Herrmannsfeldt, R. L. Burman, P. Stähelin, J. S. Allen, and T. H. Braid, *Determination of the Gamow-Teller Beta-Decay Interaction from the Decay of Helium-6*, Phys. Rev. Lett. **1**, 61 (1958)

[26] James S. Allen, *Determination of the Beta-Decay Interaction from Electron-Neutrino Angular Correlation Experiments*, Rev. Mod. Phys. **31**, 791 (1959)

[27] Y. Fukuda *et al.*, *Evidence for Oscillation of Atmospheric Neutrinos*, Phys. Rev. Lett. 81, 1562 (1998)

[28] J. R. Musser, *et al.*, *Measurement of the Michel Parameter $\rho$ in Muon Decay*, Phys. Rev. Lett. **94**, 101805 (2005)

[29] A. Gaponenko, *et al.*, *Measurement of the muon decay parameter $\delta$*, Phys. Rev. D **71**, 071101(R) (2005)

[30] P. Herczeg, *Beta decay beyond the standard model*, Prog. in Part. and Nucl. Phys, **46/2**, 413 (2001)

[31] Nathal Severijns and Marcus Beck, and Oscar Nevliat-Cuncic, *Tests of the standard electroweak model in nuclear beta decay*, Rev. Mod. Phys. **78**, 9911 (2006)

[32] J. D. Jackson, S. B. Treiman, and H. W. Wyld, Jr., *Possible Tests of Time Reversal Invariance in Beta Decay*, Phys. Rev. **106**, 517 (1957).

[33] J. D. Jackson, S. B. Treiman, and H. W. Wyld, Jr., *Coulomb corrections in allowed beta transitions*, Nucl. Phys. **4**, 206 (1957)

[34] E. G. Adelberger, C. Ortiz, A. García, H. E. Swanson, *et al.*, *Positron-Neutrino Correlation in the* $0^+ \rightarrow 0^+$ *Decay of* $^{32}Ar$, Phys. Rev. Lett. **83**, 1299 (1999).

[35] I. S. Towner and J. C. Hardy, *Superallowed* $0^+ \rightarrow 0^+$ *nuclear* $\beta$*-decays*, Nucl. Phys. A **205**, 33 (1973)

[36] I. S. Towner and J. C. Hardy, *The evaluation of* $V_{ud}$*, experiment and theory*, J. Phys. G **29**, 197 (2003)

[37] J. C. Hardy and I. S. Towner, *Superallowed* $0^+ \rightarrow 0^+$ *nuclear* $\beta$*-decays: A critical survey with tests of the conserved vector current Hypothesis and the standard model*, Phys. Rev. C **71**, 055501 (2005)

[38] G. C. Ball, S. Bishop, J. A. Behr, *et al.*, *Precise Half-Life Measurement for the Superallowed* $0^+ \rightarrow 0^+$ $\beta$ *Emitter* $^{74}Rb$*: First Results from the New Radioactive Beam Facility (ISAC) at TRIUMF*, Phys. Rev. Lett. **86**, 1454 (2001)

[39] J.A. Behr, A. Gorelov, T. Swanson, O. Häusser, K.P. Jackson, M. Trinczek, U. Giesen, J.M. D'Auria, R. Hardy, T. Wilson,P. Choboter, F. Leblond, Ł. Buchmann, M. Dombsky, C.D.P. Levy, G. Roy,B.A. Brown, and J. Dilling, *Magneto-optic Trapping of* $\beta-$*Decaying* $^{38}K^m$, $^{37}K$ *from an on-line Isotope Separator*, Phys. Rev. Lett. **79**, 375 (1997)

[40] T. B. Swanson, D. Asgeirsson, J. A. Behr, A. Gorelov and D. Melconian, *Efficient transfer in double magneto-optical trap system*, J. Opt. Soc. Am. **B15**, No. 11, 2641 (1998)

[41] A. I. Gorelov, J. A. Behr, D. Melconian, M. Trinczek, P. Dube, O. Häusser, U. Giesen, K. P. Jackson, T. Swanson, J. M. D'Auria, M. Dombsky, G. Ball, L. Buchmann, B. Jennings, J. Dilling, J. Schmid, D. Ashery, J. Deutsch, W. P. Alford, D. Asgeirsson, W. Wong, and B. Lee, *Beta-neutrino correlation experiments on laser trapped* $^{38m}K$, $^{37}K$ , Hyperfine Interactions **127**, 373 (2000)

[42] D. Melconian, M. Trinczek, A. Gorelov, W. P. Alford, J. A. Behr, J. M. D'Auria, M. Dombsky, U. Giesen, K. P. Jackson, T. B. Swanson, and W. Wong, *Release of* $^{37}K$ *from catcher foils*, Nucl. Instr. Meth. A **538**, 93 (2005)

[43] A. Gorelov, D. Melconian, W. P. Alford, *et al.*, A. Gorelov, D. Melconian, W. P. Alford, D. Ashery, G. Ball, J. A. Behr, P. G. Bricault, J. M. D'Auria, J. Deutsch, J. Dilling, M. Dombsky, P. Dube, J. Fingler, U. Giesen, F. Gluck, S. Gu, O.äusser, K. P. Jackson,

B. K. Jennings, M. R. Pearson, T. J. Stocki, T. B. Swanson, and M. Trinczek *Scalar interaction limits from the $\beta-\nu$ correlation of trapped radioactive atoms*, Phys. Rev. Lett. **94**, 142501 (2005)

[44] M. Trinczek, A. Gorelov, D. Melconian, W. P. Alford, D. Asgeirsson, D. Ashery, J. A. Behr, P. G. Bricault, J. M. D'Auria, J. Deutsch, J. Dilling, M. Dombsky, P. Dube, S. Eaton, J. Fingler, U. Giesen, S. Gu, O. Häusser, K. P. Jackson, B. Lee, J. H. Schmid, T. J. Stocki, T. B. Swanson, and W. Wong, *Novel Search for Heavy $\nu$ Mixing from the $\beta^+$ Decay of $^{38m}K$ Confined in an Atom Trap*, Phys. Rev. Lett. **90**, 012501 (2003)

[45] D. Melconian, J. A. Behr, D. Ashery, O. Aviv, P. G. Bricault, M. Dombsky, S. Fostner, A. Gorelov, S. Gu, V. Hanemaayer, K. P. Jackson, M. R. Pearson, I. Vollrath, *Measurement of the neutrino asymmetry in the $\beta$ decay of laser-cooled, polarized $^{37}K$*, Phys. Lett. B **649**, 370 (2007)

[46] E. L. Raab, M. Prentiss, A. Cable, S. Chu and D. E. Pritchard, *Trapping of neutral sodium atoms with radiation pressure*, Phys. Rev. Lett. **59**, 2631 (1987)

[47] K. P. Jackson (spokesman), *Atomic PNC in francium: preparations*, TRIUMF Experiment E714, December 1993

[48] O. Häusser (spokesman), *Spin correlations in $\beta^+$ decay of optically trapped $^{37}K$*, TRIUMF Experiment E715, December 1993

[49] E. Hagberg, *et al.*, *Tests of Isospin Mixing Corrections in Superallowed $0^+ \rightarrow 0^+$ $\beta$ Decays*, Phys. Rev. Lett. **73**, 396 (1994)

[50] Barry R. Holstein, *Recoil effects in allowed beta decay: The elementary particle approach*, Rev. Mod. Phys. **46**, 789 (1974)

[51] F. Glück, *Order-$\alpha$ radiative correction calculations for unoriented allowed nuclear, neutron and pion $\beta$ decays*, Computer Physics Communications **101**, 223 (1997)

[52] Phillip Gould, *Laser cooling of atoms to the Doppler limit*, Am. J. Phys., **65**, 1120 (1997)

[53] T. Hänsch and A. Schawlow, Opt. Comm. **13**, 68 (1975)

[54] D. Wineland and H. Dehmelt, *Proposed $10^{14}$ $D\nu <$ nu Laser Fluorescence Spectroscopy on $Tl^+$ Mono-Ion Oscillator III (side band cooling)*, Bull. Amer. Phys. Soc. **20**, 637 (1975)

[55] W. Philips and H. Metcalf, *Laser Deceleration of an Atomic Beam*, Phys. Rev. Lett., **48**, 596 (1982)

[56] S. Chu, L. Hollberg, J. Bjorkholm, A. Cable and A. Ashkin, *Three-dimensional viscous confinement and cooling of atoms by resonance radiation pressure*, Phys. Rev. Lett. **55**, 48(1985)

[57] H. Metcalf and P. van der Straten, *Cooling and trapping of neutral atoms*, Physics Reports **244**, 203 (1994)

[58] V. I. Balykin, V. G. Minogin and V. S. Letokhov, *Electromagnetic trapping of cold atoms*, Rep. Prog. Phys. **63**, 1429 (2000)

[59] G. D. Sprouse and L. A. Orozco, *Laser trapping of radioactive atoms*, Annual Reviews of Nuclear and Particle Science **47**, 429 (1997)

[60] E. Arimondo, W. D. Philips and F. Strumina, editors, *Laser Manipulation of Atoms and Ions*, Amsterdam: North Holland, 1992

[61] C. Monroe, W. Swann, H. Robinson, and C. Wieman, *Very cold trapped atoms in a vapor cell*, Phys. Rev. Lett. **65**, 1571 (1990)

[62] D. R. Swenson and L. W. Anderson, *Relaxation rates for optically pumped Na vapor on silicone surfaces*, Nucl. Instr. Meth. **B29**, 627 (1988)

[63] U. Tanaka and T. Yabusaki, In *Frequency-Stabilized Lasers and Their Applications*, edited by Y. C. Chung, SPIE Proceedings Series, Vol. 1837 (SPIE, Bellingham, WA, 1992), p. 70.

[64] J. M. D'Auria, L. Buchmann, M. Dombsky, *et al.*, *Upgrade of the TRIUMF on-line isotope separator, TISOL*, Nucl. Instr. Meth. **B70**, 75 (1992)

[65] J. M. D'Auria, J. A. Behr, L. Buchmann, *et al.*, *The TISOL facility at TRIUMF: operational status at 10 years*, Nucl. Instr. Meth. **B126**, 7 (1997)

[66] P. Bricault, M. Dombsky, P. Shmor and G. Stanford, *Radioactive ion beams facility at TRIUMF*, Nucl. Instr. Meth. **B126**, 231 (1997)

[67] S. Bishop, R. E. Azuma, L. Buchmann, *et al.*, $^{21}Na(p,\gamma)^{22}Mg$ *Reaction and Oxygen-Neon Novae*, Phys. Rev. Lett. **90**, 162501 (2003)

[68] F. Sarazin, J. S. Al-Khalili, G. C. Ball, *et al.*, *Halo neutrons and the* $\beta$ *decay of* $^{11}Li$, Phys. Rev. C **70**, 031302(R) (2004)

[69] Y. Hirayama, T. Shimoda, H. Izumi, *et al.*, *Study of 11Be structure through* $\beta$*-delayed decays from polarized* $^{11}Li$, Phys. Lett. B **611**, 239 (2005)

[70] R. Sánchez, W. Nörtershäuser, G. Ewald, *et al.*, *Nuclear Charge Radii of* $^{9,11}Li$*: The Influence of Halo Neutrons*, Phys. Rev. Lett. **96**, 033002 (2006)

[71] R. F. Kiefl, W. A. MacFarlane, G. D. Morris, *et al.*, *Low-energy spin-polarized radioactive beams as a nano-scale probe of matter*, Physica B **326**, 189 (2003)

[72] M. Dombsky, P. Bricault, P. Schmor, M. Lane, *ISAC target operation with high proton currents*, Nucl. Instr. Meth. B **204** 191 (2003)

[73] M. Dombsky, P. Bricault and V. Hanemaayer, *Increasing beam currents at the TRIUMF-ISAC Facility; techniques and experiences*, Proceedings of the Sixth International Conference on Radioactive Nuclear Beams (RNB6), Nucl. Phys. A **746**, 32 (2004)

[74] *ISAC-II A project for higher energies at ISAC*,
TRI-99-1 (1999), http://www.triumf.ca/ISAC-II/TRI-99-1.pdf

[75] CRC *Handbook of Chemistry and Physics*, CRC Press, $71^{\text{st}}$ edition, 1991, Editor-in-Chief D.R. Lide.

[76] M. Dombsky, D. Bishop, P. Bricault, *et al.*, *Commissioning and initial operation of a radioactive beam ion source at ISAC*, Rev. Sci. Instr. **71**, 978 (2000)

[77] Michael C. Trinczek, *Limits on Heavy Neutrino Mixing from the Beta Decay of* $^{38m}K$ *Confined in a Magneto-Optical Trap*, PhD Thesis, Department of Chemistry, SFU, 2001

[78] *List of Radioactive Ion Beams at ISAC*,
http://documents.triumf.ca/docushare/dsweb/Get/Document-10962/ISAC

[79] A. R. Miedema and J. W. F. Dorleijn, *Quantitative predictions of the heat of adsorption of metals on metallic substrates*, Surface Science **95**, 447 (1980)

[80] M. Stephens and C. Wieman, *High Collection Efficiency in a Laser Trap*, Phys. Rev. Lett. **72**, 3787 (1994)

[81] J. L. Wiza, *Microchannel Plate Detectors*, Nucl. Instr. Meth. **162**, 587 (1979)

[82] M. Lampton and C. W. Carlson, *Low-distortion resistive anodes for two-dimensional position-sensitive MCP systems*, Rev. Sci. Instrum. **50**, 1093 (1979)

[83] Bicron Corp., *Bicron Data Sheet*, 1997

[84] Dan G. Melconian, *A Positron Detector for Precision Beta Decay experiments from a Magneto-Optic Trap*, MSc Thesis, SFU, 2000

[85] Micron Semiconductor Ltd., *Micron Semiconductor Data Sheet*, BB2-500 design, 1998

[86] Y. Holler, J. Koch, and A. Naini, *A stabilized NE213 scintillator for neutron time-of-flight spectroscopy*, Nucl. Instr. Meth. **204**, 204 (1983)

[87] O. Häusser, TRIUMF E715 Report, 1997

[88] M. Barat, J. C. Brenot, J. A. Fayeton and Y. J. Picard, *Absolute detection efficiency of a microchannel plate detector for neutral atoms*, Rev. of Sci. Instr. **71**, 2050 (2000)

[89] J. Oberheide, P. Wilhelms and M. Zimmer, *New results on the absolute ion detection efficiencies of a microchannel plate*, Meas. Sci. Technol. **8**, 351 (1997)

[90] I. Ben-Itzhak, O. Heber, I. Gertner, and B. Rosner, *Production and mean-lifetime measurement of metastable* $Ar^-$ *ions*, Phys. Rev. A **38**, 4870 (1988)

[91] M. DiStasio and W. C. McHarris, *Electrostatic problems? Relax!*, Am. J. Phys. **47**, 440 (1979)

[92] C. J. Kost and F. W. Jones, *RELAX3D. User's Guide and Reference Manual*, TRI-CD-88-01, January 1992.

[93] H. Houtman, F. W. Jones, and C. J. Kost, *Solution of Laplace and Poisson Equations by RELAX3D*, Computers in Physics **8**, 469 (1994)

[94] D. W. Marquardt, *An Algorithm for Least-Squares Estimation of Nonlinear Parameters*, J. Soc. Ind. Appl. Math. **II**, 431 (1963)

[95] Philip R. Bevington and D. Keith Robinson, *Data Reduction and Error Analysis for the Physical Science*, Second Edition, McGraw-Hill Companies, Inc., 1992

[96] S. Ritt and P. A. Amaudruz, *Midas, User's and Programmer's Manual*, Paul Scherrer Institute and TRIUMF, Version 1.03 (1998)

[97] P. W. Green, *NOVA*, TRIUMF/The University of Edmonton, v.2.0 edition (1995)

[98] *CAMAC C212 Coincidence Buffer. Operating and Service Manual*, Copyright *EG&G/*ORTEC (1972)

[99] N. D. Scielzo, S. J. Freedman, B. K. Fujikawa, and P. A. Vetter, *Measurement of the* $\beta^+ - \nu$ *Correlation using Magneto-optically Trapped* $^{21}Na$, Phys. Rev. Lett. **93**, 102501 (2004)

[100] N. D. Scielzo, *Measurements of the* $\beta - \nu$ *Correlation in the Laser Trapped* $^{21}Na$, PhD Thesis, University of California, Berkeley, 2003

[101] O. Kofoed-Hansen, *Theoretical angular correlations in allowed beta transitions*, Dan. Mat. Fys. Medd. **28**, no. 9, 1 (1954)

[102] S. Baker and R. Cousins, *Clarification of the use of the chi-square and likelihood functions in fits to histograms*, Nucl. Instr. Meth. **221**, 437 (1984)

[103] Glen D. Cowan, *Statistical Data Analysis*, Oxford University Press UK, 1998. ISBN: 0198501552

[104] F. James and M. Roos, *"MINUIT, Function Minimization and Error Analysis", CERN D506 (Long Writeup)*, Available from the CERN Program Library Office, CERN-DD Division, CERN, CH-1211, Geneva 21, Switzerland

[105] E. T. Clifford. Private communication.

[106] Abraham Savitzky and M. J. E. Golay, *Smoothing and Differentiation of Data by Simplified Least Squares Procedures*, Analytical Chemistry **36**, 1627 (1964)

[107] *Savitzky-Golay Smoothing Filters*, Numerical Recepiesin C: The Art of Scientific Computing (ISBN 0-521-43108-5), Chapter 14. Statistical Description of Data, p.650, Copyright (C) 1988-1992 by Cambridge University Press. Programs Copyright (C) 1988-1992 by Numerical Recipes Software.

[108] George M. Lawrence, *Radiance Lifetimes in the Resonance Series of Ar I*, Phys. Rev. **175**, 40 (1968)

[109] C. F. Bunge *et al.*, *Systematic search of excited states of negative ions lying above the ground state of the neutral atom*, Nucl. Instr. Meth. **202**, 299 (1982)

[110] Norma E. Small-Warren, and Lue-Yung Chow Chiu, *Lifetime of the metastable* $^3P_2$ *and* $^3P_0$ *states of rare-gas atoms*, Phys. Rev. A **11**, 1777 (1975)

[111] Hidetoshi Katori and Fujio Shimizu, *Lifetime measurement of the* $1s_5$ *metastable state of argon and krypton with a magneto-optical trap*, Phys. Rev. Lett. **70**, 3545 (1993)

[112] M. Kaminsky, *Atomic and Ionic Impact Phenomena on Metal Surfaces*, Springer-Verlag, 1965

[113] G. W. Fraser, *The ion detection efficiency of microchannel plates (MCPs)*, Int. J. Mass Spectrom. **215**, 13 (2002)

[114] M. Galanti, R. Gott, and J. F. Renaud, *A High Resolution, High Sensitivity Channel Plate Image Intensifier for Use in Particle Spectrographics*, Rev. Sci. Instrum. **42**, 1818 (1971)

[115] R. S. Gao, P. S. Gibner, J. H. Newman, *et al.*, *Absolute and angular efficiencies of a microchannel-plate position-sensitive detector*, Rev. of Sci. Instr. **55**, 1756 (1984)

[116] W. F.Chan, G. Cooper, X. Guo, *et al.*, *Absolute optical oscillator strength for the electronic excitation of atoms at high resolution. III. The photoabsorption of argon, krypton and xenon*, Phys. Rev. A **46**, 149 (1992)

[117] Z. Chen, W. R. Johnson, L. Spruch, *Atomic screening effects on electron-neutrino angular correlation and* $\beta$*-decay asymmetry in allowed transitions*, Phys. Rev. C **40**, 1376 (1989)

[118] D. A. Verner, G. J. Ferland, K. T. Korista, *et al.*, *Atomic data for astrophysics. II. New analytic fits for photoionization cross sections of atoms and ions*, Astrophys. J. 465, 487 (1996)

[119] N. D. Scielzo, S. J. Freedman, B. K. Fujikawa and P. A. Vetter, *Recoil-ion charge-state distribution following the* $\beta^+$ *decay of* $^{21}Na$, Phys. Rev. A **68**, 022716 (2003)

[120] G. Savard, F. Buchinger, J. A. Clark, *et al.*, *Q Value of the Superallowed Decay of 46V and Its Influence on Vud and the Unitarity of the Cabibbo-Kobayashi-Maskawa Matrix*, Phys. Rev. Lett. **95**, 102501 (2005)

[121] I. S. Towner and J. C. Hardy, *Improved calculation of the isospin-symmetry-breaking corrections to superallowed Fermi $\beta$ decay*, Phys. Rev. C **77**, 025501 (2008)

[122] E. T. Clifford, E. Hardberg, V. T. Koslowsky, H. Schmeing, and R. E. Azuma, *Measurements of the response function of a hybrid detector telescope to monoenergetic beams of positrons in the energy range 0.8-3.8 MeV*, Nucl. Instr. Meth. **224**, 440-447 (1984)

[123] B. Brehm, J. Grosser, T. Ruscheinski and M. Zimmer, *Absolute detection efficiencies of a microchannel plate detector for ions*, Meas. Sci. Technol. **7**, 953 1995

[124] Particle Data Group, *Probability, statistics, and Monte Carlo*, Phys. Rev. D **45**, III.39 (1992)

[125] A. García, *Weak interactions and fundamental symmetries with rare isotopes*, Nucl. Phys. A **746**, 298c (2004)

[126] Bruce A. Campbell, David W. Maybury, *Constraints on scalar couplings from $\pi^{\pm} \to l^{\pm}\nu_l$*, Nucl. Phys. **B709**, 419 (2005)

[127] Takeyasu M. Ito and Gary Prézeau, *Neutrino Mass Constraints on $\beta$ Decay*, Phys. Rev. Lett. **94**, 161802 (2005)

[128] I. B. Khriplovich and S. K. Lamoreaux, *CP-Violation Without Strangness*, Springer-Verlag, 1997

[129] J. A. Behr (spokesman), *Upgrade of $^{38\mathrm{m}}K$ $\beta - \nu$ Correlation*, TRIUMF Experiment S1070, December 2005

[130] RoentDek Handels GmbH, www.roentdek.com

[131] A. Czasch, J. Milnes, N. Hay, W. Wicking, O. Jagutzki, *Position- and time-sensitive single photon detector with delay-line readout*, Nucl. Instr. Meth. A **580**, 1066 (2007)

[132] J. Baró, J. Sempau, J. M. Fernández-Varea and F. Salvat, *PENELOPE: An algorithm for Monte Carlo simulation of the penetration and energy loss of electrons and positrons in matter*, Nucl. Instr. Meth. B **100**, 31 (1995)

[133] J. Sempau, E. Acosta, J. Baró, J. M. Fernández-Varea and F. Salvat, *An algorithm for Monte Carlo simulation of the coupled electron-photon transport*, Nucl. Instr. Meth. B **132**, 377-390 (1997)

[134] J. Sempau, J. M. Fernández-Varea, E. Acosta and F. Salvat, *Experimental benchmarks of the Monte Carlo code PENELOPE.* Nucl. Instr. Meth. B **207**, 107-123 (2003)

[135] J. W. Martin, J. Yuan, S. A. Hoedl, *et al.*, *Measurement of electron backscattering in the energy range of neutron $\beta$ decay*, Phys. Rev. C **68**, 055503 (2003)

[136] J. W. Martin, J. Yuan, M. J. Betancourt, *et al.*, *New measurements and quantitative analysis of electron backscattering in the energy range of neutron $\beta-$decay*, Phys. Rev. C **73**, 015501 (2006)

[137] G. Audi, O. Bersillon, J. Blachot and A. H. Wapstra, *The NUBASE evaluation of nuclear and decay properties*, Nucl. Phys. A **729**, 3 (2003)

[138] E. Hagberg, I. S. Towner, T. K. Alexander, *et al.*, *Measurement of the l-forbidden Gamow-Teller branch of $^{37}K$*, Phys. Rev. C **56**, 135 (1997)

[139] P. A. Vetter and J. R. Abo-Shaeer, S. J. Freedman and R. Maruyama, *Measurement of the $\beta - \nu$ correlation of $^{21}Na$ using shakeoff electrons*, Phys. Rev. C **77**, 035502 (2008)

[140] J. A. Behr spokesman, *Search for Tensor Interactions in Recoil Nucleus Singles in Decay of Polarized $^{80}Rb$*, TRIUMF Experiment S956

[141] http://www.comsol.com